BRNO UNIVERSITY OF TECHNOLOGY

Central European Institute of Technology BUT

DOCTORAL THESIS

Brno, 2024 Mgr. Jorge Andres Navarro Giraldo

BRNO UNIVERSITY OF TECHNOLOGY
VYSOKÉ UČENÍ TECHNICKÉ V BRNĚ

CENTRAL EUROPEAN INSTITUTE OF TECHNOLOGY BUT
STŘEDOEVROPSKÝ TECHNOLOGICKÝ INSTITUT VUT

THEORETICAL STUDY OF LOW-ENERGY EXCITATIONS IN REDUCED-DIMENSIONAL MATERIALS

TEORETICKÉ STUDIUM NÍZKOENERGETICKÝCH EXCITACÍ V REDUKOVANÝCH ROZMĚRECH MATERIÁLŮ

DIZERTAČNÍ PRÁCE
DOCTORAL THESIS

AUTHOR — Mgr. Jorge Andres Navarro Giraldo
AUTOR PRÁCE

SUPERVISOR — doc. Dr. Ing. Petr Neugebauer, Ph.D.
VEDOUCÍ PRÁCE

CO-SUPERVISOR — Dr. Vinicius T. Santana
ŠKOLITEL SPECIALISTA

BRNO 2024

Abstrakt

V této práci zkoumáme elektronické vlastnosti grafenu a grafitu v mezích redukované dimenzionality, tj. když jsou elektrony efektivně omezeny na jednu (1D) nebo dvě dimenze (2D). Výběr těchto materiálů je veden jejich pozoruhodnými vlastnostmi a různými elektronickými režimy, kterých lze dosáhnout při nízkých teplotách a za působení vnějších magnetických polí. Zaměřujeme se na teoretický popis jejich základního elektronického stavu a nízkoenergetických excitací a jak se projevují při magnetospektroskopickém měření. Využitím různých analytických, numerických a ab-initio teoretických metod k predikci a podpoře experimentálních výsledků magnetooptické spektroskopie a měření elektronického transportu zkoumáme tři problémy, které vyzdvihují množství vyvstávajících fyzikálních jevů: i) vznik vln hustoty spinu v grafitu v důsledku přechodu od 3D k 1D elektronickému chování při vysokých magnetických polích, ii) slabou lokalizaci v grafenu vyvstávající ze zvýšeného koherentního elektronického transportu ve 2D systému a její detekci sub-THz magnetospektroskopií a iii) souhru mezi grafenem a jednomolekulárními magnety, která kombinuje pozoruhodnou laditelnost elektronických vlastností grafenu s magnetismem na molekulární hranici.

Abstract

In this thesis, we investigate the electronic properties of graphene and graphite in the limit of reduced dimensionality, i.e., when electrons are effectively confined to one (1D) or two dimensions (2D). The selection of these materials is driven by their remarkable properties and different electronic regimes that can be achieved at low temperatures and under external magnetic fields. We focus on the theoretical description of their electronic ground state and low-energy excitations and how they manifest in a magneto-spectroscopic measurement. Employing various analytical, numerical, and ab initio theoretical methods to predict and support experimental results of magneto-optical spectroscopy and electronic transport measurements, we investigate three problems that highlight the plethora of physical phenomena emerging in them: i) the formation of spin-density waves in graphite due to the crossover from 3D to 1D electronic behavior at high magnetic fields, ii) the weak localization in graphene arising from the enhanced coherent electronic transport in a 2D system and its detection by sub-THz magneto-spectroscopy, and iii) the interplay between graphene and single-molecule magnets, which combine the notable tuneability of the electronic properties of graphene with magnetism at the molecular limit.

Klíčová slova

Grafen; Grafit; Magnetooptická spektroskopie; Vlny hustoty spinu, Elektronický transport; Koherentní elektronický transport, Slabá lokalizace, Jednomolekulární magnety, Hartreeho-Fockova aproximace, Teorie funkcionálu hustoty, Kompletní aktivní prostor soběstačné aproximace pole.

Keywords

Graphene; Graphite; Magneto-optical spectroscopy; Spin-density waves; Electronic transport; Coherent electronic transport; Weak localization; Single-molecule magnets; Hartree-Fock approximation; Density functional theory; Complete-active space self-consistent field approximation.

NAVARRO GIRALDO, Jorge Andres. *Theoretical Study of Low-Energy Excitations in Reduced--Dimensional Materials*. Brno, 2024. 132 s. Dizertační práce. Brno University of Technology. Central European Institute of Technology BUT. Vedoucí práce Petr NEUGEBAUER.

I hereby declare that I have written my doctoral thesis topic on the theme of *Teoretické studium nízkoenergetických excitací v redukovaných rozměrech materiálů* independently, under the guidance of the thesis supervisor, doc. Dr. Ing. Petr Neugebauer, Ph.D., and using literature and other sources of information which are all properly quoted in the thesis and detailed in the list of literature at the end of the thesis.

Mgr. Jorge Andres Navarro Giraldo

Acknowledgements

I gratefully acknowledge all the people and institutions that contributed to this work in different ways and extents. I would like to thank doc. Ing. Petr Neugebauer, Ph.D., for his guidance, enormous support, and for giving me the chance to work on this project. I greatly appreciate Dr. Denis Basko at Laboratoire de Physique et Modélisation des Milieux Condensés in Grenoble, France, for his guidance and supervision on the theory of charge- and spin-density waves in graphite at high magnetic fields. I am greatly indebted to my colleagues from the Magneto-optical THz Spectroscopy -MOTES- group at CEITEC, who patiently taught me several experimental methods presented in this work: Dr. Vinicius T. Santana, Dr. Oleksii Laguta, Dr. Ivan Nemec, Dr. Ivan Šalitroš, Dr. Jakub Hruby, Dr. Matuš Šedivy, Dr. Miroslav Bartoš, and Dr. Lubomír Havlíček. I acknowledge Prof. Vladimir Fal'ko and Dr. Sergey Slizovskiy for their support during my internship at the National Graphene Institute in Manchester, U.K., where I learned the analysis of magnetoconductivity measurements in graphene and graphite. Thanks to Prof. Paola Barbara and Prof. Amy Liu at Georgetown University, U.S.A., for their guidance on molecular deposition on graphene and numerous discussions about the properties of these systems. Thanks to Dr. D. Kurt Gaskill at the University of Maryland for his advice and deep insight into the properties of graphene on SiC.

I would also like to thank all my colleagues who enriched my doctoral studies with valuable discussions, constructive criticism, and great experiences. Thanks to my colleagues from the MOTES group, Dr. Antonín Sojka, Dr. Artur Solodovnyk, Dr. Pawel Jewula, Dr. Jana Dubnická Midlíkova, Dr. Jana Juráková, Mgr. Oleh Martyniuk, Mgr. Jan Dubský, Mgr. Lucie Kotásková, Mgr. Ikram Zdeg, and Mgr. Muhammad Tahsin. To my colleagues from the CEITEC student committee, Kateřina Linhartová, Lenka Dostalová, Adriana Ladungová, Ketty Sinigaglia, Katarina Novčić, Anna Cherian, Bilal Bawab, Kaushik Baishya, Radhika Nittoor Veedu, and Michaela Vojníková. To my colleagues at CEITEC, Valeria Butera, Azin Trllová Shahsavar, Michaela Sanna, and Xia Peng. Special thanks to my friends Bruno Jimenez, Nicolas Medina, Diego Muñoz, Diego Bernal, Cristian Sierra, and Manuel Cardenas.

I am immensely indebted to my family for their unconditional support, constant motivation, and love during the five years it took to complete this work. Thanks to my parents Jorge and Myriam, and my siblings Sergio, Juan Jose, and Daniela Estefania, who gave me a strong foundation on ethics and discipline. Lastly, I would like to thank the person without whom this work could not have been done at all. Infinite thanks to my wife, Lenka, for her unrelenting support, motivation, love, and strength to overcome all obstacles. Lenka, thank you for giving me my children, Santiago and Cristina, the light of my life.

This research has been financially supported through the CzechNanoLab project LM2023051, funded by the Ministry of Education, Youth and Sports of the Czech Republic (MEYS CR); the INTER-EXCELLENCE Programme of the MEYS CR (grant LTAUSA19060), the European Research Council ERC under the European Union's Horizon 2020 Research and Innovation Programme (grant No. 714850), the Grant Agency of the Czech Republic (GAČR grant GA22-23760S), the CEITEC internal grants CEITEC VUT-J-22-8088 and CEITEC-J-21-7508, and the Brno City Municipality through the Brno Ph.D. Talent 2019 Scholarship.

Mgr. Jorge Andres Navarro Giraldo

Contents

Introduction

The discovery of graphene [1], the first two-dimensional material ever observed, prompted intense research activity around it. One of the remarkable properties of graphene is the linear dispersion of the energy bands, which implies that electrons and holes are described by an effective Dirac equation for massless particles [2], instead of the Schrödinger equation. Consequently, the charge carriers behave as relativistic fermions, where the Fermi velocity takes the role of the speed of light [2]. This fact allows for performing complex experiments of high-energy physics on a solid-state system [3, 4], and at the same time, positions graphene as a strong candidate for the fabrication of next-generation electronic devices.

Graphene boosted the search for more reduced-dimensional materials, where electrons are effectively confined to one or two spatial dimensions. This class of materials is interesting because they can exhibit quantum phenomena such as strong electron correlations [5], coherent electronic transport [6, 7], non-trivial topological phases [8, 9], and superconductivity [10, 11]. Nowadays, a plethora of materials with interesting properties are known, ranging from other two-dimensional systems like phosphorene [12], silicene [13], hexagonal boron nitride [14], to few-atoms thick multilayer graphene, transition-metal dichalcogenides [15], and van der Waals heterostructures combining several of these systems [16]. Furthermore, drastic changes in the systems can be induced by engineering different stacking and orientations between the constituent layers. For instance, superconductivity arises in a graphene bilayer where the top layer is rotated at certain angles with respect to the bottom layer [17], and topological properties of the charge carriers arise in rhombohedral graphite [18], which follows a different stacking order compared to conventional graphite. Currently, this is a very active research topic that might have profound consequences in fundamental research and could lead to interesting technological applications.

Successful integration of these novel materials into electronic devices requires a deep knowledge of their electronic properties. In general, the properties of materials are described in terms of their ground state and their elementary excitations [19]. Elementary excitations are "approximate, long-lived eigenstates of a many-body system, which evolve essentially independently of each other and are characterized (in a translationally invariant system) by a definite energy-momentum relation" [20]. A typical example of elementary excitations are the charge carriers in a metal or semiconductor at ambient conditions. Their origin lies in the individual electrons composing the system; however, due to electronic interaction with the periodic ionic potential and electron-electron interactions, electrons behave as if they had a different mass. Such elementary excitations are called "quasiparticles" and are almost independent of each other [20]. In graphene, electron interaction with the ionic potential of a distinct crystal symmetry is responsible for their behavior as massless quasiparticles [2]. Other elementary excitations are excitons (electron-hole bound states), magnons, cooper pairs, and phonons. Additionally, some materials are interesting because their ground state experiences electronic phase transitions under external conditions; for example, the emergence of charge- and spin-density waves in graphite at low temperatures and high magnetic fields [21, 22].

Several experimental methods are applied to the study of the electronic properties of materials. Traditionally, electronic properties are studied through transport experiments, where metallic contacts are applied to the sample to measure changes in longitudinal and transversal

direct current (DC) conductivity as a function of magnetic field, gate voltages, temperature, or pressure. In such experiments, the charge carrier density, Fermi energy, scattering characteristic times, and electron mobility are obtained by analyzing the Hall effect and Shubnikov-de Haas oscillations. Another important method is angle-resolved photoemission spectroscopy (ARPES), in which the band structure and Fermi surface are directly mapped. However, it has a low resolution for bands below the Fermi energy and is not sensitive to bands above it. The method we are primarily interested in and will discuss in more detail in the present doctoral thesis is magneto-optical spectroscopy with microwaves at sub-THz and far-infrared frequencies. In such experiments, electromagnetic radiation is directed at the sample, and the alternating current (AC) conductivity is investigated by analyzing the absorbed radiation by the sample as a function of the magnetic field [23]. This gives information about electronic transport properties and the band structure, the latter being inferred by the cyclotron resonance phenomenon. Magneto-optical spectroscopy presents some advantages compared to DC transport experiments; for instance, it does not require the application of metallic contacts to the sample, which is time-consuming and often leads to contamination. It also gives information about magnetic impurities [24], and is capable of probing a large sample area. The disadvantage is the increased complexity in the analysis of AC conductivity measurements compared to the DC counterpart, which requires a deeper understanding of the interaction between light at such frequencies and electrons in different regimes induced by low temperatures and external magnetic fields.

The present doctoral thesis focuses on studying low-energy elementary excitations in selected reduced-dimensional materials, emphasizing their magneto-optical response from theoretical and experimental perspectives. The materials we chose for this end are graphene and graphite, which present a rich magneto-optical response due to the relativistic nature of graphene's charge carriers and the different electronic ground states appearing in graphite at high magnetic fields and low temperatures. We develop and apply a variety of theoretical methods to describe electron behavior at different regimes induced by low temperatures and magnetic fields, in particular, whether they experience Landau quantization or not, and take it as a basis to compute the conductivity generated by microwave radiation. The versatility of magneto-optical methods in the sub-THz and far-infrared regimes will be explained, describing several phenomena observed in them, namely, cyclotron resonances, Shubnikov-de Haas oscillations, and weak localization, and how to extract the relevant physical properties from them. With this in mind, the framework is laid for studying other reduced-dimensional materials.

The structure of the thesis is as follows. In Chapter 1, the theoretical aspects are introduced. In particular, the crystal structure, Brillouin zone, and band structure of graphene, bilayer graphene, and graphite are discussed in detail. This is followed by a brief review of electrons in a magnetic field, covering the case of free electrons and electrons in a crystal, where the topic of energy quantization into Landau levels, known as Landau quantization, is presented. We introduce the optical conductivity in the classical limit and its dependence on an external magnetic field and the frequency of the electric field, and its computation for cyclotron resonances and Shubnikov-de Haas oscillations. The chapter is closed with an introduction to electron-electron interactions, presenting the Hartree-Fock method in some detail. Chapter 2 deals with a theoretical study of spin-density waves (SDW) in graphite, which appear at high magnetic fields (~ 75 T) and low temperatures. We arrive at an analytic solution to the problem and perform numerical solutions under some approximations that permit us to find the energy bands of the SDW. With this information, we calculate the magneto-optical spectra of the SDWs, finding that it enables certain electronic transitions that might allow the identification of SDWs in a far-infrared spectroscopy experiment. Chapter 3 presents a study of the weak localization in graphene measured by sub-THz spectroscopy. We perform a thorough characterization of graphene samples by transport experiments and magneto-optical spectroscopy at low frequencies (~ 10 GHz) and sub-THz frequencies. We demonstrate that when the frequency of the

electromagnetic excitation is comparable with the characteristic scattering rate of dephasing, the spectra acquires a frequency dependence not observed before in graphene. In Chapter 4, we take advantage of graphene's versatility and analyze its properties as a substrate for the deposition of single-molecule magnets. Single-molecule magnets present slow relaxation of magnetization at a molecular level [25], bringing magnetic properties to the ultimate spatial limit determined by the molecular size. We employ density functional theory (DFT) and complete active space self-consistent field (CASSCF) theory to predict the properties of the molecular interaction with graphene, such as binding energies, changes in the molecular geometry and electronic structure, charge transfer, and molecular magnetic properties, some of which were in agreement with experimental results. Chapter 5 covers the main conclusions, the references are found in Chapter 6, and Chapter 7 shows the publications and scientific outputs of my doctoral studies. Finally, the appendices cover more detailed experimental results, and analytical and numerical calculations employed throughout the thesis.

1. Theoretical Framework

1.1. Crystal Structure, Brillouin Zone, and Band Structure

The electronic properties of materials are mostly influenced by the type of atoms that conform them, and how such atoms are arranged in them. While other phenomena also affect electronic behavior, whether they are internal, such as impurity atoms and disorder, or external, such as temperature and magnetic field, they can be considered at later stages of the theoretical developments. Therefore, we will now focus on the crystal structure of the materials of our interest, and their corresponding reciprocal lattice and Brillouin zone, being necessary concepts for understanding their band structures.

1.1.1. Graphene

Graphene is an important material, not only because by itself is an interesting system, but also because it is the basic component of other multilayer carbon-based materials, such as bilayer graphene, multilayer graphene and graphite. Although graphene was isolated recently, its crystal structure and theoretical band structure has been known since 1947 by the work of Wallace [26]. In graphene, the 2s orbital of individual carbon atoms hybridize with the other $2p_x$ and $2p_y$ orbitals, forming what is known as sp^2 hybridization. Such hybridized orbitals form strong σ bonds with three neighboring carbon atoms, generating the well-known honeycomb lattice of graphene, with interatomic distance between nearest neighbors of $a = 1.42$ Å. The remaining $2p_z$ electronic orbitals of neighboring atoms form bonding π and antibonding π^* orbitals, and are responsible for electric conduction in the material.

The carbon atoms of graphene do not constitute a Bravais lattice, where the lattice should look the same at each point[1]. Instead, the graphene lattice is divided into two sublattices, denoted A and B, and the Bravais lattice is defined as only one of them (for instance, the white carbon atoms in Fig. 1.1). In this scheme, the unit cell of the Bravais lattice contains two carbon atoms, one of each sublattice. Since each carbon atom contributes with one conducting electron, this fact implies a degeneracy in the energy bands known as sublattice pseudospin degeneracy [2].

The associated reciprocal lattice of graphene is a hexagonal lattice (also called triangular lattice). For this reason, the Brillouin zone (BZ) is hexagonal, with high-symmetry points Γ, K, and K' depicted in Fig. 1.1. The corners of the BZ, denoted by K and K', are inequivalent since they are not connected by reciprocal lattice vectors. Such inequivalence is the reason of an additional degeneracy in graphene's charge carriers, denoted as valley degeneracy due to the location of conduction band valleys at these points, as will be shown in the following paragraphs. Fig. 1.1 shows the crystal structure of graphene, as well as its Bravais lattice points, lattice vectors, unit cell, and Brillouin zone.

The first description of the band structure of graphene was done by Wallace [26] in his study of the electronic properties of graphite. He applied the tight-binding model, taking as a starting

[1] This is clear by looking at Fig. 1.1 and noting that white atoms have a nearest neighbor directly below, while the dark grey atoms have a nearest neighbor directly above. In a Bravais lattice, there must not be such differences between lattice points.

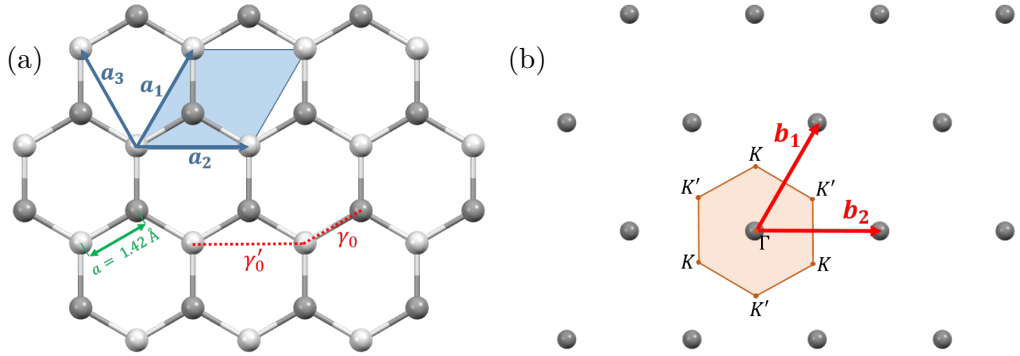

Figure 1.1: Crystal structure and reciprocal lattice of graphene. (a) Crystal structure with sublattices A and B represented by white and dark grey spheres, respectively. The lattice vectors are represented by $\boldsymbol{a}_1$ and $\boldsymbol{a}_2$, while $\boldsymbol{a}_3$ is necessary for the band structure in Eq. (1.1); the unit cell is shaded in blue, and the tight-binding couplings between nearest and next-nearest neighbors are γ_0 and γ_0', respectively. (b) Reciprocal lattice, with lattice sites in dark grey, the reciprocal lattice vectors are $\boldsymbol{b}_1$ and $\boldsymbol{b}_2$, and the Brillouin zone is shaded in orange, with high-symmetry points represented by Γ, K and K'.

point a single layer of graphite and later adding other terms that represent hopping amplitudes with neighbouring layers. By restricting his model to a single graphite layer he ended up with the electronic bands of graphene in the tight-binding approximation, which takes the following form if interaction up to next-nearest neighbors is considered [27]

$$\varepsilon_\lambda(\boldsymbol{k}) = \lambda\gamma_0\sqrt{3 + 2\sum_{i=1}^{3}\cos(\boldsymbol{k}\cdot\boldsymbol{a}_i)} + \gamma_0'\left[3 + 2\sum_{i=1}^{3}\cos(\boldsymbol{k}\cdot\boldsymbol{a}_i)\right], \tag{1.1}$$

where $\lambda = \pm 1$ is the valence (-1) or conduction (+1) band index, $\boldsymbol{k} = (k_x,k_y)$ is a wave vector in the BZ, $\boldsymbol{a}_i$ are vectors that connect neighboring atoms within the same sublattice as shown in Fig. 1.1 (a), and $\gamma_0 = -3$ eV, $\gamma_0' = 0.1\gamma_0$ [27] are the hopping amplitudes between nearest and next-nearest neighbors, respectively. Fig. 1.2 (a) shows the band structure of graphene in the entire Brillouin zone in the tight-binding approximation. The number of bands resulting from the tight-binding model is equal to the total number of atomic orbitals within the unit cell, in this case two, since each A and B site contributes with a $2p_z$ orbital. At the corners of the BZ, conduction band valleys and valence band mountains meet but do not overlap, such that there is no band gap between them. The Fermi energy at charge neutrality coincides with these touching points, that correspond to the energies of the K and K' points. This feature gives graphene a semi-metallic character, due to the very small Fermi surface containing few electronic states available for conduction.

It was quickly noted by Wallace that in the low-energy regime ($\varepsilon_\lambda(\boldsymbol{k}) \ll |\gamma_0|$) where the small γ_0' hopping from next-nearest neighbors can be neglected, the energy dispersion follows a linear relation in the vicinity of K and K'. Defining $\boldsymbol{k} = \boldsymbol{K} + \boldsymbol{q}$, being $\boldsymbol{K}$ (-$\boldsymbol{K}$) a vector indicating the position of a K (K') point, and $\boldsymbol{q} = (q_x,q_y,0)$ a small vector such that $q = |\boldsymbol{q}| \ll |\boldsymbol{K}| \sim 1/a$, the energy dispersion in the vicinity of K and K' is

$$\varepsilon_\lambda(\boldsymbol{q}) = \lambda\frac{3|\gamma_0|aq}{2} = \lambda\hbar v_{\mathrm{F}} q, \tag{1.2}$$

with $v_{\mathrm{F}} = 3|\gamma_0|a/2\hbar$ the Fermi velocity of electrons in the system [27]. The conduction and valence bands are symmetric within the low-energy limit, indicating that there is electron-hole symmetry in graphene. Nevertheless, the symmetry is broken if next-nearest neighbor hopping

γ_0' is considered [27]. The previous equation is only valid in the low-energy limit $\varepsilon_\lambda(\boldsymbol{q}) \ll |\gamma_0|$. The linear dispersion in the vicinity of the K and K' is shown in Fig. 1.2 (b).

The linear dispersion has profound consequences on the dynamics of electrons in graphene, because such behavior is distinctive of ultrarelativistic free particles, like photons. As a consequence, electrons are now described by an effective Dirac equation, valid for relativistic fermions, where the Fermi velocity takes the role of an effective speed of light. This is not the case of low-energy excitations in conventional semiconductors, which obey the non-relativistic Schrödinger equation that follows a quadratic dispersion. The effective Hamiltonian for electrons and holes in graphene, close to the K points and taking into account sublattice and valley degeneracy, is given by

$$\mathcal{H}(\boldsymbol{q}) = \hbar v_\mathrm{F} \tau_z \otimes \boldsymbol{\sigma}\cdot\boldsymbol{q} = \begin{pmatrix} \mathcal{H}_{\xi=+1} & 0 \\ 0 & \mathcal{H}_{\xi=-1} \end{pmatrix} = \begin{pmatrix} \hbar v_\mathrm{F}\boldsymbol{\sigma}\cdot\boldsymbol{q} & 0 \\ 0 & -\hbar v_\mathrm{F}\boldsymbol{\sigma}\cdot\boldsymbol{q} \end{pmatrix} \tag{1.3}$$

with $\otimes$ representing the tensor or exterior product, $\xi = +1$ (-1) denoting the valley K (K'), $\boldsymbol{\sigma} = (\sigma_x,\sigma_y,\sigma_z)$ the Pauli matrices related to the sublattice degree of freedom

$$\sigma_x = \begin{pmatrix} 0 & 1 \\ 1 & 0 \end{pmatrix}, \quad \sigma_y = \begin{pmatrix} 0 & -i \\ i & 0 \end{pmatrix}, \quad \sigma_z = \begin{pmatrix} 1 & 0 \\ 0 & -1 \end{pmatrix}, \tag{1.4}$$

and τ_z the z component of the Pauli matrices but acting on the valley degree of freedom. In Eq. (1.3), the term $\mathcal{H}_\xi = \xi\hbar v_\mathrm{F}\boldsymbol{\sigma}\cdot\boldsymbol{q}$ is equivalent to the Dirac Hamiltonian for massless fermions, therefore, the total Hamiltonian is composed by two copies of the Dirac Hamiltonian, one for each valley and having sign +1 (-1) for valley K (K'). For this reason, the points where the conduction and valence band met in a system with linear dispersion are called Dirac points, which coincide with the K and K' points of graphene. In the usual Dirac Hamiltonian, the Pauli matrices $\boldsymbol{\sigma}$ are related to the spin, while in this case, they are related to graphene sublattices, such that "spin up" corresponds to one sublattice A and "spin down" to sublattice B. For this reason, the sublattice degree of freedom is also referred to as the sublattice pseudospin [27]. In addition to this, there is a second set of Pauli matrices $\boldsymbol{\tau}$, related to the valley degree of freedom (although only τ_z appears in the Hamiltonian) [27]. This valley degree of freedom can therefore be associated to a "valley pseudospin" operator, such that the two valleys K and K' can be interpreted as the two eigenstates of it. In conclusion, electrons and holes in graphene have a fourfold degeneracy apart from the real spin: twofold lattice pseudospin degeneracy and twofold valley pseudospin degeneracy. These degeneracies can be lifted by physical mechanisms that break the sublattice symmetry, as in the interaction with a SiC substrate [28], or by lateral confinement, as in a graphene nanoribbon [29].

The wave functions associated to the effective Hamiltonian are given by

$$\Psi_\lambda^{\xi=+}(\boldsymbol{q}) = \frac{1}{\sqrt{2}}\begin{pmatrix} 1 \\ \lambda e^{i\varphi_q} \\ 0 \\ 0 \end{pmatrix}, \quad \Psi_\lambda^{\xi=-}(\boldsymbol{q}) = \frac{1}{\sqrt{2}}\begin{pmatrix} 0 \\ 0 \\ 1 \\ -\lambda e^{i\varphi_q} \end{pmatrix}, \tag{1.5}$$

with φ_q the polar angle in reciprocal space

$$\varphi_q = \arctan\left(\frac{q_y}{q_x}\right), \tag{1.6}$$

and the Hamiltonian written in the basis of

$$\Psi(\boldsymbol{q}) = \begin{pmatrix} \psi_{\mathrm{A},K}(\boldsymbol{q}) \\ \psi_{\mathrm{B},K}(\boldsymbol{q}) \\ \psi_{\mathrm{A},K'}(\boldsymbol{q}) \\ \psi_{\mathrm{B},K'}(\boldsymbol{q}) \end{pmatrix}, \tag{1.7}$$

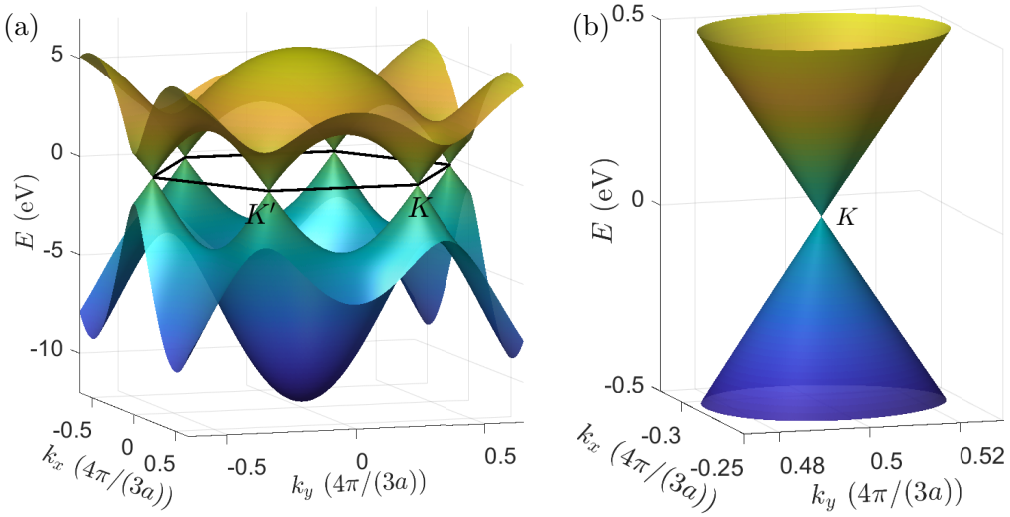

Figure 1.2: (a) Band structure of graphene in the entire BZ. (b) Linear dispersion around the K points. The dispersion near the K' points is the same.

with $\psi_{A,K}$ the component of the wave function corresponding to the sublattice A and valley K, and similarly for the other terms. By applying the effective Hamiltonian in Eq. 1.3 to the wave functions in Eq. (1.5), it can be concluded that there is no mixing between valley components $\psi_{X,K}$ and $\psi_{X,K'}$ (X =A,B).

To end the discussion on graphene, it is important to mention that the system has an associated non-trivial Berry phase. The Berry phase, which is a phase acquired by the wave function when a particle is subjected to a closed trajectory in the space of parameters that define the Hamiltonian, is non-trivial if such trajectory encloses a degeneracy point. An example of a closed trajectory in parameter space is given by a cyclotron orbit of an electron under an external magnetic field. In this case, the parameter space is given by the wave vectors k_x and k_y, which are time-dependent and form a closed trajectory that surrounds the Dirac point, being degenerated since it has a common energy for valence- and conduction-band states. The associated Berry phase has a value of π, which can be measured in Shubnikov-de Haas and van Alphen-de Haas experiments.

1.1.2. Bilayer Graphene

In terms of complexity, bilayer graphene is the next layered structure that can be made out of carbon. It consists of two graphene layers stacked on top of each other. There are several possibilities for the precise configuration of such stacking, and they have a profound implication on the material's electronic properties. A possible configuration is the A-A stacking, in which each carbon atom of the top layer has an atom from the bottom layer directly below. A more stable configuration is the Bernal or A-B stacking, in which the top layer is rotated by 60° with respect to the bottom layer. Currently, the control of rotation between the layers is a very active research topic due to the discovery of superconductivity in "magic angle" rotated bilayer graphite, where a rotation of just 1.1° with respect to the Bernal configuration induces superconductivity and strong electron correlations [17]. In the following discussion, we will focus our attention on Bernal bilayer graphite, since it is also an interesting material that hosts non-trivial low-energy excitations, i.e., not described by the Schrödinger equation.

In Bernal bilayer graphene, two graphene lattices are separated by a distance $a_z = 3.35$ Å, with the atoms in the bottom layer labeled as A1 and B1, the ones in the top layer labelled as A2 and B2, and A and B indicating the sublattice index in each layer, as shown in Fig. 1.3 (a). We

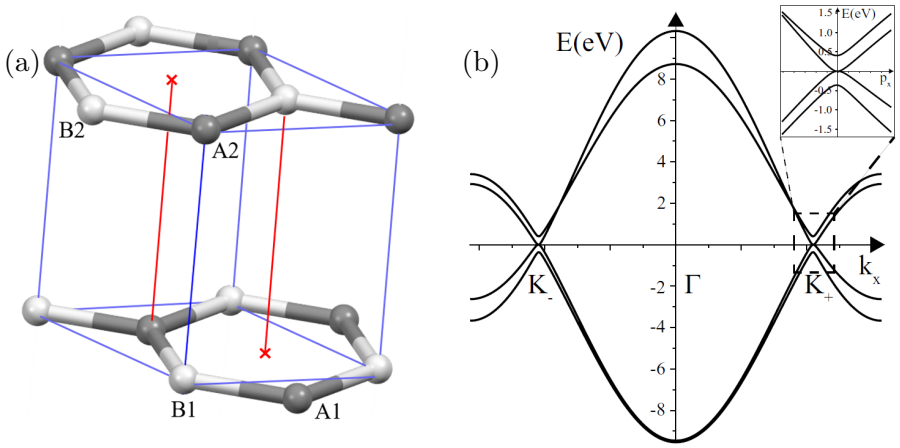

Figure 1.3: (a) Crystal structure of Bernal bilayer graphene, with unit cell highlighted in blue. The sublattice sites of each layer are indicated, with doublet sites B1-A2 and non-doublet sites A1-B2. (b) Energy bands of bilayer graphene along the K'-Γ-K line. Inset: Bands around the K point. Taken from [30].

follow the notation used by McCann and Koshino [30], where atoms from the sublattice B1 are directly below atoms from the sublattice A2. For this reason, they are called dimer sites due to the relatively strong interlayer coupling of the electronic orbitals from these two atoms [30]. Atoms from the A1 and B2 sublattices do not have a counterpart directly above or below them, therefore, they are called non-dimer sites. The primitive cell of bilayer graphene is the same to that of monolayer graphene since it is defined by the same primitive vectors, and contains four atoms, one from each sublattice in each layer. Given that bilayer graphite is a two-dimensional system with the same primitive vectors as monolayer graphene, the Brillouin zone is the same in both systems.

The band structure of bilayer graphene can also be obtained by the tight-binding model, considering four interaction terms: γ_0 for the coupling between nearest-neighbor orbitals in the same layer, and γ_1, γ_3, γ_4 for interlayer coupling, chosen to be consistent with the coupling terms of graphite shown in Fig. 1.4. Note that γ_2 is absent because it describes interlayer coupling between A2-A2 atoms in the case of a tridimensional structure. The γ_1 parameter describes the coupling between dimer sites B1-A2, γ_3 is the coupling between the non-dimer sites A1-B2, and γ_4 is the coupling between dimer and non-dimer sites B1-B2 and A1-A2.

Considering that Bloch waves from the orbitals at sites A1, A2, B1, B2 are approximately orthogonal with each other (valid in the low-energy limit $|E| < \gamma_1$), the tight-binding Hamiltonian of bilayer graphene is [30]

$$\mathcal{H}_{\text{Bilayer}} = \begin{pmatrix} \varepsilon_{A1} & -\gamma_0 f(\boldsymbol{k}) & \gamma_4 f(\boldsymbol{k}) & -\gamma_3 f^*(\boldsymbol{k}) \\ -\gamma_0 f^*(\boldsymbol{k}) & \varepsilon_{B1} & \gamma_1 & \gamma_4 f(\boldsymbol{k}) \\ \gamma_4 f^*(\boldsymbol{k}) & \gamma_1 & \varepsilon_{A2} & -\gamma_0 f(\boldsymbol{k}) \\ -\gamma_3 f(\boldsymbol{k}) & \gamma_4 f^*(\boldsymbol{k}) & -\gamma_0 f^*(\boldsymbol{k}) & \varepsilon_{B2} \end{pmatrix} \tag{1.8}$$

with

$$f(\boldsymbol{k}) = e^{ik_y a} + 2e^{-ik_y a/2} \cos\left(\frac{\sqrt{3}}{2} k_x a\right). \tag{1.9}$$

ε_{A1}, ε_{B1}, ε_{A2}, and ε_{B2} describe on-site energies of the four atomic sites, which in the general case are not equal [30]. For example, interaction with a substrate or strain may induce energy differences between the sites in each layer, such that the energy of sites in the bottom layer $\varepsilon_{A1} + \varepsilon_{B1}$ is different from the one of sites in the upper layer $\varepsilon_{A2} + \varepsilon_{B2}$. In the following, we only

consider energy difference between dimer and non-dimer states, such that $\varepsilon_{B1} = \varepsilon_{A2} = 0.022$ eV, and $\varepsilon_{A1} = \varepsilon_{B2} = 0$ eV [30].

By diagonalizing the Hamiltonian in Eq. (1.8) one obtains the bands of bilayer graphene in the Brillouin zone, which are plotted in Fig. 1.3 (b) for the path K'-Γ-K, as well as in the vicinity of the K point. Four bands are observed as a result of the $2p_z$ orbitals of each of the four sites of the primitive lattice. As in monolayer graphene, the K and K' points are special due to the touching of two bands and the Fermi level located at them. However, the dispersion in the vicinity of these points is not linear but parabolic, implying that the effective Hamiltonian is not that of massless Dirac fermions. Indeed, focusing on the low-energy limit $|E| \ll \gamma_1$, where the γ_0 and γ_1 terms are dominant, allows reducing the problem to that of two bands around the K points, described by the effective Hamiltonian

$$\mathcal{H}_\xi^{\text{eff}} = \frac{1}{2m}\begin{pmatrix} 0 & (\pi^\dagger)^2 \\ \pi^2 & 0 \end{pmatrix}, \tag{1.10}$$

where $\pi = \xi q_x + i q_y$, $\pi^\dagger = \xi q_x - i q_y$, $m = \gamma_1/2v^2$, $v = \sqrt{3}\gamma_0/2\hbar$, and $\xi = \pm 1$ is the valley index. The effective Hamiltonian is written in the basis of non-dimer sites (ψ_{A1},ψ_{B2}), such that the wave function for dimer states can be found from it by

$$\begin{pmatrix} \psi_{A2} \\ \psi_{B1} \end{pmatrix} = (E - h_\chi)^{-1} u^\dagger \begin{pmatrix} \psi_{A1} \\ \psi_{B2} \end{pmatrix}, \tag{1.11}$$

with

$$h_\chi = \begin{pmatrix} \varepsilon_{A2} & \gamma_1 \\ \gamma_1 & \varepsilon_{B1} \end{pmatrix}, \quad u = \begin{pmatrix} -v_4\pi^\dagger & v\pi^\dagger \\ v\pi & -v_4\pi \end{pmatrix}, \tag{1.12}$$

and $v_4 = \sqrt{3}\gamma_4/2\hbar$, which can be approximated to zero in the low-energy limit. In this sense, the effective Hamiltonian in Eq. (1.10) describes electrons and holes with quadratic dispersion, and as such, they may be considered as non-relativistic. Nevertheless, $\mathcal{H}_\xi^{\text{eff}}$ does not have the form of the Schrödinger Hamiltonian due to the off-diagonal structure. In reality, the effective Hamiltonian is chiral. This can be seen by introducing the sublattice pseudospin operators $\boldsymbol{\sigma} = = (\sigma_x,\sigma_y,\sigma_z)$ acting on the space (ψ_{A1}, ψ_{B2}), and defining the momentum close to the K and K' points as $\boldsymbol{q} = (\xi q\cos\varphi, q\sin\varphi, 0)$, allowing to write the effective Hamiltonian as

$$\mathcal{H}_\xi^{\text{eff}} = \frac{q^2}{2m}\boldsymbol{\sigma}\cdot\boldsymbol{n}_2, \tag{1.13}$$

with $\boldsymbol{n}_2 = -(\cos 2\varphi, \xi\sin 2\varphi, 0)$ an in-plane unit vector. The operator $\boldsymbol{\sigma}\cdot\boldsymbol{n}_2$ is the chirality operator of bilayer graphene, which projects the sublattice pseudospin into the direction of $\boldsymbol{n}_2$. Therefore, the Hamiltonian is proportional to the chirality operator, implying that its eigenstates are also chirality eigenstates. They are given by

$$\Psi_{\pm,\xi} = \frac{1}{\sqrt{2}}\begin{pmatrix} 1 \\ \mp e^{2i\xi\varphi} \end{pmatrix}, \tag{1.14}$$

with $\pm$ related to chirality eigenvalues $+1$ or -1. The eigenstates of the Hamiltonian can be understood in the following way: Ψ is written in the space of sublattices A1 and B2, such that $|\uparrow\rangle = (1,0)^{\mathrm{T}}$, with T the transpose operation, corresponds to an electron in sublattice A1, and $|\downarrow\rangle = (0,1)^{\mathrm{T}}$ to an electron in sublattice B2, written this way to highlight the fact that they are sublattice pseudospins. Since the electron density is shared equally between the two layers, the Hamiltonian eigenstates correspond to the superposition of electron states in sublattices A1 and B2 of the form $|\uparrow\rangle \mp e^{2i\xi\varphi}|\downarrow\rangle$ [30].

The chiral nature of electrons in bilayer graphite may seem a trivial feature, however, there is no equivalence of chiral and non-relativistic fermions in particle physics. In fact, it plays

an important role in many physical phenomena, like the quantum Hall effect [31] and Klein tunneling [4].

1.1.3. Graphite

Graphite consists of several graphene layers stacked on top of each other, bonded by weak van der Waals forces. Natural graphite crystals exist in two different stacking configurations, namely, Bernal or A-B stacking, and rhombohedral or A-B-C stacking. Bernal graphite is thermodynamically more stable than rhombohedral graphite and, as such, is found in more proportion in natural crystals. In consequence, Bernal graphite has been studied more intensively, however, rhombohedral graphite has recently increased in attention due to the discovery of topological properties of the band structure related to a non-trivial Berry phase [18]. In the following considerations, we will focus our attention on Bernal graphite.

Bernal graphite can be thought of as a set of infinite bilayer graphene sheets stacked on top of each other. Its unit cell is a rhombic prism that contains four carbon atoms, two from each layer, as shown in Fig. 1.4 (a). The Brillouin zone of Bernal graphite is a hexagonal prism, with high-symmetry points denoted by Γ, H, K, H', and K'. As in the case of graphene, the points H-H' and K-K' are inequivalent since they are not connected by reciprocal lattice vectors. Fig. 1.4 (b) shows the Brillouin zone of Bernal graphite.

As mentioned before, the electronic bands of Bernal graphite were studied by Wallace using the tight-binding approximation. A more successful model was proposed by Slonczewski and Weiss [32] and McClure [33], which applies a group-theoretical approach and the $\boldsymbol{k}\cdot\boldsymbol{p}$ formalism, along with tight-binding considerations, to describe the band energies of graphite along the K-H-K path of the BZ. The result is the Slonczewski-Weiss-McClure (SWM) model of graphite, which has been very successful in describing the material's electric, optical and magnetic properties [34, 35].

The full SWM model has seven parameters, γ_0,...,γ_5, and $\gamma_6 = \Delta$, corresponding to hopping terms between carbon sites, as shown in Fig. 1.4 (a). Of them, γ_0 is the only term related to intralayer hopping and has the highest value, thus, having the highest contribution to the electronic bands. The remaining terms represent interlayer interaction and have different effects on the band structure. For example, the main contribution of γ_1 is the splitting of the bands, γ_2 is responsible for band overlap, and γ_3 is responsible of the breaking of band isotropy in the k_x,k_y plane, inducing a trigonal symmetry instead of a cylindrical one, as will be evident in the following discussions. For this reason, γ_3 is called the "trigonal warping" term. γ_4 has a similar effect as γ_3, but it is lower in magnitude. γ_5 is related to the hopping between A sites in the next-nearest layer, and does not have an appreciable qualitative effect on the bands, although it does have a quantitative effect. Finally, Δ expresses the inequivalence between A and B sites due to the presence of the stacking layers.

Defining $\boldsymbol{k} = (k_x,k_y,k_z)$ as a vector in k-space with origin at the K or K' points of the BZ, the full SWM Hamiltonian is given as follows [32, 33]

$$\mathcal{H} = \begin{pmatrix} \varepsilon_1^0 & 0 & H_{13} & H_{13}^* \\ 0 & \varepsilon_2^0 & H_{23} & -H_{23}^* \\ H_{13}^* & H_{23}^* & \varepsilon_3^0 & H_{33} \\ H_{13} & -H_{23} & H_{33}^* & \varepsilon_3^0 \end{pmatrix} \tag{1.15}$$

with

$$\begin{gathered} \varepsilon_1^0 = \Delta + \gamma_1\Gamma + \frac{1}{2}\gamma_5\Gamma^2, \quad \varepsilon_2^0 = \Delta - \gamma_1\Gamma + \frac{1}{2}\gamma_5\Gamma^2, \quad \varepsilon_3^0 = \frac{1}{2}\gamma_2\Gamma^2, \\ H_{13} = \frac{1}{\sqrt{2}}(-\gamma_0 + \gamma_4\Gamma)\sigma e^{i\alpha}, \quad H_{23} = \frac{1}{\sqrt{2}}(\gamma_0 + \gamma_4\Gamma)\sigma e^{i\alpha}, \quad H_{33} = \gamma_3\Gamma\sigma e^{i\alpha}, \end{gathered} \tag{1.16}$$

and

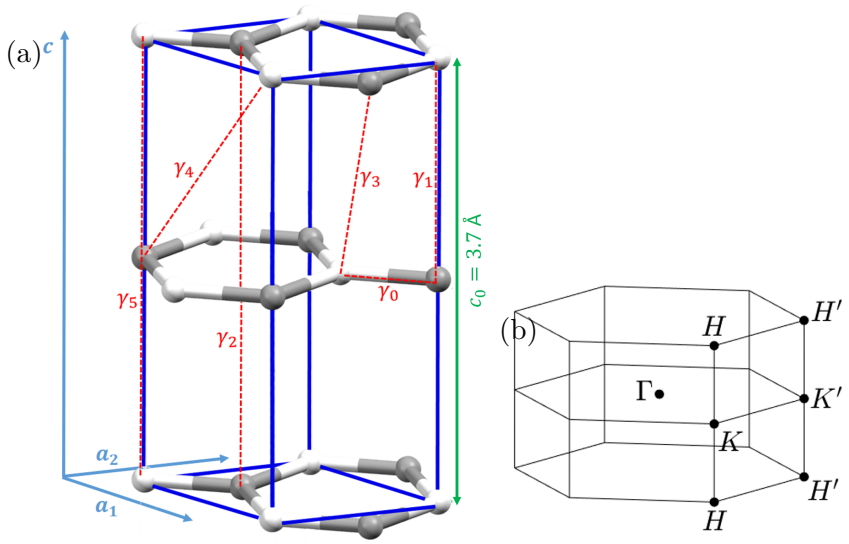

Figure 1.4: (a) Primitive lattice, unit vectors, and tight-binding parameters of Bernal graphite. (b) Brillouin zone of Bernal graphite.

$$\Gamma = 2\cos(\pi k_z), \quad \sigma = \frac{\sqrt{3}}{2}a\kappa, \quad \kappa = \sqrt{k_x^2 + k_y^2}, \quad \text{and } \alpha = \arctan\left(-\frac{k_x}{k_y}\right), \tag{1.17}$$

with k_z in units of $2\pi/c_0$, with $c_0 = 3.7$ Å the lattice parameter in the c axis, and takes the values within the Brillouin zone $-0.5 < k_z \leq 0.5$. The tight-binding parameters, as obtained by Schneider et al. by fitting the quantum oscillations of graphite's resistivity in an external magnetic field (Shubnikov-de Haas oscillations, Section 1.3.3) are $\gamma_0 = 3.37$ eV, $\gamma_1 = 363$ meV, $\gamma_2 = -24.3$ meV, $\gamma_3 = 310$ meV, $\gamma_4 = 70$ meV, $\gamma_5 = 50$ meV, $\Delta = -7$ meV [36].

The energy bands are obtained by diagonalizing the SWM Hamiltonian, finding four eigenvalues for each wave vector $\boldsymbol{k}$, *i.e.*, the energies of four bands at $\boldsymbol{k}$. Fig 1.5 (a) shows the graphite bands along the H-K-H line of the BZ, i.e. along the k_z direction. The band E_3 has a degeneracy of 2, apart from the spin and valley degeneracy, which is lifted if one moves away from the H-K-H line by a vector $\boldsymbol{\kappa}$ perpendicular to the k_z axis. The Fermi energy is found approximately in the middle of the E_3 band, having an approximate value of $E_F \sim -|\gamma_2|$, and found by the charge neutrality condition of graphite that implies an equal electron and hole density.

By observing Fig. 1.5 (a), it is noticed that all bands are flat at the K point ($k_z = 0$), while at the H point only the E_3 band is. This implies that the density of states has a high value at the K and H points, thus, making them particularly important in the description of magneto-optical properties of graphite. For this reason, we now focus on the behavior of the bands in the vicinity of such points. Fig. 1.5 (b) shows the bands near the K point, it is evidenced the degeneracy lift of the E_3 band, giving rise to the $E_{3,1}$ (hole-like) and $E_{3,2}$ (electron-like) bands, characterized by trigonal symmetry induced by the γ_3 parameter. The bands overlap near the Fermi level, and as a result, they have an interesting topology where two attributes stand out. First, the bands touch at four points, a central one and three "legs", and second, the occurrence of saddle points. In between the saddle points, the constant energy contours form four disconnected closed paths, while outside of them the constant energy contours form only one closed path, as shown in Fig. 1.5 (b). The transition from disconnected to connected energy contours is known as the Lifshitz transition [37], and has important consequences in the magneto-optical spectra.

On the other hand, near the H point the bands have a linear dispersion, reminiscent of the bands of graphene, as observed in Fig. 1.5 (c). In the figure, only two bands can be observed

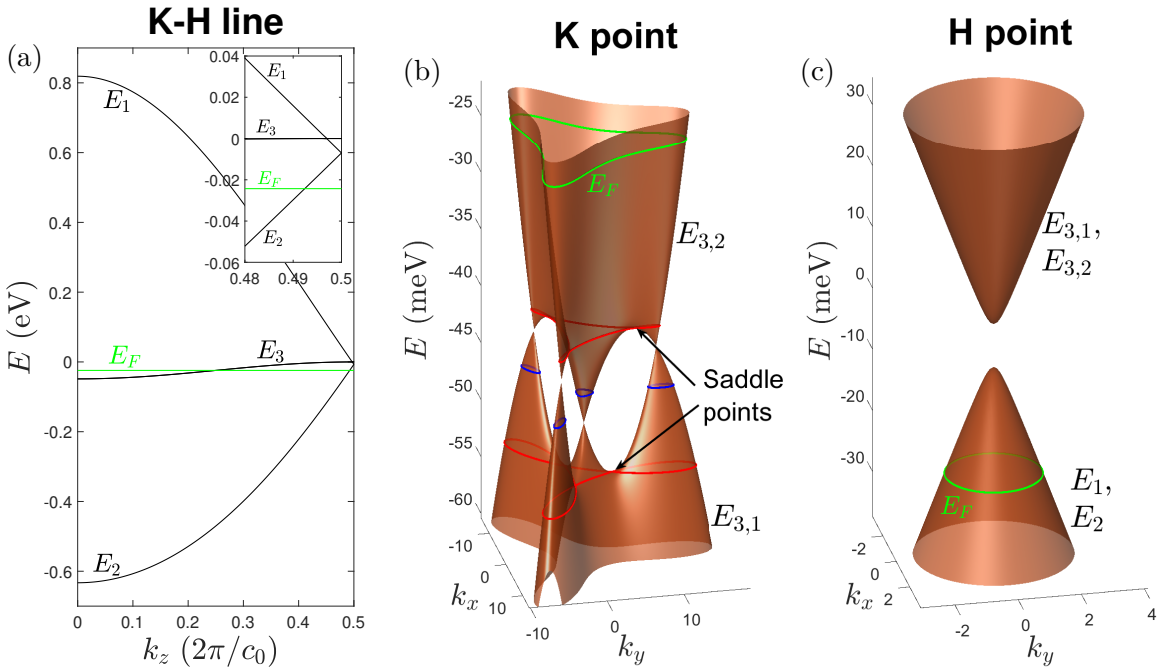

Figure 1.5: Bands of graphite as calculated by the SWM model. (a) Bands along the K-H line, with Fermi energy in green. Inset: bands in the vicinity of the H point ($k_z = 0.5(2\pi/c_0)$), the bands E_1 and E_2 are degenerate at that point. (b) Bands at the K point ($k_z = 0$). The degeneracy of the band E_3 is lifted, resulting in valence and conduction bands with trigonal symmetry. The conductance and valence bands have three saddle points each, two of them indicated in the graph. The saddle points define the separatrix energy contours (shown in red), such that in-between the separatrixes the constant energy contours are four disconnected loops (as an example, the energy contours for $E = -46$ meV are shown in blue). The Fermi energy is shown in green. Since E_F is outside the separatrix, its contour is a simply connected path. (c) Bands at the H point ($k_z = 0.5(2\pi/c_0)$). The γ_3 term does not contribute to the bands, therefore, they show cylindrical symmetry instead of a trigonal one. In (b) and (c), the units of k_x and k_y are $10^{-3} \cdot 2\pi/c_0$, with $c_0 = 6.7$ Å the lattice parameter in the c direction (Fig. 1.4 (a)).

due to the degeneracy of the E_1 and E_2 bands (observed also in Fig. 1.5 (a) at $k_z = 0.5$), which is not lifted by moving away from this point by a wave vector $\boldsymbol{\kappa} = (k_x,k_y)$. A similar situation is found in the band E_3, which remains degenerate even for non-zero $\boldsymbol{\kappa}$. The reason for this is the vanishing of the interlayer coupling contribution to the energy at the H point, since the $\gamma_1,\ldots,\gamma_5$ parameters enter the SWM Hamiltonian through terms of the form $\gamma_i\Gamma = 2\gamma_i \cos(\pi k_z)$ ($i = 1,...,5$), which give zero at $k_z = 0.5$, as seen in Eqs. (1.16, 1.17). Another consequence of this is the absence of trigonal warping, resulting in bands with cylindrical symmetry. An important difference between the bands at the H point and the bands of graphene is the presence of a small band gap of 0.01 eV, resulting from a non-zero value of Δ. In addition to this, the the Fermi level is located in the valence band, implying that the charge carriers at the H point are holes.

We focus now on the Fermi surface of graphite. Calculating the constant energy surface at $E_F \sim -|\gamma_2| = -0.0243$ eV [38] for the full SWM Hamiltonian gives the result plotted in Fig. 1.6 (a). The Fermi surface, centered along the H-K-H line, consists of one electron pocket located approximately in the interval $k_z = (-0.25,0.25)$, and two hole pockets at approximately $k_z = (0.25,0.5)$ and $k_z = (-0.5, -0.25)$. The reason for this is that close to the K point, the Fermi level is located in the conductance band, while close to the H point, it is located in the valence band. Trigonal warping also affects the Fermi surface, being stronger in the electron

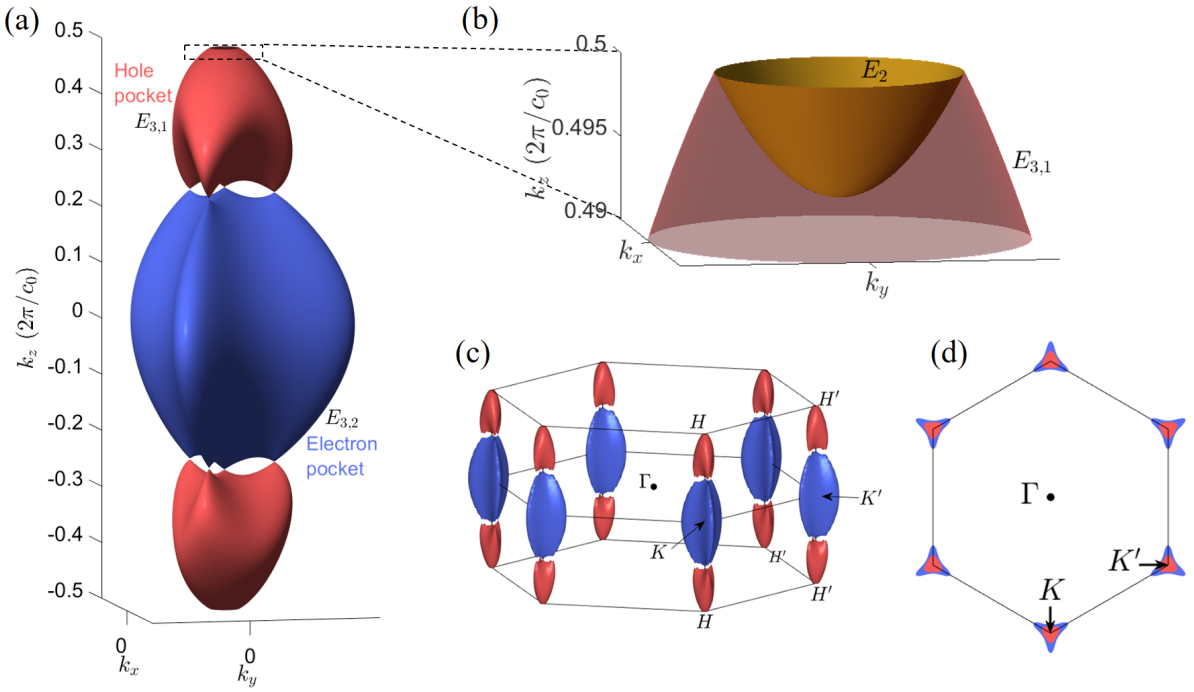

Figure 1.6: (a) Fermi surface of Graphite, showing the electron and hole pockets. (b) Zoom into the vicinity of the H point, showing a small hole-like Fermi surface due to the E_2 band. (c) Location of the Fermi surface in the BZ of graphite. The Fermi surfaces were enlarged 10 times in the $k_x - k_y$ plane for easier observation. (d) Upper view of the BZ and Fermi surfaces. The Fermi surfaces were enlarged 10 times in the $k_x - k_y$ plane.

pocket than in the hole pocket. A smaller hole pocket near the H point is present due to the E_2 band, as shown in Fig. 1.6 (b). Holes associated with this pocket are known as minority holes, in contrast to those associated with larger hole pockets, known as majority holes. Finally, Figs. 1.6 (c-d) show the location of the Fermi surface within the entire Brillouin zone, where the Fermi surface was enlarged 10 times in the $k_x - k_y$ plane. Graphite is considered a semimetal due to the low number of conducting states contained within the Fermi surface. The Fermi surface can be probed by the Shubnikov-de Haas effect, as will be explained in section 1.3.3, which in turn can be observed by THz magneto-spectroscopy.

1.2. Electrons in a Magnetic Field

By studying the behavior of charged particles under an external magnetic field, one can deduce important information about them and the medium in which they are embedded. When subjected to a magnetic field, moving electrons and charged particles experience the Lorentz force, which forces them to move in a circular trajectory known as a cyclotron orbit. From such an orbit, the mass of the particle can be obtained if its velocity and radius of motion are known. If the magnetic field is strong enough, the trajectories and energy spectrum become quantized in a physical process known as Landau quantization. These ideas can be generalized to the case of charge carriers in a crystal. In this section, we will explain the Landau quantization for a free electron gas and how the concept is extended to electrons in a crystal. The main computation techniques for a general system will be presented, as well as some results for the quantized energy spectra of the materials of interest.

1.2.1. Free-Electron Gas in a Magnetic Field: Landau Levels

As mentioned, electrons subjected to an external magnetic field move in cyclotron orbits, such that the radius of the orbit decreases as the magnetic field increases. If the magnetic field is strong enough, the orbits become quantized, giving rise to Landau quantization.

To describe this phenomenon, suppose that a gas of non-interacting electrons is confined within a box of volume $V = L^3$, being L length of the box in one of the spatial directions. A magnetic field of constant magnitude is applied in the system along the z direction, such that it is given by $\boldsymbol{B} = B\hat{z}$. It has an associated vector potential $\boldsymbol{A}(\boldsymbol{r})$, that follows the condition $\boldsymbol{B} = \nabla \times \boldsymbol{A}(\boldsymbol{r})$, being $\boldsymbol{r} = (x, y, z)$ the coordinates in real space. Under and external magnetic field, the canonical momentum $\boldsymbol{p}$ of a charged particle is changed by the minimal coupling $\boldsymbol{p} \to \boldsymbol{p} - q\boldsymbol{A}(\boldsymbol{r})$, being q the charge of the particle. In this sense, the Hamiltonian that describes an electron in the gas is

$$\mathcal{H} = \frac{\left(\hat{\boldsymbol{p}} + e\boldsymbol{A}(\hat{\boldsymbol{r}})\right)^2}{2m_0}, \tag{1.18}$$

with $\hat{\boldsymbol{p}} = (\hat{p}_x, \hat{p}_y, \hat{p}_z)$ the momentum operator, $\hat{\boldsymbol{r}} = (\hat{x}, \hat{y}, \hat{z})$ the position operator, m_0 the mass of the free electron, and $q = -e \approx -1.602 \times 10^{-19}$ C the electron's charge. There are several different vector potentials that produce a uniform magnetic field in the z direction. We choose the Landau gauge, $\boldsymbol{A} = (0, B\hat{x}, 0)$, since it only depends on one spatial operator. Under this consideration, the Hamiltonian changes to

$$\mathcal{H} = \frac{\hat{p}_x^2}{2m_0} + \frac{\left(\hat{p}_y + eB\hat{x}\right)^2}{2m_0} + \frac{\hat{p}_z^2}{2m_0}. \tag{1.19}$$

Since the Hamiltonian commutes with the operators $\hat{p}_y$ and $\hat{p_z}$, their eigenvalues $p_y = \hbar k_y$ and $p_z = \hbar k_z$ are constants of motion and represent good quantum numbers. The Schrödinger equation associated with the previous Hamiltonian can be solved by applying the method of the canonical transformation, by transforming the canonical momentum $\hat{\boldsymbol{p}}$ into the so-called kinetic momentum $\hat{\boldsymbol{\Pi}}$, in the following way

$$\hat{\Pi}_x = \hat{p}_x, \quad \hat{\Pi}_y = \hat{p}_y + eB\hat{x}, \quad \hat{\Pi}_z = \hat{p}_z. \tag{1.20}$$

The kinetic momentum operator and the position operator are still canonically conjugated operators in the sense that they still follow the commutation relations

$$\left[\hat{x},\hat{\Pi}_x\right] = i\hbar, \quad \left[\hat{y},\hat{\Pi}_y\right] = i\hbar, \quad \left[\hat{z},\hat{\Pi}_z\right] = i\hbar, \tag{1.21}$$

however, since $\hat{\Pi}_y$ depends on $\hat{x}$, it does not commute with the x component of the kinetic momentum. Calculating the commutator results in

$$\left[\hat{\Pi}_x, \hat{\Pi}_y\right] = [\hat{p}_x, \hat{p}_y + eB\hat{x}] = -i\hbar eB. \tag{1.22}$$

The problem is solved by introducing the operators $\hat{a}$ and $\hat{a}^\dagger$, defined as

$$\hat{a} = \frac{1}{\sqrt{2\hbar eB}}\left(\hat{\Pi}_x - i\hat{\Pi}_y\right), \quad \hat{a}^\dagger = \frac{1}{\sqrt{2\hbar eB}}\left(\hat{\Pi}_x + i\hat{\Pi}_y\right). \tag{1.23}$$

The normalization constant was chosen in order to obtain the usual commutation relation of creation and annihilation operators,

$$\left[\hat{a},\hat{a}^\dagger\right] = 1. \tag{1.24}$$

With these considerations, the Hamiltonian can be written in terms of the creation and annihilation operators as follows,

$$\mathcal{H} = \hbar\frac{eB}{m_0}\left(\hat{a}^\dagger\hat{a} + \frac{1}{2}\right) + \frac{\hat{\Pi}_z^2}{2m_0}. \tag{1.25}$$

Therefore, in the plane $x-y$ perpendicular to the direction of the magnetic field, the electrons follow a harmonic movement with a frequency given by $\omega_c = eB/m_0$, known as the cyclotron frequency, while remaining free in the direction parallel to the field. The energy of an electron in the system is then

$$E_{N,k_y,k_z} = \hbar\omega_c\left(N + \frac{1}{2}\right) + \frac{\hbar^2 k_z^2}{2m_0}, \quad \text{with } N = 0,1,2,... \tag{1.26}$$

This means that the energy of the system takes discrete values for a fixed value of k_z, where the discrete energies are known as "Landau levels" (LLs), being N the Landau level index. Note that k_z also takes discrete values in the case of a finite sample, however, it is approximately continuous in a sample with macroscopic length along the z direction. In the latter case, one speaks of Landau bands due to the one-dimensional character of the energy dispersion along the z direction. The energy levels are truly quantized in the case of a 2D or quasi-2D structure, such as a quantum well or graphene.

Although the eigenvalue $\hbar k_y$ of the canonical momentum operator $\hat{p}_y$ is a good quantum number, the energy does not depend on it, and as a consequence, the Landau levels have a high degeneracy. The degeneracy of a Landau level N with a given wave vector k_z is related to the number of flux quanta $\Phi_0 = h/(2e)$ threading through the transversal area of the sample $\mathcal{A} = L^2$, given by

$$N_B = \frac{2e\mathcal{A}B}{h}, \tag{1.27}$$

or considering the same quantity per unit area, called the flux density,

$$n_B = \frac{2eB}{h} = \frac{B}{\Phi_0}. \tag{1.28}$$

This means that the degeneracy, or the number of states that can be allocated in a given Landau level, increases with the magnetic field.

The Landau levels are an important concept in the magneto-optical spectroscopy investigation of the materials of interest. Our methods can probe electronic transitions between Landau levels, a process known as cyclotron resonance, or magnetic-field-induced oscillations in the microwave absorption signal due to the crossing of the Fermi energy through a Landau level, known as Shubnikov-de Haas oscillations. These physical phenomena will be explained in section 1.3.

1.2.2. Effect of a Magnetic Field on Electrons in a Crystal

As we saw in the previous section, the external field changes the canonical momentum of a free particle by means of the minimal coupling $\boldsymbol{p} \to \boldsymbol{p} - q\boldsymbol{A}(\boldsymbol{r})$. For electrons in a crystal lattice, the canonical momentum is not a conserved quantity since the translational symmetry is broken by the periodic ionic potential. Instead, electrons in a crystal are characterized by the crystal momentum $\boldsymbol{k}$. Furthermore, $\boldsymbol{k}$ vectors contained within the BZ have a special status since they completely determine the band structure of the material. Gauge invariance of the vector potential $\boldsymbol{A}$, and of the Bloch wavefunction of electrons in the crystal Ψ, allows to perform a similar transformation as the minimal coupling to the crystal momentum, known as the Peierls substitution [39, p. 234]. For a complete discussion about crystal electrons in a magnetic field, we refer to the book by Lifshitz and Pitaevskii [39, p. 232].

In the context of electrons in a crystal, the Peierls substitution is given by $\boldsymbol{k} \to \boldsymbol{K} = \boldsymbol{k} - (q/\hbar)\boldsymbol{A}(\boldsymbol{r})$, where $\boldsymbol{K}$ is the kinetic momentum[2] and $\boldsymbol{k}$ is a generalized crystal momentum[3]. The Peierls substitution is valid if the magnetic length $l_B = \sqrt{\hbar/(eB)}$ is much larger than the lattice spacing [27]. The Hamiltonian of the system is constructed by applying the Peierls substitution on the free energy bands, and then applying canonical quantization on $\boldsymbol{k}$ and $\boldsymbol{r}$ such that they get promoted to operators on a Hilbert space, as follows,

$$E_s(\boldsymbol{k}) \to \mathcal{H}_s = E_s\left(\hat{\boldsymbol{k}} - \frac{q}{\hbar}\boldsymbol{A}(\hat{\boldsymbol{r}})\right), \tag{1.29}$$

where E_s is a given energy band, for instance, the E_+ and E_- bands of graphene, or the E_1, E_2, E_3 bands of graphite. Therefore, the energy bands are now operators on a Hilbert space. In momentum representation, the momentum and position operators take the form

$$\hat{\boldsymbol{k}} = \boldsymbol{k}, \quad \hat{\boldsymbol{r}} = i\frac{\partial}{\partial \boldsymbol{k}}, \tag{1.30}$$

with $\boldsymbol{k}$ the eigenvalue of the generalized crystal momentum. Therefore, the generalized momentum operator $\hat{\boldsymbol{k}}$ and the position operator $\hat{\boldsymbol{r}}$ of electrons in a crystal follow the same commutation rules as the momentum and position of a free particle. Moreover, the kinetic momentum operator $\hat{\boldsymbol{K}}$ follows the same commutation rules as the operator $\hat{\boldsymbol{\Pi}}$ introduced before, such that $[K_x,K_y] = -ieB/\hbar$ for a uniform field in the z direction and in the Landau gauge. In conclusion, the previous considerations allow to generalize the procedure of Landau quantization presented for free electrons to the case of crystal electrons.

Until now, we have not discussed the conditions under which Landau levels appear. If spin and spin-orbit interaction terms are not considered, the magnetic field does not enter directly into the Hamiltonian. Instead, it is the vector potential that enters via the Peierls substitution. This implies that the problem does not allow a perturbative treatment for low fields since the vector potential $\boldsymbol{A} = (0,Bx,0)$ increases in magnitude as a function of the position. Consequently, even a low magnetic field could induce changes in a large system: the quantization of the energy spectrum into Landau levels should appear at arbitrarily low B. In reality, the quantized energy levels are not observed at low fields because the thermal energy k_BT, with k_B the Boltzmann constant, is greater than the difference ΔE_N between levels. For this reason, the condition $k_BT \ll \Delta E_N$ must be fulfilled to observe Landau quantization. Additionally, the requirement that electrons complete several cyclotron orbits before being scattered by impurities in the material introduces an additional condition for Landau-level formation, which can be written in the form $\omega_c\tau \gg 1$, with $\omega_c = eB/m^*$ the cyclotron frequency of electrons in the material, being m^* their effective mass, and τ the transport time or the average time between electron scattering events.

On the other hand, if the spin of the carriers is considered, it enters into the theory by adding the following term in the Hamiltonian,

$$\mathcal{H}_\mathrm{s} = \boldsymbol{\mu} \cdot \boldsymbol{B}, \tag{1.31}$$

with $\boldsymbol{\mu} = g'\mu_\mathrm{B}\boldsymbol{S}/\hbar$ the magnetic moment of the carriers, g' the so-called g-factor of the carriers in the material, which in general differs from the value for free electrons $g \sim 2.0023$; $\mu_\mathrm{B} = e\hbar/2m_0$ the Bohr magneton, m_0 the free-electron mass, and $\boldsymbol{S}$ the spin operator. Given that the spin of the carriers is 1/2, its effect is a splitting of the energy levels that is proportional to the magnitude of the magnetic field, of value $\Delta E = g'\mu_\mathrm{B}B$. This phenomenon is known as the Zeeman effect.

[2] More precisely, it should be referred to as the kinetic wave vector, but no ambiguity is intended since the momentum and wave vector are related to each other by a factor of $\hbar$.

[3] Here, we invert the nomenclature for $\boldsymbol{K}$ and $\boldsymbol{k}$ compared to Lifshitz and Pitaevskii [39], to establish a parallel with the previous subchapter. In that reference, $\boldsymbol{K}$ is the generalized crystal momentum and $\boldsymbol{k}$ is the kinetic momentum.

Another way that spin could enter into the theory is through the spin-orbit interaction of electrons in an atom. However, this interaction can be neglected in graphene and graphite since it is proportional to Z^2 [40], being Z the atomic number of the atom, and taking into account that carbon is a light element.

Computing the Landau Levels: Semiclassical Formalism

To calculate the energy levels in the semiclassical formalism, we suppose that the cyclotron trajectory in $\boldsymbol{k}$-space is closed, and then apply the Bohr-Sommerfeld quantization rule [39, p. 240]. In the semiclassical formalism, the particle trajectory is an important concept, and as such, the position and momentum are not treated as quantum-mechanical operators. The trajectory is found from the Hamilton equations of motion

$$\hbar\frac{d\boldsymbol{k}}{dt} = -\frac{\partial\mathcal{H}}{\partial\boldsymbol{r}}, \quad \frac{d\boldsymbol{r}}{dt} = \boldsymbol{v} = \frac{\partial\mathcal{H}}{\partial\boldsymbol{k}}, \quad \text{with } \mathcal{H} = E_s\left(\boldsymbol{k} + \frac{e}{\hbar}\boldsymbol{A}(\boldsymbol{r})\right). \tag{1.32}$$

From the last set of equations, and remembering that the kinetic momentum is $\boldsymbol{K} = \boldsymbol{k} + \frac{e}{\hbar}\boldsymbol{A}(\boldsymbol{r})$, it is possible to demonstrate an important result:

$$\hbar\frac{d\boldsymbol{K}}{dt} = -e\boldsymbol{v}\times\boldsymbol{B}, \quad \text{with } \boldsymbol{v} = \frac{\partial E_s(\boldsymbol{K})}{\hbar\partial\boldsymbol{K}}, \tag{1.33}$$

this is, similar to the classical Lorentz force. However, $E_s(\boldsymbol{K})$ is not a simple quadratic function of the momentum, but it is a complicated function given by the band structure, similarly for $\boldsymbol{v}$. From this result, it follows that the motion of a crystal electron in a magnetic field is characterized by

$$E_s(\boldsymbol{K}) = \text{constant}, \quad K_z = \text{constant}, \tag{1.34}$$

meaning that, for a fixed $K_z = k_z$, the cyclotron orbits in $\boldsymbol{K}$-space follow constant-energy contours of the free bands (i.e., without magnetic field).

Now, we apply the Bohr-Sommerfeld quantization rule. Considering an uniform magnetic field in the z direction, with vector potential $\boldsymbol{A}(\boldsymbol{r}) = (0,Bx,0)$, the components of the generalized crystal momentum are

$$k_x = K_x, \quad k_y = K_y - \frac{eBx}{\hbar}, \quad k_z = K_z. \tag{1.35}$$

Additionally, since the Hamiltonian does not depend on the y coordinate the y-component of the generalized crystal momentum is conserved:

$$k_y = K_y - \frac{eBx}{\hbar} = \text{constant}. \tag{1.36}$$

The Bohr-Sommerfeld quantization rule states that the integration along a closed path in $\boldsymbol{k}$-space must be equal to

$$\oint \boldsymbol{k}_t\cdot d\boldsymbol{r} = \left|\oint k_x\,dx + \oint k_y\,dy\right| = 2\pi(N+\gamma), \tag{1.37}$$

being N a positive integer number, γ a correction term related to the Berry phase such that $0<\gamma<1$, and $\boldsymbol{k}_t$ is the projection of the generalized crystal momentum on the plane perpendicular to the field, in this case corresponding to the k_x,k_y plane. The integral is performed on a period of motion, whereas $\oint k_y\,dy = k_y\oint dy = 0$ since k_y is a constant of motion. Replacing $k_x = K_x$ and $dx = (eB/\hbar)\,dK_y$ in Eq. (1.37), we arrive to

$$\oint K_x\,dK_y = \frac{2\pi\,eB}{\hbar}(N+\gamma). \tag{1.38}$$

The integral represents the area enclosed by the trajectory in K-space, i.e., the area $S(E_s,K_z)$ of the cross-section of a constant energy contour for a fixed K_z. Therefore, we have

$$S(E_s,K_z) = \frac{2\pi\, eB}{\hbar}(N+\gamma). \tag{1.39}$$

This equation represents an implicit quantization condition for the bands E_s: at fixed K_z, the only allowed energy values are those that fulfill the Bohr-Sommerfeld quantization criteria.

Computing the Landau levels: Canonical Formalism

Another method for obtaining the Landau levels of an energy band is by applying the formalism of canonical quantization, in a similar way as done for the free-electron gas in section 1.2.1. In this method, the momentum and position are again quantum-mechanical operators, where the $\hat{\boldsymbol{k}}$ operators can be transformed into the $\hat{\boldsymbol{K}}$ operators by means of the Peierls substitution:

$$\hat{K}_x = \hat{k}_x, \quad \hat{K}_y = \hat{k}_y + \frac{eB\hat{x}}{\hbar}, \quad \hat{K}_z = \hat{k}_z. \tag{1.40}$$

As mentioned in the case of free electrons, the operators $\hat{K}_x$ and $\hat{K}_y$ do not commute with each other, the commutator being

$$\left[\hat{K}_x,\hat{K}_y\right] = -\frac{ieB}{\hbar}. \tag{1.41}$$

This allows to introduce the creation and annihilation operators

$$\hat{a} = \sqrt{\frac{\hbar}{2eB}}\left(\hat{K}_x - i\hat{K}_y\right), \quad \hat{a}^\dagger = \sqrt{\frac{\hbar}{2eB}}\left(\hat{K}_x + i\hat{K}_y\right), \tag{1.42}$$

or, writing $\hat{K}_x$ and $\hat{K}_y$ in terms of them,

$$\hat{K}_x = \sqrt{\frac{eB}{2\hbar}}\left(\hat{a} + \hat{a}^\dagger\right), \quad \hat{K}_y = i\sqrt{\frac{eB}{2\hbar}}\left(\hat{a} - \hat{a}^\dagger\right). \tag{1.43}$$

The quantized energy levels of the system can be found by solving the resulting Hamiltonian written in terms of $\hat{a}$ and $\hat{a}^\dagger$, which can be done analytically in some cases, or numerically by using the matrix representation of the creation and annihilation operators.

To illustrate the method, we calculate the Landau levels of single-layer graphene in the low-energy approximation. Considering the valley-specific Hamiltonian of Eq. (1.3), and without magnetic field, the Hamiltonian is

$$\mathcal{H}_\xi = \xi\hbar v_{_F}\boldsymbol{\sigma}\cdot\hat{\boldsymbol{k}} = \xi\hbar v_{_F}\begin{pmatrix} 0 & \hat{k}_x - i\hat{k}_y \\ \hat{k}_x + i\hat{k}_y & 0 \end{pmatrix}. \tag{1.44}$$

The magnetic field is applied through the Peierls substitution $\hat{\boldsymbol{k}} \to \hat{\boldsymbol{K}}$, therefore

$$\mathcal{H}_{\xi,B} = \xi\hbar v_{_F}\begin{pmatrix} 0 & \hat{K}_x - i\hat{K}_y \\ \hat{K}_x + i\hat{K}_y & 0 \end{pmatrix} = \hbar v_{_F}\sqrt{\frac{2eB}{\hbar}}\begin{pmatrix} 0 & \hat{a} \\ \hat{a}^\dagger & 0 \end{pmatrix}. \tag{1.45}$$

The eigenvalues and eigenstates of the Hamiltonian can be obtained by solving the eigenvalue equation $\mathcal{H}_{\xi,B}\psi_N = E_N\psi_N$. Writing the eigenstate as a spinor $\psi_N = (u_{_N},v_{_N})^{\mathrm{T}}$, with T the transpose operation, the eigenvalue equation is then [27]

$$\xi\hbar v_{_F}\sqrt{2}\sqrt{\frac{eB}{\hbar}}\begin{pmatrix} 0 & \hat{a} \\ \hat{a}^\dagger & 0 \end{pmatrix}\begin{pmatrix} u_{_N} \\ v_{_N} \end{pmatrix} = E_N\begin{pmatrix} u_{_N} \\ v_{_N} \end{pmatrix}, \tag{1.46}$$

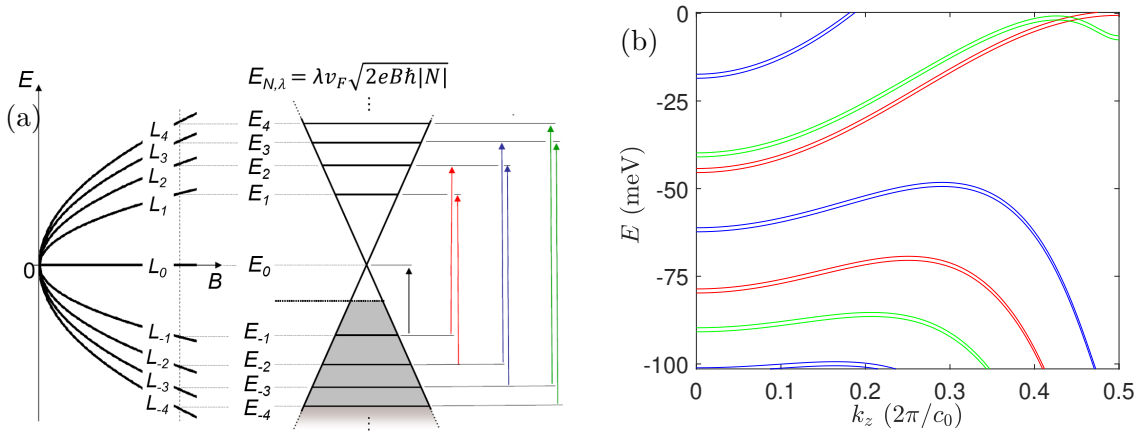

Figure 1.7: (a) Landau levels in monolayer graphene. On the left, the evolution of the energy levels with respect to the magnetic field, evidencing their characteristic $\sqrt{B}$ dependence. Such a plot is also called a fan diagram. On the right, the energy levels at a given magnetic field, showing the transition from a continuous conical dispersion to a set of discrete LLs. As an example, the LLs up to E_{-1} are filled, such that there is p doping. The black, red, blue and green arrows indicate transition between LLs that are optically allowed, which follow the rule $|m| = |n| \pm 1$, being n and m Landau-level indices. Taken from [41]. (b) Landau levels at $B = 8$ T in graphite as calculated by the SWM model. Calculated in Matlab using Scheneider's code [38] and the theory developed by Nakao [42]. Each band has a small Zeeman splitting.

with u_N and v_N the components of ψ_N, and their dependence on the eigenvalue of the number operator $\hat{N} = \hat{a}^\dagger \hat{a}$ will be shown soon. From the previous equation, we can derive the following condition for v_N,

$$\hat{a}^\dagger \hat{a} v_N = \frac{E_N^2}{2\hbar^2 v_F^2 \frac{eB}{\hbar}} v_N. \tag{1.47}$$

It can be seen that the second component of the spinor can be identified with an eigenvalue of the number operator $\hat{N} = \hat{a}^\dagger \hat{a}$, $\hat{N}|N\rangle = N|N\rangle$, up to the constant that accompanies v_N on the right-hand side of the equation. Such identification allows finding the energy eigenvalue as $E_N^2 = 2\hbar^2 v_F^2 \frac{eB}{\hbar} N$, and applying square root it is found that positive and negative energy values are allowed, therefore, a new quantum number $\lambda = \pm 1$ is introduced to acknowledge this fact. The energy eigenvalues of a charge carrier in graphene under a magnetic field are then

$$E_{N,\lambda} = \lambda v_F \sqrt{2e\hbar B\, N}. \tag{1.48}$$

It is observed that the Landau level spectrum is proportional to $\sqrt{B\,N}$ in contrary to the case of free electrons and electrons in a material with quadratic dispersion, where the dependence on B and N is linear (see Eq. (1.26)). The square-root dependence of the Landau levels is an important signature of relativistic fermions and has consequences in the physical phenomena of graphene, such as the quantum-Hall effect.

With this example, it is worth showing the Landau-level structure of graphene and graphite. Fig. 1.7 shows the Landau-level structure of both systems.

1.3. Optical Conductivity

The quantization of energy spectra into Landau levels brings important changes to some macroscopic properties of a material. For instance, the density of states (DOS) goes from being

a continuous function of the energy to become a series of peaks centered at the Landau levels. This implies that physical quantities that depend on the DOS, like the electric resistance or the magnetization, change considerably when a magnetic field is applied. Among the various experimental methods that investigate such phenomena, like magnetization measurements using torsion magnetometers or electronic transport measurements on a Hall-bar setup, we focus on magneto-optical spectroscopy using high-frequency electron paramagnetic resonance (HFEPR), where the electromagnetic radiation is in the microwave frequency range $80 - 1000$ GHz. With this method, it is possible to observe electronic transport phenomena, like Shubnikov-de Haas oscillations, through the measurement of the optical conductivity [23].

Indeed, the physical quantity measured in magneto-optical experiments is proportional to the optical conductivity [23]. Optical conductivity is the linear response function that quantifies the response of the electron current density to an electromagnetic field, which can be external or internal to the system. It can be thought of as the frequency-dependent generalization of the direct-current (DC) conductivity, which is the quantity that determines the response to a time-independent external electric field. In a magneto-optical experiment, the charge carriers are accelerated when they absorb energy from the electric field of the electromagnetic wave [23], where such a component acts as an external time-dependent field. The detection scheme of the HFEPR setup is such that the power losses due to microwave absorption in the sample are proportional to the real part of the optical conductivity's longitudinal component, $\mathrm{Re}(\sigma_{xx})$ [23].

In this section, we introduce the optical conductivity in the classical limit and its dependence on the magnetic field, as well as how it manifests as cyclotron resonances and Shubnikov-de Haas oscillations when the system undergoes Landau quantization.

1.3.1. AC Conductivity in the Classical Limit

We start by considering the electronic response to a time-dependent electromagnetic field. An alternating electric field of the form $E(\omega,t) = \mathrm{Re}[E(\omega)\exp(-i\omega t)]$, with ω the (angular) frequency of the field, induces an electric current when applied on a metal. In the classical Drude model for electron conductivity, electrons in a metal experience scattering by impurities with a characteristic time between scattering events given by the transport time τ. Between scattering events, electrons are considered free particles. In this model, the current density induced by the time-dependent electric field is given by [43, p. 16]

$$\boldsymbol{j}(\omega) = \sigma(\omega)\boldsymbol{E}(\omega), \tag{1.49}$$

with $\sigma(\omega)$ the alternating current (AC) conductivity. The Drude model predicts

$$\sigma(\omega) = \frac{\sigma_0}{1 - i\omega\tau}, \tag{1.50}$$

with $\sigma_0 = ne^2\tau/m$ the direct current (DC) conductivity predicted in the Drude model, n the electron density, and m the electron mass. If the source of the electric field is an electromagnetic wave, we may refer to this result as the optical conductivity: the electrons in the metal are accelerated by the electric field component of the electromagnetic radiation. The magnetic field component does not have a sizeable effect on electronic motion. If the force exerted by the electric field on the electrons is $-e\boldsymbol{E}$, the force generated by the magnetic field is $-(e/c)\boldsymbol{v}\times\boldsymbol{B}$ (in Gaussian units[4]), with c the speed of light. Therefore, the force exerted by the magnetic field component is v/c times smaller than the electric field component, which is around $1/100$, taking v as the Fermi velocity of graphene.

In the case of an external magnetic field applied in the z direction, the Drude model predicts a frequency-dependent conductivity tensor of the form [44, 45]

[4]Throughout this thesis we have used S.I. units, but Gaussian units are useful in this example as they permit a direct comparison between the electric and magnetic field, since they have the same units and order of magnitude in this unit system.

$$\sigma_{ij}(\omega) = \frac{\sigma_0}{(1-i\omega\tau)^2+\omega_c^2\tau^2}\begin{pmatrix}1-i\omega\tau & \omega_c\tau \\ -\omega_c\tau & 1-i\omega\tau\end{pmatrix} = \begin{pmatrix}\sigma_{xx} & \sigma_{xy} \\ -\sigma_{xy} & \sigma_{xx}\end{pmatrix}, \tag{1.51}$$

with $\omega_c = eB/m^*$ the cyclotron frequency. It was considered that the electromagnetic wave's electric and magnetic field components are along the x and y axis, respectively. In the last equality, it was considered the sample is isotropic in the x and y direction, such that $\sigma_{xx} = \sigma_{yy}$, and due to the rotational invariance of the external field in a rotation about the z axis, we have $\sigma_{yx} = -\sigma_{xy}$. In this case, σ_{xy} represents the conductivity perpendicular to the applied electric field; hence, it is the AC conductivity generalization of the Hall effect [45].

1.3.2. Cyclotron Resonance

Looking at the problem of Landau quantization from a semiclassical perspective, the charge carriers move in quantized cyclotron orbits consistent with the Bohr-Sommerfeld criteria of Eq. (1.39). If a carrier were to increase its orbit by absorbing energy from an external source, it could only do it if the final orbit is also allowed by the criteria, i.e., when the energy of the external source matches the energy difference between two allowed orbits. In this sense, the external energy satisfies a resonant condition, and the whole process is known as a "cyclotron resonance". The optical conductivity related to such a process is given by the Kubo-Greenwood formula, corresponding to [46]

$$\sigma_{ij}(\omega,B) = \frac{ge^2}{\omega}\frac{|eB|}{\hbar}\sum_{n,m}\frac{f_n - f_m}{E_m - E_n - (\hbar\omega + i\Gamma)}\langle n|\hat{v}_i|m\rangle\langle m|\hat{v}_j^*|n\rangle, \tag{1.52}$$

with ω the (angular) frequency of the electromagnetic wave, g the degeneracy of the states in the absence of magnetic field, B the magnitude of the external magnetic field, Γ a phenomenological broadening parameter, $f_n = f(E_n)$ the Fermi-Dirac distribution evaluated at the energy E_n, $|n\rangle$ and $|m\rangle$ being states of the system with associated Landu-level energies E_n and E_m, respectively, and $i,j \in \{x,y\}$ indicate the spatial component of the velocity operator $\hat{\boldsymbol{v}} = \partial\hat{H}/\partial(\hbar\boldsymbol{k})$.

Since the quantity measured in magneto-optical experiments is proportional to $\mathrm{Re}(\sigma_{xx})$, non-zero values of the matrix element $\langle n|\hat{v}_x|m\rangle$ indicate that a transition from level n to m is allowed, and therefore, absorption of electromagnetic radiation is observed in the experiment. Such processes are called "optically-allowed transitions" and depend on the form of the velocity operator $\hat{\boldsymbol{v}}$ of the system. In graphene in particular, the optically-allowed transitions follow $|m| = |n| \pm 1$ for unpolarized radiation [46], as indicated in Fig. 1.7 (a).

1.3.3. Shubnikov-de Haas Oscillations

As seen in section 1.2.1, the Landau levels are highly degenerated, with a degeneracy proportional to the magnitude of the magnetic field. The total number of electronic states per LL is given by Eq. (1.27), or electronic density per LL by Eq. (1.28). This implies that changes in the magnetic field induce changes in the population of the LLs, which in turn cause oscillations in the electric resistivity, known as Shubnikov-de Haas oscillations (SdHO) [47, 48]. SdHO can be understood in the following way [38]: suppose that the magnetic field is very high, such that the first LL can accommodate all the electrons in the system. If the magnetic field decreases, so does the number of electrons that the LL can allocate, such that at a given field, defined as B_F, the degeneracy of the LL and the total number of electrons in the system is the same. If the magnetic field decreases below B_F, the next LL starts to populate, changing the Fermi energy and the number of conduction electrons in the system. By reducing the magnetic field further, the process repeats until at $B_F/2$ the second LL becomes fully populated, and the next one starts to populate. This periodic population and depopulation of the LLs is the origin of SdHO.

The electric resistivity and conductivity of a material arise from the scattering of electrons in the system, where the scattering probability is proportional to the number of accessible states. Since the number of states is the convolution of the density of states and the Fermi distribution, they are greatest when the Fermi energy crosses a LL, while lowest when no LL is crossed by E_F, explaining the oscillating behavior in the resistivity.

A quantitative analysis of the SdHO for DC conductivity is given by Adams and Holstein [49] and summarized by Schneider [38]. Such a result can also be applied to the AC conductivity if the condition $\omega\tau \ll 1$ is fulfilled, which is valid for $\omega \ll 20$ THz if typical transport times of the order of 50 fs are considered. The electric conductivity with quantum corrections due to Landau quantization is given by

$$\sigma_{xx}(B) = \frac{\sigma_0}{1+\omega_c^2\tau^2}\left(1+\Delta\sigma_1(B)+\Delta\sigma_2(B)\right), \tag{1.53}$$

with σ_{xx} the longitudinal conductivity[5], σ_0 the classical conductivity in the absence of magnetic field, $\Delta\sigma_1(B)$ the quantum correction term due to scattering between the highest-occupied LL and levels above the Fermi surface (inter-level scattering), and $\Delta\sigma_2(B)$ the quantum correction term due to scattering within the highest-occupied LL (intra-level scattering) [38, 49].

The oscillatory part of the longitudinal conductivity is given by the following equation:

$$\frac{\Delta\sigma_{xx}}{\sigma_0} = \frac{5}{2}\sqrt{\frac{\pi e\hbar B}{E_F m^* \left|S''_{extr}\right|}}\sum_{p=1}^{\infty}\frac{1}{p^{1/2}}R_T(p)R_D(p)R_S(p)\cos\left[2\pi p\left(\frac{B_F}{B}-\gamma+\delta\right)\right]. \tag{1.54}$$

With m^* the effective mass of the carrier, $|S''_{extr}|$ the second derivative of the Fermi surface cross-section perpendicular to the direction of the magnetic field, evaluated at the extremal value (maximum or minimum of S)[6], and $\frac{1}{B_F} = \Delta\left(\frac{1}{B}\right)$ the fundamental frequency of the oscillations. The factor γ is the same as in Eq. (1.37) for the semiclassical treatment of Landau quantization, while δ is a phase factor related to the curvature of the Fermi surface in the direction parallel to the field, with $\delta = \pm 1/8$ for a three-dimensional corrugated surface (plus and minus signs related to maximum and minimum cross sections, respectively) and $\delta = 0$ for a cylindrical surface [38, 50].

The R terms are amplitude factors and are explained as follows. $R_T(p)$ is related to the broadening of the Fermi distribution due to finite T, so that electrons within a vicinity of the Fermi energy contribute to the conduction. It is given by

$$R_T(p) = \frac{\alpha m^* \frac{T}{B}}{\sinh\left(\alpha p m^* \frac{T}{B}\right)}, \quad \text{with } \alpha = \frac{2\pi^2 k_B}{\hbar e}. \tag{1.55}$$

R_D is the Dingle factor, and is related to electron scattering, which broadens the otherwise sharp LLs. It is given by

$$R_D(p) = \exp\left(-\alpha p m^* \frac{T_D(\tau)}{B}\right), \quad \text{with } T_D = \frac{\hbar}{2\pi k_B \tau}. \tag{1.56}$$

τ is the scattering lifetime, interpreted as the average time between electron-scattering events. T_D is referred to as the Dingle temperature. The final term R_S is related to the Zeeman splitting of the Landau levels due to the electron's spin. It is given by

[5] The longitudinal conductivity σ_{xx} has the same direction as a bias voltage applied to accelerate the charge carriers, as opposed to the transversal conductivity, σ_{xy}, which is perpendicular to it and is related to the classical or quantum Hall effect.

[6] If $\boldsymbol{B}$ is in the z-direction, $S''_{extr} = \left.\frac{d^2S}{dk_z^2}\right|_{k_z=k_{extr}}$ with k_{extr} the position of the maximum or minimum cross section.

$$R_S(p) = \cos\left(\frac{\pi}{2} p g \frac{m^*}{m_e}\right), \tag{1.57}$$

with g the electron's g-factor.

Eq. 1.54 shows a complicated oscillatory behavior of the conductivity, however, the periodicity of the oscillations $\frac{1}{B_F} = \Delta\left(\frac{1}{B}\right)$ depends only on each of the extremal (maximal or minimal) cross sections of the Fermi surface, S_{ex}, in the following way

$$\frac{1}{B_F} = \Delta\left(\frac{1}{B}\right) = \frac{2\pi e}{\hbar S_{\text{ex}}}. \tag{1.58}$$

Therefore, if there are several extremal cross sections in the Fermi surface, there will several superimposed SdHO signals with different periodicities.

Analysis of the SdH oscillations allows to obtain relevant information of the sample. For instance, by performing the Fourier transform of the oscillatory part of σ_{xx} as a function of $1/B$, it is possible to obtain the fundamental frequencies B_F of the different type of carriers present in the sample; by analyzing the phase of the oscillations, the parameter γ related to the Berry phase can be obtained. Additionally, by studying how the amplitude of the oscillations changes with respect to the temperature, it is possible to obtain the cyclotron masses m^* and scattering lifetime τ of the carriers.

1.4. Electron-Electron Interactions

So far, electron-electron (e-e) interactions through the Coulomb force have not been considered. In some materials, e-e interactions modify only slightly the electronic properties of the system, so that these properties are well described by a non-interacting (or single-) electron model. For instance, the effective Hamiltonians for graphene and bilayer graphene in Eqs. (1.3) and (1.10) describe non-interacting electrons and holes in each material. However, there are systems in which electron-electron interactions become relevant in the dynamics, in such a way that the single-electron picture fails to describe the system even at a qualitative level [19]. These systems are called strongly-correlated electron systems.

The criteria that determines the importance of e-e interactions is the ratio between the Coulomb energy and kinetic energy at the average interelectronic distance $l \sim k_{\text{F}}^{-1}$ [27],

$$r_s = \frac{E_{\text{int}}}{E_{\text{kin}}}, \tag{1.59}$$

with $E_{\text{int}} = e^2/\varepsilon l$ the Coulomb energy, ε the dielectric constant of the medium surrounding the electrons, and $E_{\text{kin}}(k_{\text{F}})$ the kinetic energy which depends on the Fermi wave vector k_{F}. The parameter r_s then indicates if Coulomb interactions need to be considered, such that a free-electron model is adequate if $r_s \ll 1$, while the limit $r_s \gg 1$ indicates strong electron correlations [27].

To give an estimation of r_s for the systems of our interest, let's consider first the case of parabolic dispersion, relevant for bilayer graphene and electrons at the K point of graphite. In this situation, the kinetic energy term reads $E_{\text{kin}} \sim \hbar^2 k_{\text{F}}^2/m^*$, with m^* the effective mass of the band. We have then [27]

$$r_s = \frac{m^* e^2}{\hbar^2 \varepsilon} l \sim \frac{1}{a_0^* k_{\text{F}}}, \tag{1.60}$$

with $a_0* = a_0 \varepsilon m_0/m^*$ the effective Bohr radius, $a_0 = 0.5$ Å the Bohr radius in vacuum, and m^*/m_0 the ratio between the effective mass and free-electron mass. It is then concluded that e-e interactions are relevant when $l \gg a_0^*$, this is, at large interelectronic distances which represent the dilute limit (low charge-carrier density).

For bilayer graphene specifically, the dielectric constant is of the order of $\varepsilon \sim 1$ [30], the effective mass in the two-band parabolic model is $m^* \approx 0.026\, m_0$, and the Fermi wave vector is of the order of 0.1 nm^{-1} for a typical charge-carrier density of $n = k_{\text{F}}^2/\pi = 10^{12}$ cm^{-2} [30]. This gives a result of $r_s \sim 4$, indicating that the system is in the intermediate regime where e-e interactions have a small quantitative effect on the bands that is often neglected. Decreasing the charge-carrier density or applying high magnetic fields increase the strength of e-e interactions, allowing proposals of correlated ground states inducing ordered phases such as ferromagnetism, layer antiferromagnetism, charge-density wave state, and non-trivial topological states [30].

A similar situation is found in graphite, where e-e interactions are particularly relevant at high magnetic fields. It has been found that a charge-density wave state is induced at low temperatures and a magnetic field around 22 T, collapsing at fields close to 52 T [51], which is explained in part by the renormalization (or modification) of the Landau bands by e-e interactions. If e-e interactions were neglected, then the transition and collapse of charge-density wave state would not occur and the system would remain metallic [51].

In graphene, on the other hand, the linear dispersion changes the relation between the kinetic energy and the Fermi wave vector. In this case, the kinetic energy at the Fermi level reads $E_{\text{kin}} = v_{\text{F}} k_{\text{F}}$, while the Coulomb energy remains the same. In consequence, the parameter r_s is [27]

$$r_s := \alpha_G = \frac{e^2}{\hbar \varepsilon v_{\text{F}}} \simeq \frac{2.2}{\varepsilon}, \tag{1.61}$$

independent of the charge-carrier density, in contrast to bilayer graphene. The definition α_G is made to show the similarity of this value with the fine-structure constant $\alpha = e^2/\hbar\varepsilon c = 1/137$ of quantum electrodynamics [27]. Graphene is then in the intermediate regime, such that e-e interactions are relevant at high-magnetic fields but not at low charge-carrier densities.

To introduce the effects of the magnetic field on e-e interactions and the renormalization of electronic bands would be quite involved and not necessary for the purpose of the present doctoral thesis project. They are covered in detail in the references [27] for graphene and [51, 52] for graphite. Instead, we show some representative results in each system. Fig. 1.8 (a) shows the change in the cyclotron resonance spectrum of graphene induced by band renormalization due to e-e interactions. It is shown that the predicted transitions $E_{-2} \to E_1$ and $E_{-1} \to E_2$, denoted as T_2 and represented by the dotted red line in the plot, do not match the measured values [53], shown as circles and triangles. The discrepancy is attributed to e-e interactions [53]. For graphite, the Landau bands at $B = 55$ T without and with e-e interactions are shown in Figs. 1.8 (b) and (c), respectively. The introduction of e-e interactions predict band renormalization, such that the electron-like $(-1, \downarrow)$ and hole-like $(0, \uparrow)$ bands become empty, where $\downarrow$,$\uparrow$ indicate spin down and spin up states and -1,0 the Landau-level index. This fact demonstrates the collapse of the charge-density waves supported by those bands at lower magnetic fields, and it is observed that if e-e interactions are not considered then the bands would remain partially filled [51].

1.4.1. The Hartree-Fock Approximation

The Hartree-Fock (HF) approximation provides a starting point for treating electron-electron interactions[7]. In this method, the ground state of the interacting electron system is approximated by that of an effective Hamiltonian with an approximated Coulomb interaction. In essence, this method tries to find the "best independent-electron approximation to an interacting many-electron system"[8] [20, p. 69].

Let us first consider the ground state of a system of N non-interacting electrons. It consists of the anti-symmetrized product of single-particle states, i.e., a Slater determinant of the form

[7] The discussion in this subsection is based on reference [20, p. 69].

[8] This statement applies to effective Hamiltonians that conserve the number of electrons [20, p. 69].

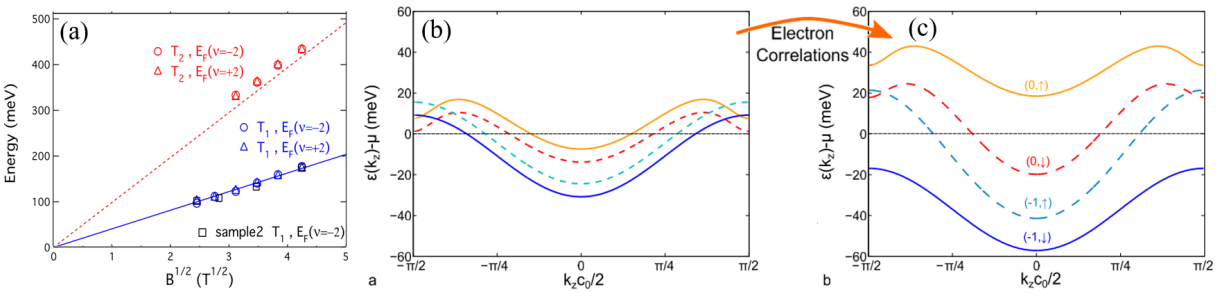

Figure 1.8: (a) Effect of e-e interactions in the cyclotron resonances of graphene. The dotted red line corresponds to the predicted LL transition without considering e-e interactions, the circles and triangles to the measured values (the experimental error is smaller than the symbols). The discrepancy between both is attributed to e-e interactions. (b) Landau levels in graphite at $B = 55$ T as a function of k_z, as calculated by the SWM model. The horizontal line denotes the Fermi level. (c) Same as (b), but considering e-e interactions. Subfigure (a) reprinted with permission from [53]. Copyright (2007) by the American Physical Society. Subfigures (b,c) reprinted with permission from [51]. Copyright (2017) by the American Physical Society.

$$\Psi_{\alpha_1\alpha_2\ldots\alpha_N}(\boldsymbol{r}_1,\boldsymbol{r}_2,\ldots,\boldsymbol{r}_N) = \begin{vmatrix} \varphi_{\alpha_1}(\boldsymbol{r}_1) & \cdots & \varphi_{\alpha_1}(\boldsymbol{r}_N) \\ \varphi_{\alpha_2}(\boldsymbol{r}_1) & \cdots & \varphi_{\alpha_2}(\boldsymbol{r}_N) \\ \vdots & \ddots & \vdots \\ \varphi_{\alpha_N}(\boldsymbol{r}_1) & \cdots & \varphi_{\alpha_N}(\boldsymbol{r}_N) \end{vmatrix}, \tag{1.62}$$

with $\varphi_{\alpha_j}(\boldsymbol{r}_i)$ the single-particle wave function of electron i in the state α_j (spin was omitted). When changing to a system of interacting electrons, the ground state can be written as a superposition of Slater determinants

$$\sum_{\alpha_1\ldots\alpha_N} C_{\alpha_1\ldots\alpha_N}\, \Psi_{\alpha_1\ldots\alpha_N}(\boldsymbol{r}_1,\boldsymbol{r}_2,\ldots,\boldsymbol{r}_N), \tag{1.63}$$

with $C_{\alpha_1\ldots\alpha_N}$ being complex numbers [20, p. 69]. In the HF approximation, one effectively approximates this ground state to a single Slater determinant, and the single-particle wave functions are found as those that minimize the expected value of the full interacting Hamiltonian. To elucidate this procedure, let us consider the Hamiltonian of a system of interacting electrons in second quantization,

$$\hat{\mathcal{H}} = \hat{T} + \hat{V} = \sum_{\boldsymbol{k}\sigma} \frac{\hbar^2 k^2}{2m} \hat{a}^\dagger_{\boldsymbol{k}\sigma}\hat{a}_{\boldsymbol{k}\sigma} + \frac{1}{2}\frac{1}{L^3}\sum_{\sigma\sigma'}\sum_{\boldsymbol{k},\boldsymbol{k}',\boldsymbol{q}} v(\boldsymbol{q})\, \hat{a}^\dagger_{\boldsymbol{k}-\boldsymbol{q},\sigma}\hat{a}^\dagger_{\boldsymbol{k}'+\boldsymbol{q},\sigma'}\hat{a}_{\boldsymbol{k}'\sigma'}\hat{a}_{\boldsymbol{k}\sigma}, \tag{1.64}$$

with $\hat{T}$ and $\hat{V}$ the kinetic energy and Coulomb interaction, $v(\boldsymbol{q}) = e^2/(\varepsilon_0 q^2)$ the Fourier transform of the Coulomb interaction in S.I. units, L^3 the volume of a box containing the electrons, and $\hat{a}^\dagger_{\boldsymbol{k}\sigma}$ and $\hat{a}_{\boldsymbol{k}\sigma}$ the fermionic creation and annihilation operators in the basis of plane waves of wave vector $\boldsymbol{k}$ and spin σ.

Despite the apparent simplicity of the Hamiltonian in Eq. (1.64), a solution to the many-body problem by finding its direct diagonalization has not been achieved. The main issue is the complexity of the Coulomb interaction, which is of fourth order in the creation and annihilation operators. The HF method tackles this problem by approximating the Coulomb interaction to an effective interaction of second order in the creation and annihilation operators, thus allowing a direct diagonalization of the resulting Hamiltonian. The HF Hamiltonian can be written as

$$\hat{\mathcal{H}}_{\mathrm{HF}} = \hat{T} + \hat{V}_{\mathrm{HF}} = \sum_{\boldsymbol{k}\sigma} \frac{\hbar^2 k^2}{2m} \hat{a}^\dagger_{\boldsymbol{k}\sigma}\hat{a}_{\boldsymbol{k}\sigma} + \sum_{\sigma\sigma'}\sum_{\boldsymbol{k},\boldsymbol{k}'} V^{\mathrm{HF}}_{\boldsymbol{k}\sigma,\boldsymbol{k}'\sigma'}\, \hat{a}^\dagger_{\boldsymbol{k}\sigma}\hat{a}_{\boldsymbol{k}'\sigma'}, \tag{1.65}$$

with $V^{\rm HF}_{\boldsymbol{k}\sigma,\boldsymbol{k}'\sigma'}$ the matrix elements of the HF interaction, that are undetermined at this point. Eq. (1.65) represents the Hamiltonian of a single particle experiencing an external field given by $V^{\rm HF}$, and is readily diagonalized by changing the basis set from plane waves to a suitable one. In this new basis, the HF Hamiltonian takes the form

$$\hat{\mathcal{H}}_{\rm HF} = \sum_{\alpha\beta}(T_{\alpha\beta} + V^{\rm HF}_{\alpha\beta})\delta_{\alpha\beta}\hat{a}^\dagger_\alpha\hat{a}_\beta = \sum_\alpha \varepsilon_\alpha\, \hat{a}^\dagger_\alpha\hat{a}_\alpha, \tag{1.66}$$

with $\hat{a}^\dagger_\alpha$, $\hat{a}_\beta$ the fermonic creation and annihilation operators of an electron in the states α, β of the new basis, respectively, and $T_{\alpha\beta}$, $V^{\rm HF}_{\alpha\beta}$ the matrix elements of each operator in the new basis. This Hamiltonian describes a single electron under the effect of the external potential $V^{\rm HF}$. In the first-quantization picture, it corresponds to the Schrödinger equation

$$-\frac{\hbar^2}{2m}\nabla^2\varphi_\alpha(\boldsymbol{r}) + \int d\boldsymbol{r'}\, V^{\rm HF}(\boldsymbol{r},\boldsymbol{r'})\varphi_\alpha(\boldsymbol{r'}) = \varepsilon_\alpha\,\varphi_\alpha(\boldsymbol{r}), \tag{1.67}$$

whose eigenstates $\varphi_\alpha(\boldsymbol{r})$ determine the new basis set. Since this corresponds to the Schrödinger equation of a non-interacting electron, the states of the many-body system will be single Slater determinants as in Eq. (1.62). The ground state is constructed by filling up the vacuum state with electrons in the states of the new basis

$$|\Psi_{\rm HF}\rangle = \prod_{\alpha<N}\hat{a}^\dagger_\alpha|0\rangle, \tag{1.68}$$

where the product runs until there are N electrons in the ground state. To find an explicit expression for $V^{\rm HF}$, necessary to determine the HF ground state, we write the full Hamiltonian of Eq. (1.64) in the basis that diagonalizes the HF Hamiltonian

$$\hat{\mathcal{H}} = \sum_{\alpha\beta} T_{\alpha\beta}\,\hat{a}^\dagger_\alpha\hat{a}_\beta + \frac{1}{2}\sum_{\alpha\beta\gamma\delta} V_{\alpha\beta\gamma\delta}\,\hat{a}^\dagger_\alpha\hat{a}^\dagger_\beta\hat{a}_\gamma\hat{a}_\delta, \tag{1.69}$$

with $T_{\alpha\beta}$ and $V_{\alpha\beta\gamma\delta}$ the matrix elements of the kinetic energy and the Coulomb interaction in the new basis:

$$T_{\alpha\beta} = -\frac{\hbar^2}{2m}\int d\boldsymbol{r}\,\varphi^*_\alpha(\boldsymbol{r})\,\nabla^2\,\varphi_\beta(\boldsymbol{r}), \tag{1.70}$$

$$\begin{aligned} V_{\alpha\beta\gamma\delta} &= \frac{1}{4\pi\varepsilon_0}\int d\boldsymbol{r}\,d\boldsymbol{r'}\varphi^*_\alpha(\boldsymbol{r})\,\varphi^*_\beta(\boldsymbol{r'})\frac{e^2}{|\boldsymbol{r}-\boldsymbol{r'}|}\,\varphi_\gamma(\boldsymbol{r'})\,\varphi_\delta(\boldsymbol{r}) \\ &= \int d\boldsymbol{r}\,d\boldsymbol{r'}\,d\boldsymbol{q}\,e^{-i\boldsymbol{q}\cdot\boldsymbol{r}}\,v(\boldsymbol{q})\,\varphi^*_\alpha(\boldsymbol{r})\,\varphi^*_\beta(\boldsymbol{r'})\,\varphi_\gamma(\boldsymbol{r'})\,\varphi_\delta(\boldsymbol{r}). \end{aligned} \tag{1.71}$$

Taking into account Wick's theorem and the normal ordering of field operators, the fourth-order operator in the Coulomb interaction can be rewritten as

$$\begin{aligned} \hat{a}^\dagger_\alpha\hat{a}^\dagger_\beta\hat{a}_\gamma\hat{a}_\delta = &\langle\hat{a}^\dagger_\alpha\hat{a}_\delta\rangle\langle\hat{a}^\dagger_\beta\hat{a}_\gamma\rangle - \langle\hat{a}^\dagger_\alpha\hat{a}_\gamma\rangle\langle\hat{a}^\dagger_\beta\hat{a}_\delta\rangle \\ &+ \langle\hat{a}^\dagger_\alpha\hat{a}_\delta\rangle :\hat{a}^\dagger_\beta\hat{a}_\gamma: + \langle\hat{a}^\dagger_\beta\hat{a}_\gamma\rangle :\hat{a}^\dagger_\alpha\hat{a}_\delta: \\ &- \langle\hat{a}^\dagger_\alpha\hat{a}_\gamma\rangle :\hat{a}^\dagger_\beta\hat{a}_\delta: - \langle\hat{a}^\dagger_\beta\hat{a}_\delta\rangle :\hat{a}^\dagger_\alpha\hat{a}_\gamma: \\ &+ :\hat{a}^\dagger_\alpha\hat{a}^\dagger_\beta\hat{a}_\gamma\hat{a}_\delta:, \end{aligned} \tag{1.72}$$

where $\langle\cdots\rangle = \langle\Psi_{\rm HF}|\cdots|\Psi_{\rm HF}\rangle$ are the field averages with respect to the HF ground state, and $:\cdots:$ is the normal ordering operation that moves to the right the operators that annihilate

$|\Psi_{\text{HF}}\rangle$[9]. Only constant terms appear in the first line of Eq. (1.72); thus, they can be omitted in the total Hamiltonian. The final line is the normal ordering of the fourth-order term, and by definition, its expected value with respect to the HF ground state is zero. Additionally, its variation with respect to the HF ground state is also zero [20, p. 79]. For these reasons, the Coulomb interaction is simplified in the HF approximation by discarding the normal-ordered fourth-order term. Since this term is responsible of quantum fluctuations, the HF approximation effectively suppresses them.

We are left then with the second and third line of Eq. (1.72). Noticing that $V_{\alpha\beta\gamma\delta} = V_{\beta\alpha\delta\gamma}$, making use of the identity : $\hat{a}^\dagger_\alpha \hat{a}_\beta := \hat{a}^\dagger_\alpha \hat{a}_\beta - \langle \hat{a}^\dagger_\alpha \hat{a}_\beta \rangle$, and omitting again constant terms, the fourth-order operator can be approximated to

$$\hat{a}^\dagger_\alpha \hat{a}^\dagger_\beta \hat{a}_\gamma \hat{a}_\delta \approx 2\langle \hat{a}^\dagger_\beta \hat{a}_\gamma \rangle \hat{a}^\dagger_\alpha \hat{a}_\delta - 2\langle \hat{a}^\dagger_\beta \hat{a}_\delta \rangle \hat{a}^\dagger_\alpha \hat{a}_\gamma. \tag{1.73}$$

Considering that we are working in the basis of eigenstates of the HF Hamiltonian, the expected value of the operators follow $\langle \hat{a}^\dagger_\beta \hat{a}_\gamma \rangle = n_\gamma \delta_{\beta\gamma}$, with $n_\gamma = 0{,}1$ the occupation of the γ state. With this in mind, and after a convenient reorganization of the indices, we arrive at the Coulomb interaction in the HF approximation

$$\hat{V} \approx \sum_{\alpha\beta\gamma\delta} (V_{\alpha\beta\gamma\delta} - V_{\alpha\beta\delta\gamma}) \langle \hat{a}^\dagger_\beta \hat{a}_\gamma \rangle \hat{a}^\dagger_\alpha \hat{a}_\delta = \sum_{\alpha\beta} \sum_{\gamma} n_\gamma \, (V_{\alpha\gamma\gamma\beta} - V_{\alpha\gamma\beta\gamma}) \hat{a}^\dagger_\alpha \hat{a}_\beta. \tag{1.74}$$

This is the desired interaction of second order in the creation and annihilation operators. From it, we can identify that the matrix elements of the HF interaction are related to those of the Coulomb interaction as

$$V^{\text{HF}}_{\alpha\beta} = \sum_{\gamma} n_\gamma \, (V_{\alpha\gamma\gamma\beta} - V_{\alpha\gamma\beta\gamma}). \tag{1.75}$$

Although the interaction of Eq. (1.74) is written in the basis that diagonalizes the HF Hamiltonian, it can be changed to any basis, retaining a similar form. In particular, in the basis of plane waves, it is given by

$$\hat{V} \approx \sum_{\sigma\sigma'} \sum_{\boldsymbol{k}\boldsymbol{k}'} \sum_{\gamma} n_\gamma \, (V_{\boldsymbol{k}\sigma,\gamma,\gamma,\boldsymbol{k}'\sigma'} - V_{\boldsymbol{k}\sigma,\gamma,\boldsymbol{k}'\sigma',\gamma}) \hat{a}^\dagger_{\boldsymbol{k}\sigma} \hat{a}_{\boldsymbol{k}'\sigma'}, \tag{1.76}$$

with

$$V^{\text{HF}}_{\boldsymbol{k}\sigma,\boldsymbol{k}'\sigma'} = \sum_{\gamma} n_\gamma \, (V_{\boldsymbol{k}\sigma,\gamma,\gamma,\boldsymbol{k}'\sigma'} - V_{\boldsymbol{k}\sigma,\gamma,\boldsymbol{k}'\sigma',\gamma}), \tag{1.77}$$

and γ still indicates states in the basis that diagonalizes the HF Hamiltonian.

Perhaps it is more illustrative to write the HF interaction in the first quantized representation as follows

$$\begin{aligned} V^{\text{HF}}(\boldsymbol{r},\boldsymbol{r}') &= \sum_{\alpha\beta} V^{\text{HF}}_{\alpha\beta} \varphi_\alpha(\boldsymbol{r}) \varphi^*_\beta(\boldsymbol{r}') \\ &= \delta(\boldsymbol{r}-\boldsymbol{r}') \int d\boldsymbol{r}'' \, \frac{1}{4\pi\varepsilon_0} \frac{e^2}{|\boldsymbol{r}-\boldsymbol{r}''|} \sum_\alpha n_\alpha \, |\varphi_\alpha(\boldsymbol{r}'')|^2 - \frac{1}{4\pi\varepsilon_0} \frac{e^2}{|\boldsymbol{r}-\boldsymbol{r}'|} \sum_\alpha n_\alpha \varphi_\alpha(\boldsymbol{r}) \varphi^*_\alpha(\boldsymbol{r}'). \end{aligned} \tag{1.78}$$

The first term on the right-hand side is the Hartree term; it is local due to its dependence on $\delta(\boldsymbol{r}-\boldsymbol{r}')$, and is interpreted as the interaction energy of an electron with the average electrostatic potential generated by the charge density of all electrons. The second term is Fock term or

[9] For instance, if the states α,β are occupied, and γ is unoccupied in the HF ground state, the normal ordering of the operators yields : $\hat{a}^\dagger_\alpha \hat{a}_\beta \hat{a}_\gamma := -\hat{a}_\beta \hat{a}^\dagger_\alpha \hat{a}_\gamma = \hat{a}_\beta \hat{a}_\gamma \hat{a}^\dagger_\alpha$, where the underline indicate operators that annihilate the HF ground state: $\underline{\hat{a}}|\Psi_{\text{HF}}\rangle = 0$. The minus sign comes from the anticommutation rules of fermionic operators.

exchange potential. Its origin is purely due to the indistinguishability of electrons, resulting in the antisymmetry of the many-body wave function.

In summary, we have constructed the HF Hamiltonian of Eqs. (1.65, 1.66), with a second-order HF interaction given by Eqs. (1.74, 1.75). The HF Hamiltonian is diagonalized by finding an appropriate basis set, from which the HF ground state of Eq. (1.68) is constructed. Nevertheless, to find the new basis states and the ground state, it is necessary to know the exact form of the HF interaction, which at the same time is written in terms of the new basis! This defines a self-consistent problem, and a way to solve it is by proposing (or guessing) the states that diagonalize the HF Hamiltonian, which determine HF interaction through Eq. (1.78), from which the new states can be re-calculated from Eq. (1.67). Therefore, Eqs. (1.67, 1.78) correspond to the self-consistent set of equations in the HF approximation.

2. Spectroscopic Signature of Spin-Density Waves in Graphite at High Magnetic Fields

When subjected to sufficiently low temperatures and external magnetic fields perpendicular to the graphite planes, graphite's energy bands become quantized into Landau bands.[1] Graphite, being a semimetal, is an interesting model system since its low carrier density allows it to enter the quantum limit, where only the lowest Landau bands are occupied, at experimentally accessible magnetic fields ($B \sim 8$ T). In this regime, graphite behaves effectively as a one-dimensional system due to the one-dimensional character of the Landau-band dispersion. One-dimensional bands are unique because Fermi-point nesting becomes trivial, i.e., a reciprocal lattice vector always connects two different points of the Landau bands at the Fermi level. This property indicates that the system is unstable under interactions, such as electron-phonon or electron-electron interactions, which lead to a phase transition into a more energetically favorable collective ground state. In graphite, these special ground states are charge- and spin-density waves (CDWs and SDWs).

The first indication of an electronic phase transition in graphite came by measurements of the in-plane magnetoresistance at high magnetic fields, where an anomalous resistance increase as a function of the magnetic field was observed [54]. Theoretical calculations attributed this anomaly to an energy gap opening in one of the graphite bands due to the emergence of a magnetic-field-induced CDW [21] and concluded that the responsible mechanism was Coulomb interactions rather than electron-phonon coupling. Subsequent measurements at higher magnetic fields unveiled the presence of additional resistance anomalies associated with the emergence and collapse of CDWs in the occupied Landau bands [22, 51, 55–57]. Electron-electron interactions were found to be also responsible for the renormalization of the bands and their depopulation at magnetic fields of the order of ~ 52 T [52], thus explaining the CDW collapse and magnetoresistance anomalies. However, recent studies show conflicting views on the nature of graphite's ground state at high magnetic fields ($\sim$70 T); while Arnold et al. argue about a transition into an insulating phase due to the depopulation of all Landau bands (thus, the collapse of all CDWs) [51], Fauqué et al. demonstrate with experimental results that graphite remains conductive above 75 T, suggesting that the Landau bands $(0, \downarrow)$ and $(-1, \uparrow)$ remain populated [57]. A direct measurement of the energy gap emerging in the CDW/SDW phase would constitute definitive proof of the true ground state of graphite, however, attempts to measure it via tunnel-junction experiments show conflicting results [58, 59], and, to the best of our knowledge, optical spectroscopy measurements have not been performed.

In the present chapter, we present a theoretical treatment of SDW in the region around $B \sim 75$ T, where only two of the Landau bands are populated, and propose an approach to detect them via their cyclotron resonance response. In our calculations, we do not aim to precisely determine the SDW transition point or the SDW gap, which cannot be done reliably even with advanced field-theoretical methods that appropriately treat the effects of electron self-energy and screening in the Coulomb interaction. Instead, we aim to study the main characteristics of

[1] The conditions for Landau band formation were outlined in Section 1.2.2.

the SDW energy bands, the order of the corresponding electronic phase transition, and evaluate how they manifest themselves in the cyclotron resonance. We argue that the proposed model captures the main spectroscopic signatures of the SDW.

The structure of the chapter is as follows: in Section 2.1, we give a brief introduction to CDWs and SDWs, explaining the concept of Fermi surface nesting responsible for the emergence of such phases; in Section 2.2, we develop an approximation to the Landau bands that permits an analytical treatment of the problem; in Section 2.3, we find an analytical solution to SDWs within the Hartree-Fock formalism, while in section 2.4, we develop approximate analytical solutions in some relevant scenarios. In Section 2.5, we perform a numerical solution to the SDW that allows us to compute the spectroscopic signature of SDW in Section 2.6, where we identify the main features that would allow an experimental verification.

The results obtained in this chapter were realized under the supervision of Dr. Denis Basko at the Laboratoire de Physique et Modélisation des Milieux Condensés (LPMMC) in Grenoble, France, to whom I acknowledge his enormous support and hospitality during my internship in the mentioned institute.

2.1. A Brief Introduction to Charge- and Spin-Density Waves

In a metal at ambient pressure and temperature, most of its electronic properties can be described by Landau's Fermi liquid theory, which is based on Landau's observation that "a system of particles satisfying Fermi statistics (not necessarily electrons) admits a phase that is qualitatively similar to an independent particle model" [20, Pag. 3]. A Fermi liquid can be accurately described by a non-interacting electron system, with the effect of electron-electron interactions accounting for modifying certain electronic properties, most notably their mass. In this model and at electron densities commonly found in metals, the ground state corresponds to the paramagnetic state [20, p. 55], where an equal number of electrons with spin up and down fill the energy states up to the Fermi level, and is characterized by no long-range ordering and a uniform electron density. However, in 1962, Overhauser demonstrated that when electron-electron interactions are introduced and treated within the Hartree-Fock formalism, the paramagnetic state is unstable to the formation of an SDW state [60]. Overhauser observed that an interaction connecting electron states on opposite sides of the Fermi surface leads to an increase in the magnitude of the exchange energy, while the kinetic energy experiences just a small increase [60, 61], generating the SDW phase with lower energy than the paramagnetic state. In a CDW, the electron density becomes non-uniform and acquires a periodic spatial modulation with wave vector $\boldsymbol{Q}$, while the spin density remains uniform. On the contrary, in an SDW, the electron density remains uniform while the spin density gets a spatial modulation [62]. The emergence of one or another depends on the spin of the electron states connected by the interaction: CDW if they have the same spin, SDW if they have opposite spins.

Although Overhauser's argument applies only to systems with a spherical Fermi surface, it was later identified that systems with anisotropic Fermi surfaces with the *nesting* property also lead to SDW formation [63]. Nesting is the property in which a single vector connects large parts of the Fermi surface. To illustrate this concept, let us consider the model of electrons in a square lattice with only nearest-neighbor interaction. In this model, the electron's energy is given by [19, pp. 403, 404]

$$E(\boldsymbol{k}) = -2t\left(\cos(k_x a) + \cos(k_y a)\right), \tag{2.1}$$

with t the hopping energy between nearest neighbors, and a the distance between lattice sites, fixed to $a = 1$ for simplicity. The k-vectors are within the Brillouin zone, which has a square shape spanning $-\pi \leq k_x < \pi$, $-\pi \leq k_y < \pi$, as shown in Fig. 2.1 (a). Fig. 2.1 (a) displays the Fermi surfaces (contours in a 2D system) at different electron densities per lattice site, n. It is observed that at a density $n = 1$, the Fermi surface is a square and that a single vector

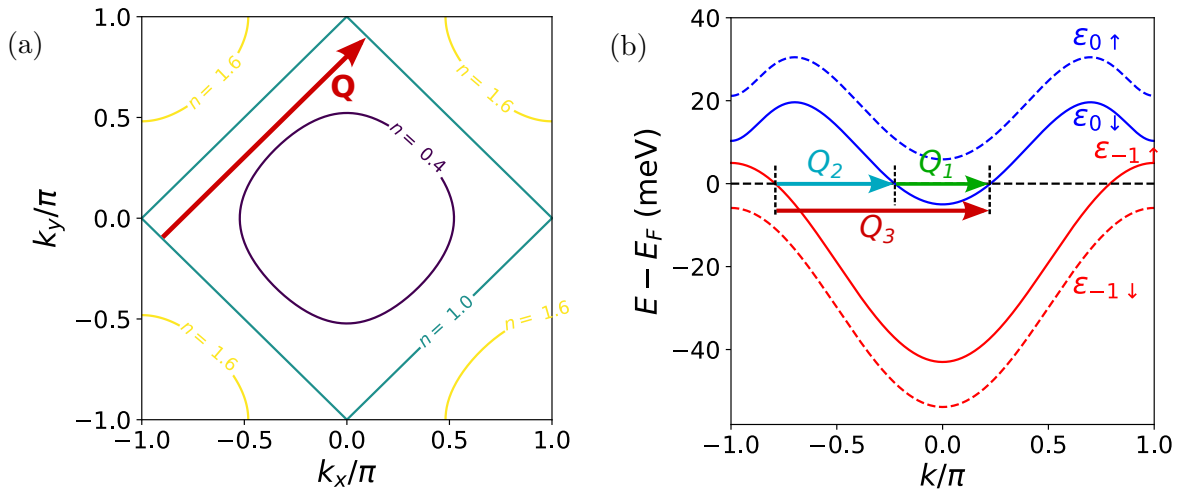

Figure 2.1: (a) Brillouin zone of the square lattice, with lines indicating the Fermi surfaces at different electron densities n. At $n = 1$, the Fermi surface is a square, with the nesting vector $\boldsymbol{Q} = (\pi,\pi)$ shown by the red arrow. (b) Scheme of the Landau bands of graphite when only the bands $\varepsilon_{-1\uparrow}$ and $\varepsilon_{0\downarrow}$ are occupied. Different nesting scenarios are shown: intraband nesting with vector $Q_1 = 2k_F$, interband nesting with vectors $Q_2 = \pi - 2k_F$, and $Q_3 = \pi$. The latter corresponds to the nesting scenario responsible for SDW formation studied in this chapter.

$\boldsymbol{Q} = (\pi,\pi)$ connects large portions of it, as shown by the red arrow in the figure. In contrast, at other densities, no unique vector fulfills this requirement. Therefore, it is said that the Fermi surface at $n = 1$ is nested. Fermi surface nesting is linked to the emergence of instabilities giving rise to electronic phase transitions, for example, the emergence of an antiferromagnetic state in the Hubbard model [19, p. 416], and the SDW state in chromium [63].

In one-dimensional systems, nesting is a trivial feature since the Fermi surface becomes "Fermi points", and there always exists a vector that connects two such points. This is what effectively happens in graphite at high magnetic fields: Landau quantization quenches the degrees of freedom perpendicular to the magnetic field, in such a way that the energy bands only depend on the wave vector parallel to it (in our case, the k_z vector), and the problem becomes one-dimensional. This is responsible for the magnetic-field-induced CDW and SDW instabilities discussed in the preceding section. To conclude this brief introduction to CDWs and SDWs, in Fig. 2.1 (b) we display different possible nesting scenarios in graphite at magnetic fields larger than 52 T, where only the two lowest Landau bands are occupied. Intraband nesting characterized by the nesting vector $Q_1 = 2k_F$ in the band $\varepsilon_{0\downarrow}$ is shown, and the same intraband nesting appears in $\varepsilon_{-1\uparrow}$. Two interband nesting possibilities are displayed, with vectors $Q_2 = \pi - 2k_F$ and $Q_3 = \pi$. It can be proven [51], that the Q_2 nesting does not generate a CDW instability.[2] The $Q_3 = \pi$ nesting scenario gives rise to the SDW instability investigated in this chapter, with the SDW having total spin $S = 1$ [51]. Nevertheless, this does not mean that the intraband instability characterized by Q_1 must be excluded, on the contrary, it constitutes an interesting problem that will be studied in the future.

[2]This is due to the Pauli blocking mechanism: if one considers a deviation $Q_2 + \delta k$, with δk small, depending on the sign of δk the resulting vector connects either occupied parts of both bands, or unoccupied parts of them, leading to a null CDW order parameter. See the supplementary information of [51].

2.2. Landau Bands of Graphite at High Magnetic Fields

When subjected to an external magnetic field perpendicular to the graphite planes, i.e. along its c-axis, graphite's energy bands become quantized into Landau bands, whose energy depends on the discrete Landau level index, N, and the wave vector k_z. In this chapter, we measure k_z in units of $1/c_0$, with $c_0 = 6.7$ Å the vertical length of graphite's unit cell (Chapter 1, Fig. 1.4 (a)), such that within the Brillouin zone it takes the values $-\pi < k_z \leq \pi$. We use the SWM model introduced in section 1.1.3 and apply to it the canonical formalism of section 1.2.2 to obtain the Landau bands of graphite.

In general, the three-dimensional single-particle wave functions of electrons in graphite can be sought as

$$\Psi(\boldsymbol{r}_\parallel,z) = \frac{e^{i\boldsymbol{K}\cdot\boldsymbol{r}_\parallel}}{\sqrt{L_z}} \sum_n e^{ik_z n} \begin{pmatrix} e^{ik_z/2}\,\psi_{1A}(\boldsymbol{r}_\parallel)\,u_{1A}(\boldsymbol{r}_\parallel,z-c_0n-c_0/2) \\ e^{ik_z/2}\,\psi_{1B}(\boldsymbol{r}_\parallel)\,u_{1B}(\boldsymbol{r}_\parallel,z-c_0n-c_0/2) \\ \psi_{2A}(\boldsymbol{r}_\parallel)\,u_{2A}(\boldsymbol{r}_\parallel,z-c_0n) \\ \psi_{2B}(\boldsymbol{r}_\parallel)\,u_{2B}(\boldsymbol{r}_\parallel,z-c_0n) \end{pmatrix}, \tag{2.2}$$

where $\boldsymbol{r}_\parallel = (x,y)$, $\boldsymbol{K}$ is the in-plane component of the wave vector at the K point, L_z the sample length along the z axis, and $\psi_{j\alpha}$ the envelope functions with subindices $j = 1,2$ representing one of the two layers in graphite's primitive cell, and $\alpha = A,B$ a sublattice within a given layer. The z dependence is obtained through the Bloch-Wannier functions $u_{j\alpha}(\boldsymbol{r}_\parallel,z)$, being periodic in $\boldsymbol{r}_\parallel$ and localized in z. They are normalized to unit average of $|u_{j\alpha}|^2$ over a unit cell.

The envelope functions $\psi_{j\alpha}$ are found from the SWM Hamiltonian. It is expanded in terms of p_x and p_y, the in-plane quasi-momentum components measured from the H-K-H line of graphite's Brillouin zone (Fig. 1.4 (b)), and the following effective single-particle Hamiltonian is obtained

$$\hat{\mathcal{H}}_{k_z}(\hat{\boldsymbol{p}}) = \begin{pmatrix} \Gamma_2 & v\hat{p}_- & -\alpha_4 v\hat{p}_- & \alpha_3 v\hat{p}_+ \\ v\hat{p}_+ & \Gamma_5 & \Gamma_1 & -\alpha_4 v\hat{p}_- \\ -\alpha_4 v\hat{p}_+ & \Gamma_1 & \Gamma_5 & v\hat{p}_- \\ \alpha_3 v\hat{p}_- & -\alpha_4 v\hat{p}_+ & v\hat{p}_+ & \Gamma_2 \end{pmatrix}, \tag{2.3}$$

with $\hat{p}_\pm = \hat{p}_x \pm i\hat{p}_y$, and

$$\Gamma_1 = 2\gamma_1\mathcal{C}, \quad \Gamma_2 = 2\gamma_2\mathcal{C}^2, \quad \alpha_{3,4} = \frac{2\gamma_{3,4}}{\gamma_0}\mathcal{C}, \quad \Gamma_5 = 2\gamma_5\mathcal{C}^2 + \Delta, \quad \mathcal{C} = \cos\frac{k_z}{2}, \quad v = \frac{3}{2}\frac{\gamma_0 a}{\hbar}, \tag{2.4}$$

with parameter values [36]

$$\begin{gathered} \gamma_0 = 3.37 \text{ eV}, \quad \gamma_1 = 363 \text{ meV}, \quad \gamma_2 = -24 \text{ meV}, \quad \gamma_3 = 310 \text{ meV}, \\ \gamma_4 = 70 \text{ meV}, \quad \gamma_5 = 50 \text{ meV}, \quad \Delta = -7 \text{ meV}, \quad a = 1.42 \text{ Å}. \end{gathered} \tag{2.5}$$

The Hamiltonian acts on the subspace of envelope functions at a given value of k_z:

$$\psi(x,y) = \begin{pmatrix} \psi_{1A}(x,y) \\ \psi_{1B}(x,y) \\ \psi_{2A}(x,y) \\ \psi_{1B}(x,y) \end{pmatrix}. \tag{2.6}$$

The magnetic field is introduced via the potential vector in the Landau gauge $\boldsymbol{A} = (-By,0,0)$, supposing that $B > 0$, and by applying the Peierls substitution $\hat{\boldsymbol{p}} \to \hat{\boldsymbol{\Pi}} = \hat{\boldsymbol{p}} + e\boldsymbol{A}$ as shown in section 1.2.1, the following commutation relations for the kinetic momentum $\hat{\boldsymbol{\Pi}}$ are found

$$\left[\hat{\Pi}_x,\hat{\Pi}_y\right] = \left[\,\hat{p}_x - eB\hat{y},\,\hat{p}_y\,\right] = -i\frac{\hbar^2}{l_B^2}, \quad \left[\hat{\Pi}_z,\hat{\Pi}_y\right] = 0, \quad \left[\hat{\Pi}_z,\hat{\Pi}_x\right] = 0. \tag{2.7}$$

From the first commutator, we can define the creation and annihilation operators

$$\hat{a} = \frac{l_B}{\sqrt{2}\hbar}\left(\hat{\Pi}_x - i\hat{\Pi}_y\right), \quad \hat{a}^\dagger = \frac{l_B}{\sqrt{2}\hbar}\left(\hat{\Pi}_x + i\hat{\Pi}_y\right), \quad \left[\hat{a},\hat{a}^\dagger\right] = 1. \tag{2.8}$$

And by defining $\varepsilon_B = \sqrt{2}\hbar v/l_B$, the effective SWM Hamiltonian describing electrons in graphite interacting with a magnetic field is found as

$$\hat{\mathcal{H}}_{k_z} = \begin{pmatrix} \Gamma_2 & \varepsilon_B\hat{a} & -\alpha_4\varepsilon_B\hat{a} & \alpha_3\varepsilon_B\hat{a}^\dagger \\ \varepsilon_B\hat{a}^\dagger & \Gamma_5 & \Gamma_1 & -\alpha_4\varepsilon_B\hat{a} \\ -\alpha_4\varepsilon_B\hat{a}^\dagger & \Gamma_1 & \Gamma_5 & \varepsilon_B\hat{a} \\ \alpha_3\varepsilon_B\hat{a} & -\alpha_4\varepsilon_B\hat{a}^\dagger & \varepsilon_B\hat{a}^\dagger & \Gamma_2 \end{pmatrix}. \tag{2.9}$$

In the case $\alpha_3 \neq 0$, the wave functions can be sought in the form [64]

$$\psi_{p_x,k_z}(x,y) = \frac{e^{ip_x x}}{\sqrt{L_x}} \sum_{N=-1}^{\infty} \begin{pmatrix} C_{1,k_z}^{(N)}\,\varphi_{N+1}(y/l_B + p_x l_B) \\ C_{2,k_z}^{(N)}\,\varphi_{N+1}(y/l_B + p_x l_B) \\ C_{3,k_z}^{(N)}\,\varphi_{N+1}(y/l_B + p_x l_B) \\ C_{4,k_z}^{(N)}\,\varphi_{N+1}(y/l_B + p_x l_B) \end{pmatrix}, \tag{2.10}$$

with L_x the sample dimensions in the x direction; $C_{j,k_z}^{(N)}$ real coefficients, and we work in the convention where graphite states are labeled from $N = -1$. φ_N are the harmonic oscillator wave functions obeying

$$\hat{a}^\dagger\varphi_N = \sqrt{N+1}\varphi_{N+1}, \quad \hat{a}\varphi_N = \sqrt{N}\varphi_{N-1}, \quad \hat{a}^\dagger\hat{a}\varphi_N = N\varphi_N. \tag{2.11}$$

When $\alpha_3 \neq 0$, the coefficient $C_{j,k_z}^{(N)}$ is coupled with $C_{j,k_z}^{(N+3)}$, which in turn is coupled with $C_{j,k_z}^{(N+6)}$, and so on, such that the secular equation associated to the Hamiltonian $\hat{\mathcal{H}}_{k_z}$ is of infinite order [42]. The problem of finding the energy bands and eigenstates of $\mathcal{H}_{k_z}$ can be solved by truncating the infinite-dimensional Hamiltonian to a finite matrix and performing numerical diagonalization [38, 42]. However, noticing that $\alpha_3 \sim 0.18$, the term $\alpha_3\varepsilon_B$ is much smaller than Γ_1,ε_B, allowing us to work in the approximation $\alpha_3 \approx 0$. This removes the coupling between the coefficients, and the infinite-dimensional Hamiltonian splits into 4×4 blocks consisting of subspaces generated by the basis vectors [64]

$$\begin{aligned} \psi_{p_x,k_z}^{(-1)}(x,y) &= \frac{e^{ip_x x}}{\sqrt{L_x}} \begin{pmatrix} 0 \\ 0 \\ 0 \\ \varphi_0(\xi) \end{pmatrix}, \quad \psi_{p_x,k_z}^{(0)}(x,y) = \frac{e^{ip_x x}}{\sqrt{L_x}} \begin{pmatrix} 0 \\ x_{2,k_z}^{(0)}\,\varphi_0(\xi) \\ x_{3,k_z}^{(0)}\,\varphi_0(\xi) \\ x_{4,k_z}^{(0)}\,\varphi_1(\xi) \end{pmatrix}, \\ \psi_{p_x,k_z}^{(N)}(x,y) &= \frac{e^{ip_x x}}{\sqrt{L_x}} \begin{pmatrix} x_{1,k_z}^{(N)}\,\varphi_{N-1}(\xi) \\ x_{2,k_z}^{(N)}\,\varphi_N(\xi) \\ x_{3,k_z}^{(N)}\,\varphi_N(\xi) \\ x_{4,k_z}^{(N)}\,\varphi_{N+1}(\xi) \end{pmatrix}, \qquad (\text{for } N \geq 1), \end{aligned} \tag{2.12}$$

with $\xi = y/l_B + p_x l_B$. N represents the Landau band index, and for each N there are four associated states, except for $N = -1,0$, for which there are one and three states, respectively.

Since we are interested in the energy spectrum and wave functions at high magnetic fields, we can approximate Eq. (2.9) by keeping only the dominant terms with higher energy. Since

$\Gamma_2 \sim -48$ meV, and $\Gamma_5 \sim 93$ meV, at $B = 75$ T we have Γ_2,$\Gamma_5 \ll \varepsilon_B = 343$ meV, and noticing that $\alpha_{3,4} \ll 1$, the Hamiltonian is approximated to

$$\hat{\mathcal{H}}_{k_z} = \begin{pmatrix} 0 & \varepsilon_B \hat{a} & 0 & 0 \\ \varepsilon_B \hat{a}^\dagger & 0 & \Gamma_1 & 0 \\ 0 & \Gamma_1 & 0 & \varepsilon_B \hat{a} \\ 0 & 0 & \varepsilon_B \hat{a}^\dagger & 0 \end{pmatrix}. \tag{2.13}$$

The wave functions of the Hamiltonian are given by Eq. (2.12), whose coefficients $x^{(N)}_{j,k_z}$ and energies can be found from the eigenvalue problem resulting by operating $\hat{\mathcal{H}}_{k_z}$ on them, as follows

$$\begin{pmatrix} -\varepsilon & \Gamma_1 & 0 \\ \Gamma_1 & -\varepsilon & \varepsilon_B \\ 0 & \varepsilon_B & -\varepsilon \end{pmatrix} \begin{pmatrix} x^{(0)}_{2,k_z} \\ x^{(0)}_{3,k_z} \\ x^{(0)}_{4,k_z} \end{pmatrix} = 0 \quad (\text{if } N = 0), \tag{2.14}$$

$$\begin{pmatrix} -\varepsilon & \varepsilon_B\sqrt{N} & 0 & 0 \\ \varepsilon_B\sqrt{N} & -\varepsilon & \Gamma_1 & 0 \\ 0 & \Gamma_1 & -\varepsilon & \varepsilon_B\sqrt{N+1} \\ 0 & 0 & \varepsilon_B\sqrt{N+1} & -\varepsilon \end{pmatrix} \begin{pmatrix} x^{(N)}_{1,k_z} \\ x^{(N)}_{2,k_z} \\ x^{(N)}_{3,k_z} \\ x^{(N)}_{4,k_z} \end{pmatrix} = 0 \quad (\text{if } N \geq 1). \tag{2.15}$$

In particular, we find a low-energy subspace spanned by wave functions with $N = -1,0$

$$\psi^{(-1)}_{p_x,k_z}(x,y) = \frac{e^{ip_x x}}{\sqrt{L_x}} \begin{pmatrix} 0 \\ 0 \\ 0 \\ \varphi_0(\xi) \end{pmatrix}, \quad \psi^{(0)}_{p_x,k_z}(x,y) = \frac{e^{ip_x x}}{\sqrt{L_x}} \frac{1}{\sqrt{\varepsilon_B^2 + \Gamma_1^2}} \begin{pmatrix} 0 \\ \varepsilon_B\, \varphi_0(\xi) \\ 0 \\ -\Gamma_1\, \varphi_1(\xi) \end{pmatrix}. \tag{2.16}$$

Although in this approximation, the energies of these states are $\varepsilon_{-1} = \varepsilon_0 = 0$, a better estimation of

$$\varepsilon_{-1} = \Gamma_2, \qquad \varepsilon_0 = \frac{\varepsilon_B^2 \Gamma_5 + \Gamma_1^2 \Gamma_2}{\varepsilon_B^2 + \Gamma_1^2} \tag{2.17}$$

is found by applying the Hamiltonian of Eq. (2.9) to the previous wave functions, while still considering $\alpha_{3,4} \approx 0$.

At higher energies, there are two additional states associated with $N = 0$, corresponding to the wave functions

$$\psi^{(0\pm)}_{p_x,k_z}(x,y) = \frac{e^{ip_x x}}{\sqrt{L_x}} \frac{1}{\sqrt{2(\varepsilon_B^2 + \Gamma_1^2)}} \begin{pmatrix} 0 \\ \Gamma_1\, \varphi_0(\xi) \\ \pm\sqrt{\varepsilon_B^2 + \Gamma_1^2}\, \varphi_0(\xi) \\ \varepsilon_B\, \varphi_1(\xi) \end{pmatrix} \tag{2.18}$$

with energies $\varepsilon_{0\pm} = \pm\sqrt{\varepsilon_B^2 + \Gamma_1^2}$, and four states $N = 1$ with energies

$$\varepsilon_{1\pm\pm} = \pm\frac{1}{\sqrt{2}} \sqrt{3\varepsilon_B^2 + \Gamma_1^2 \pm \sqrt{\varepsilon_B^4 + 6\varepsilon_B^2\Gamma_1^2 + \Gamma_1^4}}. \tag{2.19}$$

Up to this point, we have not discussed the role of spin in the Landau bands. Interaction between the electron spin and the magnetic field results in the Zeeman splitting of the Landau bands, producing a spin-dependent energy shift as follows

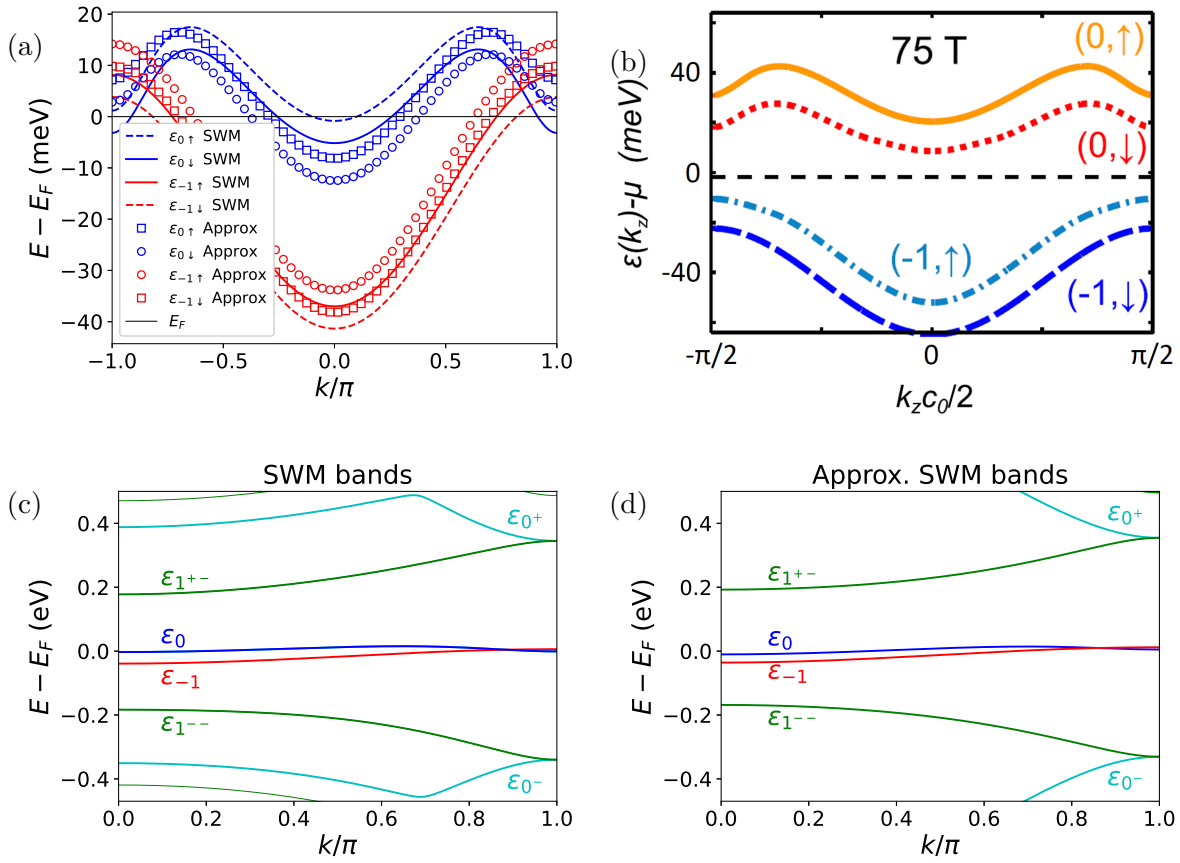

Figure 2.2: Landau bands of graphite at $B = 75$ T. (a) Comparison between the lowest-lying bands in the high magnetic field approximation of Eq. (2.17) and the bands in the full SWM model of Nakao [42] via the code in Ref. [38]. (b) Lowest-lying bands with electron-electron interactions. Reprinted with permission from Ref. [51], copyright (2017) by the American Physical Society. (c) Landau bands in the full SWM model with $\alpha_3 \neq 0$. Zeeman splitting was omitted for clarity. (d) Landau bands in the high field approximation. Zeeman splitting omitted.

$$\varepsilon_{N\uparrow} = \varepsilon_N + \frac{g}{2}\mu_B B, \qquad \varepsilon_{N\downarrow} = \varepsilon_N - \frac{g}{2}\mu_B B, \tag{2.20}$$

being $g \approx 2.5$ the z component of graphite's g-factor, and $\mu_B = e\hbar/(2m_e)$ the Bohr magneton. The wave functions are modified by adding a spin eigenstate of the form

$$\Psi^{(N)}_{p_x,k_z}(x,y,z) \to \Psi^{(N\sigma)}_{p_x,k_z}(x,y,z) = \Psi^{(N)}_{p_x,k_z}(x,y,z)\eta_\sigma, \tag{2.21}$$

with the subindex $\sigma \in \{\uparrow, \downarrow\}$, $\eta_\uparrow = (1,0)^\dagger$, and $\eta_\downarrow = (0,1)^\dagger$, obeying $\eta^\dagger_\sigma \eta_{\sigma'} = \delta_{\sigma\sigma'}$.

The Landau bands $N = -1,0$ with opposite spins generate the SDW at high magnetic fields, as will be explained in the following sections, while we are also interested in optical transitions between the SDW and the bands $N = 0,1$, which are allowed by electric-dipole selection rules. In Fig. 2.2 (a,b), we compare the lowest-lying Landau bands at $B = 75$ T computed in the outlined approximation with those of the full SWM model, as well as with the bands modified by electron-electron interactions as reported in Ref. [51]. It is observed that the approximated bands agree fairly well with those of the full SWM model. Still, as expected, there are quantitative and qualitative discrepancies when electron-electron interactions are included. Most notably, electron-electron interactions cause a depopulation of all bands, as opposed to

the SWM model prediction. However, we expect the energy corrections from electron-electron interactions to be small compared to ε_B, such that they do not modify the low-energy subspace generated by the wave functions (2.16), although the low-energy bands, being of the order of Γ_2 and Γ_5 for $N=-1$ and $N=0$, are greatly affected. Fig. 2.2 (c,d) compares the Landau bands in the outlined approximation and the full SWM model at higher energies. It is observed that the bands $\varepsilon_{1\pm-}$ agree fairly well, but the bands $\varepsilon_{0\pm}$ only agree in the interval $(0.7\pi,\pi]$. Nevertheless, as will be seen in the last section of this chapter, only this part of the bands is relevant in the optical conductivity spectra of the SDW.

2.3. Spin-Density Waves of Graphite in the Hartree-Fock Approximation: General Solution

At magnetic fields higher than 52 T, only the Landau bands $(-1,\uparrow)$ and $(0,\downarrow)$ are partially filled, such that the Coulomb interaction between electrons in these bands generates a SDW. To describe such interaction, we formulate a Hamiltonian in second quantization that involves only the low-energy Landau bands

$$\hat{\mathcal{H}} = \sum_{p,k} \left(\varepsilon_{0,\downarrow}(k)\, \hat{a}^\dagger_{pk} \hat{a}_{pk} + \varepsilon_{-1,\uparrow}(k+Q)\, \hat{b}^\dagger_{pk} \hat{b}_{pk} \right) + \hat{\mathcal{H}}_{\text{Coulomb}}, \tag{2.22}$$

being $(p,k) \equiv (p_x,k_z)$, $\hat{a}^\dagger_{pk}$ the creation operator of an electron in the band $\varepsilon_{0\downarrow}$ with momentum (p,k), $\hat{b}^\dagger_{pk}$ the creation operator of an electron in the band $\varepsilon_{-1\uparrow}$ with momentum $(p,k+Q)$, and Q the nesting vector. The operators $\hat{a}_{pk}$ and $\hat{b}_{pk}$ obey the fermionic anticommutation relations

$$\begin{gathered} \left\{ \hat{a}_{pk}, \hat{a}^\dagger_{p'k'} \right\} = \left\{ \hat{b}_{pk}, \hat{b}^\dagger_{p'k'} \right\} = \delta_{pp'}\delta_{kk'}, \\ \{\hat{a}_{pk}, \hat{a}_{p'k'}\} = \left\{ \hat{a}^\dagger_{pk}, \hat{a}^\dagger_{p'k'} \right\} = \left\{ \hat{b}_{pk}, \hat{b}_{p'k'} \right\} = \left\{ \hat{b}^\dagger_{pk}, \hat{b}^\dagger_{p'k'} \right\} = \left\{ \hat{a}_{pk}, \hat{b}_{p'k'} \right\} = \ldots = 0. \end{gathered} \tag{2.23}$$

The Coulomb interaction only considers interactions involving the $(-1,\uparrow)$ and $(0,\downarrow)$ bands, and has the form

$$\begin{aligned} \hat{\mathcal{H}}_{\text{Coulomb}} = \frac{1}{2}\frac{1}{V} \sum_{\boldsymbol{q}} \sum_{\text{all ind.}} v(\boldsymbol{q}) \Big[& \mathcal{F}_{(0\downarrow,p_1,k_1);\,(0\downarrow,p_4,k_4)}(\boldsymbol{q})\, \mathcal{F}_{(0\downarrow,p_2,k_2);\,(0\downarrow,p_3,k_3)}(-\boldsymbol{q}) \hat{a}^\dagger_{p_1k_1} \hat{a}^\dagger_{p_2k_2} \hat{a}_{p_3k_3} \hat{a}_{p_4k_4} \\ & + \mathcal{F}_{(-1\uparrow,p_1,k_1);\,(-1\uparrow,p_4,k_4)}(\boldsymbol{q})\, \mathcal{F}_{(-1\uparrow,p_2,k_2);\,(-1\uparrow,p_3,k_3)}(-\boldsymbol{q}) \hat{b}^\dagger_{p_1k_1} \hat{b}^\dagger_{p_2k_2} \hat{b}_{p_3k_3} \hat{b}_{p_4k_4} \\ & + 2\, \mathcal{F}_{(0\downarrow,p_1,k_1);\,(0\downarrow,p_4,k_4)}(\boldsymbol{q})\, \mathcal{F}_{(-1\uparrow,p_2,k_2);(-1\uparrow,p_3,k_3)}(-\boldsymbol{q}) \hat{a}^\dagger_{p_1k_1} \hat{b}^\dagger_{p_2k_2} \hat{b}_{p_3k_3} \hat{a}_{p_4k_4} \Big]. \end{aligned} \tag{2.24}$$

with $V = L_xL_yL_z$ the sample volume, $v(\boldsymbol{q}) = e^2/(\varepsilon_0 \tilde{\varepsilon}\, q^2)$ the Fourier transform of the Coulomb potential in S.I units, ε_0 the vacuum permittivity, and $\tilde{\varepsilon}$ a dimensionless effective dielectric constant. A rigorous treatment of the Coulomb potential should include the screening by occupied bands, which may change its functional form from $1/q^2$ to a different function. Nevertheless, our goal is not to precisely calculate the Coulomb potential; therefore, we qualitatively model this screening by the effective dielectric constant $\tilde{\varepsilon}$. The form factors $\mathcal{F}_{(N\sigma,p,k);\,(N'\sigma',p',k')}(\boldsymbol{q})$ are included to take into account the non-plane-wave nature of the eigenstates of the Landau bands, and are defined as

$$\mathcal{F}_{(N\sigma,p,k);\,(N'\sigma',p',k')}(\boldsymbol{q}) = \delta_{\sigma\sigma'} \int d\boldsymbol{r} e^{-i\boldsymbol{q}\cdot\boldsymbol{r}} \Psi^{(N\sigma)\dagger}_{pk}(\boldsymbol{r}) \Psi^{(N'\sigma')}_{p'k'}(\boldsymbol{r}) \tag{2.25}$$

In Appendix A, we find the form factors explicitly and show that, after some approximations, the Coulomb interaction Hamiltonian can be written as

$$\hat{\mathcal{H}}_{\text{Coulomb}} = \frac{1}{2}\frac{1}{L_x L_z}\sum_{p,p',q}\sum_{k,k',\kappa} e^{iq_y l_B^2(p-p'-q)}\Big[V_{aa}(q,\kappa)\,\hat{a}^\dagger_{p-q,k-\kappa}\hat{a}^\dagger_{p'+q,k'+\kappa}\hat{a}_{p',k'}\hat{a}_{p,k} + V_{bb}(q,\kappa)\,\hat{b}^\dagger_{p-q,k-\kappa}\hat{b}^\dagger_{p'+q,k'+\kappa}\hat{b}_{p',k'}\hat{b}_{p,k} + 2V_{ab}(q,\kappa)\,\hat{a}^\dagger_{p-q,k-\kappa}\hat{b}^\dagger_{p'+q,k'+\kappa}\hat{b}_{p',k'}\hat{a}_{p,k}\Big], \tag{2.26}$$

with $\boldsymbol{q} = (q_x,q_y,q_z) = (q,q_y,\kappa/c_0)$, $-\pi \le \kappa \le \pi$, and

$$\begin{aligned} V_{aa}(q,\kappa) &= \int \frac{dq_y}{2\pi}\, v\left(q,q_y,\frac{\kappa}{c_0}\right) e^{-q_\parallel^2 l_B^2/2}\left(1-\frac{2\gamma_1^2}{\varepsilon_B^2+4\gamma_1^2}q_\parallel^2 l_B^2\right)^2, \\ V_{bb}(q,\kappa) &= \int \frac{dq_y}{2\pi}\, v\left(q,q_y,\frac{\kappa}{c_0}\right) e^{-q_\parallel^2 l_B^2/2}, \\ V_{ab}(q,\kappa) &= \int \frac{dq_y}{2\pi}\, v\left(q,q_y,\frac{\kappa}{c_0}\right) e^{-q_\parallel^2 l_B^2/2}\left(1-\frac{2\gamma_1^2}{\varepsilon_B^2+4\gamma_1^2}q_\parallel^2 l_B^2\right). \end{aligned} \tag{2.27}$$

with $\boldsymbol{q}_\parallel = (q,q_y)$.

We now work in the Hartree-Fock (HF) approximation to treat the Coulomb Hamiltonian. Within the HF approximation, the Coulomb Hamiltonian, which is of fourth order in the creation and annihilation operators, is approximated to a quadratic one by taking a pair-wise average of the field operators. In Appendix A section A.3, we elaborate on the technical details to demonstrate that the Hamiltonian in the HF approximation takes the form

$$\hat{\mathcal{H}}_{\text{HF}} = \sum_{p,k}\Big[(\varepsilon_{0\downarrow}(k)+\Sigma^a_k)\,\hat{a}^\dagger_{pk}\hat{a}_{pk} + \left(\varepsilon_{-1\uparrow}(k+Q)+\Sigma^b_{k+Q}\right)\hat{b}^\dagger_{pk}\hat{b}_{pk} - \Delta_k\,\hat{a}^\dagger_{pk}\hat{b}_{pk} - \Delta^*_k\,\hat{b}^\dagger_{pk}\hat{a}_{pk}\Big] \tag{2.28}$$

with

$$\begin{aligned} \Sigma^a_k &= -\int \frac{dk'}{2\pi c_0}\frac{dq}{2\pi}\, V_{aa}(q,k-k')\left\langle \hat{a}^\dagger_{p'k'}\hat{a}_{p'k'}\right\rangle \\ \Sigma^b_{k+Q} &= -\int \frac{dk'}{2\pi c_0}\frac{dq}{2\pi}\, V_{bb}(q,k-k')\left\langle \hat{b}^\dagger_{p'k'}\hat{b}_{p'k'}\right\rangle \\ \Delta_k &= \int \frac{dk'}{2\pi c_0}\frac{dq}{2\pi}\, V_{ab}(q,k-k')\left\langle \hat{b}^\dagger_{p'k'}\hat{a}_{p'k'}\right\rangle \end{aligned} \tag{2.29}$$

where the field average $\langle ... \rangle = \langle \Psi_{\text{HF}}|...|\Psi_{\text{HF}}\rangle$ is taken with respect to the HF ground state, $|\Psi_{\text{HF}}\rangle$, which will be determined. To find the ground state and energies of the SDW, the HF Hamiltonian of Eq. (2.28) is diagonalized by means of a Bogoliubov transformation

$$\begin{aligned} \hat{a}_{pk} &= v_k\,\hat{\alpha}_{pk} + u_k\,\hat{\beta}_{pk}, \\ \hat{b}_{pk} &= -u_k\,\hat{\alpha}_{pk} + v_k\,\hat{\beta}_{pk}. \end{aligned} \tag{2.30}$$

With u_k and v_k parameters to be found in the problem. Requiring the transformation to be canonical, i.e. that the operators $\hat{\alpha}_{pk}$ and $\hat{\beta}_{pk}$ fulfill the same fermionic anticommutation relations of Eq. (2.23) as $\hat{a}_{pk}$ and $\hat{b}_{pk}$, the parameters must satisfy $u_k^2 + v_k^2 = 1$. This allows us to define $u_k \equiv \sin\vartheta_k$ and $v_k \equiv \cos\vartheta_k$, $0 \le \vartheta_k \le \pi/2$. Inserting these definitions into the HF Hamiltonian, we get

$$\begin{aligned} \hat{\mathcal{H}}_{\text{HF}} = \sum_{p,k}\Big[&\left(\bar{\varepsilon}_0(k)\,u_k^2 + \bar{\varepsilon}_{-1}(k)\,v_k^2 - 2\Delta_k u_k v_k\right)\hat{\beta}^\dagger_{pk}\hat{\beta}_{pk} \\ &+ \left(\bar{\varepsilon}_0(k)\,v_k^2 + \bar{\varepsilon}_{-1}(k)\,u_k^2 + 2\Delta_k u_k v_k\right)\hat{\alpha}^\dagger_{pk}\hat{\alpha}_{pk} \\ &+ \left((\bar{\varepsilon}_0(k)-\bar{\varepsilon}_{-1}(k))u_k v_k - \Delta_k(v_k^2-u_k^2)\right)\left(\hat{\beta}^\dagger_{pk}\hat{\alpha}_{pk} + \hat{\alpha}^\dagger_{pk}\hat{\beta}_{pk}\right)\Big], \end{aligned} \tag{2.31}$$

with $\overline{\varepsilon}_0(k)$, $= \varepsilon_{0\downarrow}(k) + \Sigma^a_k$ and $\overline{\varepsilon}_{-1}(k) = \varepsilon_{-1\uparrow}(k+Q) + \Sigma^b_{k+Q}$. In this sense, the terms Σ^a_k, Σ^b_{k+Q} renormalize the lowest-lying bands, such that $\varepsilon_{-1\uparrow}$ and $\varepsilon_{0\downarrow}$ are called the bare bands, while $\overline{\varepsilon}_{-1}$ and $\overline{\varepsilon}_0$ are called the renormalized bands. The Hamiltonian is diagonalized by imposing the following condition on the parameters:

$$\frac{u_k v_k}{v_k^2 - u_k^2} = \frac{1}{2}\tan 2\vartheta_k = \frac{\Delta_k}{\overline{\varepsilon}_0(k) - \overline{\varepsilon}_{-1}(k)}. \tag{2.32}$$

The diagonalized Hamiltonian reveals the energy dispersion of the SDW bands. The SDW consists of two states, each of them generated by the operators $\hat{\beta}^\dagger_{pk}$ and $\hat{\alpha}^\dagger_{pk}$, with energies

$$\begin{aligned} \varepsilon_-(k) &= \overline{\varepsilon}_0(k)\, u_k^2 + \overline{\varepsilon}_{-1}(k)\, v_k^2 - 2\Delta_k u_k v_k, \\ \varepsilon_+(k) &= \overline{\varepsilon}_0(k)\, v_k^2 + \overline{\varepsilon}_{-1}(k)\, u_k^2 + 2\Delta_k u_k v_k, \end{aligned} \tag{2.33}$$

respectively. From Eq. (2.32) and knowing that $u_k^2 + v_k^2 = 1$, the SDW bands can also be written as

$$\varepsilon_\pm(k) = \frac{\overline{\varepsilon}_0(k) + \overline{\varepsilon}_{-1}(k)}{2} \pm \frac{1}{2}\sqrt{(\overline{\varepsilon}_0(k) - \overline{\varepsilon}_{-1}(k))^2 + 4\Delta_k^2}. \tag{2.34}$$

To determine how the low energy bands of graphite combine to produce the SDW state, we find the following relations from Eq. (2.30)

$$\begin{aligned} \hat{\alpha}_{pk} &= v_k \hat{a}_{pk} - u_k \hat{b}_{pk} = \cos\vartheta_k\, \hat{a}_{pk} - \sin\vartheta_k\, \hat{b}_{pk}, \\ \hat{\beta}_{pk} &= u_k \hat{a}_{pk} + v_k \hat{b}_{pk} = \sin\vartheta_k\, \hat{a}_{pk} + \cos\vartheta_k\, \hat{b}_{pk}, \end{aligned} \tag{2.35}$$

from which we obtain the SDW wave functions

$$\begin{aligned} \Psi^{(+)}_{pk}(x,y) &= \cos\vartheta_k\, \Psi^{(0\downarrow)}_{pk}(x,y) - \sin\vartheta_k\, \Psi^{(-1\uparrow)}_{p,k+Q}(x,y) \\ \Psi^{(-)}_{pk}(x,y) &= \sin\vartheta_k\, \Psi^{(0\downarrow)}_{pk}(x,y) + \cos\vartheta_k\, \Psi^{(-1\uparrow)}_{p,k+Q}(x,y) \end{aligned} \tag{2.36}$$

In this sense, the SDW state is a linear combination of the single-particle states $\Psi^{(-1,\uparrow)}_{p,k+Q}$ and $\Psi^{(0,\downarrow)}_{pk}$, with u_k and v_k (or ϑ_k) indicating the degree of mixing between them.

With this in mind, we can now propose the ground state of the system. In general, the ground state consists of filling the vacuum state, $|0\rangle$, with the SWD states $\hat{\alpha}^\dagger_{pk}$ and $\hat{\beta}^\dagger_{pk}$ up to the Fermi wave vector k_F, as follows

$$|\Psi_{\rm HF}\rangle = \prod_{\hat{\gamma}=\hat{\alpha},\hat{\beta}} \prod_{k<k_F} \hat{\gamma}^\dagger_{pk}|0\rangle. \tag{2.37}$$

However, the ground state is greatly simplified when considering that at high magnetic fields, charge neutrality guarantees that the nesting vector is $Q = \pi$ [51], and in this situation, the band $\varepsilon_-(k)$ is completely filled, while $\varepsilon_+(k)$ is empty. For this reason, the ground state is entirely comprised of $\hat{\beta}^\dagger_{pk}$ states

$$|\Psi_{\rm HF}\rangle = \prod_{p,k} \hat{\beta}^\dagger_{pk}|0\rangle = \prod_{p,k} \left(u_k \hat{a}_{pk} + v_k \hat{b}_{pk}\right)|0\rangle. \tag{2.38}$$

From the HF ground state, we compute the field averages that enter in Eq. (2.29),

$$\begin{aligned} \left\langle \hat{a}^\dagger_{p'k'} \hat{a}_{pk} \right\rangle &= \delta_{pp'}\delta_{kk'} u_k^2, \quad \left\langle \hat{b}^\dagger_{p'k'} \hat{b}_{pk} \right\rangle = \delta_{pp'}\delta_{kk'} v_k^2, \\ \left\langle \hat{a}^\dagger_{p'k'} \hat{b}_{pk} \right\rangle &= \left\langle \hat{b}^\dagger_{p'k'} \hat{a}_{pk} \right\rangle = \delta_{pp'}\delta_{kk'} u_k v_k, \end{aligned} \tag{2.39}$$

allowing us to find the self-energies and gap

$$\begin{aligned}
\Sigma_k^a &= -\int \frac{dk'}{2\pi}\,\Xi_{aa}(k-k')\,u_{k'}^2 = -\int \frac{dk'}{2\pi}\,\Xi_{aa}(k-k')\,\sin^2\vartheta_{k'},\\
\Sigma_{k+Q}^b &= -\int \frac{dk'}{2\pi}\,\Xi_{bb}(k-k')\,v_{k'}^2 = -\int \frac{dk'}{2\pi}\,\Xi_{bb}(k-k')\,\cos^2\vartheta_{k'},\\
\Delta_k &= \int \frac{dk'}{2\pi}\,\Xi_{ab}(k-k')\,u_{k'}v_{k'} = \int \frac{dk'}{2\pi}\,\Xi_{ab}(k-k')\,\frac{\sin 2\vartheta_{k'}}{2},
\end{aligned} \tag{2.40}$$

where it was defined

$$\begin{aligned}
\Xi_{aa}(\kappa) &= \int \frac{dq}{2\pi}\frac{V_{aa}(q,\kappa)}{c_0} = \int \frac{d\boldsymbol{q}_\parallel}{(2\pi)^2}\,\frac{v(\boldsymbol{q}_\parallel,\kappa/c_0)}{c_0}e^{-q_\parallel^2 l_B^2/2}\left(1-\frac{2\gamma_1^2}{\varepsilon_B^2+4\gamma_1^2}q_\parallel^2 l_B^2\right)^2,\\
\Xi_{bb}(\kappa) &= \int \frac{dq}{2\pi}\frac{V_{bb}(q,\kappa)}{c_0} = \int \frac{d\boldsymbol{q}_\parallel}{(2\pi)^2}\,\frac{v(\boldsymbol{q}_\parallel,\kappa/c_0)}{c_0}e^{-q_\parallel^2 l_B^2/2},\\
\Xi_{ab}(\kappa) &= \int \frac{dq}{2\pi}\frac{V_{ab}(q,\kappa)}{c_0} = \int \frac{d\boldsymbol{q}_\parallel}{(2\pi)^2}\,\frac{v(\boldsymbol{q}_\parallel,\kappa/c_0)}{c_0}e^{-q_\parallel^2 l_B^2/2}\left(1-\frac{2\gamma_1^2}{\varepsilon_B^2+4\gamma_1^2}q_\parallel^2 l_B^2\right).
\end{aligned} \tag{2.41}$$

In addition to Eq. (2.32), Eqs. (2.40) constitute the set of self-consistent equations for the SDW problem. By themselves, they represent the general solution, from which a numerical solution can be found provided that the bands $\varepsilon_{-1\uparrow}$ and $\varepsilon_{0\downarrow}$ corrected by electron-electron interactions are known. In section 2.4, we attempt to find analytic expressions for Δ_k and Σ_k by considering approximations to the bands and their interaction. Nevertheless, we arrive at the conclusion that a first-order phase transition from the SDW to the normal phase appears, implying that it is necessary to find a numerical solution. Therefore, in section 2.5 we find numerical solutions to the SDW problem, using approximations to the graphite bands that still provide an accurate picture of the SDW behavior.

2.3.1. Self-Consistent Equations from the Hartree-Fock Energy Functional

An equivalent method to obtain the self-consistent equations for the SDW problem is by evaluating the energy functional from the Hartree-Fock ground state, and minimizing it through the functional derivative. The total energy (per particle) is defined as the expected value of the Hamiltonian with respect to the HF ground state,

$$\mathcal{E} = \frac{1}{\mathcal{N}}\langle\Psi_{\mathrm{HF}}|\hat{\mathcal{H}}|\Psi_{\mathrm{HF}}\rangle, \tag{2.42}$$

being $\mathcal{N} = L_xL_yL_z/(2\pi l_B^2 c_0)$ the total number of electrons in the system. To compute this quantity, we consider the Coulomb interaction of Eq. (2.26), which is of fourth-order in the field operators, and evaluate the averages with respect to the HF ground state of Eq. (2.38). Evaluating the field averages we find

$$\begin{aligned}
\left\langle \hat{a}^\dagger_{p+q,k+\kappa}\hat{a}^\dagger_{p'-q,k'-\kappa}\hat{a}_{p',k'}\hat{a}_{p,k}\right\rangle &= \delta_{q,0}\delta_{\kappa,0}u_k^2u_{k'}^2 - \delta_{q,p'-p}\delta_{\kappa,k'-k}u_k^2u_{k'}^2,\\
\left\langle \hat{b}^\dagger_{p+q,k+\kappa}\hat{b}^\dagger_{p'-q,k'-\kappa}\hat{b}_{p',k'}\hat{b}_{p,k}\right\rangle &= \delta_{q,0}\delta_{\kappa,0}v_k^2v_{k'}^2 - \delta_{q,p'-p}\delta_{\kappa,k'-k}v_k^2v_{k'}^2,\\
\left\langle \hat{a}^\dagger_{p+q,k+\kappa}\hat{b}^\dagger_{p'-q,k'-\kappa}\hat{b}_{p',k'}\hat{a}_{p,k}\right\rangle &= \delta_{q,0}\delta_{\kappa,0}u_kv_ku_{k'}v_{k'} - \delta_{q,p'-p}\delta_{\kappa,k'-k}u_kv_ku_{k'}v_{k'}.
\end{aligned} \tag{2.43}$$

The Hartree terms, i.e. those proportional to $\delta_{q,0}\delta_{\kappa,0}$, cancel out with the energy contribution of the positive ions that constitute the graphite lattice, and therefore do not contribute to the energy functional. With these results, we find the total energy as

$$\begin{aligned}\mathcal{E} = &\int \frac{dk}{2\pi}\left(\varepsilon_{0\downarrow}(k)\,u_k^2 + \varepsilon_{-1\uparrow}(k+\pi)\,v_k^2\right)\\ &-\frac{1}{2}\int \frac{dk}{2\pi}\frac{dk'}{2\pi}\left(\Xi_{aa}(k-k')\,u_k^2u_{k'}^2 + \Xi_{bb}(k-k')\,v_k^2v_{k'}^2 + 2\Xi_{ab}(k-k')\,u_kv_ku_{k'}v_{k'}\right),\end{aligned} \tag{2.44}$$

where the sums over k and k' were replaced by integrals using the rule $\sum_k \to \int dk\, L_z/(2\pi c_0)$; and Ξ_{aa}, Ξ_{bb}, and Ξ_{ab} as defined in Eq. (2.41). From the last equation, it is deduced that the total energy is a functional of the parameter u_k (or ϑ_k). It is more convenient to write the energy functional in terms of the angular parameter ϑ_k instead of u_k and v_k, as follows

$$\begin{aligned}\mathcal{E}[\vartheta_k] = &\int \frac{dk}{2\pi}\left\{\left(\varepsilon_{0\downarrow}(k) - \varepsilon_{-1\uparrow}(k+\pi) + \frac{1}{2}\int \frac{dk'}{2\pi}\Xi_{bb}(k-k')\right)\sin^2\vartheta_k\right.\\ &\left.-\frac{1}{2}\int \frac{dk'}{2\pi}\left[\left(\Xi_{aa}(k-k') + \Xi_{bb}(k-k')\right)\sin^2\vartheta_k\sin^2\vartheta_{k'} + \frac{1}{2}\Xi_{ab}(k-k')\,\sin 2\vartheta_k \sin 2\vartheta_{k'}\right]\right\},\end{aligned} \tag{2.45}$$

where constant terms were omitted. The parameter ϑ_k is found by minimizing the energy functional through the application of the functional derivative

$$\delta\mathcal{E}[\vartheta_k] = 0 \to \frac{\delta I[\vartheta_k]}{\delta\vartheta_k} = 0, \tag{2.46}$$

with $I[\vartheta_k]$ the term within curly braces in Eq. (2.45), which is also a functional of ϑ_k. By applying the chain rule of the functional derivative, it is found

$$\frac{1}{2}\tan 2\vartheta_k = \frac{\Delta_k}{\varepsilon_{0\downarrow}(k) + \Sigma_k^a - \varepsilon_{-1\uparrow}(k+\pi) - \Sigma_{k+\pi}^b}, \tag{2.47}$$

where it was defined

$$\begin{aligned}\Sigma_k^a &= -\int \frac{dk'}{2\pi}\Xi_{aa}(k-k')\sin^2\vartheta_{k'},\\ \Sigma_{k+\pi}^b &= -\int \frac{dk'}{2\pi}\Xi_{bb}(k-k')\cos^2\vartheta_{k'},\\ \Delta_k &= \int \frac{dk'}{2\pi}\Xi_{ab}(k-k')\frac{\sin 2\vartheta_{k'}}{2}.\end{aligned} \tag{2.48}$$

These results are the same as Eqs. (2.32, 2.40) found in the previous section.

The energy functional is simplified by defining

$$\Sigma_k = -\int \frac{dk'}{2\pi}\left(\Xi_{aa}(k-k') + \Xi_{bb}(k-k')\right)\sin^2\vartheta_{k'}, \tag{2.49}$$

which is also a functional of ϑ_k, allowing us to write

$$\mathcal{E}[\vartheta_k] = \int \frac{dk}{2\pi}\left[\left(\varepsilon_{0\downarrow}(k) - \varepsilon_{-1\uparrow}(k+\pi) + \frac{\Sigma_k}{2} + \frac{1}{2}\int \frac{dk'}{2\pi}\Xi_{bb}(k-k')\right)\sin^2\vartheta_k - \frac{\Delta_k}{2}\sin 2\vartheta_k\right]. \tag{2.50}$$

The energy functional has the advantage of giving not only the ground-state energy of the SDW but also the energy at arbitrary values of ϑ_k, being a helpful property that will be applied to verify whether the system is in the normal or SDW phase.

2.4. Approximate Solutions to Spin-Density Waves

We now focus our study on the behavior of the SDW as a function of the external magnetic field. As was already mentioned, it is possible to solve the self-consistent equations numerically to find the parameters ϑ_k and Δ_k, which establish the formation of the SDW phase. However, the numerical procedure would require the precise knowledge of the graphite bands corrected by electron-electron interactions at arbitrary magnetic fields, as was found in Refs. [51, 52], which in turn requires a considerable computation effort. Instead, we will work with approximate expressions for the bands and their interaction that capture the main features of the SDW phase. From the aforementioned references, we derive the following conclusions:

1. Around $k = 0$, the bands $\varepsilon_{-1\uparrow}(k+\pi)$ and $\varepsilon_{0\downarrow}(k)$ have an approximate quadratic dependence with respect to k.

2. As the magnetic field increases, the separation between the bands $\varepsilon_{-1\uparrow}(k)$ and $\varepsilon_{0\downarrow}(k)$ increases, until at $B \approx 75$ T there is no overlap between them.

With this in mind, we proceed to approximate some of the terms that enter into the SDW self-consistent equations (2.32,2.40). First, we consider that the bands have a quadratic dependence on k,

$$\varepsilon_{-1\uparrow}(k+\pi) = -\mu_b k^2, \quad \varepsilon_{0\downarrow}(k) = \mu_a k^2 + \tilde{\delta}, \tag{2.51}$$

with μ_a,$\mu_b > 0$ the curvature of the bands, and $\tilde{\delta}$ the energy gap. From the Taylor expansion of Eq. (2.17), we find $\mu_a = 10.5$ meV and $\mu_b = 12$ meV. The band gap $\tilde{\delta}$ has the role of the phase transition control parameter: the SDW emerges below a certain value of it. Experimentally, the control parameter is the magnetic field, which increases the band gap $\tilde{\delta}$ as it increases, but the precise functional relation between them is not known. On the other hand, we assume that the effective masses μ_a and μ_b remain constant with respect to magnetic field changes. In this approximation, we find

$$\begin{aligned}\overline{\varepsilon}_0(k) - \overline{\varepsilon}_{-1}(k) &= \varepsilon_0(k) - \varepsilon_{-1}(k+\pi) + \Sigma^a_k - \Sigma^b_{k+\pi} \\ &= \mu k^2 + \tilde{\delta} + \int \frac{dk'}{2\pi} \Xi_{bb}(k-k') - \int \frac{dk'}{2\pi} \left(\Xi_{aa}(k-k') + \Xi_{bb}(k-k')\right) \sin^2 \vartheta_{k'},\end{aligned} \tag{2.52}$$

with $\mu = \mu_a + \mu_b$. The integration in the third term on the right-hand side of Eq. (2.52) is just a constant (it does not depend on k by substituting $k - k' \to k'$). Therefore, we can redefine the energy gap of the bare bands as

$$\delta = \tilde{\delta} + \int \frac{dk'}{2\pi} \Xi_{bb}(k-k'). \tag{2.53}$$

With this in mind, Eq. (2.32) reads

$$\frac{1}{2}\tan 2\vartheta_k = \frac{\Delta_k}{\mu k^2 + \delta + \Sigma_k}, \tag{2.54}$$

with Σ_k defined in Eq. (2.49).

Then, to approximate the terms Ξ_{aa}, Ξ_{bb}, and Ξ_{ab} that contain the Coulomb interaction, $v(\boldsymbol{q})$, we must take into account that the exact form of $v(\boldsymbol{q})$ at $|\boldsymbol{q}| \sim 1/l_B$ is unknown due to screening by high Landau levels. However, the long-range part is expected to be unscreened and has the form

$$v(\boldsymbol{q}_\parallel, q_z) = \frac{e^2/(\varepsilon_0 \tilde{\varepsilon})}{q_\parallel^2 + q_z^2}. \tag{2.55}$$

This term enters in Eqs. (2.41), which are proportional to the following integrals

$$\begin{aligned}
\int dq_\parallel \frac{q_\parallel}{q_\parallel^2+q_z^2}\exp\left(-\frac{l_B^2 q_\parallel^2}{2}\right) &= -\frac{1}{2}e^A \mathrm{Ei}(-A), \quad \text{with } A=\frac{l_B^2 q_z^2}{2},\\
\int dq_\parallel \frac{q_\parallel^3}{q_\parallel^2+q_z^2}\exp\left(-\frac{l_B^2 q_\parallel^2}{2}\right) &= \frac{1}{l_B^2}\left(1+Ae^A\mathrm{Ei}(-A)\right) \approx \frac{1}{l_B^2}\frac{1}{1+A},\\
\int dq_\parallel \frac{q_\parallel^5}{q_\parallel^2+q_z^2}\exp\left(-\frac{l_B^2 q_\parallel^2}{2}\right) &= \frac{2}{l_B^4}\left(1-A+A^2e^A\mathrm{Ei}(-A)\right) \approx \frac{2}{l_B^4}\frac{1}{1+A},
\end{aligned} \tag{2.56}$$

where $\mathrm{Ei}(x) = -\int_{-x}^{\infty} dt\, e^{-t}/t$ is the exponential integral. The second and third integrals converge for all values of q_z and are well approximated by the indicated values, but the first one diverges logarithmically at $q_z \to 0$, although this will not affect the subsequent results qualitatively. At $q_z = \kappa/c_0 \sim 1/l_B$, the first integral can be approximated to

$$\int dq_\parallel \frac{q_\parallel}{q_\parallel^2+\kappa^2/c_0^2}\exp\left(-\frac{l_B^2 q_\parallel^2}{2}\right) \approx \frac{1}{2}\frac{1}{1+l_B^2\kappa^2/(2c_0^2)}. \tag{2.57}$$

For this reason, we can approximate the terms Ξ_{aa}, Ξ_{bb}, and Ξ_{ab} to

$$\Xi_{ab}(\kappa) = \frac{\Xi_0}{1+l_B^2\kappa^2/(2c_0^2)}, \qquad \frac{\Xi_{aa}(\kappa)+\Xi_{bb}(\kappa)}{2} = \frac{\Xi_1}{1+l_B^2\kappa^2/(2c_0^2)}. \tag{2.58}$$

Ξ_0 and Ξ_1 are constants of the same order of magnitude as $e^2/(\varepsilon_0\tilde{\varepsilon}c_0)$, that also depend on γ_1 and ε_B.[3] We expect $\Xi_1 > \Xi_0$ because looking at Eq. (2.41) we can infer

$$1+\left(1-\frac{2\gamma_1^2}{\varepsilon_B^2+4\gamma_1^2}q_\parallel^2 l_B^2\right)^2 > 1-\frac{2\gamma_1^2}{\varepsilon_B^2+4\gamma_1^2}q_\parallel^2 l_B^2. \tag{2.59}$$

We now attempt to find an analytical solution to the SDW self-consistent equations. First, from Eq. (2.32) we can obtain

$$\begin{aligned}
\frac{\sin 2\vartheta_k}{2} &= \frac{\Delta_k}{\sqrt{(\bar{\varepsilon}_0(k)-\bar{\varepsilon}_{-1}(k))^2+4\Delta_k^2}},\\
\sin^2\vartheta_k &= \frac{1}{2}-\frac{1}{2}\frac{\bar{\varepsilon}_0(k)-\bar{\varepsilon}_{-1}(k)}{\sqrt{(\bar{\varepsilon}_0(k)-\bar{\varepsilon}_{-1}(k))^2+4\Delta_k^2}},\\
\cos^2\vartheta_k &= \frac{1}{2}+\frac{1}{2}\frac{\bar{\varepsilon}_0(k)-\bar{\varepsilon}_{-1}(k)}{\sqrt{(\bar{\varepsilon}_0(k)-\bar{\varepsilon}_{-1}(k))^2+4\Delta_k^2}}.
\end{aligned} \tag{2.60}$$

Replacing the first line into the equation for Δ_k in Eq. (2.40),

$$\Delta_k = \int \frac{dk'}{2\pi}\frac{\Xi_0}{1+l_B^2(k-k')^2/(2c_0^2)}\frac{\Delta_{k'}}{\sqrt{(\mu k'^2+\delta+\Sigma_{k'})^2+4\Delta_{k'}^2}}, \tag{2.61}$$

and the second line into Eq. (2.49),

$$\Sigma_k = -\int \frac{dk'}{2\pi}\frac{\Xi_1}{1+l_B^2(k-k')^2/(2c_0^2)}\left(1-\frac{\mu k'^2+\delta+\Sigma_{k'}}{\sqrt{(\mu k'^2+\delta+\Sigma_{k'})^2+4\Delta_{k'}^2}}\right). \tag{2.62}$$

For a large δ, the only solution to Eqs. (2.61,2.62) is $\Delta_k = \Sigma_k = 0$; therefore, the system is in the normal phase where no SDW emerges. As δ is reduced, a critical point is reached that

[3] In section 2.4.1 we compute an estimation for Ξ_0 and Ξ_1.

marks the formation of the SDW. Near the critical point, $\Sigma_k = O(\Delta_k^2)$, such that the critical band separation δ_{sdw} is found from Eq. (2.61) keeping only linear terms in Δ_k,

$$\begin{aligned}\Delta_k &= \int \frac{dk'}{2\pi} \frac{\Xi_0}{1 + l_B^2(k-k')^2/(2c_0^2)} \frac{\Delta_{k'}}{\mu k'^2 + \delta_{\text{sdw}}}, \\ &= \frac{\Xi_0}{\pi\mu} \frac{c_0^2}{l_B^2} \int dk' \frac{1}{(k-k')^2 + 2c_0^2/l_B^2} \frac{\Delta_{k'}}{k'^2 + \delta_{\text{sdw}}/\mu}.\end{aligned} \tag{2.63}$$

The integration domain is $[-\pi,\pi]$; however, due to the fast decay of the argument, it can be extended to $(-\infty,\infty)$. The last equation represents the integral of two Lorentzians, and depending on which of the two decays faster, we obtain the critical separation as[4]

$$\delta_{\text{sdw}} = \begin{cases} \dfrac{\Xi_0^2}{4\mu}, & \text{if } \dfrac{\Xi_0}{2\mu} \ll \dfrac{\sqrt{2}c_0}{l_B}, \\ \dfrac{c_0}{\sqrt{2}l_B}\Xi_0, & \text{if } \dfrac{\Xi_0}{2\mu} \gg \dfrac{\sqrt{2}c_0}{l_B}. \end{cases} \tag{2.64}$$

In the considered limiting cases, it was assumed that Δ_k is approximately constant in the integration domain. For δ slightly below δ_{sdw}, we expand Eqs. (2.61,2.62) around $\delta_{\text{sdw}} - \delta$, considering Δ_k, Σ_k constant, using the approximation

$$\begin{aligned}\frac{1}{\sqrt{(\mu k^2 + \delta + \Sigma)^2 + 4\Delta^2}} &= \frac{1}{\mu k^2 + \delta_{\text{sdw}}} \frac{1}{\sqrt{1 + \dfrac{2(\Sigma + \delta - \delta_{\text{sdw}})}{\mu k^2 + \delta_{\text{sdw}}} + \dfrac{4\Delta^2}{(\mu k^2 + \delta_{\text{sdw}})^2} + O(\Delta^4)}} \\ &\approx \frac{1}{\mu k^2 + \delta_{\text{sdw}}} \left(1 - \frac{\Sigma + \delta - \delta_{\text{sdw}}}{\mu k^2 + \delta_{\text{sdw}}} - \frac{2\Delta^2}{(\mu k^2 + \delta_{\text{sdw}})^2} + O(\Delta^4)\right),\end{aligned} \tag{2.65}$$

from which Eqs. (2.61,2.62) become

$$1 = \int \frac{dk}{2\pi} \frac{\Xi_0}{1 + l_B^2 k^2/(2c_0^2)} \left(\frac{1}{\mu k^2 + \delta_{\text{sdw}}} - \frac{\Sigma + \delta - \delta_{\text{sdw}}}{(\mu k^2 + \delta_{\text{sdw}})^2} - \frac{2\Delta^2}{(\mu k^2 + \delta_{\text{sdw}})^3}\right), \tag{2.66}$$

$$\Sigma = -\int \frac{dk}{2\pi} \frac{\Xi_1}{1 + l_B^2 k^2/(2c_0^2)} \frac{2\Delta^2}{(\mu k^2 + \delta_{\text{sdw}})^2}. \tag{2.67}$$

The integrations can be solved in the limiting cases applied to find δ_{sdw}. In these situations, the last two equations reduce to algebraic expressions that allow us to find Δ and Σ. In the case $\Xi_0/(2\mu) \ll \sqrt{2}c_0/l_B$, we have

$$\Sigma = -\frac{\Xi_1}{\Xi_0} \frac{\Delta^2}{\delta_{\text{sdw}}}, \tag{2.68}$$

$$\frac{\delta - \delta_{\text{sdw}} + \Sigma}{2\delta_{\text{sdw}}} + \frac{3\Delta^2}{4\delta_{\text{sdw}}^2} = 0 \Rightarrow \Delta^2 = \frac{2\delta_{\text{sdw}}(\delta_{\text{sdw}} - \delta)}{3 - 2\Xi_1/\Xi_0}. \tag{2.69}$$

In the case $\Xi_0/(2\mu) \gg \sqrt{2}c_0/l_B$, we obtain

$$\Sigma = -\frac{\Xi_1}{\Xi_0} \frac{2\Delta^2}{\delta_{\text{sdw}}}, \tag{2.70}$$

$$\frac{\delta - \delta_{\text{sdw}} + \Sigma}{\delta_{\text{sdw}}} + \frac{2\Delta^2}{\delta_{\text{sdw}}^2} = 0 \Rightarrow \Delta^2 = \frac{\delta_{\text{sdw}}(\delta_{\text{sdw}} - \delta)}{2(1 - \Xi_1/\Xi_0)}. \tag{2.71}$$

[4] We use $\displaystyle\int_{-\infty}^{\infty} dx \frac{1}{a^2 + x^2} \frac{1}{b^2 + x^2} = \frac{\pi}{ab(a+b)}$, which is further simplified if $a \gg b$ or $b \gg a$.

Since we expect $\Xi_1 > \Xi_0$, there is the problem of finding an imaginary Δ in the second case, and potentially in the first case as well if $\Xi_1/\Xi_0 > 3/2$. To clarify these issues, we study these cases in more detail in the following sections.

2.4.1. Spin-Density Wave When $\Xi_0/(2\mu) \ll \sqrt{2}c_0/l_B$

This case represents the limit of a small interaction corresponding to a large value of the effective dielectric constant $\tilde{\varepsilon}$. To give an idea of the energy scales in this situation, at $B = 75$ T we have $\sqrt{2}c_0/l_B \sim \sqrt{2}(0.67\text{ nm})/(2.96\text{ nm}) \sim 0.32$, and $e^2/(\varepsilon_0\tilde{\varepsilon}c_0) \sim 27\text{ eV}/\tilde{\varepsilon}$. Taking $\mu = 22.5$ meV from the effective masses of the bands, we get $\Xi_0/(2\mu) \sim e^2/(2\mu\varepsilon_0\tilde{\varepsilon}c_0) \sim 600/\tilde{\varepsilon}$, implying that a large dielectric constant the order $\tilde{\varepsilon} \sim 10^4$ is necessary to fulfil the requirement, making this scenario very unlikely. Nevertheless, we will estimate the conditions for Ξ_0 and Ξ_1 at which the SDW phase can emerge.

From Eq. (2.69), we identified that Δ has imaginary values if $\Xi_1/\Xi_0 > 3/2$. It is then convenient to estimate the ratio Ξ_1/Ξ_0 by evaluating the integrations of Eqs. (2.41). Defining $C = 2\gamma_1^2/(\varepsilon_B^2 + 4\gamma_1^2)$, Eqs. (2.41) read

$$\begin{aligned}
\Xi_{aa}(\kappa) &= \frac{2e^2}{\varepsilon_0\tilde{\varepsilon}c_0}\int_0^\infty dq_\parallel \frac{q_\parallel\, e^{-q_\parallel^2 l_B^2/2}}{q_\parallel^2 + \kappa^2/c_0^2}\left(1 - 2Cl_B^2q_\parallel^2 + C^2l_B^4q_\parallel^4\right)\\
\Xi_{bb}(\kappa) &= \frac{2e^2}{\varepsilon_0\tilde{\varepsilon}c_0}\int_0^\infty dq_\parallel \frac{q_\parallel\, e^{-q_\parallel^2 l_B^2/2}}{q_\parallel^2 + \kappa^2/c_0^2},\\
\Xi_{ab}(\kappa) &= \frac{2e^2}{\varepsilon_0\tilde{\varepsilon}c_0}\int_0^\infty dq_\parallel \frac{q_\parallel\, e^{-q_\parallel^2 l_B^2/2}}{q_\parallel^2 + \kappa^2/c_0^2}\left(1 - Cl_B^2q_\parallel^2\right),
\end{aligned} \tag{2.72}$$

and applying the approximations in Eqs. (2.56),

$$\begin{aligned}
\Xi_{aa}(\kappa) &\approx \frac{e^2}{\varepsilon_0\tilde{\varepsilon}c_0}\left(1 - 4C + 4C^2\right)\frac{1}{1 + l_B^2\kappa^2/(2c_0^2)}\\
\Xi_{bb}(\kappa) &\approx \frac{e^2}{\varepsilon_0\tilde{\varepsilon}c_0}\frac{1}{1 + l_B^2\kappa^2/(2c_0^2)},\\
\Xi_{ab}(\kappa) &\approx \frac{e^2}{\varepsilon_0\tilde{\varepsilon}c_0}(1 - 2C)\frac{1}{1 + l_B^2\kappa^2/(2c_0^2)}
\end{aligned} \tag{2.73}$$

Therefore, from the definitions of Ξ_0 and Ξ_1 in Eq. (2.58), we conclude

$$\Xi_0 = \frac{e^2}{\varepsilon_0\tilde{\varepsilon}c_0}(1 - 2C), \qquad \Xi_1 = \frac{e^2}{\varepsilon_0\tilde{\varepsilon}c_0}\left(1 - 2C + 2C^2\right). \tag{2.74}$$

At $B = 75$ T, $\varepsilon_B \approx 343$ meV, and given that $\gamma_1 = 363$ meV, we can estimate $\varepsilon_B \sim \gamma_1$ in the magnetic field range from 60 T to 100 T, such that $C \sim 2/5$ and

$$\frac{\Xi_1}{\Xi_0} \sim \frac{13}{5} > \frac{3}{2}. \tag{2.75}$$

Consequently, at typical magnetic field ranges the SDW does not appear according to the solution in Eq. (2.69). Only for magnetic fields of the order $B \sim 210$ T or higher, corresponding to $\varepsilon_B > 573$ meV, the condition $\Xi_1/\Xi_0 < 3/2$ is fulfilled.

2.4.2. Spin-Density Wave When $\Xi_0/(2\mu) \gg \sqrt{2}c_0/l_B$

This case is the most likely scenario and represents the limit of a large interaction $\Xi_0 \sim e^2/(\varepsilon_0\tilde{\varepsilon}c_0)$. Following the initial discussion of the preceding section, at $B = 75$ T we have $\sqrt{2}c_0/l_B \sim 0.32$ and $\Xi_0/(2\mu) \sim 600/\tilde{\varepsilon}$. Therefore, $\tilde{\varepsilon} \lesssim 200$ is sufficient to fulfil the requirement. Exploring the

case of a large interaction will give us a deeper insight into the SDW phase. In particular, it allows us to infer that it involves a first-order phase transition.

In the limiting case where the interaction terms Ξ dominate the self-consistent integrals, we can approximate them to Dirac deltas of the form

$$\Xi_{ab}(k-k') \approx \frac{\sqrt{2}\pi c_0}{l_B}\Xi_0\delta(k-k'), \quad \frac{\Xi_{aa}(k-k')+\Xi_{bb}(k-k')}{2} \approx \frac{\sqrt{2}\pi c_0}{l_B}\Xi_1\delta(k-k'), \tag{2.76}$$

such that the critical band separation is still $\delta_{\text{sdw}} = c_0\Xi_0/(\sqrt{2}l_B)$, and the energy functional in Eq. (2.45) is rewritten to

$$\mathcal{E}[\vartheta_k] = \int \frac{dk}{2\pi}\left[\delta - \delta_{\text{sdw}} + \mu k^2 + \frac{c_0}{\sqrt{2}l_B}(\Xi_0-\Xi_1)\sin^2\vartheta_k\right]\sin^2\vartheta_k, \tag{2.77}$$

with constant terms omitted. Finding the extreme values of the energy functional through the functional derivative $\delta\mathcal{E}=0$ we obtain

$$2\cos\vartheta_k\sin\vartheta_k\left[\delta - \delta_{\text{sdw}} + \mu k^2 + \frac{2c_0}{\sqrt{2}l_B}(\Xi_0-\Xi_1)\sin^2\vartheta_k\right] = 0. \tag{2.78}$$

Therefore, besides the trivial minimum at $\vartheta_k = 0$, an additional energy minimum is found at $\vartheta_k = (\pi/2)\Theta(k_F - |k|)$, with $\Theta(x)$ the step function, and k_F the Fermi wave vector that determines the occupation of the renormalized bands $\bar{\varepsilon}_{-1}$ and $\bar{\varepsilon}_0$. To understand this situation, consider that the bare bands $\varepsilon_{-1\uparrow}(k+\pi)$ and $\varepsilon_{0\downarrow}(k)$ are initially separated by a positive energy gap δ such that the $\varepsilon_{0\downarrow}$ band is empty, as depicted in Fig. 2.3 (a). When corrected by the self-energy terms, the renormalized bands overlap, making the $\bar{\varepsilon}_0$ band occupied up to k_F, found as

$$\begin{aligned}\bar{\varepsilon}_0(k_F) = \bar{\varepsilon}_{-1}(k_F) \Rightarrow \mu k_F^2 + \delta + \Sigma_{k_F} = 0,\\ \mu k_F^2 = \sqrt{2}\frac{c_0}{l_B}\Xi_1 - \delta,\end{aligned} \tag{2.79}$$

where the Dirac delta approximation for Ξ was used in the total self-energy of Eq. (2.49). Nevertheless, since $\vartheta_k = (\pi/2)\Theta(k_F - |k|)$, the SDW gap of Eq. (2.40) is zero, meaning that this situation corresponds to the trivial filling of the band $\bar{\varepsilon}_0$ with no mixing between the two bands, no gap opening, and no SDW.

Let us relax the Dirac delta approximation for the interaction terms Ξ, such that they take the Lorentzian form of Eq. (2.58), and consider the self-consistent problem with $\vartheta_k = (\pi/2)\Theta(k_F - |k|)$ and $\Delta_k = 0$. In this case, the self-energy of Eq. (2.49) takes the form

$$\Sigma_k = -2\int_{-k_F}^{k_F}\frac{dk'}{2\pi}\frac{\Xi_1}{1+l_B^2(k-k')^2/(2c_0^2)} = \frac{\sqrt{2}c_0}{l_B}\frac{\Xi_1}{\pi}\left(\arctan\frac{k-k_F}{\sqrt{2}c_0/l_B} - \arctan\frac{k+k_F}{\sqrt{2}c_0/l_B}\right), \tag{2.80}$$

where the Fermi wave vector is found from

$$\mu k_F^2 + \delta + \Sigma_{k_F} = 0. \tag{2.81}$$

For δ sufficiently large, the previous equation has no solutions, but at a certain $\delta_* > 0$, two solutions bifurcate at $k_F = k_*$ as shown in the numerical solution of Fig. 2.3 (b). In the figure, one of the solutions goes unphysical ($k_F < 0$) when $\delta < 0$, so it is discarded. In the limiting cases of small and large interaction, we find

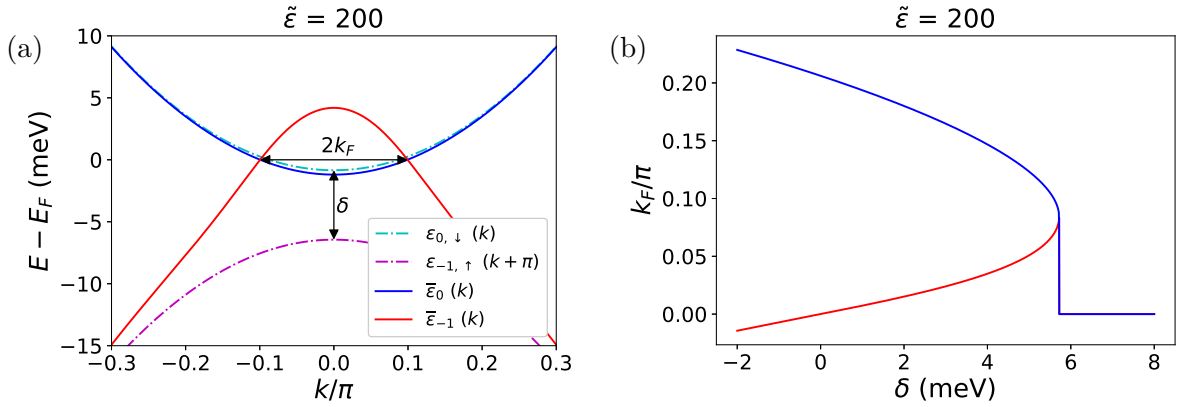

Figure 2.3: (a) Bare bands ($\varepsilon_{-1\uparrow}$, $\varepsilon_{0\downarrow}$) and renormalized bands ($\bar{\varepsilon}_{-1}$, $\bar{\varepsilon}_0$) in the limit $\vartheta_k = = (\pi/2)\Theta(k_F - |k|)$. The self-energy was computed from Eq. (2.80) using an effective dielectric constant of $\tilde{\varepsilon} = 200$. The band gap of the bare bands is $\delta = 5.6$ meV. (b) Numerical solutions for the Fermi wave vector k_F from Eq. (2.81). The critical band separation at which a solution is found is $\delta_* \approx 5.7$ meV, with $k_* \approx 0.08\pi$.

$$\delta_* = \begin{cases} \dfrac{\Xi_1^2}{\pi^2\mu}, & \text{if } \dfrac{\Xi_1}{\pi^2\mu} \ll \dfrac{c_0}{\sqrt{2}l_B}, \\ \dfrac{c_0}{\sqrt{2}l_B}\Xi_1, & \text{if } \dfrac{\Xi_1}{\pi^2\mu} \gg \dfrac{c_0}{\sqrt{2}l_B}, \end{cases} \tag{2.82}$$

and

$$k_* = \begin{cases} \dfrac{\Xi_1}{\pi\mu}, & \text{if } \dfrac{\Xi_1}{\pi\mu} \ll \dfrac{c_0}{\sqrt{2}l_B}, \\ \left(\dfrac{c_0}{\sqrt{2}l_B}\right)^{2/3}\left(\dfrac{\Xi_1}{\pi\mu}\right)^{1/3}, & \text{if } \dfrac{\Xi_1}{\pi\mu} \gg \dfrac{c_0}{\sqrt{2}l_B}. \end{cases} \tag{2.83}$$

We focus now on the behavior of the total energy at $\vartheta_k = (\pi/2)\Theta(k_F - |k|)$. Evaluating the energy functional we obtain

$$\begin{aligned} \mathcal{E}(k_F) &= \int_{-k_F}^{k_F} \frac{dk}{2\pi}(\delta + \mu k^2) - \int_{-k_F}^{k_F} \frac{dk}{2\pi}\frac{dk'}{2\pi}\frac{\Xi_1}{1 + (k-k')^2 l_B^2/(2c_0^2)} \\ &= \frac{1}{\pi}\left(\delta k_F + \frac{\mu k_F^3}{3}\right) + \frac{c_0^2}{2l_B^2}\frac{\Xi_1}{\pi^2}\left[\ln\left(1 + \frac{2k_F^2 l_B^2}{c_0^2}\right) - 2\frac{\sqrt{2}k_F l_B}{c_0}\arctan\frac{\sqrt{2}k_F l_B}{c_0}\right]. \end{aligned} \tag{2.84}$$

In Fig. 2.4, we display this total energy as a function of k_F for several values of the band separation δ. At $\delta < \delta_*$, the energy has a local maximum and minimum, and the minimum value becomes negative at a certain $\delta < \delta_1$. Since the total energy of the normal phase is $\mathcal{E}[\vartheta_k = 0] = 0$, this means that the state with $\vartheta_k = (\pi/2)\Theta(k_F - |k|)$ is more energetically favorable at $\delta < \delta_1$, leading to a first-order phase transition. The transition is of the first order because of the sudden change from $k_F = 0$ in the normal phase to a finite k_F of the phase with $\vartheta_k = (\pi/2)\Theta(k_F - |k|)$.

Nevertheless, the solution $\vartheta_k = (\pi/2)\Theta(k_F - |k|)$ that leads to $\Delta_k = 0$ is unstable. Expanding $\vartheta_k = (\pi/2)\Theta(k_F - |k|) + \tilde{\vartheta}_k \mathrm{sign}(|k| - k_F)$, with $\tilde{\vartheta}_k$ small, we obtain for the energy functional

$$\mathcal{E}[\vartheta_k] = \mathcal{E}(k_F) + \int \frac{dk}{2\pi}|\delta + \mu k^2 + \Sigma_k|\tilde{\vartheta}_k^2 - \int \frac{dk}{2\pi}\frac{dk'}{2\pi}\frac{\Xi_0\,\tilde{\vartheta}_k\tilde{\vartheta}_{k'}}{1 + (k-k')^2 l_B^2/(2c_0^2)} + O(\tilde{\vartheta}_k^4), \tag{2.85}$$

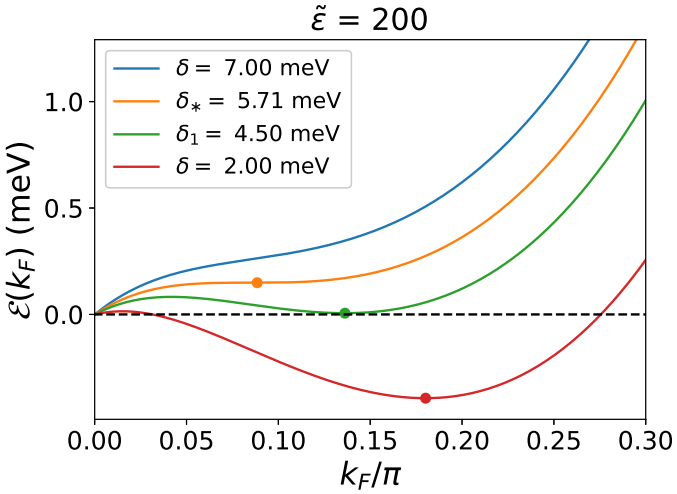

Figure 2.4: Energy functional at $\vartheta_k = (\pi/2)\Theta(k_F - |k|)$, as a function of the Fermi wave vector k_F for different values of δ. The dots indicate local minima of the energy.

therefore, approximating $\tilde{\vartheta}_k \propto \delta(k - k_F)$ necessarily gives negative energy, since near k_F we can approximate

$$\delta + \mu k^2 + \Sigma_k \approx v_F(|k| - k_F), \quad v_F = 2\mu k_F + \frac{\Xi_1}{\pi}\frac{2k_F^2\, l_B^2}{2k_F^2\, l_B^2 + c_0^2}. \tag{2.86}$$

This means that there must be a smooth change from $\vartheta_k = 0$ to $\vartheta_k = \pi/2$ in the vicinity of k_F, which favours the emergence of the SDW phase, as is indeed observed in the numerical solutions shown in the following section.

2.5. Self-Consistent Calculation of the Spin-Density Wave State

Finding out that the transition into the SDW state involves a first-order phase transition explains why the approximate solutions in Eqs. (2.68-2.71) fail. When we performed the expansion around δ_{sdw} in Eqs. (2.66, 2.67), it was implicitly assumed that Δ_k grows continuously from zero in the normal phase to an arbitrarily small value as one gets arbitrarily close the transition point. This would be true if $\Xi_1 < \Xi_0$, implying that Eqs. (2.68-2.71) would describe a second-order phase transition. Instead, in a transition of the first order the SDW gap grows discontinuously from zero to a finite value at the transition point. A prominent consequence of first-order transitions is the emergence of hysteresis in certain physical quantities as the transition point is reached, for example, in the electric resistance of graphite at the transition to charge-density waves at $B \sim 53$ T [51]. Therefore, we will employ numerical calculations to determine the SDW, considering different situations that lead to a hysteresis in the SDW gap.

We will continue working in the quadratic approximation of the bands $\varepsilon_{-1\downarrow}$ and $\varepsilon_{0\uparrow}$ near $k = \pi$ and $k = 0$, respectively, such that the set of self-consistent equations reduces to Eqs. (2.61, 2.62):

$$\Delta_k = \int \frac{dk'}{2\pi} \frac{\Xi_0}{1 + l_B^2(k-k')^2/(2c_0^2)} \frac{\Delta_{k'}}{\sqrt{(\mu k'^2 + \delta + \Sigma_{k'})^2 + 4\Delta_{k'}^2}},$$

$$\Sigma_k = -\int \frac{dk'}{2\pi} \frac{\Xi_1}{1 + l_B^2(k-k')^2/(2c_0^2)} \left(1 - \frac{\mu k'^2 + \delta + \Sigma_{k'}}{\sqrt{(\mu k'^2 + \delta + \Sigma_{k'})^2 + 4\Delta_{k'}^2}}\right),$$

and the mixing parameter ϑ_k found from Eq. (2.54):

$$\frac{1}{2}\tan 2\vartheta_k = \frac{\Delta_k}{\mu k^2 + \delta + \Sigma_k}.$$

The procedure is as follows:

1. For a given δ, suppose initial Δ_k, Σ_k. We considered two different sets of initial conditions: First, the SDW gap and self-energy took small and constant values along k, being $\Delta_k^{(\text{init})} = = 0.1$ meV and $\Sigma_k^{(\text{init})} = -0.1$ meV. The second set of initial conditions is taking converged values of Δ_k and Σ_k from a previous self-consistent calculation at a smaller δ. The Fermi wave vector is found from Eq. (2.81).

2. Compute $\Delta_k^{(\text{new})}$ and $\Sigma_k^{(\text{new})}$ from Eqs. (2.61, 2.62) using the Δ_k and Σ_k from the previous step.

3. Check the convergence of Δ_k. The convergence criterion was a relative error of less than 0.2%. If it did not converge, repeat step 2.

The two sets of initial conditions emulate different experimental conditions. Considering small values of Δ_k and Σ_k corresponds to the system being initially in the normal phase with large values of δ and B. On the other hand, considering converged values of Δ_k and Σ_k from a previous smaller δ means that the system is initially in the SDW phase (provided that the previous calculation converged to non-zero values), which can be destroyed as the band separation, and thus, the magnetic field, is increased.

Although it is difficult to be certain about the precise values of $\tilde{\varepsilon}$, Ξ_0, and Ξ_1, we work with the estimations of $\tilde{\varepsilon} = 200$ and $\Xi_1 = 70$ meV computed from Eq. (2.74). While Eq. (2.74) predicts a ratio $\Xi_0/\Xi_1 \approx 0.35$ at $B = 75$ T, we work with $\Xi_0/\Xi_1 = 0.7$ because it results in higher values of the SDW gap Δ_k, facilitating the analysis. In Appendix A section A.4, we show results choosing different values for these parameters. Fig. 2.5 presents the results of the self-consistent calculation using the second choice of initial conditions. The bare bands are depicted in Fig. 2.5 (a), showing a band gap $\delta = 4.6$ meV. At this separation, the Coulomb interaction generates the SDW phase and the bands ε_-, ε_+, as shown in Fig. 2.5 (b). The behaviour of the bands is depicted in more detail in Fig. 2.5 (c). We observe that initially, the bare bands have a positive energy gap δ, but self-energy corrections make the renormalized bands cross at a finite k_F. The SDW phase appears as a reconfiguration of the renormalized bands, such that at the crossing point of the renormalized bands a band gap of value $2\Delta_{k_F}$ appears, and close to $k = 0$ the SDW bands are essentially an inversion of the renormalized ones. Fig. 2.5 (d,e) depicts the SDW gap and self-energy as a function of k, for different values of δ. We find that Δ_k gets its maximum value at k_F, while $|\Sigma_k|$ is at its highest at $k = 0$. Both terms decrease in value as $|k|$ is increased. At $\delta > 4.6$ meV, the system is in the normal phase, such that the solution to the self-consistent problem is $\Delta_k = \Sigma_k = 0$. Finally, the parameter ϑ_k that indicates the degree of mixing of the bare bands is illustrated in Fig. 2.5 (f). It grows smoothly in the vicinity of k_F (different for each δ but not indicated in the figure), acquiring the maximum value at $k = 0$. We observe that as δ is decreased, the behavior of ϑ_k starts to resemble that of $(\pi/2)\Theta(k_F - |k|)$, with Θ the step function.

We now investigate how the SDW gap depends on δ. Fig. 2.6 (a) shows the maximum value of Δ_k at a given δ, for the two sets of initial conditions. We observe that at a certain value of δ, the SDW gap drops sharply to zero, as it is characteristic of the order parameter of first-order phase transitions. Additionally, Δ_k drops to zero at different values of δ for the two sets of initial conditions, indicating a hysteresis behaviour of the SDW gap. In the figure, the arrows indicate the values that $\max(\Delta_k)$ acquires if the band separation parameter δ is increased or decreased, corresponding to the experimental situation of increasing or decreasing the magnetic

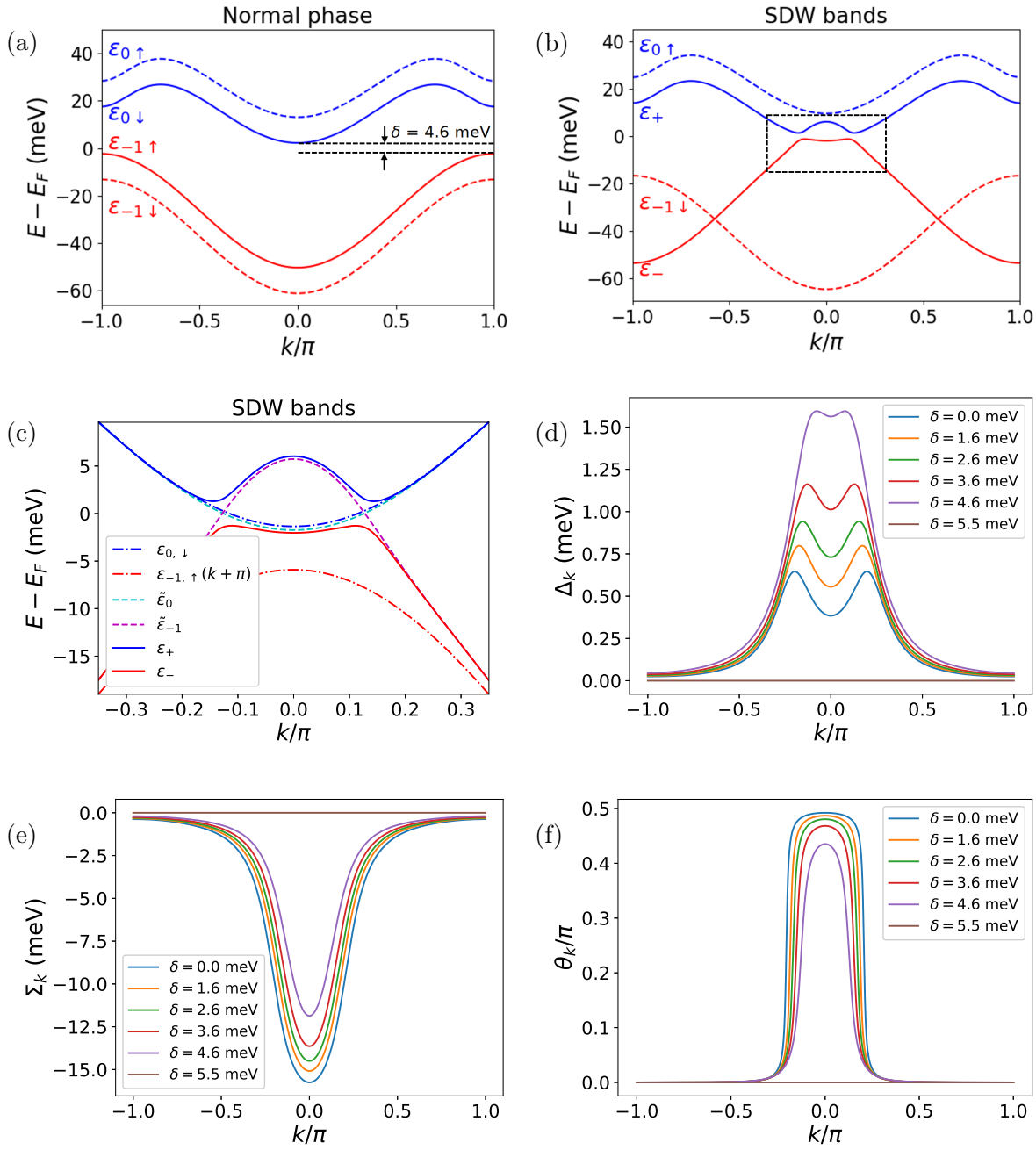

Figure 2.5: Results of numerical self-consistent calculations of the SDW state. The parameters are $\tilde{\varepsilon} = 200$, $\Xi_1 = 70$ meV, and $\Xi_0/\Xi_1 = 0.7$. (a) Example of initial bare bands in the normal phase, with a band gap $\delta = 4.6$ meV. (b) Formation of the SDW bands, the bare band gap is $\delta = 4.6$ meV. (c) Closer look at the SDW bands showing in detail the region in the dashed square of (b). The bare bands (ε_{-1}, ε_0), renormalized bands ($\bar{\varepsilon}_{-1}$, $\bar{\varepsilon}_0$) and SDW bands (ε_-, ε_+) are indicated. (d) SDW gap Δ_k as a function of k for different values of δ. (e) Self-energy term Σ_k for different values of δ. (f) Band mixing term ϑ_k for different values of δ.

field, respectively. The hysteresis is also seen in the total energy $\mathcal{E}[\vartheta_k]$ of Eq. (2.50), as seen in Fig. 2.6 (b). It can be observed that for $\delta < \delta_1$, the energy associated with the SDW state is lower than that of the normal state, $\mathcal{E}[\vartheta_k = 0] = 0$, marking the transition to the SDW state in the case of an increasing B. In the case of decreasing B, there is a discontinuous jump in the total energy around $\delta = 3.7$ meV.

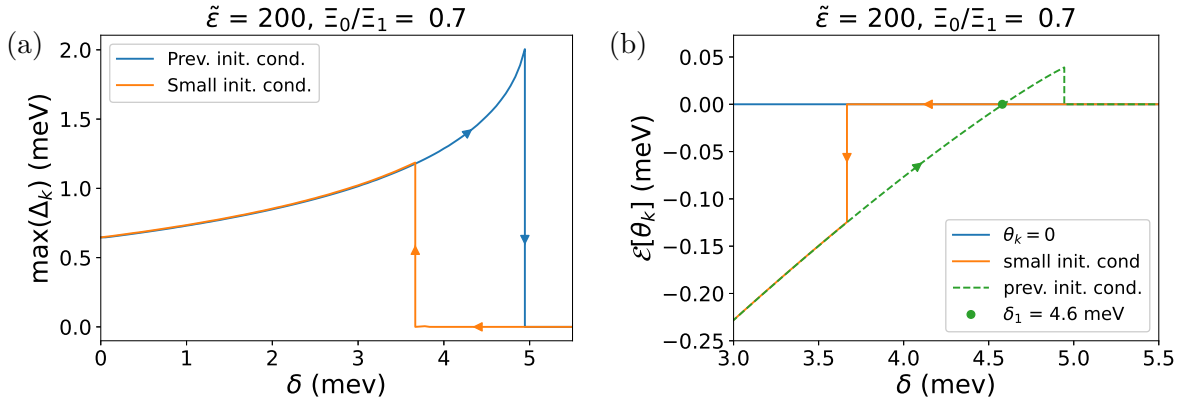

Figure 2.6: (a) Maximum value of the SDW gap, Δ_k, as a function of the bare band gap δ. The results for the different sets of initial conditions are indicated, with the arrows showing the expected value of max(Δ_k) as δ is increased or reduced, corresponding to an increase or reduction in the magnetic field. (b) Total energy $\mathcal{E}[\vartheta_k]$ as a function of δ. The arrows have the same meaning as in (a).

Although the precise values of the SDW gap depend on precise estimations of $\tilde{\varepsilon}$, Ξ_0, and Ξ_1, in Appendix A we show that lower values of $\tilde{\varepsilon}$ or higher values of Ξ_0/Ξ_1 lead to a higher Δ_k. This is, a stronger interaction increases the SDW gap. We also expect that the hysteresis in Δ_k remains independent parameter values, except when Ξ_0/Ξ_1 gets close to 1, at which the phase transition is of second order, as shown in Appendix A.

2.6. Spectroscopic Signature of Spin-Density Waves

Our main objective is to identify the distinct signature of the SDW in a spectroscopic experiment. The physical quantity being measured in such an experiment is the optical conductivity, defined (in S.I. units) as

$$\sigma_{ij}(\omega) = \frac{2\pi i}{\omega}\frac{e^2\hbar}{V}\sum_{N,N'}\sum_{\sigma,\sigma'}\sum_{p,p'}\int \frac{dk\,dk'}{(2\pi c_0/L_z)^2}[f(\varepsilon_{N'\sigma'})-f(\varepsilon_{N\sigma})]\,\frac{\langle N_{\sigma pk}|\hat{v}_i|N'_{\sigma'p'k'}\rangle\,\langle N'_{\sigma'p'k'}|\hat{v}_j|N_{\sigma pk}\rangle}{\hbar\omega-(\varepsilon_{N\sigma}-\varepsilon_{N'\sigma'})+i\Gamma}, \tag{2.87}$$

with $|N_{\sigma pk}\rangle$ representing the electron states of Eq. (2.21), except for $|-1_{\uparrow pk}\rangle$ and $|0_{\downarrow pk}\rangle$, which are replaced by the SDW states $|-\rangle$ and $|+\rangle$ of Eq. (2.36). Other terms in the equation are the subindices $i,j \in \{x,y\}$, ω the (angular) frequency of the incident light, $V = L_xL_yL_z$ the sample volume, $f(\varepsilon_{N\sigma})$ the occupation of the energy level $\varepsilon_{N\sigma}$ given by the Fermi distribution, $\hat{v}_i$ the i component of the velocity operator, and Γ a phenomenological broadening factor.

The velocity operator is defined as $\hat{v}_i = \partial\hat{\mathcal{H}}_{k_z}/\partial p_i$, with the Hamiltonian given in Eq. (2.3), and takes the form

$$\hat{v}_x = \begin{pmatrix} 0 & v & -\alpha_4 v & 0 \\ v & 0 & 0 & -\alpha_4 v \\ -\alpha_4 v & 0 & 0 & v \\ 0 & -\alpha_4 v & v & 0 \end{pmatrix}, \qquad \hat{v}_y = \begin{pmatrix} 0 & -iv & i\alpha_4 v & 0 \\ iv & 0 & 0 & i\alpha_4 v \\ -i\alpha_4 v & 0 & 0 & -iv \\ 0 & -i\alpha_4 v & iv & 0 \end{pmatrix}, \tag{2.88}$$

with $\alpha_3 = 0$. It is more convenient to work with circularly polarized light because it restricts the transition rules between Landau levels. The optical conductivity for counterclockwise and clockwise polarized light, $\sigma_\pm$, is obtained from Eq. (2.87) by replacing $\hat{v}_i$ and $\hat{v}_j$ by

$$\hat{v}_\pm = \hat{v}_x \pm i\hat{v}_y; \qquad \hat{v}_+ = (\hat{v}_-)^\dagger = 2v \begin{pmatrix} 0 & 1 & -\alpha_4 & 0 \\ 0 & 0 & 0 & -\alpha_4 \\ 0 & 0 & 0 & 1 \\ 0 & 0 & 0 & 0 \end{pmatrix}. \tag{2.89}$$

The allowed electronic transitions between Landau bands are dictated by the matrix elements of the velocity operator, $\langle f|\hat{v}_i|i\rangle$, with $|i\rangle$ and $|f\rangle$ the initial and final states. Operating them directly using the wave functions of Eq. (2.12), it is found that $\hat{v}_+$ allows transitions of the form $|N\rangle \to |N+1\rangle$, and $\hat{v}_-$ transitions of the form $|N\rangle \to |N-1\rangle$.

Computing the matrix elements explicitly, we obtain

$$\langle 0_{\sigma pk}|\hat{v}_+|-1_{\sigma' p' k'}\rangle = \delta_{kk'} \int dx\, dy\; \Psi^{(0,\sigma)\,\dagger}_{pk}(x,y)\, \hat{v}_+ \Psi^{(-1,\sigma')}_{p'k'}(x,y) = -\frac{2\alpha_{4,k}\varepsilon_B v}{\sqrt{\varepsilon_B^2 + \Gamma_{1,k}^2}} \delta_{\sigma\sigma'}\delta_{pp'}\delta_{kk'}, \tag{2.90}$$

where the dependence of Γ_1 and α_4 on k was made explicitly. Other matrix elements of interest are

$$\langle 0^+_{\sigma pk}|\hat{v}_+|-1_{\sigma' p' k'}\rangle = -\langle -1_{\sigma pk}|\hat{v}_-|0^-_{\sigma' p' k'}\rangle \approx \sqrt{2}v\, \delta_{\sigma\sigma'}\delta_{pp'}\delta_{kk'}, \tag{2.91}$$

$$\langle 1^{+\pm}_{\sigma pk}|\hat{v}_+|0_{\sigma' p' k'}\rangle = \langle 0_{\sigma pk}|\hat{v}_-|1^{-\pm}_{\sigma' p' k'}\rangle \approx \frac{2v}{\sqrt{\varepsilon_B^2 + \Gamma_{1,k'}^2}} \left(\varepsilon_B x_{1,k}^{(1\pm\pm)} - \Gamma_{1,k'} x_{3,k}^{(1\pm\pm)}\right) \delta_{\sigma\sigma'}\delta_{pp'}\delta_{kk'}, \tag{2.92}$$

$$\langle 1^{+\pm}_{\sigma pk}|\hat{v}_+|0^-_{\sigma' p' k'}\rangle = \langle 0^+_{\sigma pk}|\hat{v}_-|1^{-\pm}_{\sigma' p' k'}\rangle \approx \frac{\sqrt{2}v}{\sqrt{\varepsilon_B^2 + \Gamma_{1,k'}^2}} \left(\Gamma_{1,k'} x_{1,k}^{(1\pm\pm)} + \varepsilon_B x_{3,k}^{(1\pm\pm)}\right) \delta_{\sigma\sigma'}\delta_{pp'}\delta_{kk'}, \tag{2.93}$$

where the approximation $\alpha_4 \ll 1$ was used.

Considering that the SDW states are of the form

$$\begin{aligned} |+_{pk}\rangle &= \cos\vartheta_k\, |0_{\downarrow pk}\rangle - \sin\vartheta_k\, |-1_{\uparrow p,k+\pi}\rangle, \\ |-_{pk}\rangle &= \sin\vartheta_k\, |0_{\downarrow pk}\rangle + \cos\vartheta_k\, |-1_{\uparrow p,k+\pi}\rangle, \end{aligned} \tag{2.94}$$

we identify the following matrix elements related to transitions active in the counterclockwise polarization:

$$\langle 0_{\uparrow p,k+\pi}|\hat{v}_+|-_{pk}\rangle = -\frac{2\alpha_{4,k+\pi}\varepsilon_B v}{\sqrt{\varepsilon_B^2 + \Gamma_{1,k+\pi}^2}} \cos\vartheta_k, \tag{2.95}$$

$$\langle +_{pk}|\hat{v}_+|-1_{\downarrow pk}\rangle = -\frac{2\alpha_{4,k}\varepsilon_B v}{\sqrt{\varepsilon_B^2 + \Gamma_{1,k}^2}} \cos\vartheta_k, \tag{2.96}$$

$$\langle 0^+_{\uparrow p,k+\pi}|\hat{v}_+|-_{p,k}\rangle = \sqrt{2}v\cos\vartheta_k, \tag{2.97}$$

$$\langle 1^{+\pm}_{p,k,\downarrow}|\hat{v}_+|-_{p,k}\rangle = \frac{2v}{\sqrt{\varepsilon_B^2 + \Gamma_{1,k}^2}} \left(\varepsilon_B x_{1,k}^{(1+\pm)} - \Gamma_{1,k} x_{3,k}^{(1+\pm)}\right) \sin\vartheta_k, \tag{2.98}$$

and in the clockwise polarization:

$$\langle +_{pk}|\hat{v}_-|1^{-\pm}_{\downarrow pk}\rangle = \frac{2v}{\sqrt{\varepsilon_B^2 + \Gamma_{1,k}^2}} \left(\varepsilon_B x_{1,k}^{(1-\pm)} - \Gamma_{1,k} x_{3,k}^{(1-\pm)}\right) \cos\vartheta_k, \tag{2.99}$$

$$\langle +_{pk}|\hat{v}_-|0^-_{\uparrow p,k+\pi}\rangle = \sqrt{2}v\,\sin\vartheta_k. \tag{2.100}$$

With these results, we can write the optical conductivity in both circular polarizations in a simplified way:

$$\begin{aligned}\sigma_\pm(\omega) &= \frac{2\pi i}{\omega}\frac{e^2\hbar}{V}g\sum_{N,N'}\sum_{\sigma,\sigma'}\int\frac{dk}{2\pi c_0/L_z}[f(\varepsilon_{N'\sigma'})-f(\varepsilon_{N\sigma})]\,\frac{|\langle N_{\sigma p,k+Q}|\hat{v}_\pm|N'_{\sigma' p',k'+Q'}\rangle|^2}{\hbar\omega-(\varepsilon_{N\sigma}-\varepsilon_{N'\sigma'})+i\Gamma},\\ &= \frac{ie^2\hbar}{\omega}\frac{gL_z}{Vc_0}\sum_{N,N'}\sum_{\sigma,\sigma'}\int\frac{dE_{N\sigma,N'\sigma'}}{(dE_{N\sigma,N'\sigma'}/dk)}[f(\varepsilon_{N'\sigma'})-f(\varepsilon_{N\sigma})]\,\frac{|\langle N_{\sigma p,k+Q}|\hat{v}_\pm|N'_{\sigma' p',k'+Q'}\rangle|^2}{\hbar\omega-E_{N\sigma,N'\sigma'}+i\Gamma}.\end{aligned} \tag{2.101}$$

with $E_{N\sigma,N'\sigma'}=\varepsilon_{N\sigma}-\varepsilon_{N'\sigma'}$, and Q,$Q'=0$, except for the matrix elements of Eqs. (2.95, 2.97, 2.100), for which they acquire the value Q,$Q'=\pi$, depending on the case. In the last equation, the term $dE_{N\sigma,N'\sigma'}/dk$ in the denominator implies that there is a peak in the optical conductivity whenever both bands are flat, which always happens at $k=0$,π. Since none of the terms depends on p, the sum over p,p' is equal to the degeneracy per Landau level

$$g = g_v\frac{2eBA}{h} = 2\frac{A}{\pi l_B^2}, \tag{2.102}$$

with $g_v=2$ the valley degeneracy, and $A=L_xL_y$ the transversal area of the sample. Spin degeneracy is not considered since the Landau levels include the Zeeman splitting.

We compute numerically the optical transitions in each polarization using Eq. (2.101), taking the graphite bands of Eqs. (2.17, 2.19), and the numerical solutions of the SDW bands found in the previous section. We choose the values $\Gamma=1$ meV for the broadening factor and $T=0$ for the occupation probabilities $f(\varepsilon)$. In Fig. 2.7, we show the optical conductivity in the counterclockwise and clockwise polarization, comparing the spectra in the SDW and normal phases, the latter in the case of partially occupied $\varepsilon_{-1\uparrow}$ and $\varepsilon_{0\downarrow}$ bands with a negative band gap of $\delta=-3$ meV. Since the spectra is proportional to $1/\omega$, we plotted the quantity $\omega\sigma(\omega)$ for a better visualization. The spectra contain the optical transitions that do not involve the SDW bands, such as $|-1_\downarrow\rangle\to|0^+_\downarrow\rangle$ and $|1^{-\pm}_\uparrow\rangle\to|0_\uparrow\rangle$. In the spectra, we identify two types of transitions involving the SDW bands, i.e., those that are diminished and those that they enable, that can be understood from the $\cos\vartheta_k$ and $\sin\vartheta_k$ factors in the matrix elements of the velocity operator. Blue lines indicate the diminished transitions, while enabled transitions are shown in green ($|-\rangle\to|1^{+-}_\downarrow\rangle$) and cyan ($|0^-_\uparrow\rangle\to|+\rangle$). Focusing on the spectra in the counterclockwise polarization of Fig. 2.7 (a,b), we see that the enabled transition $|-\rangle\to|1^{+-}_\downarrow\rangle$ in the SDW phase, and the transition $|0_\downarrow\rangle\to|1^{+-}_\downarrow\rangle$ in the normal phase, both indicated in green, have a similar profile and transition energy close to 190 meV. These transitions are shown in the Landau band diagram of Fig. 2.8 (a,b), indicated by the green arrow. In the SDW case, the transition results from the $|0_\downarrow\rangle$ component of the ε_- band near $k=0$, which enables a transition to $\varepsilon_{1^{+-}}$. In principle, the same transition would lead to a second peak at $k=\pi$ since both bands involved are flat at this point. However, at $k=\pi$ the SDW band ε_- has a dominant $|-1_{\uparrow,k+\pi}\rangle$ character which prohibits the transition, as indicated in Fig. 2.8 (a). In the normal phase, partial occupation of the band $\varepsilon_{0_\downarrow}$ around $k=0$ is responsible for the peak in the spectra. It is easier to identify the SDW phase when comparing the transition $|-\rangle\to|0^+_\uparrow\rangle$ with its normal phase counterpart $|-1_\uparrow\rangle\to|0^+_\uparrow\rangle$, indicated in blue in Fig. 2.7 (a,b). In the normal phase, the transition has a sharp peak close to 400 meV, while in the SDW phase, it gets broadened due to the factor $\cos\vartheta_k$ of the corresponding velocity matrix element.

Electronic transitions between the SDW and the lowest-lying Landau bands $\varepsilon_{-1,\downarrow}$ and $\varepsilon_{0,\uparrow}$ are also active in the counterclockwise polarization. The spectra are shown in Fig. 2.7 (c,d) in the SDW and normal phases, and diagrams of the bands with approximate energy transitions are displayed in Fig. 2.8 (c,d). Comparing the spectra, it can be concluded that the shape

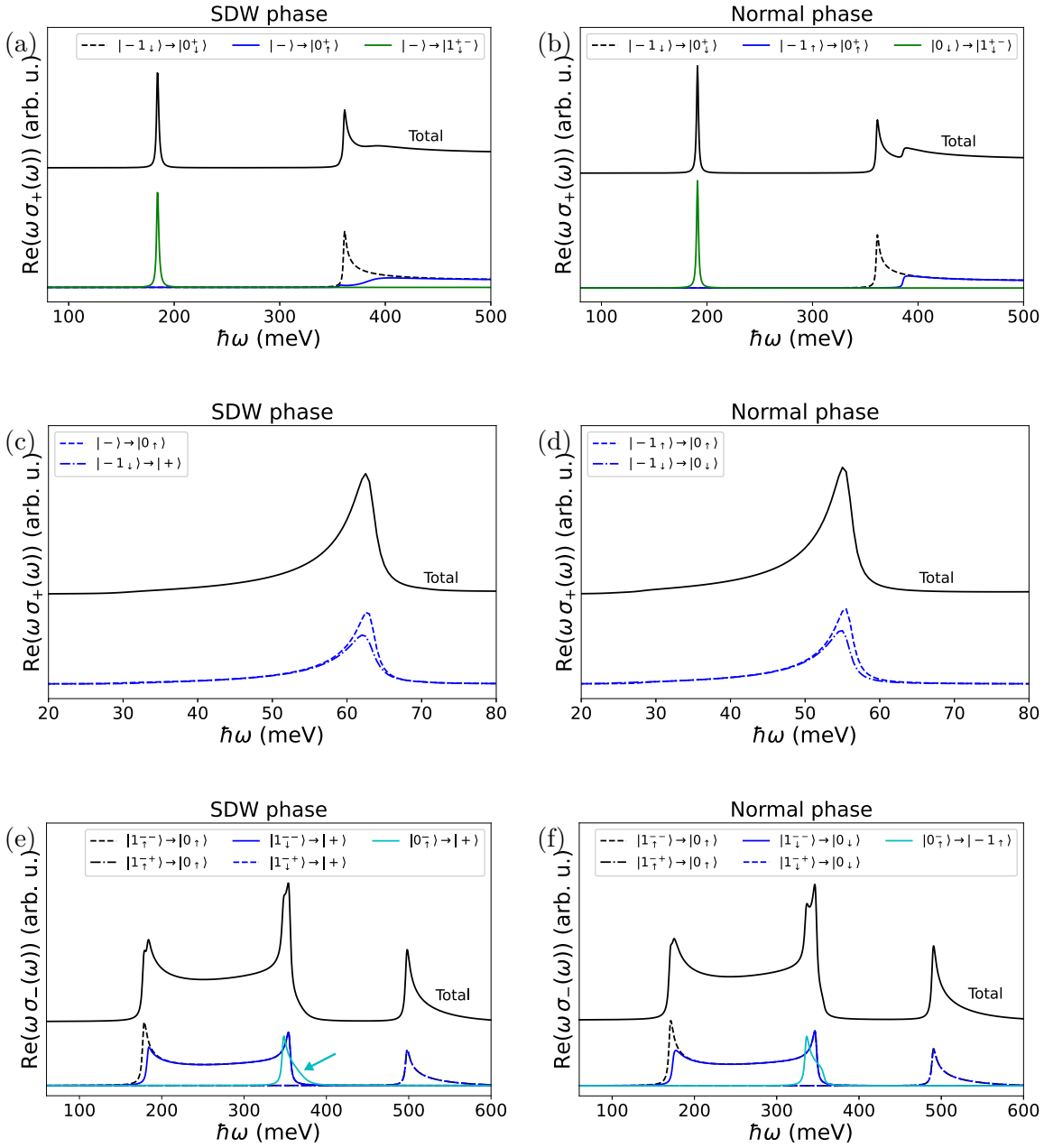

Figure 2.7: Real part of the optical conductivity for circularly polarized light in the SDW and normal phases. The bare band separation in the SDW phase is $\delta = 4.6$ meV, while $\delta = = -3$ meV in the normal phase without SDW formation. Blue, green/cyan, and dashed black lines indicate electronic transitions that are diminished by, enabled by, and independent from the SDW, respectively. (a,c) Spectra in the counterclockwise polarization in the SDW phase at different energy scales. (b,d) Spectra in the counterclockwise polarization in the normal phase. (e) Spectra in the clockwise polarization in the SDW phase. (f) Spectra in the clockwise polarization in the normal phase.

of each transition is very similar in both cases, which might make the identification of the SDW phase from these transitions alone difficult. Analyzing the allowed transitions in the SDW phase, $|-_k\rangle \to |0_{\downarrow,k+\pi}\rangle$ at $k = \pi$ is allowed due to the matrix element in Eq. (2.95), and gives the strongest spectral peak around 63 meV. On the other hand, the transition $|-1_{\downarrow k}\rangle \to |+_k\rangle$ at $k = 0$, represented by the crossed vertical arrow in Fig. 2.8 (c), is diminished by the SDW state,

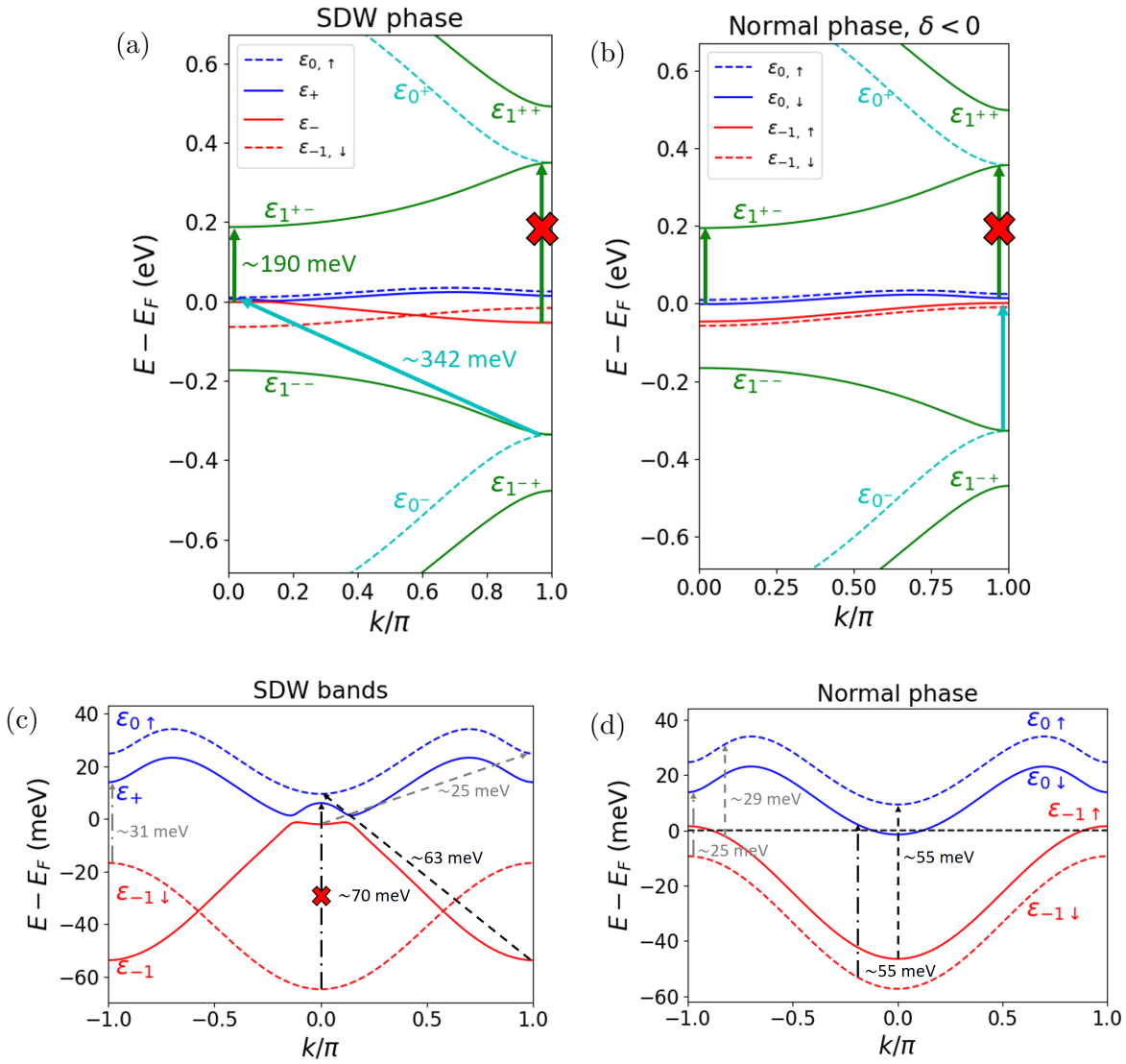

Figure 2.8: (a) Landau bands of graphite showing the SDW-enabled electronic transitions. The transitions $|-_{k=0}\rangle \to |1^{+-}_{\downarrow,k=0}\rangle$ and $|0^{-}_{\uparrow,k=\pi}\rangle \to |+_{k=0}\rangle$ are indicated by the green and cyan arrows, respectively. The transition $|-_{k=\pi}\rangle \to |1^{+-}_{\downarrow,k=\pi}\rangle$ is prohibited and is shown as a crossed vertical green arrow. (b) Electronic transitions in the absence of SDW and with $\delta < 0$, implying a partial occupation of the bare bands $\varepsilon_{-1\uparrow}$, $\varepsilon_{0\downarrow}$. The band gap is $\delta = -3$ meV. (c) Transitions between the lowest-lying graphite bands in the SDW phase. The dashed and dash-dotted vertical arrows were chosen to match the convention of the spectra in Fig. 2.7(c,d). The transition $|-1_{\downarrow,k=0}\rangle \to |+_{k=0}\rangle$ is diminished by the SDW state and is represented by the crossed vertical arrow. The transitions indicated by grey arrows are absent in the spectra due to the $\alpha_{4,k=\pi} = 0$ dependence of the matrix element in Eqs. (2.95, 2.96). (d) Transitions between the lowest-lying graphite bands in the normal phase and $\delta = -3$ meV.

explaining the absence of a peak in the spectra at 70 meV. Finally, the transitions $|-1_{\downarrow,k}\rangle \to |+_k\rangle$ at $k = \pi$, and $|-_k\rangle \to |0_{\downarrow,k+\pi}\rangle$ at $k = 0$, do not appear in the optical conductivity due to the $\alpha_{4,k=\pi} = 0$ dependence of the matrix element in Eqs. (2.95, 2.96). These transitions are indicated by grey arrows in Fig. 2.8 (c). In the normal phase, these transitions become $|-1_{\downarrow k}\rangle \to |0_{\downarrow k}\rangle$ and $|-1_{\uparrow k}\rangle \to |0_{\uparrow k}\rangle$, and as mentioned, the corresponding spectra is similar to the SDW one due to similar band shapes and transition energies (Fig. 2.8 (c)). Nevertheless, it is worth mentioning

that if the SDW gap Δ_k is high, i.e., comparable to the bandwidth on the bands ∼40 meV, the SDW bands would get a considerable deformation, changing the shape of the optical transition spectra.

In the clockwise polarization σ_-, there are more active transitions in the energy range 50 − 600 meV compared to the counterclockwise polarization, as shown in Fig. 2.7 (e,f). In this case, the only SDW-enabled transition is $|0^-_\uparrow\rangle \to |+\rangle$, indicated in cyan. Comparing this transition with its normal-phase counterpart $|0^-_\uparrow\rangle \to |-1_\uparrow\rangle$, we observe that their shape is only slightly different, with the SDW transition having a long tail around 390 meV indicated by the arrow in Fig. 2.7 (e). Such a long tail is more visible when the system is deeper into the SDW state, this is, at lower δ, as will be seen in Fig. 2.10 (c). Since this peak is superimposed with the transition $|1^{--}_\downarrow\rangle \to |+\rangle$ in the SDW phase, and $|1^{--}_\downarrow\rangle \to |0_\downarrow\rangle$ in the normal phase, looking at its evolution as δ is decreased (i.e., as the magnetic field is decreased) will be useful for the identification of the SDW phase, as discussed in the following paragraphs. In Fig. 2.7 (e), it is also seen that the transitions $|1^{-+}_\downarrow\rangle \to |+\rangle$ and $|1^{-+}_\uparrow\rangle \to |0_\uparrow\rangle$ are degenerate, showing a peak close to 500 meV due to the transition at $k = \pi$. At this point, the band ε_+ is entirely composed of the $\varepsilon_{0\downarrow}$ component, thus, the transition effectively becomes $|1^{-+}_\downarrow\rangle \to |0_\downarrow\rangle$ which is spin degenerate, as observed for the spectra in the normal phase of Fig. 2.7 (f).

We complete our analysis by studying the evolution of the optical conductivity across the transition between the SDW and normal phases by changing the band separation δ. Although we know that δ increases as the magnetic field increases, the precise relationship is not known, so we assumed that $\delta = 0$ at $B = 75$ T, and that it increases at a rate 1 meV/T. We study the evolution of the optical conductivity in three situations: first, without the formation of SDW, such that the bands always have the shape in Fig. 2.8 (d); second, with $\Xi_0/\Xi_1 = 0.7$, corresponding to the first-order phase transition studied so far; and third, with $\Xi_0/\Xi_1 = 1.1$, corresponding to a hypothetical second-order phase transition. The spectra in the counterclockwise polarization are displayed in Fig. 2.9 (a,c,e) for each case, with Fig. 2.9 (b,d,f) showing the contribution of each transition. The corresponding results in the clockwise configuration are shown in Fig. 2.10. The SDW phase is more easily identified in the counterclockwise polarization, with the strongest indication of the SDW phase being the sudden disappearance of the peak around 190 meV at the transition to the normal phase, with the transition designated by the red spectra of the figures. This peak corresponds to the SDW-enabled transition $|-\rangle \to |1^{+-}_\downarrow\rangle$, as observed in Fig. 2.9 (c,d). On the contrary, without SDW formation and in a second-order phase transition, the peak gradually decreases in intensity until it disappears at the transition point. In the case of no SDW formation of Fig. 2.9 (a,b), the transition point indicates the depopulation of the band $\varepsilon_{0\downarrow}$, which justifies the disappearance of the transition $|0_\downarrow\rangle \to |1^{+-}_\downarrow\rangle$. Another signature of the SDW phase in the counterclockwise polarization is the lack of a second sharp peak around 350 meV. In the case of no SDW formation, two sharp peaks merge as the transition point is reached, as indicated by the blue arrows in Fig. 2.9 (a). However, in the SDW phase, in both first- and second-order phase transitions, the second feature is much broader (marked by the blue arrows in 2.9 (c)), such that there is effectively only one peak around 350 meV.

The SDW phase can also be identified in the optical conductivity in clockwise polarization (Fig. 2.10). The main indicator is the SDW-enabled transition $|0^-_{\uparrow,k+\pi}\rangle \to |+_k\rangle$, indicated by the cyan spectra of Fig. 2.10 (b,d,f). For no SDW formation, the transition becomes $|0^-_{\uparrow k}\rangle \to |-1_{\uparrow k}\rangle$, which has a sharp peak lower in energy as the transition $|1^{--}_\uparrow\rangle \to |_\uparrow\rangle$ at $k = \pi$, approximately at 340 meV, as indicated by the arrows in Fig. 2.10 (a). On the contrary, for SDW formation in both first- and second-order transitions, the peak is observed above 340 meV when the system is deep into the SDW phase, for example, at $\delta = -2.4$ meV, as indicated by the arrows of Fig. 2.10 (c,e). It is important to note that such situation never happens if there is no SDW formation. As δ increases and approaches the transition to the normal phase, the peak shifts below 340 meV, in a similar way as in the case of no SDW formation. Another feature of the SDW phase is the presence of a long tail in the $|0^-_{\uparrow,k+\pi}\rangle \to |+_k\rangle$ transition, as shown by the

arrows of Fig. 2.10 (c,e) at $\delta = -0.4$ meV. However, in the clockwise polarization we do not see major qualitative differences in the spectra of the first- and second-order phase transition, and conclude that the order of the transition is best identified in the counterclockwise polarization by the sudden or gradual disappearance of the peak at 190 meV.

We finish our discussion with a few comments. First, the effect of the first-order phase transition and the hysteresis of the SDW gap is simply the appearance of the described features at different magnetic field values, depending if it is swept up or swept down, particularly the SDW-enabled transitions $|-\rangle \rightarrow |1^{+-}_{\downarrow}\rangle$ and $|0^{-}_{\uparrow,k+\pi}\rangle \rightarrow |+_k\rangle$. Second, the energy values of the electronic transitions shown in the optical conductivity spectra are only approximate, with the real experimental values being different due to the screening effects of the Landau levels, which change the energies (and, to a lesser extent, the shape) of the energy bands. Nevertheless, the overall shape of the spectra should remain the same. Lastly, there are electronic transitions at higher energies involving the SDW bands. However, at those energies, there are many transitions between Landau levels that do not involve the SDW bands, which would complicate the analysis considerably. For this reason, they were not discussed in the present chapter.

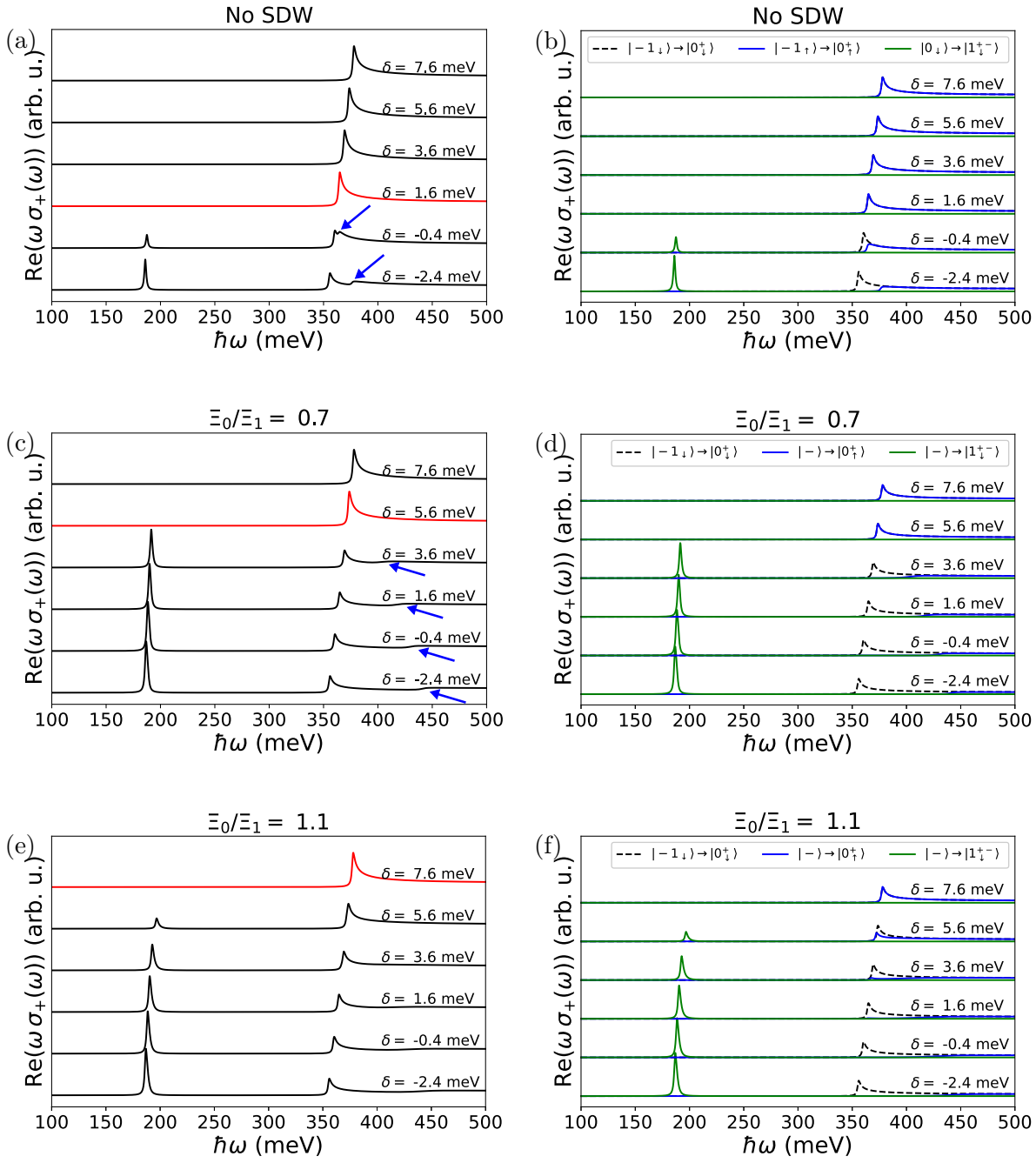

Figure 2.9: Real part of the optical conductivity in the counterclockwise polarization as a function of the bare band gap δ. (a,c,e) indicate respectively: the spectra in the case of no formation of the SDW phase, the case of a first-order phase transition ($\Xi_0/\Xi_1 = 0.7$), and the case of a second-order phase transition ($\Xi_0/\Xi_1 = 1.1$). The red spectra indicate the depopulation of the bare bands $\varepsilon_{-1\downarrow}$, $\varepsilon_{0\uparrow}$ for (a), and the spectra in the normal phase for (c,e). The arrows show particular features discussed in the text. (b,d,f) Contribution of each electronic transition to the spectra in the absence of SDW, the first-order transition, and the second-order transition, respectively.

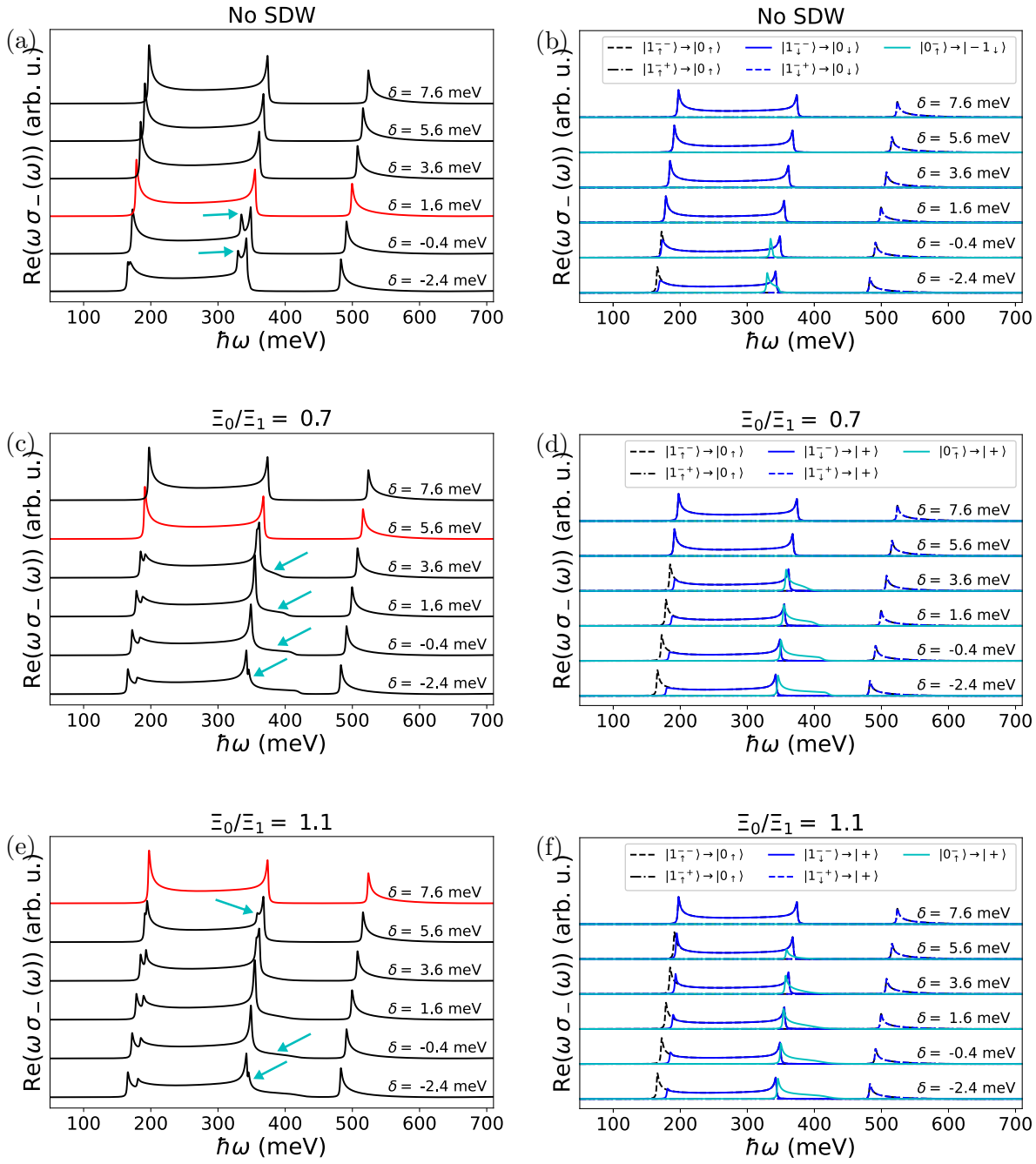

Figure 2.10: Real part of the optical conductivity in the clockwise polarization as a function of the bare band gap δ. The meaning of each sub-figure is similar as in Fig. 2.9.

2.7. Summary and Outlook

In this chapter, we presented the theoretical description of spin density waves of graphite at high magnetic fields, arising from the mixing of the $\varepsilon_{-1,\uparrow}$ and $\varepsilon_{0,\downarrow}$ bands with nesting vector $Q = \pi$. Our main objective was to identify the spectral features related to the SDW in a spectroscopic experiment. To this end, we applied the Hartree-Fock formalism to find a general solution to SDW, arriving at the set of self-consistent equations (2.32, 2.40). In general, the set of self-consistent equations can be solved numerically, however, with the aim of obtaining an analytical solution, we performed approximations to the interaction terms $\Xi_{aa}(k)$, $\Xi_{bb}(k)$, and $\Xi_{ab}(k)$, outlined in Eq. (2.58), and considered a quadratic approximation to the graphite bands, which simplify greatly the problem. With these approximations, in section 2.4 we arrived at the analytic solutions for the SDW gap and self-energy, Δ_k and Σ_k, outlined in Eqs. (2.68-2.71). Nevertheless, in section 2.4.2 we found that the energy scales of the interaction parameters Ξ_0 and Ξ_1 imply that the transition to the SDW phase is of the first order, in agreement with experimental evidence [51], invalidating our analytic solutions. Therefore, we proceeded to find a numerical solution to the simplified self-consistent problem of Eqs. (2.61, 2.62). We considered two different initial conditions for the numerical procedure and found that the SDW gap as a function of the bare-band separation δ follows a hysteresis loop, consistent with the behaviour of the order parameter in a first-order phase transition. The total energy follows a hysteresis loop as well.

The numerical solution to the SDW allowed us to obtain the SDW energy bands $\varepsilon_{\pm}$. With this information, as well as the approximation to the Landau bands of graphite at high magnetic fields in Eqs. (2.17, 2.19), we numerically calculated the optical conductivity in the SDW and normal phases. We focused on the spectra in the clockwise and counterclockwise circular polarization because they limit the transition rules between the levels. We identified electronic transitions that are enhanced and others that are diminished by the SDW phase, and by studying their shape and evolution as the band gap δ increased, we determined how the SDW phase manifests in the optical spectra. Of the enhanced electronic transitions, the strongest is $|-_k\rangle \rightarrow |1^{+-}_{\downarrow k}\rangle$ close to 190 meV, active in the counterclockwise polarization. It arises due to the mixing of the $\varepsilon_{-1\uparrow}$ and $\varepsilon_{0\downarrow}$ bands in the SDW phase, the degree of mixing given by the parameter ϑ_k, which leads to a partial occupation of the $\varepsilon_{0\downarrow}$ band. This spectral feature disappears suddenly in the normal phase if the phase transition is of the first order, but in the absence of SDWs or in a second-order phase transition, the intensity of the peak decreases gradually, as observed in Fig. 2.9. The SDW phase also manifests in the intensity reduction and change in the shape of certain spectral features, as evidenced in Figs. 2.9, 2.10. In our study, we used the following estimations for the relevant physical parameters: $\tilde{\varepsilon} = 200$ for the effective dielectric constant, $\Xi_1 = 70$ meV and $\Xi_0 = 0.7\Xi_1$ for the interaction terms. Although their precise value will affect the SDW gap Δ_k, the energy scale of the SDW bands, and the energies at which the optical transitions are found, we believe that the model we developed captures the main characteristics of the spectral features of the SDW state of graphite at $B \sim 75$ T.

Finally, it is worth mentioning that to this date, there is no consensus on the precise electronic ground state of graphite at high magnetic fields and low temperatures. We explored in detail the spectroscopic signature of the SDW state arising from the nesting of the bands $\varepsilon_{-1\uparrow}$ and $\varepsilon_{0\downarrow}$, but other possibilities are the coexistence of intraband charge-density wave states arising from the nesting within each band $\varepsilon_{-1\uparrow}$ and $\varepsilon_{0\downarrow}$, with nesting vector $2k_F$, or the excitonic insulator phase, which consists of the bound state of an electron in the band $\varepsilon_{0\downarrow}$ and a hole in the band $\varepsilon_{-1\uparrow}$. Each of these phases modifies the lowest-lying graphite bands in different ways, thus having different spectroscopic signatures that are worth investigating.

3. Weak Localization in Graphene Measured by Sub-THz Spectroscopy

Electric resistance in metals arises from the scattering of their charge carriers with different system constituents, such as crystal impurities, charged or magnetic impurities, other carriers, and phonons [65, p. 36][43, p. 6]. The classical model of electron conductivity, the Drude-Sommerfeld model, considers that there is an average time between scattering events that characterize the main transport properties of the system, called the relaxation time or transport time [43, p. 6]. In this approximation, scattering is a Markovian process, i.e., its dynamics are not affected by previous scattering events, and quantum effects do not play an important role in electron conductivity [65, p. 209]. However, at low temperatures, inelastic scattering events, like inelastic electron-electron or electron-phonon scattering, have a longer characteristic time than elastic scattering with impurities [66, p. 4]. Since inelastic scattering does not conserve the phase of the electron wave function, electron conductivity is dominated by phase-conserving elastic scattering processes, and transport becomes coherent: charge carriers having identical phases can exhibit quantum-mechanical interference after several scattering events, provided that there are no processes that break the time reversal invariance [66, p. 4]. In this context, weak localization (WL) is a phenomenon that arises from the constructive interference of self-intersecting scattering trajectories [67], which leads to a measurable decrease in electron conductance or an increase in electron resistance. In materials with strong spin-orbit coupling, the interference is destructive and leads to an increase in electron conductance; the phenomenon is then called weak antilocalization (WAL). Since an external magnetic field breaks the time-reversal invariance, it also affects WL by restoring the classical conductivity result.

Regarding coherent transport, graphene is peculiar because it can exhibit both WL and WAL [7, 68]. Due to the Berry phase of graphene, there is a phase difference of π in the opposite ways an electron can follow a self-crossing trajectory (Fig. 3.1), favoring destructive interference and leading to WAL [69]. However, intervalley scattering due to atomically sharp defects in the graphene crystal, such as vacancies, restores WL [7, 69]. WL is typically measured in direct-current (DC) magnetotransport experiments, and it manifests as a decrease in the conductivity at low magnetic fields compared to the classical prediction of the Drude-Sommerfeld model. It is also manifested in the alternating-current (AC) conductivity by measuring the optical absorption in a magneto-optical spectroscopic experiment, as has been done in graphene in the microwave frequency range ($\sim$10 GHz) [70]. Such frequency range is small compared to the typical values of the transport scattering rate $\tau^{-1} \sim 1/(0.05\text{ ps}) \sim 20000$ GHz, or the characteristic rates of dephasing in graphene at $T = 1 - 100$ K, being of the order of $\tau_\varphi^{-1} \sim 1/(0.1-10\text{ ps}) \sim 100-10000$ GHz [71]. Therefore, microwave radiation in low frequencies does not play an important role in the dephasing dynamics, and the WL effect can be analyzed by the WL theory in the DC limit [70]. At frequencies much higher than the dephasing rate, the main dephasing mechanism is the action of the external electromagnetic field, and the dephasing rate τ_φ^{-1} is replaced by the frequency ω [65, p. 214]. However, at frequencies comparable to the dephasing rate, the picture is more complex, and to the best of our knowledge, there are no experimental studies of WL in graphene in this regime.

In this chapter, we present experimental results of WL measurements on three graphene samples, performed in a magneto-optical setup in the frequency range $95 - 350$ GHz. We characterized the transport properties of the samples by DC conductivity, X-band spectroscopy, and sub-THz spectroscopy, extracting the main transport properties. Analysis of WL by DC magnetotransport and X-band spectroscopy revealed that the dephasing rate is in the sub-THz range, and sub-THz spectroscopy showed that the WL signal has a frequency dependence not observed before.

I gratefully acknowledge everyone who contributed to the results presented in this chapter. Thanks to Dr. Oleksii Laguta from CEITEC, who provided guidance with DC transport and sub-THz spectroscopy measurements and performed the X-band spectroscopy measurements at the Institute of Physics of the Czech Academy of Sciences in Prague, Czech Republic. To Ing. Valentyn Laguta, DrSc., for giving us access to his laboratory in the aforementioned institute, where X-band spectroscopy was carried out. Dr. Vinicius T. Santana from CEITEC for his enormous support during Sub-THz spectroscopy experiments and their analysis. To Dr. Kurt D. Gaskill for providing the graphene samples and for many enlightening discussions. Finally, special thanks to doc. Ing. Petr Neugebauer, Ph.D., for his continuous support, guidance, and supervision in the ongoing development of this project.

3.1. Theoretical Background

The calculation of the quantum correction to the conductivity due to coherent transport, both in the general case of an ordinary conductor and in the particular case of graphene, requires the methods of quantum field theory [7, 67, 68]. Instead of introducing these formalisms, in this section, we follow and reproduce the arguments exposed by Abrikosov in Ref. [65, p. 209] that allows us to obtain the order of magnitude of these corrections, with the advantage of gaining a clear physical picture of the origin of these effects. This serves as a justification for introducing the result in graphene and extending it to the case of AC conductivity.

3.1.1. Weak Localization in an Ordinary Conductor

First, let us consider the problem of electron scattering from impurities in an ordinary conductor in the absence of an external magnetic field. Suppose that an electron moves from point A to point B while being scattered by impurities. The electron can achieve this by following several different trajectories, each with a probability given by $|A_i|^2$, being A_i, the probability amplitude of a given trajectory. According to quantum mechanics, the total probability of going from A to B is not the sum of the probabilities of each trajectory but rather the squared norm of the sum of all probability amplitudes:

$$W = \left| \sum_i A_i \right|^2 = \sum_i |A_i|^2 + \sum_{i \neq j} A_i A_j^*. \tag{3.1}$$

The first term is the sum of the probabilities of all paths, while the second term represents the interference between trajectories. For most trajectories, the interference term is not important since their length varies greatly between each other, in such a way that changes in the wave function phase

$$\Delta\varphi = \hbar^{-1} \int_A^B \boldsymbol{p} \cdot d\boldsymbol{l} \tag{3.2}$$

differ greatly between trajectories. In consequence, the interference term vanishes when adding over all the different trajectories due to its random nature. Nevertheless, certain trajectories give a non-vanishing contribution to the total probability. They are self-intersecting trajectories in

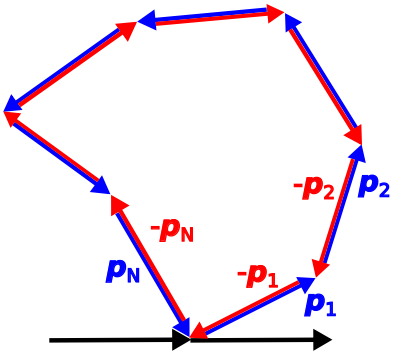

Figure 3.1: Example of a self-intersecting trajectory with a non-zero contribution to the interference correction to the conductivity. Two opposite ways to follow the trajectory are shown in blue and red, with changes in the momentum generated by elastic scattering events.

which the electron can travel in two ways differing in the direction of motion through the closed loop (Fig. 3.1). Supposing that the counterclockwise direction of motion has a phase difference given by Eq. (3.2), the phase of the clockwise direction is found by inverting the direction of the momentum ($\boldsymbol{p} \to -\boldsymbol{p}$) and the path element ($d\boldsymbol{l} \to -d\boldsymbol{l}$), yielding the same result. Therefore, the probability amplitudes are coherent, i.e., they have the same phase, and the probability of the self-intersecting trajectory is

$$|A_1 + A_2|^2 = |A_1|^2 + |A_2|^2 + A_1 A_2^* + A_1^* A_2 = 4|A_1|^2, \tag{3.3}$$

that is, twice as large as upon the addition of probabilities. This increase in the scattering probability leads to an increase in the resistivity, or a decrease in the conductivity, and is the origin of WL.

We now proceed to estimate the order of magnitude of the interference correction to the DC conductivity. The value of the conductivity correction relative to the total conductivity is proportional to the probability of the self-crossing trajectory. For a point particle in a classical motion, such probability is zero, but the electron trajectory must be treated as a tube of finite thickness equal to the wavelength $\lambda \sim \hbar/p_\mathrm{F}$, with p_F the electron's Fermi momentum. Since the electronic motion is diffusive due to scattering with impurities, after a time t, the electron covers a distance $\sqrt{x^2} \sim (Dt)^{1/2}$, with D the diffusion coefficient of the system. For self-intersection to occur during a time interval dt, it is required that the final point of the electron's path enter the volume element $v\,dt\,\lambda^2$, with v the electron's velocity. The total probability of a self-intersected trajectory is then the ratio between such volume element and the volume covered by the diffusive trajectory, $(Dt)^{d/2}\,b^{3-d}$, with $d = 1,2,3$ the dimension of the sample, and b the sample thickness in the case of a thin film ($d = 2$), or the sample thickness and width in the case of a thin wire ($d = 1$), which is assumed small compared to the coherence length introduced below. The relative conductivity is then found by integrating the total probability over time,

$$\frac{\Delta\sigma}{\sigma} \sim -\int_\tau^{\tau_\varphi} \frac{v\lambda^2\,dt}{(Dt)^{d/2}\,b^{3-d}} \sim -\frac{v\lambda^2}{D} \times \begin{cases} b^{-2}[(D\tau_\varphi)^{1/2} - (D\tau)^{1/2}], & \text{if } d = 1, \\ b^{-1}\ln(\tau_\varphi/\tau), & \text{if } d = 2, \\ [(D\tau)^{-1/2} - (D\tau_\varphi^{-1/2})], & \text{if } d = 3. \end{cases} \tag{3.4}$$

The lower integration limit, τ, corresponding to the transport characteristic time, was chosen since it is the point from which the electronic motion can be considered diffusive. The upper limit, τ_φ, is the time at which coherence is lost due to inelastic scattering with electrons or phonons, and is referred to as the dephasing characteristic time. The last equation can be put in a more convenient form by defining the dephasing length as $L_\varphi = (D\tau_\varphi)^{1/2}$, also by considering $\tau \sim l/v$ and $D \sim lv$, with l the electron's mean free path, and making use of the conductivity estimation for free electrons

$$\sigma = \frac{ne^2\tau}{m} \sim \frac{ne^2 l}{p_{\mathrm{F}}} \sim \frac{e^2 p_{\mathrm{F}}^2 l}{\hbar^3} \sim \frac{e^2 l}{\hbar\lambda^2}, \tag{3.5}$$

with $n = p_{\mathrm{F}}^3/(3\pi^2\hbar^3)$ the electron density. With this in mind, the conductivity correction acquires the form

$$\Delta\sigma \sim -\frac{e^2}{\hbar} \times \begin{cases} b^{-2}(L_\varphi - l), & \text{if } d = 1, \\ b^{-1}\ln(L_\varphi/l), & \text{if } d = 2, \\ (l^{-1} - L_\varphi^{-1}), & \text{if } d = 3. \end{cases} \tag{3.6}$$

Since at low temperatures the dephasing length is expected to be much higher than the transport length ($L_\varphi \gg l$), the interference correction is small in a three-dimensional sample. However, the correction becomes more relevant for a sample of one and two dimensions, being of the same order of magnitude as conductivity corrections from electron-electron interactions for $d = 2$, and the dominant correction term for $d = 1$ [65].

An external magnetic field modifies the interference correction. In this situation, the momentum is modified by the Peierls substitution $\boldsymbol{p} \to \boldsymbol{p} + e\boldsymbol{A}$. In the self-crossing trajectory discussed above, it was noted that the momentum $\boldsymbol{p}$ changes its sign depending on the direction of motion along the closed loop; however, the vector potential $\boldsymbol{A}$ does not change the sign. As a result, phase coherence is lost and interference in the self-crossing trajectory is destroyed. Another way of interpreting the effect of the external magnetic field is by noticing that it does not conserve the time-reversal symmetry. Therefore, the clockwise and anticlockwise directions along the closed loop, which may be regarded as time-reversed counterparts, are not equivalent anymore with regards to the phase change, hence losing coherence. Nevertheless, this coherence loss does not eliminate WL suddenly as the magnetic field is applied, rather, there is a continuous transition from WL to the classical magnetoconductivity as the field is increased.

To compute the order of magnitude of the correction in a magnetic field, consider the phase difference between the clockwise and anticlockwise directions of the self-intersecting trajectory

$$\Delta\varphi_B = \frac{2e}{\hbar}\oint \boldsymbol{A}\cdot d\boldsymbol{l} = \frac{2e}{\hbar}\int (\nabla\times\boldsymbol{A})\cdot d\boldsymbol{S} = 2\pi\frac{\Phi}{\Phi_0}, \tag{3.7}$$

with Φ the magnetic flux across the loop and $\Phi_0 = \pi\hbar/e$ the flux quantum. If we consider that the diffusion length $l = (Dt)^{1/2}$ is the typical size of the loop, then the magnetic flux across the loop is $\Phi \sim Bl^2 = BDt$. Defining τ_B as a characteristic field such that the phase difference in Eq. (3.7) is $\Delta\varphi_B \sim 2\pi$, we find

$$\tau_B \sim \frac{\Phi_0}{BD} = \frac{\pi\hbar}{eBD} \sim \frac{l_B^2}{D}, \tag{3.8}$$

with $l_B = \sqrt{\hbar/(eB)}$ the magnetic length. Then the order of magnitude of the conductivity correction is found from Eq. (3.4) by replacing the transport time τ by τ_B, obtaining

$$\sigma(B) - \sigma(0) \sim -\frac{e^2}{\hbar} \times \begin{cases} b^{-1}\ln\left(\dfrac{eBD\tau_\varphi}{\hbar}\right), & \text{if } d = 2, \\ \left(\dfrac{eB}{\hbar}\right)^{1/2}, & \text{if } d = 3. \end{cases} \tag{3.9}$$

This estimation is valid in the limit $\tau_B \ll \tau_\varphi$ and for weak fields obeying $\Omega\tau \ll 1$, with $\Omega = eB/m$ the Larmor frequency [65].

3.1.2. Theory of Weak Localization in Monolayer and Bilayer Graphene

In monolayer and bilayer graphene, the conductivity correction due to coherent transport considers several subtleties related to their band structure and the nature of the defects present in

the material. In monolayer graphene, electrons traveling in opposite directions of a self-crossing trajectory acquire an additional phase difference of π due to the non-trivial Berry phase [7, 69]. This implies that the probability of Eq. (3.3) vanishes due to destructive interference, and in consequence, electrons in monolayer graphene would tend to delocalize rather than localize in the presence of disorder, thus exhibiting WAL behavior. In bilayer graphene, a Berry phase of 2π implies that the correction to the conductivity is always of the WL type [7]. However, this picture is changed when considering how different impurities affect electron scattering. If the range of the scattering potential generated by the impurity is larger than the lattice constant $a = 1.42$ Å, the electron's valley state is unaffected after scattering [69]. This is the case of conventional impurities, such as charged dopants in the substrate, and the scattering is called "long-range" although distances of the order of a lattice constant are sufficient [69]. The second type of impurity generates an interaction potential of a range smaller than a lattice constant that can change the valley state [69]. This so-called intervalley scattering is generated by atomically sharp impurities, such as crystal vacancies, and has the effect of restoring the WL behavior in monolayer graphene [7]. Intervalley scattering is also present in bilayer graphene, keeping the conductivity correction of the WL type. The presence of intervalley scattering is so relevant for coherent transport in monolayer and bilayer graphene, that its absence results in neither WL nor WAL due to trigonal warping of the band structure [7, 68], which have a decoherence effect owing to the asymmetric band dispersion.[1]

The WL correction to the conductivity in monolayer graphene is [7, 68]

$$-\Delta\sigma_{xx}^{(\mathrm{ML})} = \frac{\Delta\varrho_{xx}}{\varrho^2} = \frac{\varrho_{xx}(B)-\varrho_{xx}(0)}{\varrho^2(B)} = -N\left[F\left(\frac{B}{B_\varphi}\right) - F\left(\frac{B}{B_\varphi+2B_i}\right) - 2F\left(\frac{B}{B_\varphi+B_*}\right)\right], \tag{3.10}$$

and for bilayer graphene,

$$-\Delta\sigma_{xx}^{(\mathrm{BL})} = \frac{\Delta\varrho_{xx}}{\varrho^2} = -N\left[F\left(\frac{B}{B_\varphi}\right) - F\left(\frac{B}{B_\varphi+2B_i}\right) + 2F\left(\frac{B}{B_\varphi+B_*}\right)\right], \tag{3.11}$$

(notice the change of sign in the last term,) with ϱ and ϱ_{xx} the total and longitudinal resistivity, $N = e^2/(\pi h)$,

$$F(z) = \ln(z) + \psi\left(\frac{1}{2}+\frac{1}{z}\right), \tag{3.12}$$

and ψ the digamma function, B_φ, B_i, B_* are the characteristic magnetic fields for dephasing, intervalley, and long-range scattering events, which are related to the characteristic lengths and times by $B_X = \hbar/(4eL_X^2) = \hbar/(4eD\tau_X)$, with $X = \varphi,i,*$, and $D = v_F^2\tau/2$ the diffusion coefficient. Taking into account that the digamma function has the asymptotic behavior

$$\psi(z) \sim \ln z - \frac{1}{2z}, \qquad \text{for } |z| \to \infty \tag{3.13}$$

it can be proven that in the limits $B \gg B_i, B_* \gg B_\varphi$ ($\tau_B \ll \tau_\varphi$), the correction to the conductivity in monolayer graphene takes the form

$$\begin{aligned}\Delta\sigma_{xx}^{(\mathrm{ML})} &\sim \frac{e^2}{\pi h}\left[\ln\left(\frac{B}{B_\varphi}\right) - \ln\left(\frac{B}{2B_i}\right) - 2\ln\left(\frac{B}{B_*}\right)\right] \\ &\sim \frac{e^2}{\pi h}\left[\ln\left(\frac{4eBD\tau_\varphi}{\hbar}\right) - \ln\left(\frac{2eBD\tau_i}{\hbar}\right) - 2\ln\left(\frac{4eBD\tau_*}{\hbar}\right)\right],\end{aligned} \tag{3.14}$$

[1] Trigonal warping is less evident in monolayer graphene with low electron density. In this case, WL and WAL tend to be suppressed in the absence of intervalley scattering by the presence of non-sharp lattice defects, such as ripples and bending of the graphene sheet [7].

which has the logarithmic dependence predicted by the semiclassical model in Eq. (3.9).

The results above are valid for the static (frequency-independent) DC conductivity. If electrons are accelerated by an AC electric field, as in the case of a microwave excitation, the frequency of the field enters as an imaginary term of the form $B_\omega = \hbar\omega/4eD$ [66, p. 30][67, 72]. The dynamic conductivity with WL corrections in monolayer graphene is rewritten as

$$\begin{aligned}\Delta\sigma_{xx}^{(\mathrm{ML})}(\omega) &= N\mathrm{Re}\left[F\left(\frac{B}{B_\varphi + iB_\omega}\right) - F\left(\frac{B}{B_\varphi + 2B_i + iB_\omega}\right) - 2F\left(\frac{B}{B_\varphi + B_* + iB_\omega}\right)\right], \\ &= N\mathrm{Re}\left[F\left(\frac{\tau_B^{-1}}{\tau_\varphi^{-1} + i\omega}\right) - F\left(\frac{\tau_B^{-1}}{\tau_\varphi^{-1} + 2\tau_i^{-1} + i\omega}\right) - 2F\left(\frac{\tau_B^{-1}}{\tau_\varphi^{-1} + \tau_*^{-1} + i\omega}\right)\right],\end{aligned} \tag{3.15}$$

the last line written in terms of the scattering rates τ_X^{-1}, with $\tau_B^{-1} = 4eDB/\hbar$. To illustrate the order of magnitude of τ_B^{-1}, for a typical diffusion coefficient of $D = 0.024$ m^2/s, we have $\tau_B^{-1} \sim 1.5$ THz at $B = 0.01$ T. In bilayer graphene, the dynamic conductivity is similar to Eq. (3.15), but with a positive sign in the third term of the right-hand side.

3.2. Experimental Methods

3.2.1. Raman Spectroscopy

The sample uniformity was inspected by Raman spectroscopy since it permits a fast, unambiguous, and non-destructive identification of the number of graphene layers [73]. The spectra were acquired with a confocal Raman microscope WITec Alpha300 R+ (WITec, Ulm, Germany). The wavelength of the laser source was 532 nm, and the power output was 7.5 mW. On each sample, an area of 10×10 m in three different places was probed in scanning mode, with the aim of obtaining the distribution of Raman spectra within the region. Each area was sampled by 20×20 points, and the spectra in each point were obtained with an exposition time of 10 s. With this procedure, the Raman maps in Fig. 3.4 (f-h) were obtained.

3.2.2. DC Transport Experiments

We investigated the transport properties of three epitaxial graphene samples of approximate size 4×4 mm^2, grown on the (0001) 6H face of SiC. Further details of sample preparation are found in Ref. [74]. The samples were not annealed prior to measurements, justified by the robustness of the electronic properties of epitaxial graphene to sample aging. To characterize the sample properties by DC transport experiments, the sample was glued to a chip expander using low-temperature varnish, and wire bonds were contacted to it in the van der Pauw configuration using silver paint or conductive paint based on carbon (Fig. 3.2). Transport measurements in two different setups, a custom-built high-frequency electron paramagnetic resonance (HFEPR) spectrometer, and a cryogen-free high field measurement system (Cryogenic ltd.). The HFEPR spectrometer operates in a temperature range of $1.9-300$ K and magnetic fields up to 16 T. More information about the spectrometer is shown in Section 3.2.4. A Keithley 2450 was employed as a device for the measurement and source of voltage and current. The Cryogenic ltd. setup employs a cryostat incorporating a cryocooler, a superconducting magnet (up to 9 T), and a variable temperature insert (VTI, temperature range $5 - 300$ K).

In the van der Pauw configuration, contacts are connected at the corners of the sample and enumerated from 1 to 4, as indicated in Fig. 3.2. The four-point resistance is measured, defined as

$$R_{12,34} = \frac{V_{34}}{I_{12}}, \tag{3.16}$$

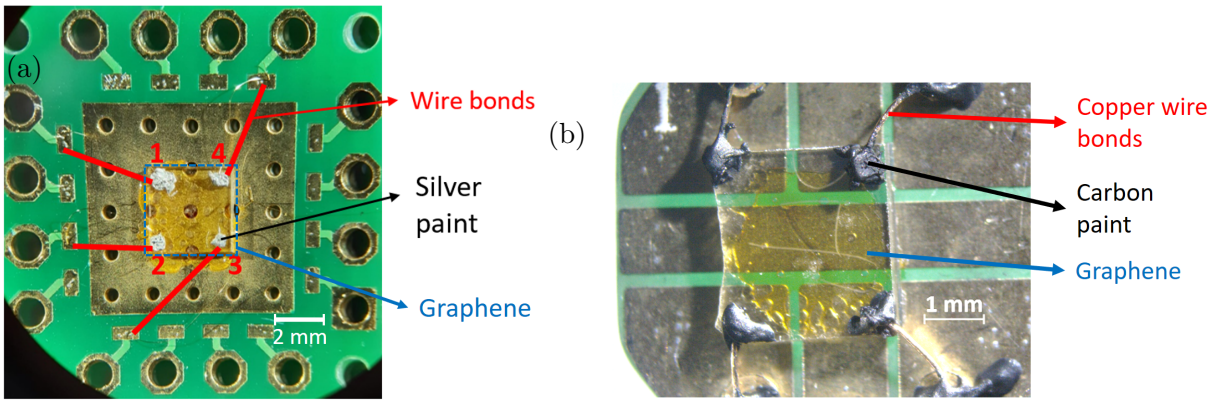

Figure 3.2: Scheme of graphene on sample holders with wire bonds in the van der Pauw configuration, used for the characterization of their transport properties. (a) Holder used in the HFEPR setup. (b) Holder used in the Cryogenic ltd. setup.

with $V_{34} = V_4 - V_3$ the voltage between contacts 3 and 4, and I_{12} a positive current injected into contact 1 and taken out of contact 2. The sheet resistance of the sample, R_s, can be found from the van der Pauw formula [75]

$$e^{-\pi R_\mathrm{v}/R_s} + e^{-\pi R_\mathrm{h}/R_s} = 1, \tag{3.17}$$

with $R_\mathrm{v} = (R_{12,34}+R_{34,12})/2$ and $R_\mathrm{h} = (R_{23,41}+R_{41,23})/2$; denoted as the vertical and horizontal resistances. The van der Pauw formula can be solved numerically to find R_S, or in the case $R_\mathrm{v} = = R_\mathrm{h} = R$, the result $R_s = \pi R/\ln 2$ can be found.

For Hall effect measurements, a constant current $I_{24} = 5$ µA is applied, and the Hall voltage $V_H = V_{13}$ is recorded as a function of the external magnetic field. We measured the Hall voltage in the magnetic field range $(-1,1)$ T and at different temperatures ranging from $1.9 - 80$ K, finding similar results as shown in the next section. The Hall voltage depends linearly on the field [76],

$$V_\mathrm{H} = \frac{IB}{en_s}, \tag{3.18}$$

with I the applied current, n_s the sheet carrier concentration, and e the electron charge. The sign of the proportionality factor between V_H and B gives the species of the majority carriers: holes if it is positive, electrons if it is negative. In general, measurements of the Hall voltage contain error terms due to the geometry of the sample, misalignment of the contacts, systematic errors, among others [77]. To correct them, measurements of the Hall voltage on different contacts, and polarizations of the current and magnetic field are necessary. Averaging the Hall voltage V_{24} at a fixed positive magnetic field and opposite current polarities gives[2] [77]

$$V_{24}^{B+} = \frac{V_{24}^{B+}(I_{31}) - V_{24}^{B+}(I_{13})}{2}, \tag{3.19}$$

in a magnetic field of negative direction we have

$$V_{24}^{B-} = \frac{V_{24}^{B-}(I_{31}) - V_{24}^{B-}(I_{13})}{2}, \tag{3.20}$$

averaging both we obtain

$$V_{24,\mathrm{H}} = \frac{V_{24}^{B+} - V_{24}^{B-}}{2}. \tag{3.21}$$

[2] In the equations, $V_{24}^{B+}(I_{31})$ means the voltage V_{24} at a positive magnetic field and a current I_{31}.

Similarly, for V_{13} we have

$$V_{13}^{B+} = \frac{V_{13}^{B+}(I_{24}) - V_{24}^{B+}(I_{42})}{2}, \tag{3.22}$$

$$V_{13}^{B-} = \frac{V_{13}^{B-}(I_{24}) - V_{24}^{B-}(I_{42})}{2}, \tag{3.23}$$

$$V_{13,\mathrm{H}} = \frac{V_{13}^{B+} - V_{13}^{B-}}{2}. \tag{3.24}$$

The final Hall voltage is found as the average of both results,

$$V_{\mathrm{H}} = \frac{V_{24,\mathrm{H}} + V_{13,\mathrm{H}}}{2}. \tag{3.25}$$

In general, conduction in a material can result from a mixture of holes and electrons. However, supposing that only one carrier species dominates the electric conduction, as is indeed the case in graphene, the mobility of the material is found as [77]

$$\mu_{\mathrm{H}} = \frac{1}{e n_s R_s}, \tag{3.26}$$

with the subindex H indicating that the mobility was found from the Hall effect. From the carrier concentration, the effective mass of carriers in graphene is found as

$$E_F = \mathrm{sign}(n_s)\,\hbar v_F \sqrt{\pi |n_s|}, \quad m^* = |E_F|/v_F^2 = \hbar\sqrt{\pi|n_s|}/v_F, \tag{3.27}$$

with E_F the Fermi energy and $v_F = 10^6$ m/s the Fermi velocity of graphene. Finally, the transport characteristic time and diffusion coefficient can be obtained from

$$\tau = \frac{m^*\mu}{e}, \quad D = \frac{v_F^2 \tau}{2}. \tag{3.28}$$

Sample characterization by DC transport is completed by analyzing the Shubnikov-de Haas oscillations (SdHO) and weak localization. In both cases, a two-point measurement of V_{12} at a constant current $I_{12} = 5$ µA was employed since the four-point measurement gave results with a low signal-to-noise ratio. Transport properties of the sample are obtained by studying the temperature and magnetic field dependence of the SdHO amplitude. The theoretical fundamentals of SdHO were outlined in Chapter 1, Section 1.3.3, where it was mentioned that the oscillatory part of the conductivity follows the Adams and Holstein formula of Eq. (1.54)

$$\frac{\Delta\sigma_{xx}}{\sigma_0} = \frac{5}{2}\sqrt{\frac{\pi e\hbar B}{E_F m^* |S''_{extr}|}} \sum_{p=1}^{\infty} \frac{1}{p^{1/2}} R_T(p) R_D(p) R_S(p) \cos\left[2\pi p\left(\frac{B_F}{B} - \gamma + \delta\right)\right], \tag{3.29}$$

with m^* the effective mass of the carrier, $|S''_{extr}|$ the second derivative of the Fermi surface cross-section perpendicular to the direction of the magnetic field, evaluated at the extremal value, and $1/B_F$ the fundamental frequency of the oscillations. The terms γ and δ are phase factors related to the Berry phase and to the curvature of the Fermi surface in the direction parallel to the field, respectively. The temperature dependence of the SdHO follows Eq. (1.55),

$$R_T(p) = \frac{\alpha m^* T/B}{\sinh\left(\alpha p m^* T/B\right)}, \tag{3.30}$$

with $\alpha = 2\pi^2 k_B/(\hbar e)$, and the damping of the oscillations given by Eq. (1.56),

$$R_D(p) = \exp\left(-\alpha p m^* \frac{T_D}{B}\right), \quad \text{with } T_D = \frac{\hbar}{2\pi k_B \tau}, \tag{3.31}$$

being T_D the so-called dingle temperature, τ the transport characteristic time, and the remaining terms having their usual meaning. The final term, R_S, is related to the Zeeman splitting of the Landau levels due to the electron's spin, it does not depend on the temperature or the magnetic field, and it is given by

$$R_S(p) = \cos\left(\frac{\pi}{2} p g \frac{m^*}{m_e}\right). \tag{3.32}$$

with g the electron's g-factor.

In Eq. (3.29), the largest contribution to the oscillations comes from $p = 1$. Therefore, discarding all terms $p > 1$ in the sum, it is found that the temperature dependence of the oscillations at a given field is

$$\frac{\Delta\sigma_{xx}(T)}{\Delta\sigma_{xx}(T_0)} = \frac{T}{T_0}\frac{\sinh(\alpha m^* T_0/B)}{\sinh(\alpha m^* T/B)}, \tag{3.33}$$

whose only undetermined parameter is m^*. At a given temperature, the magnetic field dependence of the oscillation maxima (or minima) follows

$$\ln\left[A\frac{\sqrt{B}}{T}\sinh\left(\frac{\alpha m^* T}{B}\right)\right] = -\frac{\alpha m^* T_D}{B} + C, \tag{3.34}$$

with A the oscillation amplitude, and C a constant. The plot $\ln\left[AB^{1/2}T^{-1}\sinh\left(\alpha m^* T/B\right)\right]$ vs. $1/B$ is referred to as the Dingle plot. Fitting the experimental measurements to Eqs. (3.33, 3.34) permits the determination of m^* and T_D, from which the transport time and mobility can be obtained as

$$\tau = \frac{\hbar}{2\pi k_B T_D}, \qquad \mu = \frac{e\tau}{m^*}. \tag{3.35}$$

3.2.3. Magneto-Optical Spectroscopy in the X-Band Range

Contactless measurements of electric conductivity using microwaves in the X-band frequency range ($\sim$ 10 GHz) were done in the Institute of Physics of the Czech Academy of Sciences, employing a setup for electron paramagnetic resonance (EPR) experiments. They were performed with the Bruker EPR spectrometer EMX plus operating at 9.2−9.8 GHz. An Oxford Instrument ESR900 cryostat was used for the temperature measurements range from 5 to 70 K with the stability ±0.05 K.

3.2.4. Magneto-Optical Spectroscopy at Sub-THz Frequencies

Contactless measurements of electric conductivity at sub-THz frequencies were done in a home-built magneto-optical spectrometer designed for high-frequency electron paramagnetic resonance (HFEPR) experiments (Fig. 3.3). It features a signal generator (Virginia Diodes, Charlottesville, USA), an amplifier–multiplier chain spanning a frequency range of 80−450 GHz (Virginia Diodes, Charlottesville, USA), a quasi-optical bridge (Thomas Keating, Billingshurst, UK), and a 16 T solenoid cryomagnet (Cryogenic, London, UK) with heterodyne signal detection. The sample is placed within a variable temperature insert, reaching temperatures from 1.9 K to room temperature. We employed a custom-made sample holder appropriate for electrical measurements [78]. The detection system employs the phase-sensitive magnetic field modulation method, where a weak magnetic field oscillating at a frequency f_{mod} in the kHz range is applied with the help of a small modulation coil close to the sample [79]. This results in the amplitude modulation of the measured signal, which is later demodulated to obtain the first derivative of the absorption spectrum [79]. Further information about the experimental setup and fundamentals of the HFEPR method is found in [79, 80].

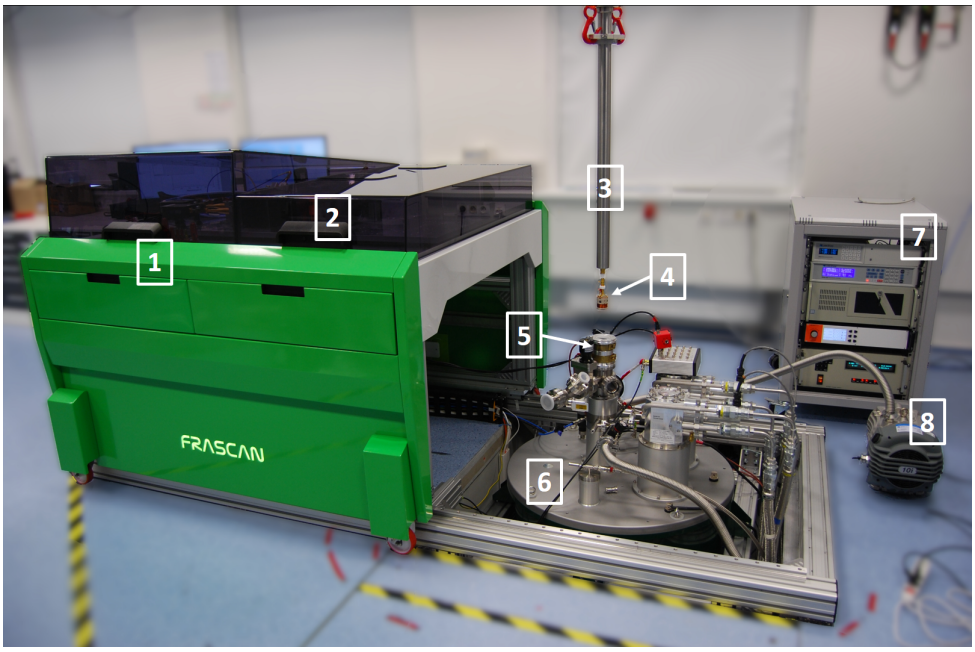

Figure 3.3: HFEPR spectrometer used for contactless measurements of electric conductivity. Indicated in the picture: (1) EPR table. (2) Covers of the quasi-optical system. (3) EPR probe. (4) Sample holder. (5) Air-lock. (6) Magnet. (7) Control console. (8) Air-lock pump. Taken and adapted from [81].

3.3. Sample Characterization by Raman Spectroscopy

Raman spectroscopy was performed to test the sample uniformity. By analyzing the position and width of the Raman peaks of the samples at different locations, one can obtain information on the number of graphene layers within the region [73, 82]. Fig. 3.4 (a-c) shows optical images of the three studied samples, taken from the optical microscope of the Raman spectrometer, and Fig. 3.4 (d,e) shows typical Raman spectra of graphene on SiC, denoted as single-point since it is taken at a specific location on the sample. The presence of graphene is confirmed by the D peak ($\sim$1340 cm^{-1}), G peak ($\sim$1580 cm^{-1}), and the 2D peak ($\sim$2680 cm^{-1}). Since the G peak has a similar location to the SiC peaks [83, 84], it is easier to perform our analysis on the 2D peak. In addition, the width of the 2D peak is the only unambiguous signature of single or multi-layer graphene that can be obtained from Raman spectra [85]. Comparing the single-point spectra of two different samples, we observe a difference in the position and width of the 2D peak: while in sample 1, it has a position of 2676 cm^{-1}, in sample 2, it is centered at 2701 cm^{-1}. This might indicate that sample 2 is composed of bilayer or multi-layer graphene, or a doped monolayer, since doping is a known factor for peak shift [82]. However, optical microscope images of sample 1 (Fig. 3.4 (a)) evidence a high amount of impurities, residues, or pores, compared to the high uniformity of sample 2. For this reason, the Raman spectra of sample 1 taken at the location of the impurity (3.4 (d)) reveal the presence of peaks in the interval $2800 - 3000$ cm^{-1} that do not correspond to graphene. We do not know the precise physical origin of these peaks, other than they are present only in the location of the impurities.

The variable location and width of the 2D peak evidence the necessity for performing scans of Raman spectra within a sample area in order to find a better comparative distribution of the peak. Fig. 3.4 (f,g,h) shows the Raman maps of the 2D peak width in a 10×10 µm^2 region of each sample. In all samples, the presence of linear regions with increased width (of the order of 40-60 cm^{-1}) is observed, which indicates the presence of two or more graphene layers grown on the substrate. This behavior is typical of epitaxial graphene grown on SiC [74, 86]. In Appendix B, we analyzed the distribution of the 2D peak position, observing that it is almost uniform in

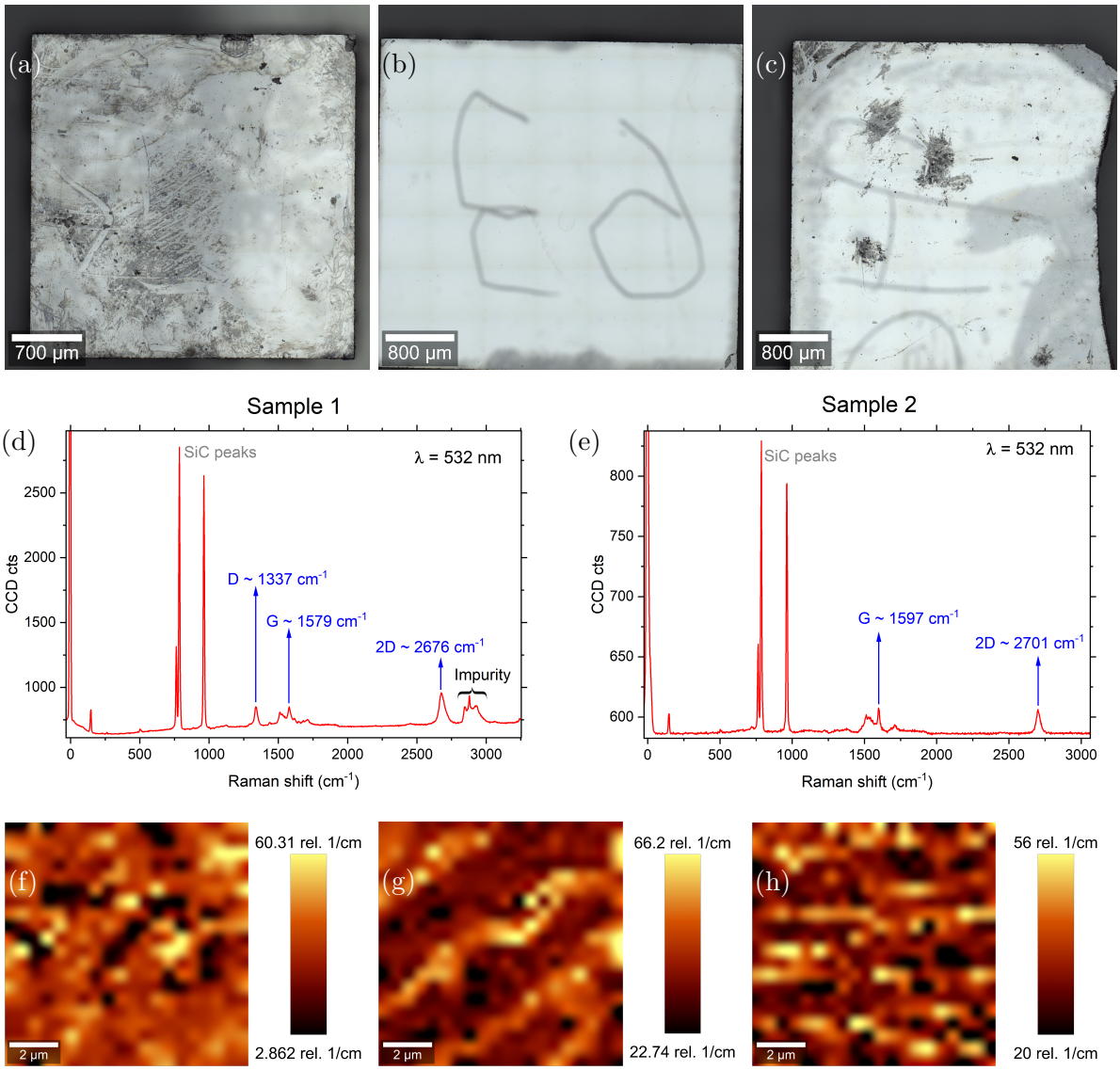

Figure 3.4: Optical microscope images of the studied samples of graphene on SiC. (a) Sample 1. (b) Sample 2. (c) Sample 3. (d) Single-point Raman spectrum of sample 1. The units of the Raman spectra are in counts in the charge-coupled device (CCD) detector of the spectrometer. (e) Single-point Raman spectrum of sample 2. (f,g,h) Raman maps indicating the width of the 2D peak in an area of 10×10 µm^2. (f) Sample 1. (g) Sample 2. (h) Sample 3.

all the samples. Finally, for all samples, we studied the presence of the impurity peaks in the interval $2800 - 3000$ cm^{-1}, and we conclude that their location in the Raman maps coincides with their location in the optical microscopy images. These results are displayed in Appendix B.

3.4. Sample Characterization by DC Transport Experiments

The electronic properties of all samples were found by studying the Hall effect and Shubnikov-de Haas oscillations in magnetotransport measurements. Samples 1 and 2 were characterized in the HFEPR spectrometer, where the magnetic field can reach up to 15 T; sample 3 was characterized on the Cryogenic ltd. setup, with fields up to 9 T. A bias current of $I = 5$ µA was applied at low temperatures of 1.9, 80 K for sample 1, 2.5 and 50 K for sample 2, and

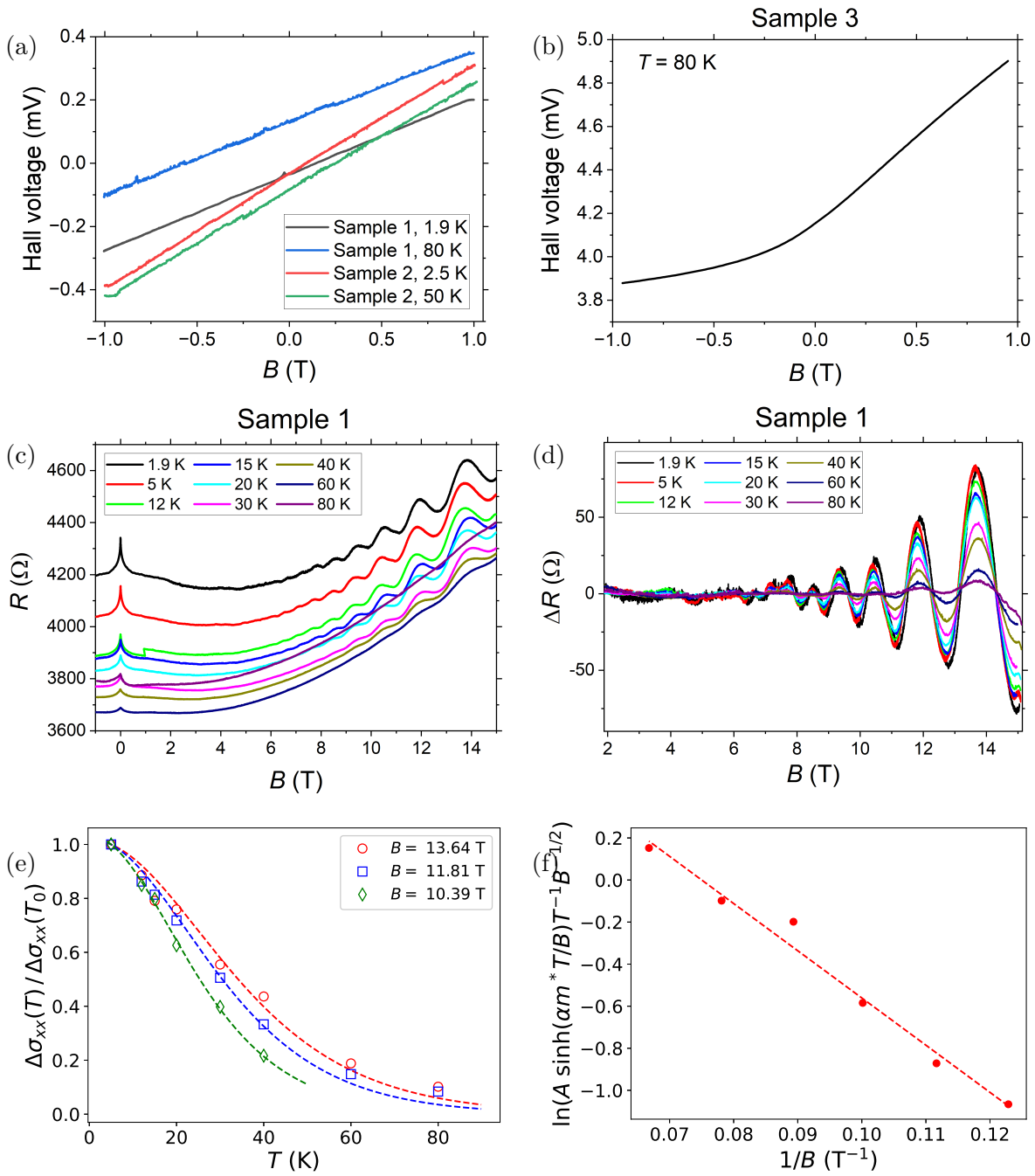

Figure 3.5: DC magnetotransport measurements on the graphene samples. (a) Hall voltage in samples 1 and 2 as a function of the external magnetic field at different temperatures. (b) Hall voltage in sample 3 exhibiting non-linear behavior. (c) Magnetoresistance R_{xx} of sample 1 in the magnetic field range studied, showing WL around $B = 0$, and SdHO at high magnetic fields. (d) Background-subtracted resistance ΔR of sample 1, showing SdHO. The background was subtracted by a window average of R_{xx}. (e) SdHO analysis of sample 1. The relative amplitude of the SdHO as a function of the temperature for three different magnetic fields. (f) Dingle plot of the SdH amplitude of sample 1 at $T = 1.9$ K.

80 K for sample 3. Uncertainties in the physical quantities were obtained using standard error propagation procedures and considering one standard deviation for the fitted parameters. We measured the sheet resistance at $B = 0$ following the procedure in Section 3.2.2, Eq. (3.17),

finding the values $R_s = (1298 \pm 2)\ \Omega$ at 1.9 K, $(521 \pm 2)\ \Omega$ at 2.5 K, and $(1851 \pm 3)\ \Omega$ at 80 K for samples 1, 2, and 3, respectively. Sample 3 exhibited a high anisotropy between the horizontal and vertical resistances, giving a ratio of $R_\mathrm{h}/R_\mathrm{v} = 0.14$. This could be due to terraces of graphene monolayers and bilayers, as Raman spectroscopy shows.

The Hall voltage as a function of the external magnetic field is displayed in Fig. 3.5 (a,b) for samples 1, 2, and 3. The Hall voltage of samples 1 and 2 showed a linear behavior, with a linear fit to Eq. (3.18) revealing a sheet carrier concentration of $n_s = (-12.89 \pm 0.03) \times 10^{12}\ \mathrm{cm}^{-2}$ at 1.9 K and $(-13.73 \pm 0.03) \times 10^{12}\ \mathrm{cm}^{-2}$ at 80 K for sample 1; $n_s = (-8.76 \pm 0.02) \times 10^{12}\ \mathrm{cm}^{-2}$ at 2.5 K and $(-9.17 \pm 0.02) \times 10^{12}\ \mathrm{cm}^{-2}$ at 50 K for sample 2; the negative sign indicating hole doping. The Hall voltage in sample 3 was non-linear, which could result from the sample anisotropy. To extract the average Hall voltages and carrier concentrations in this case, we employed the procedure outlined in Section 3.2.2, Eq. (3.25), and found an average Hall voltage of $V_\mathrm{H} = (1.022 \pm 0.002)$ mV at $B = 0.95, -0.95$ T, from which the carrier concentration $n_s = = (-2.91 \pm 0.02) \times 10^{12}\ \mathrm{cm}^{-2}$ was found. The Hall mobilities of each sample, as obtained by Eq. (3.26), are $\mu_\mathrm{H} = (373 \pm 1)\ \mathrm{cm}^2/\mathrm{Vs}$ at 1.9 K, $(1366 \pm 9)\ \mathrm{cm}^2/\mathrm{Vs}$ at 2.5 K, and $(1160 \pm 7)\ \mathrm{cm}^2/\mathrm{Vs}$ at 80 K for samples 1, 2, and 3, respectively. The significant hole doping in sample 1 places it in the limit of high doping, while the mobility is an order of magnitude lower compared to similar reported samples [71, 87]. The effective masses are estimated from Eq. (3.27), finding $m^* = (0.0737 \pm 0.0001)\, m_e$, $(0.0607 \pm 0.0001)\, m_e$, and $(0.0350 \pm 0.0001)\, m_e$ for samples 1,2, and 3, respectively, being m_e the electron's mass. From the electron mobilities and effective masses, the transport time and diffusion coefficients are obtained from Eq. (3.28), arriving at $\tau = (15.62 \pm 0.08)$ fs, (47.2 ± 0.4) fs, and (23.1 ± 0.2) fs; and $D = (7.81 \pm 0.04) \times 10^{-3}\ \mathrm{m}^2/\mathrm{s}$, $(23.6 \pm 0.2) \times 10^{-3}\ \mathrm{m}^2/\mathrm{s}$, and $(11.5 \pm 0.1) \times 10^{-3}\ \mathrm{m}^2/\mathrm{s}$ for samples 1,2, and 3, respectively.

Shubnikov-de Haas oscillations were only observed in sample 1. Two-point transport measurements with a constant bias current $I = 5\ \mu\mathrm{A}$ and at high magnetic fields revealed the onset of SdHO at $B \approx 6$ T (Fig. 3.5 (c,d)). Analysis of the SdHO amplitude as a function of the temperature allows us to estimate the effective mass of the carriers by fitting the amplitudes to Eq. (3.33). Fitting the amplitudes at three different magnetic fields (Fig. 3.5 (e)) resulted in effective mass estimation of $m^* = (0.062 \pm 0.002)\, m_e$, $(0.058 \pm 0.002)\, m_e$, and $(0.060 \pm 0.001)\, m_e$, for the fields 10.39 T, 11.81 T, and 13.84 T, respectively. Averaging these values we find an effective mass of $m^* = (0.060 \pm 0.004)\ m_e$ for sample 1. Knowing the carrier concentration $n_s = -12.89 \times 10^{12}\ \mathrm{cm}^{-2}$, the theoretical effective mass can be estimated from Eq. (3.27) as $m^* = 0.0737\, m_e$. The breakdown of the linear band approximation of graphene at high doping could explain the disagreement between the obtained values.

The analysis is completed by finding the transport characteristic time from the magnetic field dependence of the SdHO amplitude. Performing the Dingle plot, displayed in Fig. 3.5 (e), and doing a linear fit to Eq. (3.34), we find a Dingle temperature of $T_D = (25 \pm 1)$ K. From the Dingle temperature and using Eq. (3.35), it is possible to estimate the transport time $\tau = (48 \pm 2)$ ps, and mobility $\mu = (1400 \pm 20)\ \mathrm{cm}^2/(\mathrm{Vs})$. The mobility found by SdHO is four times larger than the one from the Hall effect measurement. The transport time allows us to estimate a diffusion coefficient of value $D = v_F^2 \tau/2 = (24 \pm 1) \times 10^{-3}\ \mathrm{m}^2/\mathrm{s}$.

The results for each sample are summarized in table 3.1.

Quantity	Sample 1	Sample 2	Sample 3
R_s (Ω)	1298 ± 2 (at 1.9 K) 1290 ± 2 (at 80 K)	521 ± 2 (at 2.5 K) 538 ± 2 (at 50 K)	1851 ± 3 (at 80 K)
n_s (10^{12} cm^{-2})	-12.89 ± 0.03 (at 1.9 K) -13.73 ± 0.03 (at 80 K)	-8.76 ± 0.02 (at 2.5 K) -9.17 ± 0.02 (at 50 K)	-2.91 ± 0.02 (at 80 K)
μ_{H} (cm^2/Vs)	373 ± 1 (at 1.9 K) 352 ± 1 (at 80 K)	1366 ± 9 (at 2.5 K) 1264 ± 8 (at 50 K)	1160 ± 7 (at 80 K)
μ_{SdHO} (cm^2/Vs)	1400 ± 20	-	-
m^*/m_e (from Eq. (3.27)) m^*/m_e (from SdHO)	0.0737 ± 0.0001 0.060 ± 0.004	0.0607 ± 0.0001	0.0350 ± 0.0001
T_D (K)	25 ± 1	-	-
τ (fs)	15.62 ± 0.08 48 ± 2 (SdHO)	47.2 ± 0.4	23.1 ± 0.2
D ($\times 10^{-3}$m^2/s)	7.81 ± 0.04 24 ± 1 (SdHO)	23.6 ± 0.2	11.5 ± 0.1

Table 3.1: Transport properties of each sample.

3.5. Weak Localization in DC Transport Experiments

Two-point DC magnetotransport measurements exhibited a WL signal in all samples, as shown in Fig. 3.6 (a,b) for samples 1 and 2, and Fig. B.9 (b-d) of Appendix B for sample 3. To analyze the WL behavior according to Eq. (3.10), we studied the quantity $(\varrho_{xx}(B) - \varrho_{xx}(0))/\varrho^2(B)$, with the resistivity $\varrho_{xx} = R_{xx}L/W \approx R_{xx}$, considering that the length L and width W of the two-dimensional samples were the same, as it is approximately true in our case. The total resistivity $\varrho^2 = \varrho_{xx}^2 + \varrho_{xy}^2$ was approximated to ϱ_{xx}^2 since the longitudinal resistivity is much higher than the Hall resistivity, compare for instance the maximum Hall resistivity of 80 Ω (0.4 mV at 5 µA, Fig. 3.5 (a)) with a longitudinal resistivity of 4000 Ω (Fig. 3.5 (c)). In sample 1, WL was observed at temperatures as high as 80 K (Fig. 3.5 (a)), while in samples 2 and 3, it disappeared at 40 K, being well-resolved until 30 K.

To extract the characteristic scattering lengths and rates, fittings to Eq. (3.10) were performed using the trust-region-reflective algorithm implemented in the routine `optimize.curve_fit` of scipy/python. Such a procedure allows the introduction of boundaries in the fitting parameters, which are necessary to ensure that they remain within physically reasonable values. Since satisfactory fittings with $N = e^2/(\pi h)$ were not possible, N was set as a free parameter. The value of N was determined by fitting the measurement at the lowest temperature because, in this regime, we have $L_\varphi \gg L_i$, L_* ($B_\varphi \ll B_i$, B_*), and therefore, the WL correction to the conductance is dominated by the first term within square brackets of Eq. (3.10). With this procedure, we found $N \approx 0.14\, e^2/\pi h$ for sample 1, $0.41\, e^2/\pi h$ for sample 2, and $0.076\, e^2/\pi h$ for sample 3, which were kept constant in subsequent fittings. Fig. 3.6 (a,b) shows the fittings in all temperatures, keeping B_φ, B_i, and B_* as free parameters, and Fig. 3.6 (c-f) shows the characteristic scattering lengths and rates of samples 1 and 2. It is important to mention that the parameters B_i and B_* have a very similar contribution in Eq. (3.10); thus, their results from the fitting procedure are highly correlated. Nevertheless, successful fittings were found by assuming the initial condition $B_* \gg B_i$ ($L_* \ll L_i$, $L_* = 10$ nm, $L_i = 80$ nm), which reduces their correlation and allows assigning the error to two standard deviations of the obtained parameters. For samples 1 and 2, the best fits still reflect $L_* \ll L_i$, typical of graphene samples tightly bound to an insulating substrate [7]. In sample 3, these parameters are closer in value, but the inequality $B_* > B_i$ ($L_* < L_i$) still holds (see Appendix B, Fig. B.9). The fitting results confirm that the dephasing length L_φ has a stronger temperature dependence compared to L_i and L_*, in agreement with the literature [71, 87–89]. The results for the characteristic scattering lengths and rates are in the same order of magnitude as those found in similar studies [71, 87–89].

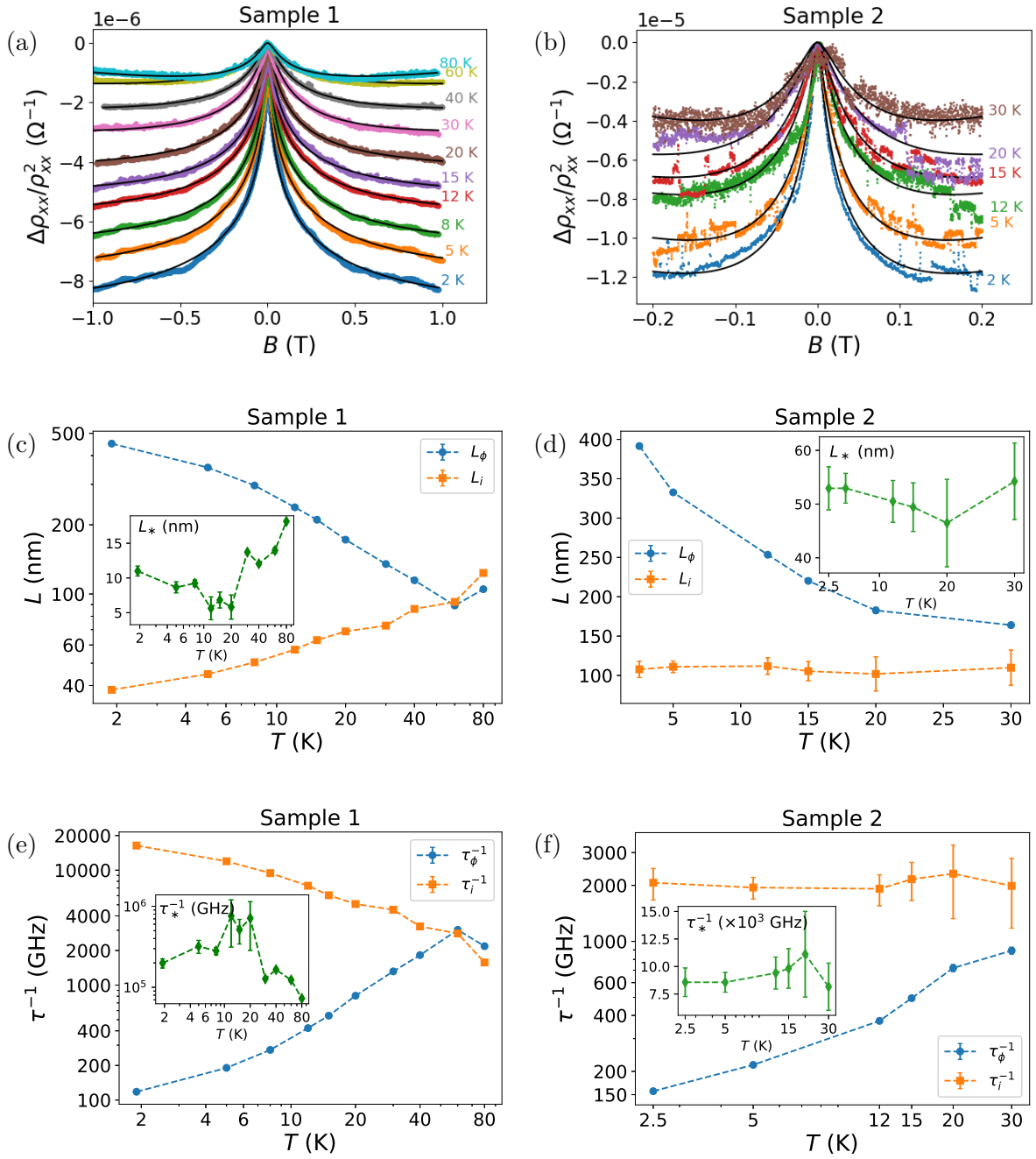

Figure 3.6: Weak localization fittings according to Eq. (3.10) in samples 1 (a) and 2 (b), black lines correspond to the fitted curves. Characteristic scattering lengths obtained from the fittings using a log-log scale for sample 1 (c) and a linear scale for sample 2 (d). Characteristic scattering rates in log-log scale for samples 1 (e) and 2 (f).

Studying the characteristic scattering rates of Fig. 3.6 (e,f), it is observed that the dephasing rate τ_φ^{-1} for all samples is of the order of $100-600$ GHz in the temperature range $1.9-20$ K. The scattering rates τ_i^{-1} and τ_*^{-1} are much higher, with τ_i^{-1} being of the same order of magnitude as the dephasing rate at 60 K in sample 1, taking a value of 3000 GHz. In samples 1 and 2, the rate τ_*^{-1} is orders of magnitude higher than τ_φ^{-1} and τ_i^{-1}, meaning that scattering by sources such as long-range charged scatterers is much more probable than intervalley scattering or dephasing events. In comparison, for sample 1, the transport rate is $\tau^{-1} = 21$ THz, with $\tau = 48$ fs

found from SdHO, which is three orders of magnitude lower than τ_*^{-1}. These results allow us to conclude that at low temperatures, WL is dominated by the dephasing characteristic rate τ_φ^{-1}, which is of the same order of magnitude as the achievable frequencies in our magneto-optical spectroscopy setup.

3.6. Weak Localization in X-band Spectroscopy

DC magnetotransport experiments demonstrated that the dephasing rate is in the sub-THz range, the same as the frequency of our spectroscopic setup. In this section, we demonstrate that a spectroscopic measurement at frequencies much lower than the dephasing rate results in a WL signal that is similar to the one found in DC magnetotransport. We measured the microwave absorption of sample 1 in the X-band frequency range ($\sim$ 10 GHz), the results are displayed in Fig. 3.7 (a). The measurements employed the lock-in method, such that the measured quantity is the derivative of the microwave absorption with respect to the magnetic field, which is proportional to the derivative of the longitudinal conductivity $d\sigma_{xx}/dB$. From the figure, it is observed that weak localization manifests as a sharp peak close to $B = 0$, superimposed on a linear background that represents the classic magnetoconductance proportional to B^2 ($d\sigma_{xx}/dB \propto B$). At such a low frequency, the measurements can be analyzed with the WL theory in the DC limit, but in this case, we work with the derivative of Eq. (3.10) with respect to the magnetic field,

$$\frac{d\Delta\sigma_{xx}^{(\mathrm{ML})}}{dB} = N\left[\frac{1}{B_\varphi}F'\left(\frac{B}{B_\varphi}\right) - \frac{1}{B_\varphi + 2B_i}F'\left(\frac{B}{B_\varphi + 2B_i}\right) - \frac{2}{B_\varphi + B_*}F'\left(\frac{B}{B_\varphi + B_*}\right)\right], \quad (3.36)$$

with a positive sign in the prefactor because we are working with conductivity, and

$$F'(z) = \frac{1}{z} - \frac{1}{z^2}\psi^{(1)}\left(\frac{1}{2} + \frac{1}{z}\right), \quad (3.37)$$

with $\psi^{(1)}(z)$ the trigamma function.

In Fig. 3.7 (b), we fitted the X-band measurements in the magnetic field range $(-0.4, 0.4)$ T after extracting the linear background, finding a good agreement with the experiment. Although the fitting was performed in a wide field range, the sharp WL feature was well reproduced, as shown in the figure. The results for the characteristic lengths and rates are displayed in Fig. 3.7 (c,d). Although showing a similar trend as those obtained in the DC measurement, the characteristic scattering lengths are generally higher, and the scattering rates are lower. At 5 K, the dephasing length is $L_\varphi = 672$ nm, being nearly twice as large as the value found in DC transport ($L_\varphi = 353$ nm), while the intervalley length has a value of $L_i = 140$ nm, compared to $L_i = 41$ nm from DC transport. At higher temperatures, the characteristic lengths for intervalley and other scattering events take an approximately constant value around $L_i = 200$ nm and $L_* = = 25$ nm, respectively. Notably, the fittings suggest a dephasing scattering rate of 50 GHz at 5 K, obtained by considering a diffusion coefficient of $D = 0.024$ m^2/s. Although higher, such a dephasing rate is of the same order of magnitude as the microwave frequency. Nevertheless, no visible change in the signal shape at low temperatures was observed, which could imply the outset of frequency dependence in the WL.

The discrepancies between the X-band and DC transport experiments could be ascribed to different electronic transport paths in each method: while in DC experiments electrons tend to follow specific paths with low resistance, in X-band measurements the microwave absorption takes place in all the sample, therefore, the whole sample is probed. Despite the quantitative inconsistencies between transport and X-band measurements, we can conclude that the theory of WL of graphene in the static case (i.e., without frequency dependence) reproduces well the spectroscopic measurements at frequencies close to 10 GHz, which are low compared to the

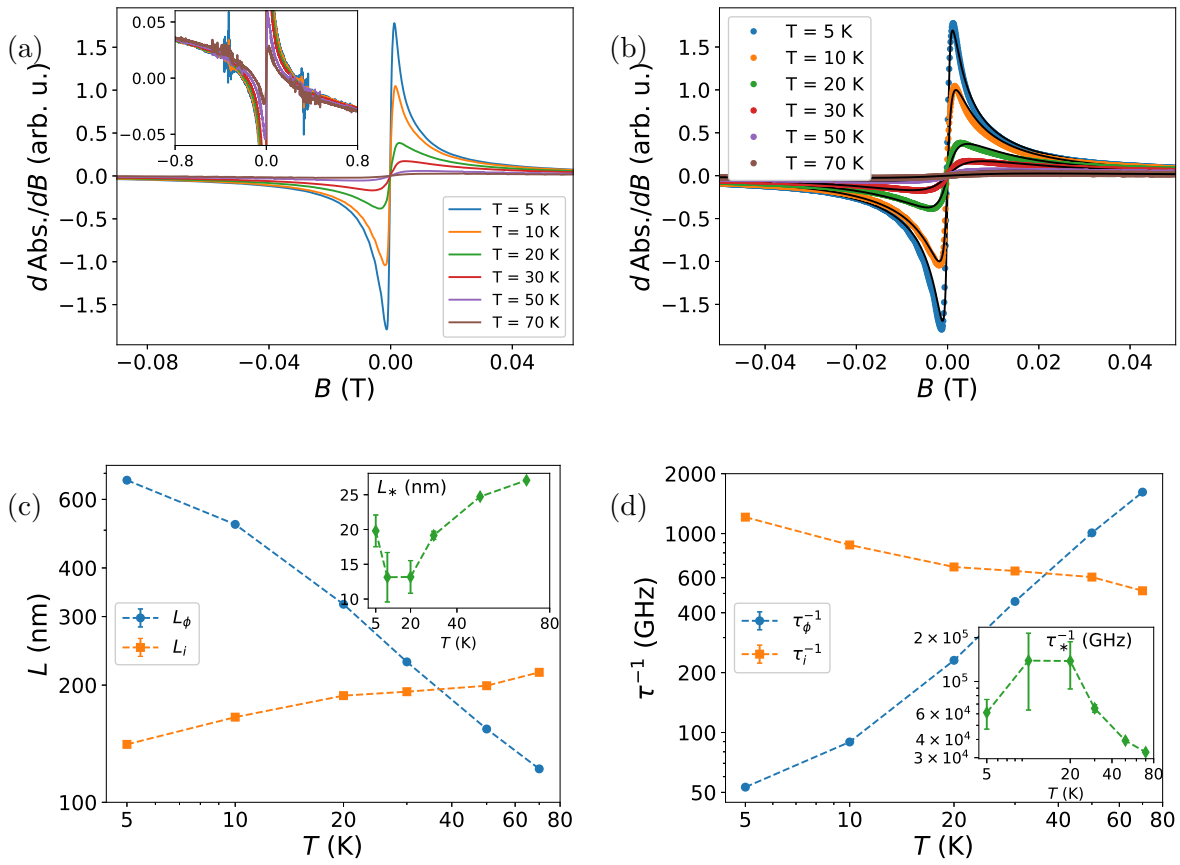

Figure 3.7: (a). X-band measurements of WL on sample 1, featuring the derivative of the microwave absorption with respect to B. The magnetic field range $(-0.08, 0.05)$ T was chosen to highlight the peak sharpness. Inset: Same measurement in the range $(-0.8, 0.8)$ T, with the range in the vertical axis chosen to display the linear background of the measurement. (b) Fittings to the WL theory in the DC limit of Eq. (3.36). Measurements are displayed as dots and fittings in black lines. (c) Characteristic lengths obtained from from the fittings. (d) Characteristic rates.

dephasing scattering rate, found to be of the order of $100 - 600$ GHz in transport measurements. A question that arises is whether it would be possible to observe changes in the WL signal as the temperatures are lowered further, in such a way that the dephasing scattering rate acquires a similar value as the microwave frequency.

3.7. Weak Localization Measured by Sub-THz Spectroscopy

The samples were investigated using sub-THz spectroscopic measurements in the HFEPR setup. The spectroscopic response is rich; we observed signals coming from vanadium impurities in the SiC substrate, SdH oscillations, WL, and possible molecular oxygen impurities, as displayed in Appendix B, Fig. B.10 (a,b). We performed continuous-wave (CW) measurements in the range $95 - 350$ GHz, in which the magnetic field is swept at a constant frequency, the results for all samples displayed in Fig. 3.8 and Appendix B, Fig. B.10 (c-f). In the figures, no data post-processing was done besides normalization and offset correction for easier visualization. The spectra have markedly different behavior compared to the DC and X-band measurements. For sample 1, the X-band spectra have only one local maximum, consistent with the first derivative of the conductivity of DC transport measurements in Fig. 3.6 (a). In contrast, Fig. 3.8

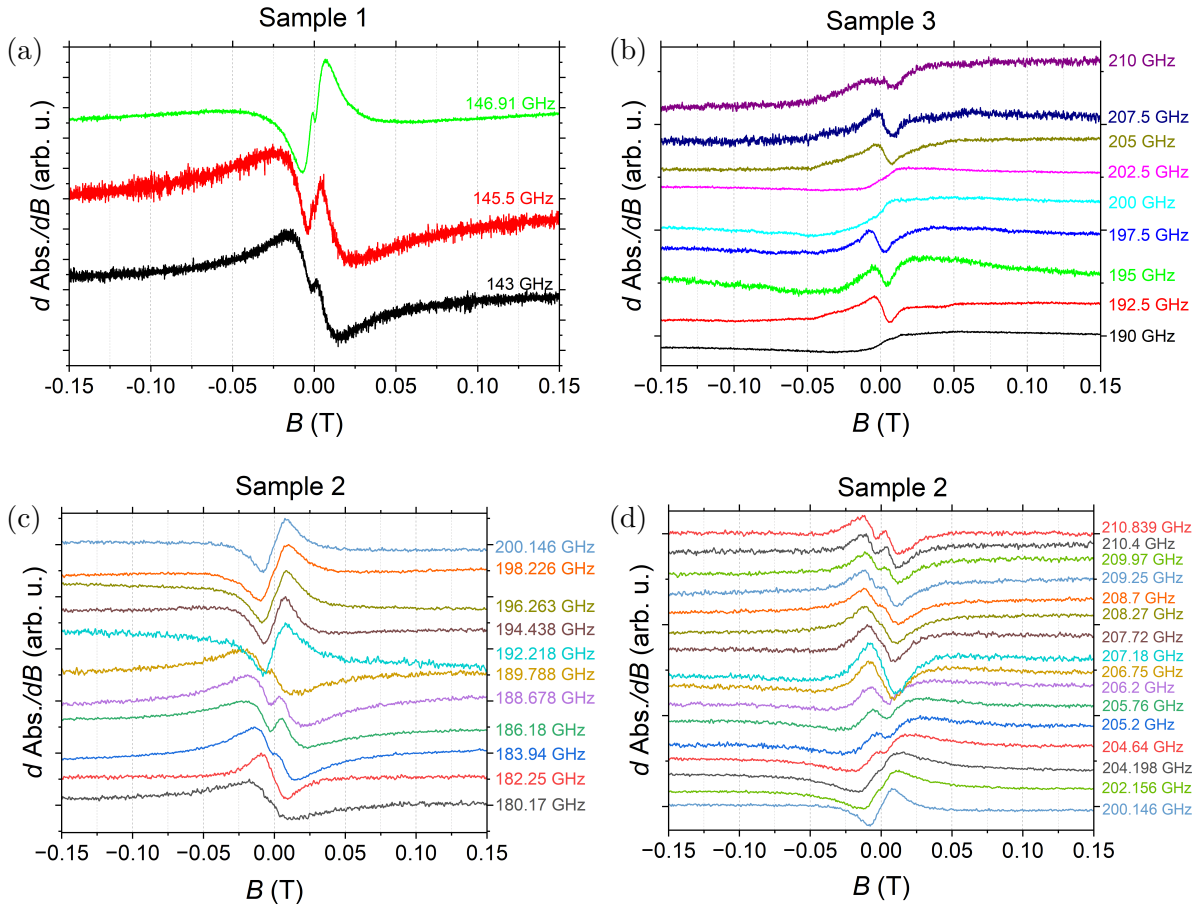

Figure 3.8: Weak localization in graphene at different sub-THz frequencies. (a) Sample 1 at 3.5 K. (b) Sample 3 at 6.7 K. (c) Sample 2 at $T \sim 5$ K, frequency range $180 - 200$ GHz. (d) Sample 2 at $T \sim 5$ K, frequency range $200 - 210$ GHz.

(a) displays two and even three local maxima, which evolve in intensity and location as the frequency increases 4 GHz. Such a peak evolution is observed in all samples and in the probed frequency range, as shown in Fig. B.10 (c-f) of Appendix B. We will focus our analysis on sample 2, as it presented the highest spatial uniformity and the lowest density of impurities. Fig. 3.8 (c,d) shows how the weak localization signal evolves in the range $180 - 210$ GHz, at a temperature of approximately 5 K. Although temperature stability could not be ensured in all measurements, and sometimes, variations of up to 2 K occur between them, we verified that it does not have a significant impact on the signal shape at that probed temperature, such that the shape is mostly affected by the microwave frequency. From the figures, it is observed that at 180.17 GHz only one local maximum is present, but as the frequency is increased, a central feature starts developing and increasing in intensity, and at 192.218 GHz becomes dominant. As the frequency increases further, the peak broadens and moves towards a higher magnetic field, until at 204.64 GHz a new peak starts developing, becoming dominant at 207.18 GHz. The cycle repeats and at 208.7 GHz a new peak develops again.

To obtain a better visualization of the frequency dependence of the WL signal, we performed spectral maps in which the signal is recorded as the microwave frequency and the magnetic field are swept continuously; the results are displayed in Fig. 3.9. The frequency was swept in intervals of 10 GHz, and the resulting maps were post-processed by subtracting the background of each individual frequency to a sixth-degree polynomial and normalizing the WL peak; this guaranteed that the absolute WL peak at all frequencies was obtained, neglecting the effects

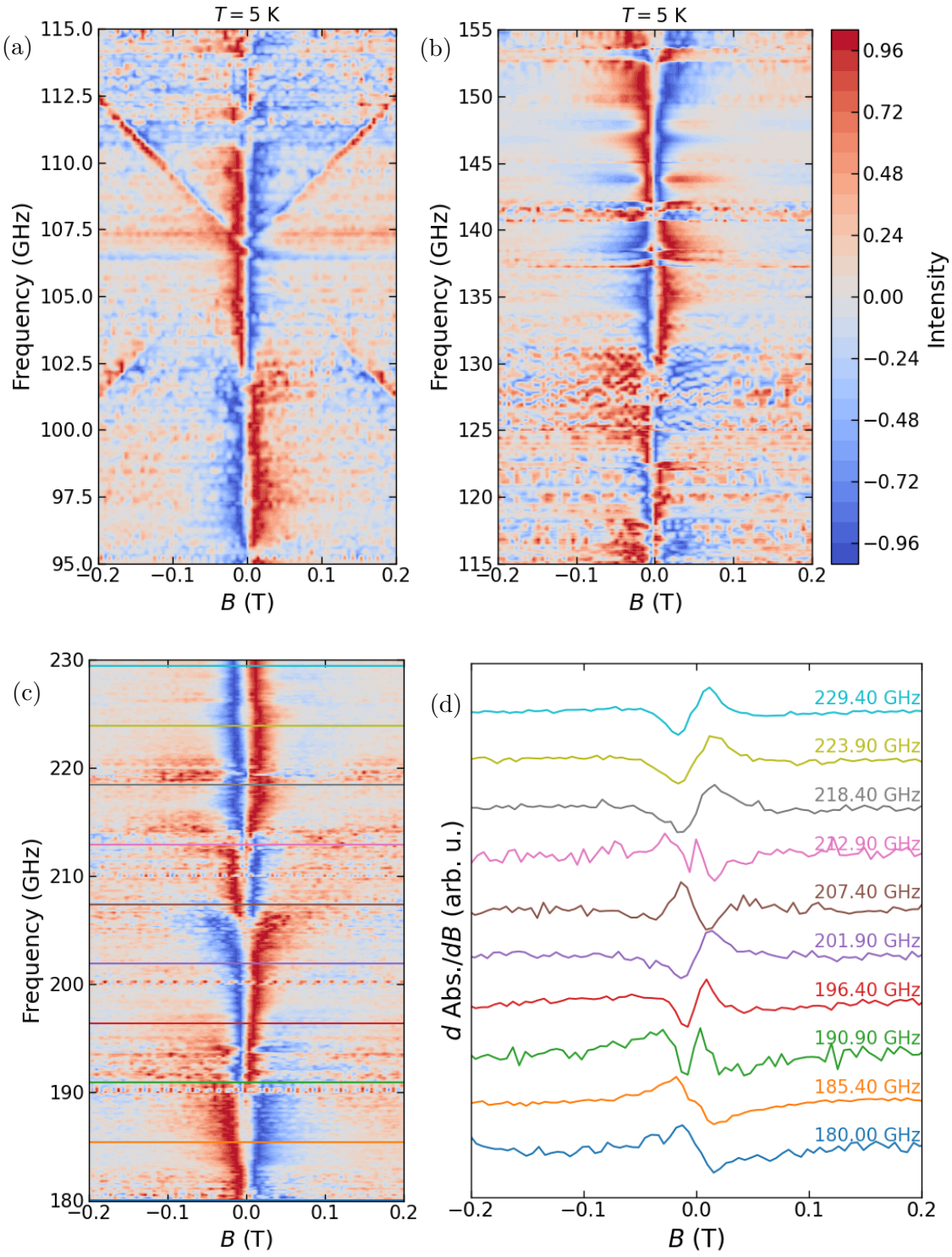

Figure 3.9: Spectral maps of weak localization in sample 2 at $T = 5$ K. (a) Frequency range $95 - 115$ GHz. (b) Frequency range $115 - 155$ GHz. (c) Frequency range $180 - 230$ GHz. The horizontal lines correspond to the selected frequencies for the spectra in (d). (d) CW spectra extracted from the map in (c).

of microwave power differences across the frequency range. The spectral map of Fig. 3.9 (c) presents a clear picture of the peak evolution outlined in Fig. 3.8 (c,d): we observe a continuous emergence and broadening of WL peaks as the microwave frequency is increased. It also allows

us to conclude that this effect is not due to temperature changes in the sample or to possible measurement artifacts introduced by the detection scheme of the spectrometer, since the peaks evolve in a consistent way over the frequency range. The disadvantage of the spectral maps is the reduced signal-to-noise ratio, as evidenced in Fig. 3.9 (a,b) for some of the probed frequencies. Nevertheless, the emergence of peaks is clearly observed in the range $95-115$ GHz, the lowest studied. Notably, Fig. 3.9 (a) reveals a signal that evolves linearly with the magnetic field and frequency, and crosses the $B=0$ axis at approximately 107.5 GHz. Such a signal could originate from the zero-field splitting of molecular oxygen impurities in the sample, which is supported by EPR resonances at higher frequencies, as shown in Appendix B, Fig. B.10 (a,b). It is possible to extract the CW spectra from the maps, as displayed in Fig. 3.9 (d) for the range $180-230$ GHz. This range partially coincides with the CW spectra of Fig. 3.8 (c,d) for the same sample, and it can be concluded that the signal shape is the same for the frequencies that can be compared directly (180 GHz, 196.4 GHz, 201.9 GHz, 207.4 GHz). This further supports our claim that the effect comes from the electronic properties of graphene rather than being induced by the experimental setup.

To analyze the experiments, we work with the derivative of the dynamic conductivity of Eq. (3.15):

$$\frac{d\Delta\sigma_{xx}^{(\mathrm{ML})}(\omega)}{dB}=\frac{4De}{\hbar}N\ \mathrm{Re}\left[\frac{1}{\tau_\varphi^{-1}+i\omega}F'\left(\frac{\tau_B^{-1}}{\tau_\varphi^{-1}+i\omega}\right)-\frac{1}{\tau_\varphi^{-1}+2\tau_i^{-1}+i\omega}F'\left(\frac{\tau_B^{-1}}{\tau_\varphi^{-1}+2\tau_i^{-1}+i\omega}\right)-\frac{2}{\tau_\varphi^{-1}+\tau_*^{-1}+i\omega}F'\left(\frac{\tau_B^{-1}}{\tau_\varphi^{-1}+\tau_*^{-1}+i\omega}\right)\right], \tag{3.38}$$

valid for monolayer graphene and in terms of the scattering rates, with $F'(z)$ defined in Eq. (3.37). For bilayer graphene, the third term on the right-hand side of the equation has a positive sign,

$$\frac{d\Delta\sigma_{xx}^{(\mathrm{BL})}(\omega)}{dB}=\frac{4De}{\hbar}N\ \mathrm{Re}\left[\frac{1}{\tau_\varphi^{-1}+i\omega}F'\left(\frac{\tau_B^{-1}}{\tau_\varphi^{-1}+i\omega}\right)-\frac{1}{\tau_\varphi^{-1}+2\tau_i^{-1}+i\omega}F'\left(\frac{\tau_B^{-1}}{\tau_\varphi^{-1}+2\tau_i^{-1}+i\omega}\right)+\frac{2}{\tau_\varphi^{-1}+\tau_*^{-1}+i\omega}F'\left(\frac{\tau_B^{-1}}{\tau_\varphi^{-1}+\tau_*^{-1}+i\omega}\right)\right]. \tag{3.39}$$

We simulated the spectra considering that the diffusion coefficient and the scattering rates do not depend on the microwave frequency and have a similar value as those obtained by DC transport at $T=5$ K: $D=0.024$ m^2/s, $\tau_\varphi^{-1}=250$ GHz, $\tau_i^{-1}=1500$ GHz, and $\tau_*^{-1}=$ $=10$ THz. The simulated spectra in frequency and field range comparable to the experimental results are shown in Fig. 3.10. As the samples are composed of monolayers and bilayers of graphene in different proportions, the simulations consider three situations: the spectra from monolayer graphene, spectra from bilayer graphene, and the sum of both in equal proportion. The latter emulates the situation in which the sample is composed of monolayer and bilayer in the same ratio, with each part contributing to the dynamic conductivity. The simulated spectra at each frequency were normalized to compare directly with the experimental results. As a first observation, monolayer and bilayer graphene spectra are qualitatively similar due to the large value of τ_*^{-1} compared to the other scattering rates, such that the dynamic conductivity is dominated by the contributions from τ_φ^{-1} and τ_i^{-1}. From the simulations, we observe that the theory reproduces some of the observed spectral features. For instance, the emergence of a narrow peak that shifts and broadens as the frequency increases, as is observed from 50 GHz in the simulated CW spectra of Fig. 3.10 (d-f). Nevertheless, the model fails to explain the rich spectroscopic features found experimentally in Figs. 3.8, 3.9. In particular, the successive

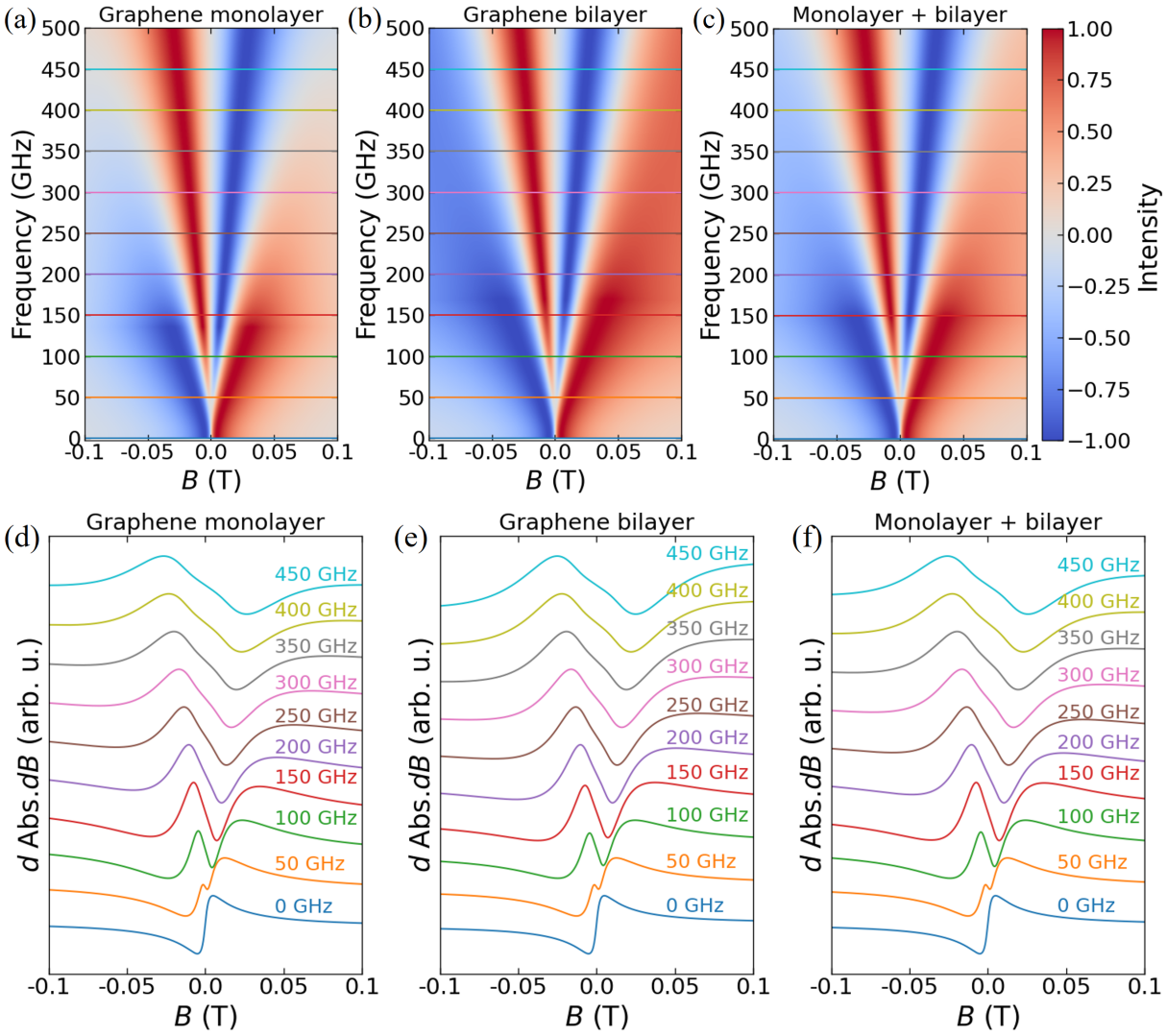

Figure 3.10: Simulated frequency maps exhibiting the frequency dependence of the WL in (a) monolayer graphene, (b) bilayer graphene, and (c) considering the signal coming from both monolayer and bilayer graphene in equal proportion. The horizontal lines correspond to the selected frequencies for the CW spectra in (d-f). Simulated CW spectra at selected frequencies, as extracted from the frequency maps, for (d) monolayer graphene, (e) bilayer graphene, and (f) the sum of monolayer and bilayer graphene contributions. In all cases, the parameters used in the simulation are $D = 0.024$ m^2/s, $\tau_\varphi^{-1} = 250$ GHz, $\tau_i^{-1} = 1500$ GHz, and $\tau_*^{-1} = 10$ THz.

emergence of several peaks in the relatively short frequency range $180 - 230$ GHz displayed in Fig. 3.9 (c), but also observed in the other ranges. In contrast, the theory only explains one of such transitions (two in the case of monolayer graphene, see Appendix B, Fig. B.12) in the much larger range of $0 - 500$ GHz. It is important to mention that different values of the scattering rates do not result in the emergence of more peaks at different frequency values; rather, they affect the peak width and rate of shift as the frequency increases.

Another possibility is to perform fittings of the CW spectra to the dynamic conductivity of Eq. (3.38), being equivalent to the assumption that the scattering rates and the diffusion coefficient acquire a frequency dependence. This can be attempted, although there is a problem of overparametrization since there are five fitting parameters (τ_φ^{-1}, τ_i^{-1}, τ_*^{-1}, D, and the normalization constant N). To simplify the fittings, we assumed that the signal comes entirely from monolayer graphene, and we reduce the parameter space by neglecting the effect of intervalley

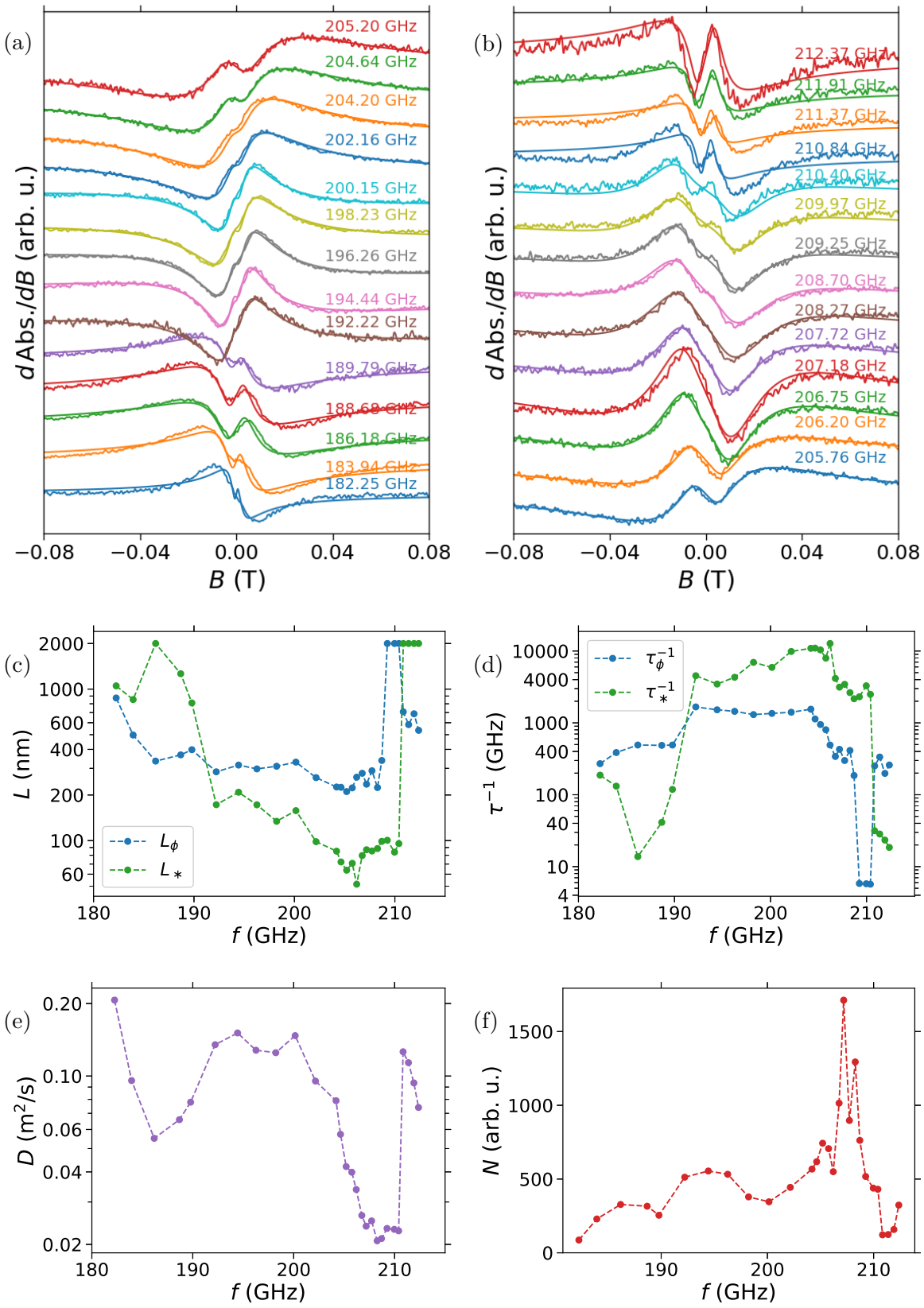

Figure 3.11: Fittings of the frequency-dependent WL signal of sample 2. The value of the intervalley characteristic field was fixed to $B_i = 10$ T ($L_i = 4$ nm). (a) Experimental signal and fittings in the range $182.25 - 205.20$ GHz. Continuous lines indicate the fitted curve. (b) Experimental signal and fittings in the range $205.76 - 212.37$ GHz. Fitting results for (c) the characteristic lengths, (d) characteristic rates, (e) diffusion coefficient, (f) normalization factor.

scattering, fixing B_i to an arbitrarily large value of 10 T ($L_i \sim 4$ nm). This effectively gets rid of the second term in Eqs. (3.15, 3.38). We justify it by the fact that although B_i and B_* have a similar effect on the dynamic conductivity, B_* is more determinant on the signal shape due to the prefactor of 2 in the function $F(z)$. We fitted the spectra of sample 3 in the range $182.25-212.37$ GHz, chosen since it presents the emergence of two peaks. The results, displayed in Fig. 3.11, show that successful fits can be obtained with reasonable values for the parameters in the majority of the frequency range. Nevertheless, discontinuities in the parameters can be found in the transition regions where a new peak emerges, as observed from 209.25 GHz, from which long dephasing and long-range scattering lengths of 2000 nm are required. (It corresponds to the maximum limit allowed in the fitting procedure.) The diffusion coefficient D presents a strong variation with the frequency as well, taking values as high as 0.2 m^2/s and dropping to more reasonable ones around 0.02 m^2/s. The diffusion coefficient also exhibits a discontinuity around 210.40 GHz, where a new peak is more pronounced. Such discontinuities in the parameters lead us to conclude that either the theoretical description of the problem at frequencies comparable to the dephasing rate is incomplete or that the samples are not uniform enough for a successful analysis. It is then necessary to perform measurements on samples with exceptional uniformity to arrive at a definitive answer to the questions arising in this study.

3.7.1. Temperature Dependence

Since the characteristic scattering lengths and rates depend on the temperature, especially the dephasing term, we investigated the temperature dependence of the dynamic conductivity. We focused on the frequency range $190-220$ GHz for sample 2, shown in Fig. 3.12, and $290-350$ GHz for sample 1, shown in Appendix B, Fig. B.13. Due to the difficulty in performing a meaningful quantitative analysis of the measurements, as evidenced in the preceding Section, we focus on a qualitative description of the results. In both samples, WL was observed at temperatures as high as 50 K, which leads us to conclude that the effect indeed arises from the robust electron coherence properties of graphene rather than originating from other sources, like the SiC substrate or induced by the HFEPR spectrometer. The most notable observation is that the frequencies at which new peaks emerge, denoting a transition in the signal shape, remain constant with temperature, as indicated by the dashed lines in Fig. 3.12. Although the precise origin of these transitions is unknown, their weak dependence on the temperature might indicate that they are not related to the dephasing rates τ_φ^{-1}, but rather to the scattering rates τ_i^{-1} and τ_*^{-1}, or have a different unidentified source. The spectral maps also indicate that the main effect of the temperature is the broadening and decrease of the WL peaks, in a similar way as observed in the X-band spectra of Fig. 3.7 (b). An updated, more complete theory of WL at high frequencies would permit a fitting of the spectra to obtain the characteristic lengths and rates, as was done for the transport and X-band measurements.

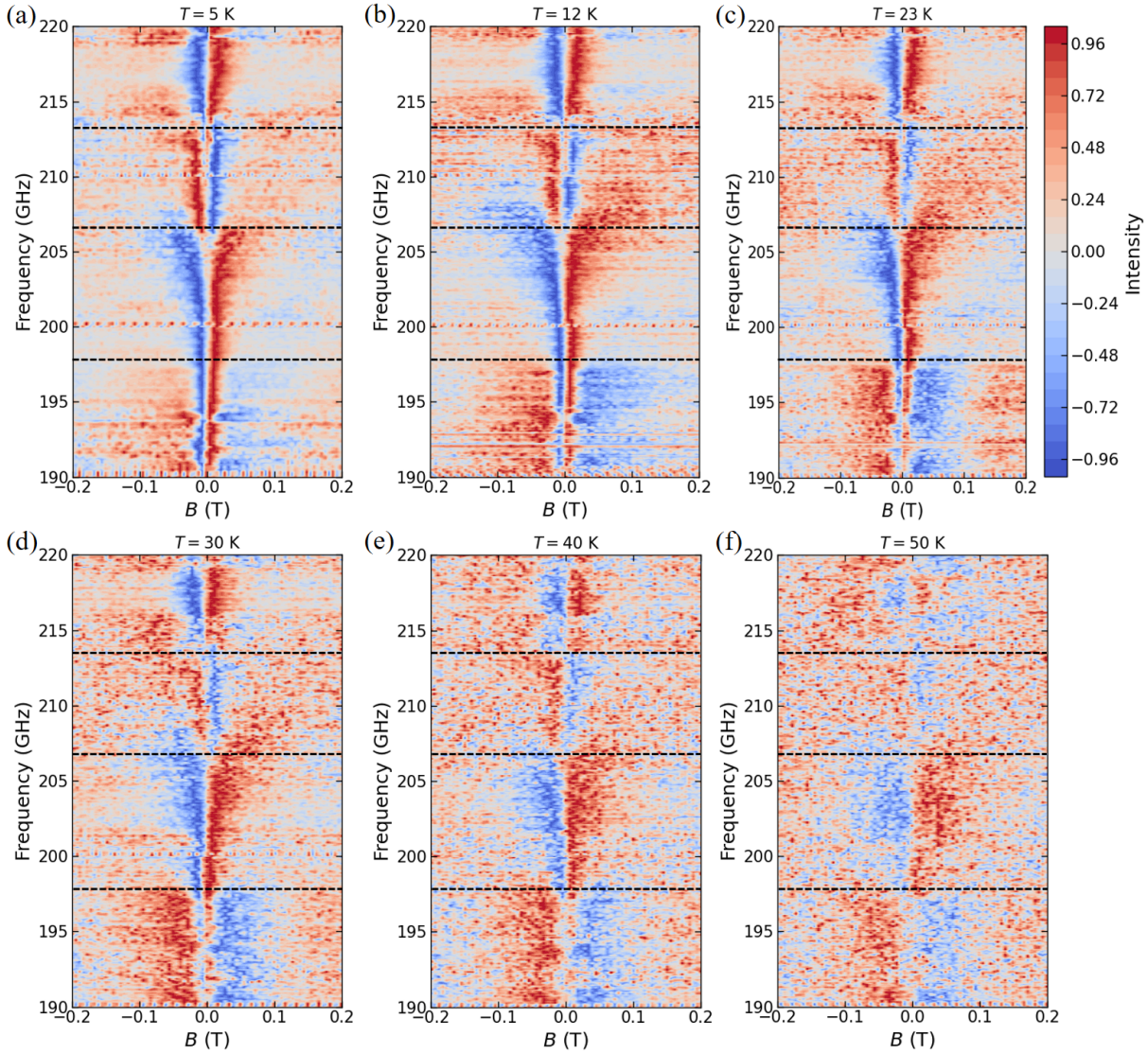

Figure 3.12: Spectral maps of WL in sample 2 at temperatures (a) 5 K, (b) 12 K, (c) 23 K, (d) 30 K, (e) 40 K, (f) 50 K. Horizontal dashed lines at frequencies 198 GHz, 206.5 GHz, and 213.5 GHz indicate transitions in the spectral shape that remain constant with temperature

3.8. Conclusions

We studied the weak localization in three epitaxial graphene samples using conventional magneto-transport measurements and magneto-optical spectroscopy. Sample characterization by Raman spectroscopy confirmed that the samples are composed of terraces of graphene monolayers and bilayers, as it is typical of epitaxial graphene on SiC, with the width of the monolayer terraces ranging from 1 to 3 µm depending on the sample. DC transport measurements revealed electron mobilities ranging from 352 to 1366 cm^2/Vs and transport characteristic times of $\tau = 48$ fs, 48 fs, and 23 fs in samples 1, 2, and 3, respectively. They resulted in transport scattering rates of the order of $\tau^{-1} \sim 20$ THz, much higher than the frequencies accessible in our spectroscopic setup. Transport measurements showed the WL signal in all samples, present at temperatures as high as 80 K in sample 1. By fitting the transport measurements to the WL theory of graphene, we obtained the characteristic lengths and rates of dephasing, intervalley scattering, and long-range scattering events. The main result from transport measurements is that the dephasing characteristic rate is in the range $\tau_\varphi^{-1} \sim 100 - 600$ GHz at temperatures $1.9 - 20$ K, achievable in our spectrometer. Our main hypothesis was that a microwave excitation at such frequencies

affects the dephasing dynamics of electrons in graphene. To test it, we employed magneto-optical spectroscopy measurements at low frequencies ($\sim$ 10 GHz) and demonstrated that the WL behavior is similar to the static (DC) case, in accordance with what was reported in the literature [70]. However, when performing measurements in the sub-THz range, the spectra of all samples exhibited a clear frequency dependence. We conclude that the spectrometer does not induce such frequency dependence due to the consistent peak emergence, shift, and broadening as the frequency increases. Additionally, the persistence of the signal at temperatures as high as 50 K confirms that it arises from graphene's robust electron coherence properties instead of, for example, other effects from the SiC substrate or induced by the experimental setup.

A quantitative analysis of the frequency-dependent WL based on Eq. (3.38) posed a substantial challenge. Considering constant values for the dephasing, intervalley scattering, long-range scattering, and diffusion coefficient parameters, the theory predicts a peak emergence, broadening, and shift towards higher magnetic fields, partially in agreement with our observations. Nevertheless, it fails to explain the emergence of several peaks in a relatively short frequency range, as observed clearly for sample 2 in the range $180-230$ GHz, but seen in the other samples as well. Allowing the parameters to acquire a frequency dependence can partially explain the observed changes in the signal shape; however, discontinuities in τ_φ^{-1}, τ_*^{-1}, and D as a function of the frequency become necessary to reproduce the peak emergence. Such discontinuous changes could be related to the assumed simplifications done to avoid overparametrization of the fittings, but nonetheless, cannot be justified in a satisfactory description of the coherent transport of electrons at frequencies comparable to the dephasing rate.

Our main conclusion is the demonstration of the frequency dependence of WL in graphene at sub-THz frequencies, which the current theoretical model of WL cannot completely explain. Despite the good quality of the studied graphene samples, corroborated by mobilities of the order of 1300 cm^2/Vs, the reduced uniformity due to the presence of monolayer and bilayer terraces of graphene on SiC introduces additional complications in the analysis, obscuring a precise explanation for the emergence of WL peaks at different sub-THz frequencies. To clarify these discrepancies, we argue that further measurements in monolayer and bilayer graphene samples with exceptional uniformity are necessary before exploring extensions to the WL theory.

4. Deposition of Tetracoordinated Cobalt(II) Single-Molecule Magnets on Graphene Studied by Ab Initio Methods

Functionalization of graphene with other systems has been suggested as an attractive route to enhance their properties, such that the guest material induces new attributes in graphene, like magnetization [90, 91], superconductivity [92], improved electrocatalysis [93], among others, while graphene acts as a substrate for the deposition of thin layers of material, bringing structural stability and tuneability. Of these systems, paramagnetic molecules with slow relaxation of magnetization [25], also known as single-molecule magnets (SMMs), are great candidates due to their remarkable properties like magnetic susceptibility hysteresis at the individual, molecular level, in contrast to the magnetic domains in ferromagnetic materials, being typically of the order of 1-100 µm [94]. For this reason, SMMs have been proposed as candidates for new technologies, such as qubits [95], high-density memory storage [96], and spintronic devices [97–99]. Nevertheless, these applications require the individual addressing and manipulation of the molecular magnetic state, which can be attained after molecular deposition on a given substrate [98]. In this context, graphene is an ideal substrate due to the non-covalent interaction with the organic ligands of SMMs, which induces low structural changes in both systems [100], while at the same time permits the readout of the molecular spin state thanks to the subtle changes in graphene's transport properties [99].

The objective of this chapter is to present a study of the deposition of selected cobalt-based SMMs on graphene by ab-initio methods such as density functional theory (DFT) and complete active space self-consistent field (CASSCF) theory, the latter complemented by N-electron valence state second-order perturbation theory (NEVPT2). Some predicted results were compared with experimental techniques such as Raman spectroscopy, electric transport measurements, atomic force microscopy (AFM), and HFEPR spectroscopy. The structure of the chapter is as follows. First, we describe the three SMMs under study, chosen due to their stability at ambient conditions and high temperatures, making them suitable for deposition on graphene by drop-cast and thermal sublimation. We briefly discuss the successful adsorption of the SMMs on graphene and their integrity after deposition, as demonstrated experimentally by XPS, Raman spectroscopy, and AFM. We show the details of the applied theoretical and experimental methods, and then we perform a theoretical study of molecular deposition on graphene by DFT, showing the structural changes and main binding mechanisms between both systems. Furthermore, we study the charge transfer between molecule and graphene by performing a Bader charge analysis [101–103] and a density of states (DOS) analysis, and show how it is related to changes in the magnetization of the SMMs; the charge transfer results being validated by Raman spectroscopy and electric transport measurements. Finally, we compute the magnetic properties of the SMMs by CASSCF-NEVPT2 and broken symmetry density functional theory (BS-DFT), in particular, the g-factors, magnetic anisotropy parameters D and E, and the intermolecular exchange interaction J, comparing them with the experimental values obtained by DC magnetometry and HFEPR measurements.

For the experimental results shown in this chapter, I gratefully acknowledge the work of Ondřej Fellner, Mgr. on the synthesis and characterization of the molecules; Ing. Jakub Hrubý, Ph.D. and Ing. Šárka Vavrečková on molecular deposition on graphene and characterization by Raman spectroscopy, XPS, and AFM; Prof. Paola Barbara, DaVonne Henry, MSc. and Shehan de Silva for the depositions of the compounds on graphene field effect transistors and transport measurements; Lubomír Havlíček, Ph.D. and Radovan Herchel, Ph.D. on DC magnetometry experiments and analysis; Ivan Nemec, Ph.D. and Radovan Herchel, Ph.D. on their support with DFT, BS-DFT, and CASSCF-NEVPT2 calculations; and Vinicius T. Santana, Ph.D. and Ing. Antonin Sojka, Ph.D. on the support with HFEPR measurements and analysis.

The results in this chapter were published in J. Hrubý *et al.*, Deposition of Tetracoordinate Co(II) Complex with Chalcone Ligands on Graphene, Molecules **25**, 5021 (2020) [104]; and J. A. Navarro Giraldo *et al.*, Tetracoordinate Co(II) Complexes with Semi-Coordination as Stable Single-Ion Magnets for Deposition on Graphene, Phys. Chem. Chem. Phys. **25**, 29516 (2023) [105].

4.1. Theoretical Background

In the present section, we introduce some important concepts needed in the rest of the chapter. The objective is to give the reader the most basic ideas about SMMs, DFT, and the CASSCF method, which justify their application and the interest of the community in them, but without the aim of presenting them exhaustively. For a deeper explanation of these concepts, we refer to the available literature covering recent developments on SMMs [98], the application of SMMs in spintronic devices [106], SMMs based on a single Co(II) centre [107], various reviews and books on DFT [108–111], and the fundamentals of CASSCF [111].

4.1.1. A Brief Introduction to Single-Molecule Magnets

SMMs are molecular compounds that present slow relaxation of magnetization, i.e., they maintain their magnetization in the absence of external magnetic fields for a relatively long time [25], characterized by the relaxation time τ, which can be as long as years at low temperatures [112]. The ground state of SMMs has a non-zero total spin S, and the spin projection S_m acquires a non-zero value, which is doubly degenerate (i.e., the states have the same energy) in the absence of an external magnetic field. The ground state of SMMs is bistable: the two lowest-energy S_m states are separated from each other by an energy barrier, which must be overcome in order to switch the magnetization (Fig. 4.1 (a)). At low temperatures, the probability of overcoming the energy barrier is exponentially suppressed, effectively "freezing" the system in one of the lowest S_m states. SMMs can be prepared in one of the two lowest S_m states employing an external magnetic field, such that reversing its direction switches the ground state to the second S_m state. In this sense, the magnetization curve of SMMs follows a hysteretic behaviour similar to ferromagnets. However, magnetism in SMMs is purely of molecular origin, in contrast to the long-range interactions of magnetic moments in ferromagnets. This gives rise to striking quantum phenomena, most notably, the quantum tunnelling of the magnetization [112], manifested in step-like features in the hysteresis curve of SMMs (Fig. 4.1 (b)).

The main properties of SMMs are described by the spin Hamiltonian

$$\hat{H} = D\hat{S}_z^2 + E\left(\hat{S}_x^2 - \hat{S}_y^2\right) + g\mu_B \boldsymbol{B}\cdot\hat{\boldsymbol{S}}, \tag{4.1}$$

with $\hat{\boldsymbol{S}} = (\hat{S}_x, \hat{S}_y, \hat{S}_z)$ the spin operator, D and E the axial and rhombic magnetic anisotropy terms, g the molecule's g-factor, and $\mu_B = e\hbar/(2m_e)$ the Bohr magneton. The magnetic anisotropy terms lift the degeneracy of the S_m states even at $B = 0$, such that the energy diagram follows a double-well form, with $S_m = \pm S$ the lowest energy levels for $D < 0$ (Fig. 4.1

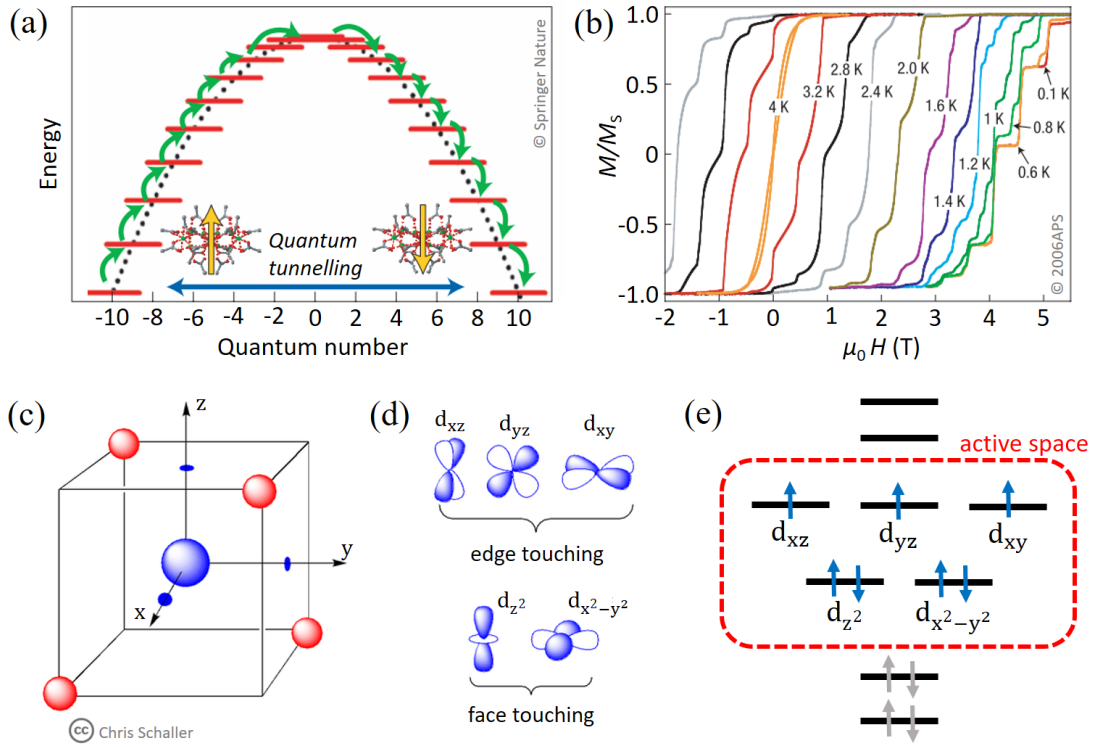

Figure 4.1: (a) Energy diagram in the double-well structure of an SMM with total spin $S = 10$. Green arrows indicate thermally activated transitions enabled by the absorption or emission of phonons. The blue arrow indicates the quantum tunnelling of the magnetization. Reproduced from [106] with permission from Springer Nature. (b) Magnetization curve of the SMM $Mn_{12}O_{12}(O_2CCH_2C(CH_3)_3)_{16}(CH_3OH)_4$ [114]. The step-like behaviour is a manifestation of the quantum tunnelling of the magnetization. Reproduced from [114] with permission from the American Physical Society. (c) Representation of the tetrahedral coordination, with the ligand atoms (in red) located at the opposite corners of a cube centred at the ion (in blue). (d) Molecular d orbitals classified by their proximity to the edges or faces of the cube. Edge-touching orbitals are spatially closer to the coordinating bonds (located along a line between the central and ligand atoms) than face-touching orbitals. Thus, they are higher in energy. (c,d) were reproduced from [115]. (e) Energy diagram and electron occupation of tetracoordinate Co(II). The red box indicates the active orbitals selected for the CASSCF calculation. Outside the box, the orbitals are either doubly occupied or unoccupied.

(a)). For this reason, D is also called the "zero-field splitting" term. Since the allowed transitions of spin states follow the rule $S_m - S_{m'} = \pm 1$, a magnetization reversal requires "climbing" through all the energy levels of the potential well, which is characterized by an energy barrier of value $\Delta = |D|S^2$ or $\Delta = |D|(S^2 - 1/4)$ for integer or half-integer spin, respectively. This magnetization reversal is a thermally activated process, with the relaxation time increasing exponentially as the temperature is lowered. The blocking temperature is defined as the temperature below which the relaxation time is greater than $\tau = 100$ s; it is typically in the range $2-60$ K, although temperatures as high as 80 K (above liquid nitrogen) have been found in Dy-metallocene compounds [113].

The energy barrier, relaxation time, and blocking temperature are among the most important parameters of SMMs, and they are desired to be as large as possible. The energy barrier can be increased by increasing the total spin or the magnetic anisotropy of the molecule. The first SMMs consisted of clusters with several transition-metal, lanthanide, or actinide atoms surrounded by organic ligands, where the interaction between the magnetic centers produced ground states with a large spin, for instance, $S = 10$ for the Mn_{12} compound (the first SMM)

[25]. Alternative routes now focus on molecules with fewer or a single central atom, thus a lower total spin, but with an increased magnetic anisotropy parameter D [107, 116]. In this chapter, we will focus on the latter case.

We will study SMMs with a single metallic center consisting of a Co(II) ion, covalently bonded to organic ligands in tetrahedral coordination. The electronic configuration of the valence shell of Co is $3d^7 2s^2$. In the second oxidation state, two electrons in the 2s orbital are lost, changing the electronic configuration to $3d^7$. For an isolated Co(II) ion, the five 3d orbitals are degenerate. However, the degeneracy is lifted by the crystal field of the ligands, which makes some orbitals more energetically favorable, lifting the orbital degeneracy [117]. In an ideal tetrahedral coordination, the $3d_{x^2-y^2}$ and $3d_{z^2}$ orbitals are lower in energy than the $3d_{xy}$, $3d_{zy}$ and $3d_{zx}$ orbitals (Fig. 4.1 (c,d)). This favours a high-spin state of $S = 3/2$ (Fig. 4.1 (e)). A large magnetic anisotropy is obtained from the large spin-orbit coupling of the Co(II) ion in the coordination environment, making Co(II) compounds interesting candidates for SMMs [107].

4.1.2. Density Functional Theory

DFT is among the most successful theories applied to the description and prediction of the properties of molecules and solid-state materials[1]. It is based on the Hohenberg-Kohn theorem [118], which states that the Hamiltonian of a many-particle system is a unique functional of ground-state electron density, $n(\boldsymbol{r})$. Thus, the ground-state wave function of the system is uniquely determined by $n(\boldsymbol{r})$, and ground-state properties of the system can be computed from it. To understand the importance of this theorem, note that the wave function of a system of N particles, $\Psi(\boldsymbol{r}_1,...,\boldsymbol{r}_N)$, has $3N$ degrees of freedom (omitting the spin and with Ψ real). In principle, Ψ can be found by solving the Schrodinger equation, however, exact solutions are found only in the simplest cases of a single-particle under certain potentials or for a non-interacting many-particle system, and even an approximate problem with a few particles ($N \approx 10$) becomes intractable on the most powerful computers [108]. On the contrary, the electron density has three degrees of freedom corresponding to the three spatial coordinates, independently of the number of particles. This permits to escalate the problem and find approximate solutions to the ground state of systems with hundreds of particles, with sufficient precision as to accurately describe chemical and physical properties like dissociation energies, ionization energies and electron affinities, molecular vibrational modes, phonon spectra, bulk moduli, among many others.

To outline the general procedure of a DFT calculation, we start by noting that due to the Hohenber-Kohn theorem, the ground-state energy is a functional of the electron density and thus can be written as

$$E[n] = T[n] + U[n] + V[n], \tag{4.2}$$

with T, U, and V the kinetic energy, the electron-electron interaction given by the Coulomb potential, and the external potential, e.g. generated by the ions in a crystal for a solid-state system, respectively. Considering that n_0 is the true density of the ground state, then for any other density n' the inequality

$$E[n_0] \leq E[n'] \tag{4.3}$$

holds, where the equality is obtained when $n_0 = n'$. The inequality means that the ground-state density minimizes the energy functional $E[n]$, and therefore, n_0 can be found by a minimization procedure of the energy functional. This important result is referred to as the second Hohenberg-Kohn theorem and is at the core of the practical applications of DFT in real systems.

Although a minimization of the energy functional with respect to the electron density in principle allows to find n_0, this procedure is often not the most efficient [108]. Instead, one

[1] Most of the discussion in this sub-section is based on Ref. [108].

employs the Kohn-Sham equations [119] to obtain the ground-state density indirectly. To arrive at the Kohn-Sham equations, let us write the energy functional as

$$\begin{aligned} E[n] &= T_s[\{\varphi_i[n]\}] + T_c[n] + U_H[n] + (U[n] - U_H[n]) + V[n] \\ &= T_s[\{\varphi_i[n]\}] + U_H[n] + E_{xc}[n] + V[n], \end{aligned} \tag{4.4}$$

where it was defined the single-particle kinetic energy as

$$T_s[\{\varphi_i[n]\}] = -\frac{\hbar^2}{2m}\sum_i^N \int d^3r \varphi_i^*(\boldsymbol{r})\nabla^2\varphi_i(\boldsymbol{r}) \tag{4.5}$$

with $\varphi_i[n]$ single-particle orbitals of a non-interacting system, which are in turn functionals of the electron density, and the Hartree energy as

$$U_H[n] = \frac{e^2}{2}\int d^3r d^3r' \frac{n(\boldsymbol{r})n(\boldsymbol{r'})}{|\boldsymbol{r} - \boldsymbol{r'}|}. \tag{4.6}$$

The term $T_c[n]$ is called the correlation kinetic energy, and is related to the kinetic energy of an interacting electron system. $U[n] - U_H[n]$ is the potential energy of interacting electrons minus the Hartree term, which includes the effects of particle exchange (or Fock term, see chapter 1 section 1.4.1) and higher orders representing electron correlations. These two terms are condensed in the so-called exchange-correlation functional $E_{xc}[n]$, whose exact functional form with respect of n is unknown.

Let us minimize the ground-state energy by means of the functional derivative

$$\begin{aligned} \frac{\delta E[n]}{\delta n(\boldsymbol{r})} &= \frac{\delta T_s[\{\varphi_i[n]\}]}{\delta n(\boldsymbol{r})} + \frac{\delta U_H[n]}{\delta n(\boldsymbol{r})} + \frac{\delta E_{xc}[n]}{\delta n(\boldsymbol{r})} + \frac{\delta V[n]}{\delta n(\boldsymbol{r})} = 0, \\ 0 &= \frac{\delta T_s[\{\varphi_i[n]\}]}{\delta n(\boldsymbol{r})} + u_H(\boldsymbol{r}) + u_{xc}(\boldsymbol{r}) + v(\boldsymbol{r}). \end{aligned} \tag{4.7}$$

The key observation is that this minimization problem resembles that of a non-interacting single particle in the potential

$$v_s(\boldsymbol{r}) = u_H(\boldsymbol{r}) + u_{xc}(\boldsymbol{r}) + v(\boldsymbol{r}). \tag{4.8}$$

Therefore, one can reformulate it to a single-particle Schrodinger equation

$$\left(-\frac{\hbar^2\nabla^2}{2m} + v_s(\boldsymbol{r})\right)\varphi_i(\boldsymbol{r}) = E_i\varphi_i(\boldsymbol{r}), \tag{4.9}$$

where the electron density can be found from the single-particle orbitals φ_i as

$$n(\boldsymbol{r}) := n_s(\boldsymbol{r}) = \sum_i^N f_i|\varphi_i(\boldsymbol{r})|^2, \tag{4.10}$$

with f_i the occupation of each orbital. Eqs. (4.8-4.10) are the Kohn-Sham equations. They allow to solve an interacting, many-body problem by solving the Schrodinger equation for a single particle. In doing so, important information of the interacting system was included in the exchange-correlation functional, and the price to pay in this procedure is that its exact dependence on the density is unknown. In this sense, a great part of DFT development and application lies in the approximation and correct selection of an exchange-correlation functional that reproduces the main features of the physical system of interest.

To recapitulate, we observe that the potential v_s depends on the density n, which in turn depends on φ_i, which at the same time depends on v_s. Therefore, the way to solve a DFT problem through the Kohn-Sham equations is by a self-consistent procedure: one starts with an initial guess for the density n, and from it, the potential v_s is obtained, provided that a suitable

approximation for the exchange-correlation functional was previously chosen. Then, the single-particle orbitals φ_i are found from Eq. (4.9) and a new density n is computed. A convergence test is done, which may compare the initial and computed ground-state energy, density, or another quantity. If the test fails, the procedure starts again with the newly computed density. Usually, convergence is found after a couple of dozen self-consistent cycles.

The previous considerations described the general procedure of a DFT calculation. One can directly conclude that its precision and performance depend greatly on the choice of the exchange-correlation functional and the initial guess of the electron density. In this sense, different DFT implementations are obtained depending on the choice of E_{xc} and the selection of basis sets in which φ_i is expanded. Given the broad range of possibilities of E_{xc} functionals available, we will mention only briefly those used in this chapter. The first is the PBE functional proposed by Perdew, Burke, and Ernzerhof [120, 121]. It belongs to the family of generalized-gradient approximation (GGA) functionals, which, roughly speaking, depends not only on the electron density but also on its spatial derivatives, ∇n. The PBE functional is widely used in solid-state physics and predicts reliable results for the main chemical bonding processes. On the other hand, it does not reliably account for the weak van der Waals interaction. In such a case, van der Waals correcting terms are added into the functional; in our case, we employed the D2 and D3 methods of Grimme [122–124]. The second functional employed was the B3LYP (Becke, 3-parameter, Lee-Yang-Parr) [125–127]. It belongs to the family of hybrid functionals, where the exact exchange energy (the Fock term) is mixed with a GGA functional. Since it is not possible to explain it in detail in this brief introduction, we will mention that it is among the most used functionals in quantum chemistry. However, it has been convincingly pointed out that it performs worse than other functionals, even when compared within the same family of hybrid functionals [128].

We end our introduction by mentioning the basis sets for the single-particle orbitals φ_i used in this chapter, which depend on the DFT computation package employed. The first type of basis sets are plane waves, as implemented in the Vienna Ab-Initio Simulation Package (VASP) [129–132]. VASP uses the projector augmented wave (PAW) method [132, 133], where the electronic basis functions acquire a plane-wave form outside a certain region centred at ions, and smooth functions within it. An important term in the PAW method is the energy cut-off of the plane-wave expansion, which indicates the maximum energy (thus, the frequency) of the plane waves in the basis. This is, the higher the cut-off, the higher the number of plane waves used in the expansion of φ_i, increasing the precision of computed ground-state energy in the DFT procedure. Plane-wave basis sets are commonly used to calculate solid-state materials since they can be easily applied in periodic systems, although molecules are also routinely modelled as well. The second type is Gaussian basis sets, as implemented in ORCA [134]. As indicated by its name, the single-particle orbitals are expanded in a linear combination of Gaussian functions. It is the most common method applied to molecular systems, and currently, very accurate Gaussian basis sets are available [135, 136].

4.1.3. Complete Active Space Self-Consistent Field Approximation

In the previous section, it was observed that the correlation energy arising from electron-electron interactions is fundamental for accurately describing the electronic properties of materials. In DFT, due to the energy description in terms of the electron density, its precise dependence on the density is unknown, and it is necessary to approximate it using functionals with different degrees of complexity. On the other hand, other methods exist to treat the electron correlation. Retaking the picture of atomic orbitals instead of working with the electron density offers a route for this objective, perhaps providing a clearer physical insight into electron correlation.

We start by taking the Hartree-Fock approximation introduced in chapter 1, section 1.4.1. For a non-interacting electron system, the wave function corresponding to a given state is the anti-symmetrized product of individual electron states, i.e., a Slater determinant of the form

$$\Psi_{\alpha_1\alpha_2\ldots\alpha_N}(\boldsymbol{r}_1,\boldsymbol{r}_2,\ldots,\boldsymbol{r}_N) = \begin{vmatrix} \varphi_{\alpha_1}(\boldsymbol{r}_1) & \cdots & \varphi_{\alpha_1}(\boldsymbol{r}_N) \\ \varphi_{\alpha_2}(\boldsymbol{r}_1) & \cdots & \varphi_{\alpha_2}(\boldsymbol{r}_N) \\ \vdots & \ddots & \vdots \\ \varphi_{\alpha_N}(\boldsymbol{r}_1) & \cdots & \varphi_{\alpha_N}(\boldsymbol{r}_N) \end{vmatrix}, \tag{4.11}$$

with $\varphi_{\alpha_j}(\boldsymbol{r}_i)$ the single-particle wave function in the state α_j (spin was omitted). When changing to a system of interacting electrons, the ground state can be written as a superposition of Slater determinants

$$\sum_{\alpha_1\ldots\alpha_N} C_{\alpha_1\ldots\alpha_N}\, \Psi_{\alpha_1\ldots\alpha_N}(\boldsymbol{r}_1,\boldsymbol{r}_2,\ldots,\boldsymbol{r}_N), \tag{4.12}$$

with $C_{\alpha_1\ldots\alpha_N}$ being complex numbers [20, p. 69]. For example, if the physical system is the H_2 molecule, $N = 2$ due to the two valence electrons and φ_{α_i} are the eigenstates (ground- and excited states) of the hydrogen atom. The Hartree-Fock approximation thus approximates the ground state of the interacting system by a single Slater determinant, determining the single-particle states φ_{α_i} by minimizing the expectation value of the total Hamiltonian using the variational principle. In essence, the Hartree-Fock approximation attempts to find the non-interacting electron system that best describes the interacting many-body ground state.

It is then natural to extend the Hartree-Fock model by allowing more Slater determinants in the expansion of the many-body ground state. This is the basic idea of configuration interaction methods, in which a *configuration* is defined as a linear combination of Slater determinants that represent the ground or an excited state of the many-body wave function, and *interaction* is related to the combination of the configurations in the ground-state wave function. In configuration interaction methods, the coefficients in the expansion of Eq. (4.12) are optimized to minimize the total ground-state energy, while the single-particle states are not optimized [111, p. 137]. Configuration interaction methods have limited applicability in practice because of the rapid increase of possible configurations as the number of electrons and single-particle states increases, escalating as $O(N!)$ with N the number of electrons [111, p. 141].

The complete active space self-consistent field (CASSCF) method is similar to configuration interaction methods. In CASSCF, an expansion of the ground state as in Eq. (4.12) is carried out. However, besides optimizing the parameters $C_{\alpha_1\ldots\alpha_N}$, the single-particle wave functions are also variationally optimized as in the Hartree-Fock approximation [111, p. 155]. The way to perform such optimization is by doing a self-consistent procedure, taking as a starting point the orbitals (states) of a Hartree-Fock calculation, thereby the name "self-consistent field". In CASSCF, the issue of a large number of configurations is addressed by separating the molecular orbitals into "inactive" and "active", with inactive orbitals typically being unoccupied or doubly occupied, and the active ones being those energetically close to the highest occupied or lowest unoccupied orbitals. Within the active space generated by the active orbitals, a full configuration interaction calculation is carried out. In this sense, like in the configuration interaction method, CASSCF can only be applied to relatively small systems.

It is common to find the notation CASSCF(n,m) in the literature, indicating that the active space is constituted by m orbitals with n electrons. In all the studied molecules, we employed CASSCF(7,5), corresponding to the seven valence electrons of Co(II) distributed in five d orbitals. Fig. 4.1 (e) shows a pictorial representation of the active space used in our calculations.

4.2. Single-Molecule Magnets Under Study

We studied three tetracoordinate SMMs, composed of a cobalt (II) center and organic ligands. The first and second complexes use the same family of Schiff base ligands derived from the condensation of aromatic 2-hydroxobezaldehydes and 2-amino-6-picoline. The first compound consists

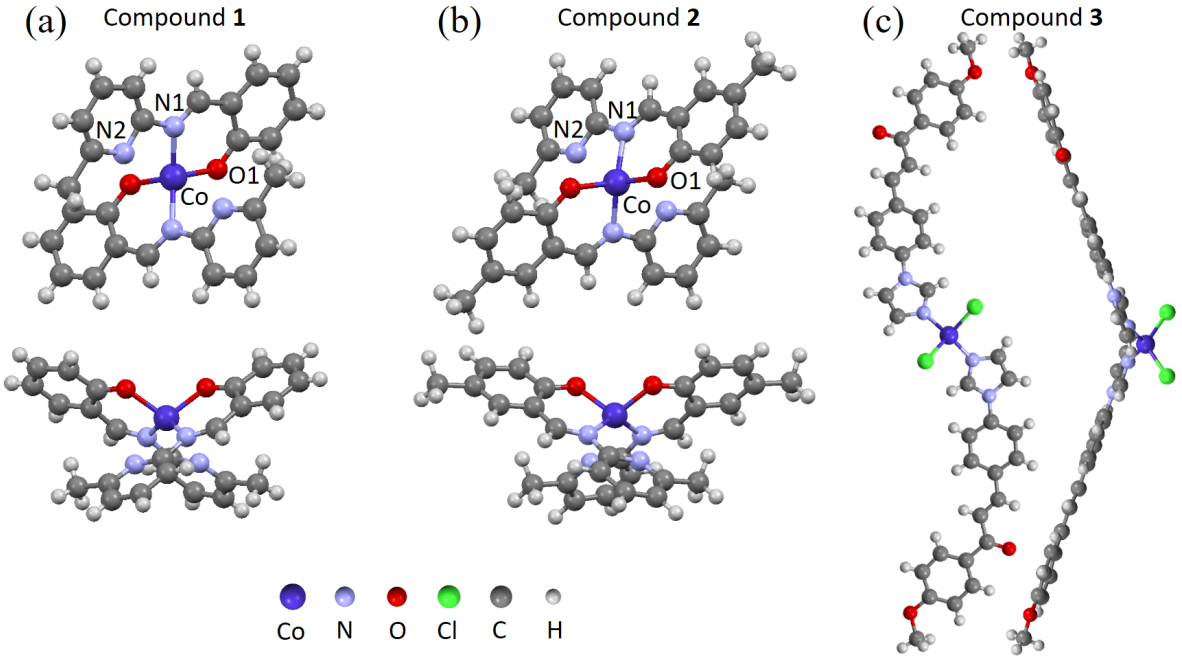

Figure 4.2: Different views of the compounds under study.

of two deprotonated Hsalapi ligands (Hsalapi = 2-Methyl-6-(2'-oxybenzylideneamino)pyridine) coordinating the Co(II) atom in a bidentate manner, giving rise to the [Co(salapi)$_2$] molecule (hereafter **1**, Fig. 4.2(a)). Compound **1** crystallizes in the monoclinic *I2/a* space group [137]. The second compound is the structurally related [Co(me-salapi)$_2$ (Hme-salapi = 2-Methyl-6-(2'-oxy-4'-methyl-benzylideneamino)pyridine, hereafter **2**, Fig. 4.2(b)). Although **1** and **2** present similar structures, they are not isostructural since **2** crystalizes in the orthorhombic *Pbcn* space group. In both structures, the cobalt atom sits at a two-fold rotational axis, and thus, only half of the complex molecule is symmetrically independent. Compounds **1** and **2** present enhanced stability at ambient conditions and high temperatures due to the presence of pyridine nitrogen atoms (labeled as N2 in Fig. 4.2(a,b)), which point towards the metal center. Still, the Co $\cdots$ N2 distances are relatively long (2.625(14) and 2.708(14) Å) and present non-covalent interactions [105], making them semi-coordinative atoms from the perspective of structural coordination chemistry.

For the third compound, the complex [Co(4MeO-L)$_2$Cl$_2$] (hereafter **3**, Fig. 4.2) the chalcone imidazole-derivative ligand 4MeO-L = (2E)-3-[4-(1H-imidazol-1-yl)phenyl]-1-(4-methoxyphenyl)prop-2-en-1-on was employed. It crystallizes in the monoclinic space group *Pc*, and it consists entirely of the tetracoordinate molecules **3**. The 4MeO-L ligands coordinate to the Co atom by the imidazolyl nitrogen atoms forming the Co-N bonds ($d_{\text{Co-N}}$ = 2.014(4) and 2.016(4) Å), while the chlorido ligands form longer bonds ($d_{\text{Co-Cl}}$ = 2.255(2) and 2.257(2) Å). Further details are found in reference [104].

Thermogravimetry measurements on compounds **1**, **2**, and **3** showed structural stability up to 280 °C, 280 °C, and 310 °C, respectively, demonstrating their capability of being deposited by drop-cast or thermal sublimation [104, 105]. Deposition of the compounds on graphene by both methods was successful, with their structural integrity after deposition verified by Raman spectroscopy and XPS. Optical microscopy (Fig. 4.3) and AFM images of the deposited samples showed the formation of islands of the compounds on graphene in all cases, with sizes of a few micrometers and thicknesses from hundreds of nanometers to a few micrometers, depending on the deposition method. For compounds **1** and **2**, drop-cast produced microcrystals on graphene of thickness up to 4 µm, while thermal sublimation yielded thinner islands of height up to 150 nm.

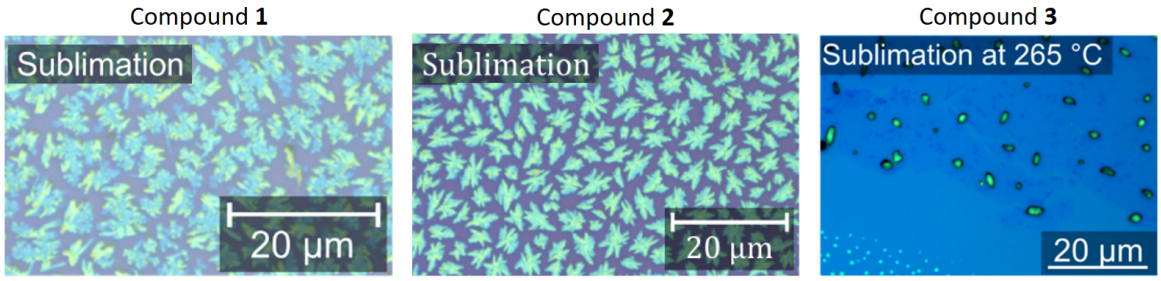

Figure 4.3: Optical microscope images of the deposited molecular compounds (green) on graphene (dark blue) by thermal sublimation. The figures were taken from references [104, 105]

On the other hand, drop-cast of compound **3** produced nanodroplets of thickness up to 50 nm, while thermal sublimation gave microcrystals of hundreds of nanometers high [104, 105].

With this motivation, we aimed at the investigation of the molecule+graphene hybrid system from a theoretical perspective using DFT in order to reveal the main binding mechanisms, structural changes, charge transfer between molecule and substrate, and change in the electronic structure of the constituents. Of paramount importance is to demonstrate that the magnetic properties of each molecule are unaffected in the deposition. Therefore, we computed them using CASSCF-NEVPT2 for the structures before and after deposition.

4.3. Computing and Experimental Methods

4.3.1. Computing Methods

To simulate molecular adsorption on graphene, DFT calculations were done using the Vienna Ab-Initio Simulation Package (VASP) [129–132] version 5.4.4. It uses a plane-wave basis for the Kohn–Sham orbitals, the Projector Augmented Wave method [132, 133], and pseudopotentials. In all cases, the exchange–correlation potential was approximated by the generalized gradient approximation (GGA) in Perdew–Burke–Ernzerhof (PBE) parametrization [120, 121]. In the calculations, the kinetic energy cut-off for the plane waves was 520 eV, the cut-off energy of the plane wave representation of the augmentation charges was 644.9 eV, and the threshold for electronic self-consistency loops was 10^{-6} eV. Van der Waals (vdW) corrections were included through the D3 method with Becke-Johnson damping [123, 124] for compounds **1** and **2**, and the D2 method of Grimme [122] for compound **3**. Computations with and without electric dipole corrections were also considered. Ionic relaxation was performed at different stages of the procedure, sampling the reciprocal space (k-space) with only one point located at the zone center, also known as a Γ-point calculation. The relaxations used different thresholds for the residual forces, as explained in the following paragraphs.

The overall procedure is depicted in the flux diagram of Fig. 4.4. The initial point of the calculations is the experimental crystal structure of graphene with a unit cell containing two carbon atoms, as shown in Fig. 1.1, while for the molecular compounds we take the structure resulting from X-ray diffraction (XRD) experiments. From graphene's unit cell, we construct a supercell that can allocate each molecule. In the case of compounds **1** and **2**, we used a graphene supercell of size 10×10, being 1×1 the unit cell, resulting in a parallelepiped of spatial dimensions $24.67 \times 24.67 \times 30$ Å^3 (Fig. D.1 (a) of appendix D). The 30 Å in the vertical direction ensured a negligible interaction between the repeated images of the unit cell that take place in plane-wave DFT. For compound **3**, two graphene supercells of size 17×8 and 13×7 were used, corresponding to two different molecule orientations on the substrate (Fig. D.1 (b,c) of appendix D). Afterward, ionic relaxation of the individual systems was done, i.e. the isolated graphene

supercells and isolated molecules, keeping the supercell volume constant. For the graphene supercells, relaxation was performed until residual forces on each ion were below 0.001 eV/Å. For the molecules, the criterion for residual forces was 0.02 eV/Å.

The next step was the computation of the energy profile of the system molecule+graphene, with respect to the relative distance between them, without performing ionic relaxation. This procedure, described in more detail in the following section, allows for estimating the equilibrium distance of the molecule on graphene. Once the equilibrium distance was found, we did ionic relaxation of the whole system in such an equilibrium position until residual forces on all ions were below 0.02 eV/Å. With these procedures, we were able to predict the binding energy and structural changes in the molecules after deposition.

To analyze the change in the electronic structure and charge transfer dynamics, we computed the charge density of each system in their final relaxed form by increasing the sampling of the reciprocal space to a Γ-centered $2 \times 2 \times 1$ Monkhorst-Pack grid [138]. The obtained charge densities were kept constant in DOS calculations (VASP tag `ICHARG=11`), where the reciprocal space was sampled with a Γ-centered $4 \times 4 \times 1$ Monkhorst–Pack grid. In all of the previous calculations, reciprocal space integration used Gaussian smearing of k-points equal to 0.1 eV.

The g-factors and magnetic anisotropy parameters were calculated with the ORCA 4.2.1 and 5.0 electronic structure package [134]. It uses a gaussian-basis DFT approach, and in particular, we employed the triple-ζ def2-TZVP basis functions for all atoms except for carbon and hydrogen, for which the def2-SVP basis set was applied [135]. Additionally, the def2/J and def2-TZVP/C auxiliary basis sets were utilized together with RIJCOSX approximation [136, 139]. To account for exchange-correlation, we employed the Becke-3 Parameter-Lee-Yang-Parr

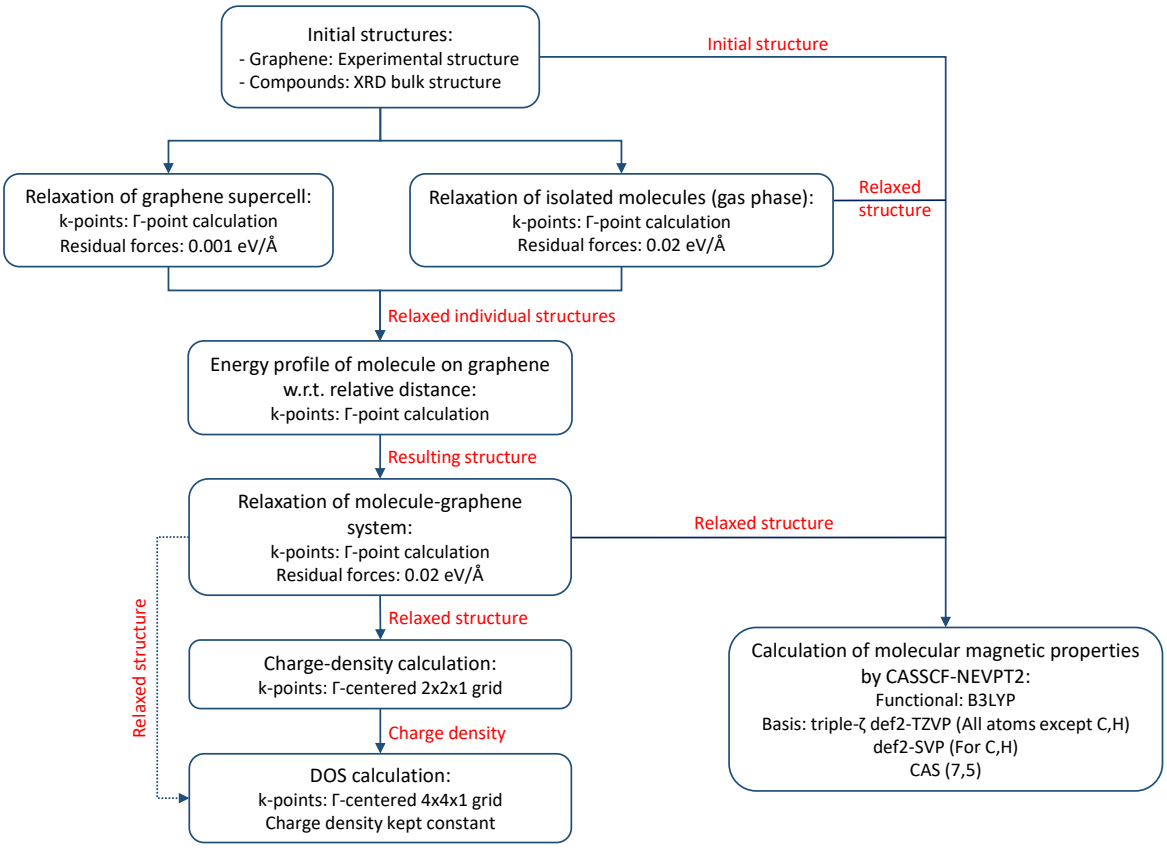

Figure 4.4: Workflow of the DFT calculations. In red are the results from the previous step used for the next step. (Files in VASP nomenclature: Relaxed structure = CONTCAR; charge density = CHGCAR.)

(B3LYP) functional [126, 140], with a threshold for the convergence of total electronic energy after self-consistent steps of 1×10^{-6} Ha ($\sim 2.72 \times 10^{-5}$ eV). To compute the spin-Hamiltonian parameters (g-factors and magnetic anisotropy terms), the multi-configurational character of the studied Co(II) complexes was handled by calculations utilizing state-averaged CASSCF (SA-CASSCF) wave functions [141], complemented by NEVPT2 [142]. The active space of the CASSCF calculation was set to five d-orbitals of Co(II) (CAS(7,5)). The D- and g-tensors, based on dominant spin-orbit coupling contributions from excited states, were calculated through quasi-degenerate perturbation theory (QDPT) [143]. We utilized approximations to the Breit-Pauli form of the spin-orbit coupling operator (SOMF approximation) [144], and effective Hamiltonian theory [145]. HFEPR spectra were simulated using EasySpin 5.2.33 [146].

BS-DFT calculations in ORCA 5.0 were done to estimate the isotropic exchange interaction. Two DFT hybrid functionals, B3LYP [125–127] and PBE0 [147], were selected based on their good performance on previously studied coordination compounds [148–153]. Moreover, the calculations were performed with Ahlrichs triple-ζ basis sets def2-TZVP and also with their relativistic analogs ZORA-def2-TZVP [135]. The non-local density-dependent dispersion correction to DFT was accounted for in two ways, as non-self-consistent (DFT-NL) and as self-consistent (DFT-SCNL) implementation [154, 155].

Appendix C shows the main files and procedures used in the calculations.

4.3.2. Experimental Methods

To deposit the compounds on graphene, we employed two methods: drop-cast, in which the compound is dissolved in a liquid solution that is evaporated on the substrate, and thermal sublimation, where the compound is sublimated under high-vacuum conditions and then adsorbed by the substrate. For both processes, a chemical vapor deposition (CVD) grown monolayer graphene on a Si/SiO_2 substrate was used (300 nm thickness of SiO_2, Si (100), p-doped, $1 - 10\ \Omega$ cm from Graphenea, San Sebastian, Spain). The drop-cast sample was prepared by dissolving the bulk compound **1** or **2** in acetone (99%, Penta, Czech Republic) to make a final solution with a 1 mM concentration. The actual drop-casting was conducted in ambient conditions as 40 µL was drop-cast onto graphene. For the thermal sublimation, we used a home-built high-vacuum sublimation chamber equipped with a quartz crucible heated by a ceramic heater (BACH RC, Seefeld, Germany) with a thermocouple in thermal contact with the heater. The base chamber pressure during the sublimation was 1×10^{-6} mbar. The sublimations for **1** and **2** were performed at 270 °C and 283 °C, respectively. The optical images in Fig. 4.3 were acquired on a confocal Raman microscope WITec Alpha300 R+ (WITec, Ulm, Germany).

To perform electric transport measurements of deposited samples on graphene, the compounds were drop-cast onto graphene field-effect transistors (GFETs). The preparation of the devices was as follows. Graphene was grown by chemical vapor deposition on Cu foil (Sigma Aldrich) and wet-transferred onto Si/SiO2 wafers. (p-doped (100) Si with 3000 Å dry thermal oxide from University Wafer – South Boston, MA, USA). Standard photolithography methods were used to pattern the graphene into Hall-bar geometries. Cr/Au contact pads were deposited by magnetron sputtering (15 Å Cr and 4000 Å Au). The clean devices were vacuum annealed at 140°C for 1 hour before electrical measurements were taken using a probe station in ambient conditions. Powder samples of **1** and **2** were dissolved in acetone to make 0.1 mM solutions. Directly after measuring the clean devices, the solutions were drop-cast via a syringe onto the clean devices. The solvent was given about 30 s to evaporate and electrical measurements were then taken on the coated devices.

DC magnetometry measurements were collected using a Low-Temperature Vibrating Sample Magnetometer (Cryogenic Limited, London, United Kingdom) with a temperature range from 1.6 K to 400 K and a magnetic field from 0 to 9 T. The samples (compounds **1** and **2**) were mixed with eicosane and studied in a form of a sphere with a 4 mm diameter.

HFEPR spectra were acquired on a home-built spectrometer featuring a signal generator (Virginia Diodes, Charlottesville, USA), an amplifier–multiplier chain (Virginia Diodes, Charlottesville, USA), a quasi-optical bridge (Thomas Keating, Billingshurst, UK), and a 16 T solenoid cryomagnet (Cryogenic, London, UK) with heterodyne signal detection. The reference powder sample of the complex was studied as a pressed powder pellet sample with a diameter of 5 mm.

4.4. Calculation of Equilibrium Distances, Binding Energies, and Structural Changes After Deposition

As mentioned in the previous section, the graphene superlattices and individual molecules were relaxed separately. The graphene superlattices were relaxed using the conjugate-gradient algorithm [156] (VASP tag IBRION=2) until residual forces on each ion were below 0.001 eV/Å. To relax the individual, isolated molecules in gas phase, first, we used the conjugate-gradient algorithm, which performs better for systems that are far from the equilibrium configuration, such as the case of the individual molecules that are removed from the bulk crystal structure. When the residual forces on each molecular ion were below 0.1 eV/Å, we changed the relaxation algorithm to the "residual minimization scheme, direct inversion in the iterative subspace" method [157] (RMM-DIIS, VASP tag IBRION=1) until residual forces were below 0.02 eV/Å. After relaxation, there is a change in the coordination tetrahedron of the cobalt center, both in the distance between the cobalt center and its nearest neighbors, and the overall shape of the tetrahedron. Fig. 4.5 shows such changes, and Table 4.1 contains the distance changes to the cobalt center.

The relaxed graphene and molecular structures were then joined together in the same unit cell, and calculations of the total energy (without ionic relaxation) were performed by varying the relative distance between molecule and substrate. Since upon deposition, the molecules can have a great number of possible orientations relative to the graphene substrate, we decided to compute four representative orientations for each of the compounds **1** and **2**, and two orientations of compound **3**, based on the possible enhancement of the interaction between the aromatic rings of molecule and graphene (Fig. 4.6). To identify the equilibrium distance between the molecules and graphene, we calculated the total energy of each system varying the vertical distance between them. The resulting energy profiles with respect to the relative distance were calculated in three different situations: without vdW interactions (Fig. 4.7 (a,c,e)), with vdW interactions, and with vdW interactions in addition to electric dipole corrections (Fig. 4.7 (b,d,f)). The results, shown in Fig. 4.7, indicate that vdW corrections considerably affect the total energy of the system, reducing it by approximately 20 eV compared to the calculations without it and displacing the energy minima to lower values of the relative distance. On the other

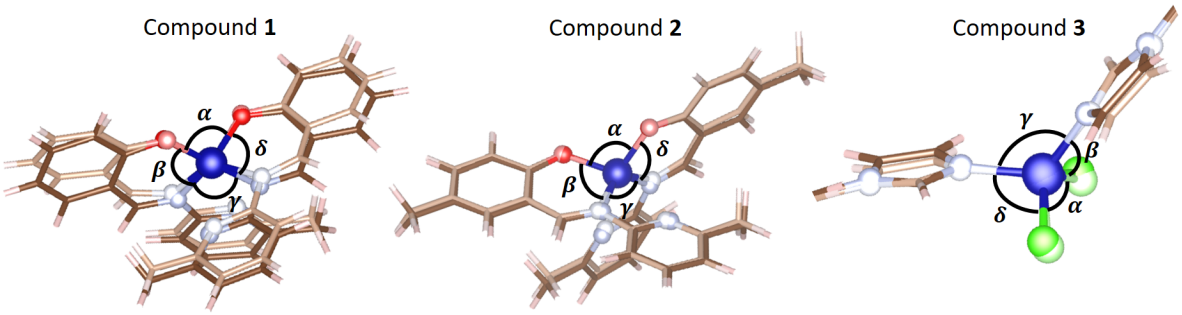

Figure 4.5: Comparison between the molecular compounds in the bulk structure (light colors) and the DFT-relaxed molecules in gas phase (darker colors).

Table 4.1: Binding energies, equilibrium distances, and distances between the Co center and its nearest neighbors.

System	$d_{\text{eq, vdW}}$ (Å)	$d_{\text{eq, no vdW}}$ (Å)	$E_{\text{bin, vdW}}$ (eV)	$E_{\text{bin, no vdW}}$ (meV)	$d_{\text{Co-N1}}$ (Å)	$d_{\text{Co-N2}}$ (Å)	$d_{\text{Co-X1}}$ (Å)	$d_{\text{Co-X2}}$ (Å)
1 Bulk (exp.)	-	-	-	-	1.991	1.991	1.953	1.953
1 DFT relax.	-	-	-	-	1.955	1.955	1.917	1.917
1 Conf. 1	2.61	3.30	-0.83	-46.8	1.955	1.955	1.917	1.917
1 Conf. 2	2.59	3.25	-0.70	-51.7	1.957	1.957	1.918	1.917
1 Conf. 3	2.50	3.18	-0.73	-48.7	1.955	1.955	1.917	1.918
1 Conf. 4	2.72	3.43	-1.08	-68.7	1.958	1.956	1.919	1.918
2 Bulk (exp.)	-	-	-	-	1.995	1.995	1.960	1.960
2 DFT relax.	-	-	-	-	1.952	1.952	1.917	1.917
2 Conf. 1	2.56	3.24	-0.90	-46.5	1.955	1.955	1.921	1.921
2 Conf. 2	2.65	3.34	-0.92	-65.3	1.955	1.955	1.917	1.918
2 Conf. 3	2.54	3.23	-0.80	-49.8	1.954	1.954	1.918	1.917
2 Conf. 4	2.24	2.96	-1.15	-76.0	1.957	1.957	1.919	1.921
3 Bulk (exp.)	-	-	-	-	1.995	1.995	1.960	1.960
3 DFT relax.	-	-	-	-	1.952	1.952	1.917	1.917
3 Conf. 1	2.56	3.06	-0.90	-54.7	1.955	1.955	1.921	1.921
3 Conf. 2	2.65	2.78	-0.92	-75.9	1.955	1.955	1.917	1.918

hand, electric dipole corrections along the vertical axis (z-axis) only add a small correction to the total energy of the order of tens of meV without displacing the energy minimum. Although electric dipole corrections have a negligible effect on the total energy, it will be seen that it affects considerably the charge density of the system. The presence of an energy minimum in the profiles demonstrates the existence of an attractive interaction between the molecules and graphene, such that the distance at which this minimum occurs corresponds to the equilibrium distance, d_{eq}. In this sense, we determined d_{eq} for the three methods by fitting the energy profiles to a third-degree polynomial. The results are summarized in Table 4.1. This calculation indicates that the interaction between molecule and substrate is dominated by vdW forces which are weak and long-range in nature.

After locating the equilibrium distance, we performed ionic relaxation of each system at their equilibrium distance using the RMM-DIIS algorithm (VASP tag IBRION=1). After relaxation, only small structural changes resulted in the molecules due to the weak interaction with the substrate, as evidenced in Table 4.1 where we recorded the distance change between the cobalt

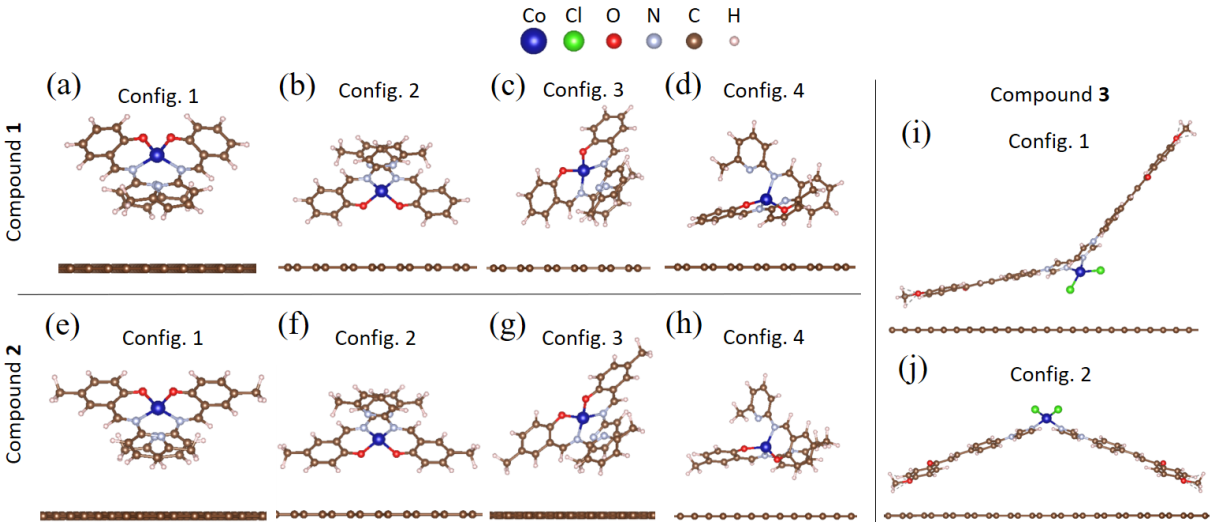

Figure 4.6: Different configurations (orientations) of molecules on graphene considered for DFT calculations.

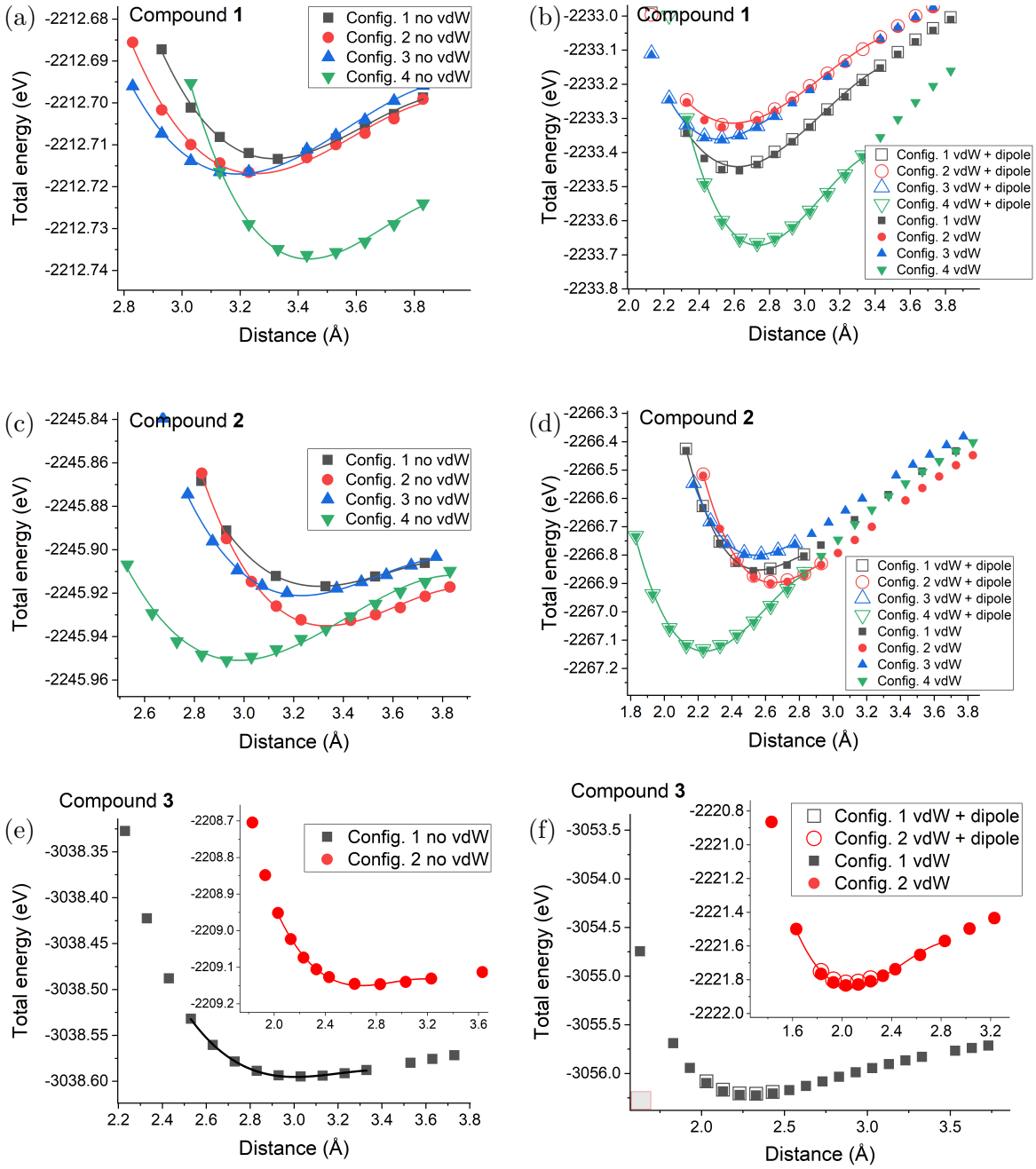

Figure 4.7: Total energy as a function of the molecular distance to graphene for each compound, computed without vdW corrections (a,c,e for compounds **1**, **2** and **3**, respectively), with vdW corrections and with vdW + dipole corrections (b,d,f for compounds **1**, **2** and **3**, respectively).

center and its nearest neighbors. Since the magnetic properties of the molecules are greatly affected by the coordination environment of the metallic center, such small structural changes hint at their preservation after deposition. The calculation of the magnetic properties of the molecules is presented in section 4.6 and predicts that only slight changes in the g-factors and ZFS parameters occur after deposition.

The previously described procedure of ionic relaxation allowed us to obtain the final structure of the molecules on graphene. From them, we isolated the molecules and graphene and computed

the total energy of the individual systems with the aim of obtaining the binding energy between them. The binding energy is calculated as

$$E_{\text{bin}} = E_{\text{mol+subs}} - E_{\text{mol}} - E_{\text{subs}}. \tag{4.13}$$

The binding energies computed with and without vdW interactions are summarized in Table 4.1. Once again, the dominant role of vdW interactions in the binding energy is evident and suggests that the binding mechanism is through vdW forces (physisorption) rather than a chemical bond (chemisorption). Furthermore, the low binding energy ($|E_{\text{bin}}| < 1.15$ eV ≈ 111 kJ/mol) in all studied configurations supports this conclusion. On the other hand, we observe that configuration 4 of compounds **1** and **2** has the highest binding energy (in absolute value); however, since the binding energies of the other configurations are similar in value, we cannot conclude that it is indeed the most probable orientation of the molecule on graphene.

4.5. Charge Transfer and Density of States Analysis

We studied the charge transfer between molecule and substrate after adsorption using the Bader charge analysis [101] as implemented by Henkelman et al. [102, 103]. For these calculations, the charge density of all systems was computed with an increased sampling of the reciprocal space to a $2 \times 2 \times 1$ grid, as explained in section 4.3. Furthermore, we considered calculations with and without electric dipole corrections along the z-axis. The results, shown in Table 4.2, indicate that there is a consistent charge transfer from molecule to graphene for all compounds in the considered configurations, leading to n doping of graphene, except in Conf. 2 of compound **3**.

The role of dipole corrections is not clear by just analyzing the charge transfer since in some cases it increases and in others reduces the transfer; further analysis of the charge-density difference will clarify its contribution. The charge transfer, although small, conduces to an increase in the magnetization of the whole system, compared to the value for isolated molecules of 3.00 μ_{B}, being μ_{B} the Bohr magneton, corresponding to the three unpaired electrons of Co(II). The molecular magnetization calculated with and without dipole corrections is found in Table 4.2. From the table, it is seen that a higher charge transfer is correlated with a higher molecular magnetization; the reason for this increase, as will be explained in the DOS analysis, is the depopulation of the spin-polarized highest occupied molecular orbital (HOMO), thus increasing the overall spin polarization of the molecule.

To further analyze the charge transfer dynamics, we computed the charge density difference, which allows identifying regions of charge accumulation and depletion in the system after deposition. It is defined as

Table 4.2: Electron transfer from molecule to substrate (Δq, in units of number of electrons) computed with and without electric dipole corrections, total magnetization of each configuration of molecule on surface (μ), and HOMO-LUMO gap (ΔE_{HL}) computed with dipole corrections.

System	$\Delta q_{\text{no dipl.}}$ (e^-)	$\Delta q_{\text{dipl.}}$ (e^-)	$\mu_{\text{no dipl.}}$ (μ_B)	$\mu_{\text{dipl.}}$ (μ_B)	ΔE_{HL} (eV)
1 Bulk	-	-	3.000	3.000	0.64
1 Isolated, DFT relax.	-	-	3.000	3.000	0.85
1 Conf. 1	0.059	0.065	3.060	3.078	0.76
1 Conf. 2	0.015	0.003	3.013	3.006	0.73
1 Conf. 3	0.054	0.056	3.058	3.075	0.76
1 Conf. 4	0.029	0.016	3.024	3.020	0.74
2 Bulk	-	-	3.000	3.000	0.65
2 Isolated, DFT relax.	-	-	3.000	3.000	0.84
2 Conf. 1	0.078	0.084	3.079	3.099	0.75
2 Conf. 2	0.033	0.014	3.030	3.020	0.74
2 Conf. 3	0.076	0.078	3.078	3.095	0.76
2 Conf. 4	0.047	0.033	3.047	3.045	0.73

$$\Delta\varrho = \varrho_{\text{mol+subs}} - \varrho_{\text{mol}} - \varrho_{\text{subs}}, \tag{4.14}$$

with $\varrho_{\text{mol+subs}}$, ϱ_{mol}, and ϱ_{subs} the charge densities of the molecule+substrate, isolated molecule, and isolated substrate, respectively. To obtain a better visualization of regions of charge depletion and accumulation, we performed the planar average of the charge density difference in the xy plane, defined as

$$\Delta\varrho_z = \frac{1}{S}\int dx\, dy\, \Delta\varrho(x,y,z), \tag{4.15}$$

with S the area of the supercell in the xy plane. This quantity was computed using the VASPKIT [158] package using the charge densities found from VASP calculations.

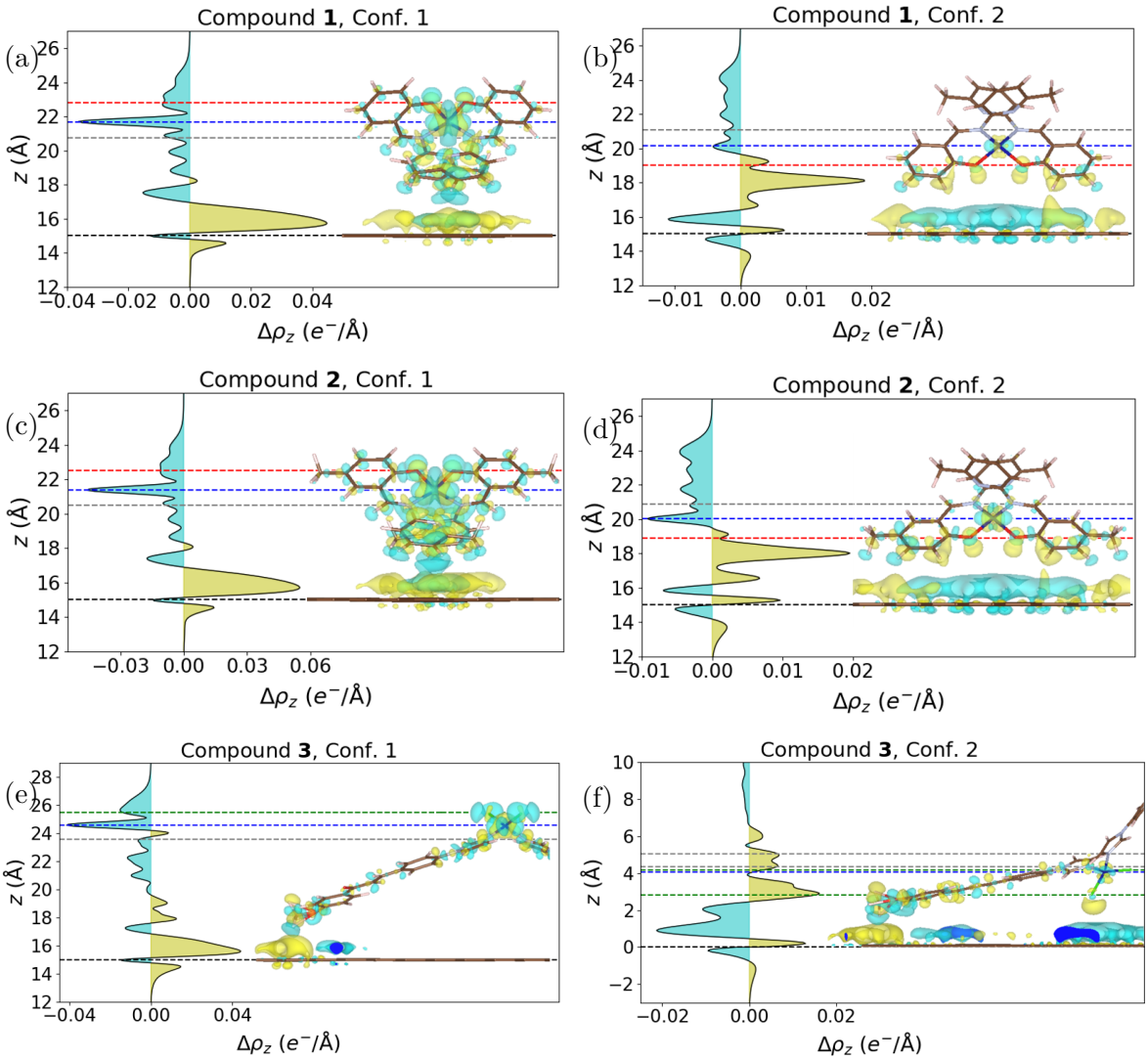

Figure 4.8: (a-f) Planar average of the charge-density difference of compounds **1**, **2**, and **3** in Confs. 1 and 2. Superimposed on each figure are isosurface plots of the charge density difference, with isosurface level 10^{-3} e$^-$/Å^3. Yellow and cyan colors represent charge accumulation and depletion, respectively. The dashed lines correspond to the vertical locations of graphene (in black), the Co center (blue), and the coordinating nitrogen (grey), oxygen (red), and chlorine (green) atoms.

Fig. 4.8(a-f) shows isosurface plots of the charge density difference calculated with dipole corrections for the compounds in Confs. 1 and 2 (Fig. D.2 in appendix D shows the plots of the remaining configurations), as well as the planar average of the charge density difference, $\Delta\varrho_z$. In Confs. 1 and 3 of **1** and **2**, and config 1. of **3**, we observe a clear charge accumulation near graphene and charge depletion in the molecule, supporting the findings of the Bader charge analysis. In Confs. 2 and 4 of **1** and **2**, and config 2 of compound **3**, regions of charge accumulation near the nitrogen, oxygen, and chlorine atoms appear in the molecule which can be attributed to their high electronegativity. In these configurations, some of the hydrogen, nitrogen, oxygen, and chlorine atoms are located closer to graphene than in the respective Confs. 1 and 3, implying that they interact more strongly with graphene and reduce the electron transfer to it, as it is indeed observed in the electron transfer results of Table 4.2. In the case of compound **3** in Conf. 2, the closeness of a coordinating chlorine atom to graphene implies a net charge transfer from graphene to molecule, contrary to the other studied systems.

We analyzed how dipole corrections affect the charge transfer behavior in the system. Generally, systems with a net charge or with a large electric dipole induce non-physical external electrostatic fields arising from the periodic boundary conditions of plane-wave DFT procedures [159]. In our case, charge transfer between molecule and substrate generates an electric dipole that creates this artificial electrostatic field. A way to remove this error is to introduce an electric dipole that generates an electrostatic field that compensates the mentioned non-physical field [159]. We performed a charge-transfer analysis with and without electric dipole corrections, in Fig. 4.9 we show a comparison between the planar average of the charge-density difference of

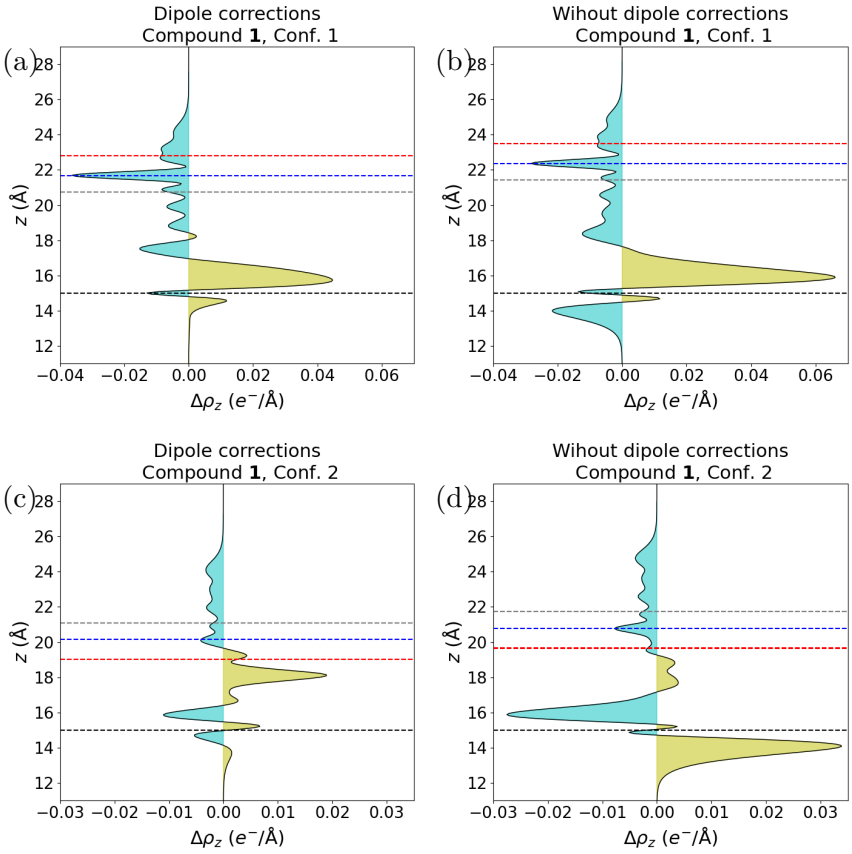

Figure 4.9: Comparison of the planar average of the charge-density difference computed with (a,c) and without (b,d) electric dipole corrections, for molecule **1** in Confs. 1 and 2. Dashed lines indicate the locations of the graphene substrate (black), the cobalt center (blue), and coordinating oxygen (red) and nitrogen (grey) atoms.

molecule **1** Confs. 1 and 2 computed in both cases (appendix D shows similar plots for the other Confs. of molecules **1** and **2**). We observe that dipole corrections induce a significant charge reconfiguration in the system, most notably close to the graphene where the interaction between molecule and substrate is the highest. Without dipole corrections, regions of high charge accumulation and depletion occur close to the graphene, which decrease when dipole corrections are considered. The case of conf. 2 of molecule **1** is particularly interesting because the net charge transfer almost vanishes in dipole-corrected calculations (Table 4.2), however, the interaction between molecule and substrate is still manifested in the charge depletion of the Co center, as it is evident by a minimum in $\Delta\varrho_z$ at the location of this atom.

Analysis of the density of states gives additional information about the charge transfer mechanism. We performed DOS calculations, increasing the sampling of the reciprocal space to a $4 \times 4 \times 1$ grid but keeping the charge density obtained in the previous step constant, as explained in section 4.3. After obtaining the DOS of the molecule + graphene system, we isolated the individual contributions of the molecule and graphene, finding the so-called partial density of states (PDOS). Fig. 4.10(a-c) shows the PDOS of Conf. 1 of compounds **1**, **2**, **3** (Fig. D.5 shows the PDOS of the remaining configurations). It revealed a depopulation of the HOMO of the molecule, compared to the DOS of the isolated molecule in bulk configuration where the HOMO is completely full (shown at the top of the mentioned figures). Since the HOMO of all compounds has a spin-down polarization, its depopulation implies that the spin density of the molecule (this is, the difference between spin-up and spin-down charge densities) increases, explaining the magnetization increase of the molecules after deposition. On the other hand, we observe that the conduction band of graphene gets populated due to the electron transfer from the molecules, increasing the Fermi energy above the Dirac point, consistent with the Bader charge and charge density difference analysis.

Charge transfer from molecule to graphene for compounds **1** and **2** was confirmed experimentally by Raman spectroscopy and electric transport experiments. Raman spectroscopy, which

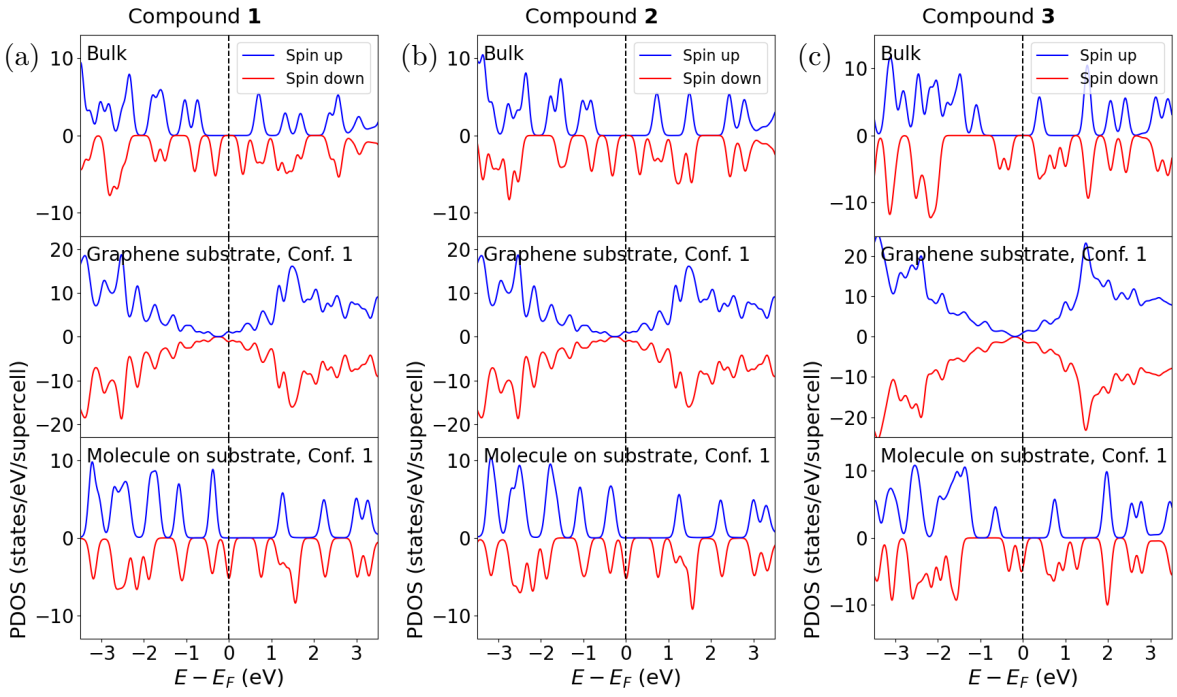

Figure 4.10: (a) Comparison between the DOS of **1** in bulk (XRD) structure, the PDOS of graphene in Conf. 1, and the PDOS of compound **1** on graphene in Conf. 1. The dashed vertical line indicates the Fermi energy. (b,c) Same plots for compounds **2** and **3**, respectively.

probes lattice vibrations in the sample via the inelastic scattering of light by phonons, can reveal doping in graphene due to electron-phonon coupling [82, 160]. Raman spectra revealed a consistent shift of graphene's Raman 2D peak (~2690 cm^{-1}) towards lower energy values after the deposition of both compounds (Fig. 4.11 (a)), which, considering that graphene was initially p-doped due to the contact with impurities at ambient conditions, suggests n-doping of graphene arising from electron transfer from the compounds [160]. n-doping was further confirmed in transport measurements on samples deposited on graphene field-effect transistors (GFETs). In transport measurements, the conductivity of the sample is measured as a function of the gate voltage applied to the GFET, where the latter is responsible for populating and de-populating the conductance or valence bands of graphene. Transport measurements give a direct detection of electron doping via the shift of the charge neutrality point, which in graphene corresponds to the Dirac point. To assess the charge transfer characteristics, **1** and **2** were drop-cast onto GFETs, following the procedure described in section 4.3. The conductance through the devices was monitored as the gate voltage was varied from zero to 100 V, as shown in Fig. 4.11 (b,c). As fabricated, the charge neutrality point (conductivity minimum) of the devices was at approximately 95 V. With **2** deposited, the charge neutrality point shifted by -23 V, indicating significant electron transfer to the graphene. Charge transfer was less apparent in devices

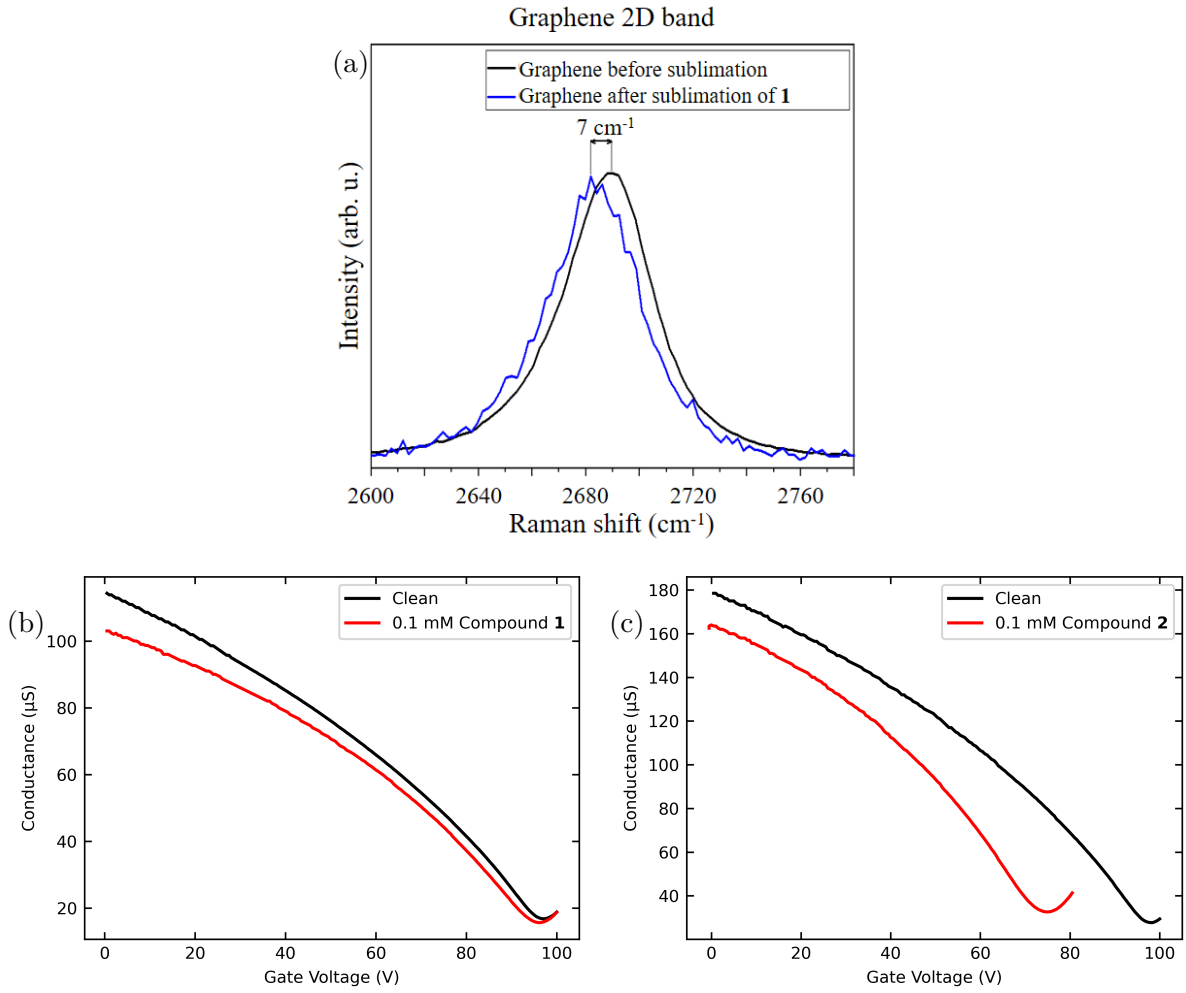

Figure 4.11: (a) Raman spectra of the 2D band of graphene before and after sublimation of compound **1**. The wavelength of the laser source was 532 nm. (b) Conductance of a GFET before and after the deposition of compound **1** as a function of the gate voltage. (c) Conductance of a GFET before and after the deposition of compound **2** as a function of the gate voltage.

coated with **1**. The charge transfer effect may be much weaker with **1**, a lower coverage of the devices may have muted the effect, or as seen from DFT calculations, the adsorbed compound is arranged in a configuration with a low electron transfer.

4.6. Calculation of Magnetic Properties and Comparison with Experiments

The magnetic properties of the compounds obtained from ionic relaxation were calculated with the CASSCF-NEVPT2 method using the ORCA 4.2.1 package [134], further details are found in section 4.3. The g-factors, magnetic anisotropy parameters, and intermolecular magnetic exchange interaction are modeled through the spin Hamiltonian

$$\hat{H} = D\left(\hat{S}_z^2 - \frac{S^2}{3}\right) + E\left(\hat{S}_x^2 - \hat{S}_y^2\right) + g\mu_B B\hat{S}_a - J\hat{S}_i \cdot \hat{S}_{i+1}, \tag{4.16}$$

with D and E the axial and rhombic magnetic anisotropy terms, J the intermolecular magnetic exchange interaction, the subindices i and $i+1$ indicate nearest-neighbor molecules in the bulk crystal structure of the compounds, and the g-factor was defined in the direction of the magnetic field, $\boldsymbol{B}_a = B(\sin(\vartheta)\cos(\varphi), \sin(\vartheta)\sin(\varphi), \cos(\vartheta))$, with ϑ and φ the polar and azimuthal angles, respectively. To compute these parameters, we took the compounds in their bulk form, isolated (gas phase) + DFT relaxed, and relaxed on graphene, and performed a CASSCF-NEVPT2 calculation with an active space corresponding to five d-orbitals and seven valence electrons of cobalt (II) (CAS(7,5)). The results are shown in Table 4.3.

Table 4.3: Exchange interaction parameters calculated by BS-DFT and spin Hamiltonian parameters found by CASSCF-NEVPT2 for each system, compared to the experimental results obtained by HFEPR and DC magnetometry.

System	J (cm^{-1})	D (cm^{-1})	E/D	g_x	g_y	g_z	g_{iso}
1 Bulk[†]	−0.247 [¶]	-25.3	0.084	2.185	2.126	2.462	2.258
1 Isolated, DFT relax.[‖]	-	-18.5	0.009	2.139	2.141	2.368	2.216
1 Conf. 1[‖]	-	-18.5	0.011	2.139	2.142	2.368	2.216
1 Conf. 2[‖]	-	-18.6	0.014	2.139	2.143	2.370	2.217
1 Conf. 3[‖]	-	-18.4	0.010	2.139	2.141	2.367	2.216
1 Conf. 4[‖]	-	-18.4	0.016	2.139	2.144	2.368	2.217
1 HFEPR	-0.30	$<$ -20	0.122	2.20	2.15	2.40	2.25
1 DC magn.	-0.19	-15.3	0.012	-	-	-	2.272
2 Bulk[†]	-0.268 [¶]	-28.3	0.107	2.201	2.119	2.501	2.274
2 Isolated, DFT relax.[‖]	-	-18.2	0.040	2.129	2.152	2.364	2.215
2 Conf. 1[‖]	-	-18.9	0.030	2.131	2.151	2.373	2.218
2 Conf. 2[‖]	-	-18.5	0.033	2.131	2.151	2.368	2.217
2 Conf. 3[‖]	-	-18.4	0.038	2.129	2.152	2.367	2.216
2 Conf. 4[‖]	-	-19.2	0.034	2.131	2.152	2.378	2.220
2 DC magn.	-0.27	-17.5	0.044	-	-	-	2.213
3 Bulk[‖]	-	+14.5	0.150	2.325	2.378	2.163	2.289
3 Conf. 1[‖]	-	+16.4	0.090	2.346	2.364	2.150	2.287
3 Conf. 2[‖]	-	+17.5	0.132	2.345	2.381	2.143	2.290
3 HFEPR	-	+14.6	0.235	2.320	2.380	2.160	2.287

[†] Computed by the CASSCF-NEVPT2 def2-TZVP method in ORCA 5.0, except J.
[¶] J^{Y} computed by the B3LYP-NL method.
[‖] Computed by the CASSCF-NEVPT2 def2-TZVP method in ORCA 4.2.1, except J.

The results show that compounds **1** and **2** have a negative D parameter, indicating that they have an easy axis of magnetization, while compound **3** has a positive D and therefore it has an easy plane of magnetization. Usually, easy-axis systems are preferred over easy-plane ones because they exhibit a magnetization barrier (Fig. 4.1 (a)) that induces a slow relaxation

of magnetization [161], which is the absolute indicator of magnetism at the molecular level. It is also observed that the highest parameter discrepancy within the same compound is between the bulk structure and the DFT relaxed structures (either isolated or on a substrate), which can be attributed to the structural changes after ionic relaxation. Furthermore, the minimal structural changes between the relaxed isolated molecules and the relaxed molecules after adsorption explain the similar values of the g-factors and magnetic anisotropy parameters between them.

In addition to the calculation of magnetic anisotropy parameters and g-factors of the compounds, we studied the intermolecular exchange interaction in **1** and **2**, since as will be seen from the experimental results, it plays an important role in the molecular magnetic properties. To this end, we selected molecular dimers from the crystal structure of each compound, as shown in Fig. 4.12, and conducted BS-DFT calculations following the procedure of Sec. 4.3 to estimate the isotropic exchange of the spin Hamiltonian defined as $\hat{H} = -J\hat{\boldsymbol{S}}_1 \cdot \hat{\boldsymbol{S}}_2$, with $\hat{\boldsymbol{S}}_1$ and $\hat{\boldsymbol{S}}_2$ corresponding to the spin operator of each molecule in the dimer. The comparison of the energy difference between the high-spin (HS, $S_{1\uparrow} \cdots S_{2\uparrow}$) and broken-symmetry spin states (BS, $S_{1\uparrow} \cdots S_{2\downarrow}$), defining $\Delta = E_{\mathrm{BS}} - E_{\mathrm{HS}}$ as the energy difference between both states, was utilized to calculate J according to the formulas of Ruiz [162] and Yamaguchi [163]:

$$J^{\mathrm{R}} = \frac{2\Delta}{(S_1 + S_2)(S_1 + S_2 + 1)}, \quad J^{\mathrm{Y}} = \frac{2\Delta}{\langle S^2_{\mathrm{HS}} \rangle - \langle S^2_{\mathrm{BS}} \rangle}. \tag{4.17}$$

All approaches predicted a weak antiferromagnetic coupling within the dimer for compounds **1** and **2** using all tested functionals and bases, as seen in Table 4.4 and Fig. 4.12, which shows the isosurface plot of the spin density (difference between spin-up and spin-down electron densities) of the dimer. For example, using the functional B3LYP+NL we find $J^{\mathrm{Y}} = -0.247$ cm^{-1} and -0.268 cm^{-1} for **1** and **2**, respectively. A slightly stronger antiferromagnetic exchange was predicted for **2**, which is consistent with its shorter C$\cdots$C and C$\cdots$N distances between the $\pi - \pi$ stacked ligands of the neighboring molecules compared to those in compound **1**. The magnetic exchange interaction between neighboring molecules is expected to be weak due to the relatively large Co $\cdots$ Co distances being 5.94479(9) and 5.82467(7) Å in compounds **1** and **2**, respectively.

The calculated parameters were validated experimentally by DC magnetization and HFEPR experiments. DC magnetization experiments on compounds **1** and **2**, and HFEPR experiments on **1** and **3** were performed, whose analysis yielded fair agreement with the predicted parameters. Since in all experiments, the samples were in the form of compressed powder pellets, the results can only be compared with the CASSCF-NEVPT2 predictions on the bulk structures.

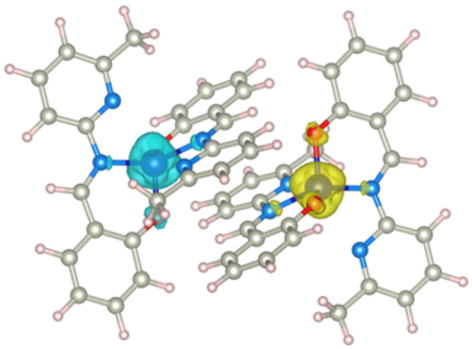

Figure 4.12: Molecular dimer of compound **1** used for BS-DFT calculations. A similar configuration was chosen for compound **2**. The isosurface corresponds to the outcome of the BS-DFT calculation of the spin density, with yellow and cyan representing spin-up and spin-down polarization of the electron density, respectively. This indicates an antiferromagnetic coupling between neighboring molecular spins.

Comp., functional	Basis	$\langle S^2_{HS}\rangle$	$\langle S^2_{BS}\rangle$	Δ (cm^{-1})	J^R (cm^{-1})	J^Y (cm^{-1})
1, B3LYP+NL	def2-TZVP	12.0246	3.0246	-1.110	-0.185	-0.247
1, B3LYP+NL	ZORA-def2-TZVP	12.0264	3.0263	-1.066	-0.178	-0.237
1, B3LYP+SCNL	ZORA-def2-TZVP	12.0274	3.0273	-1.093	-0.182	-0.243
1, PBE0+NL	def2-TZVP	12.0231	3.0231	-0.781	-0.130	-0.174
1, PBE0+NL	ZORA-def2-TZVP	12.0247	3.0247	-0.766	-0.128	-0.170
1, PBE0+SCNL	ZORA-def2-TZVP	12.0253	3.0253	-0.762	-0.127	-0.169
2, B3LYP+NL	def2-TZVP	12.0257	3.0257	-1.206	-0.201	-0.268
2, B3LYP+NL	ZORA-def2-TZVP	12.0276	3.0276	-1.216	-0.203	-0.270
2, B3LYP+SCNL	ZORA-def2-TZVP	12.0287	3.0287	-1.205	-0.201	-0.268
2, PBE0+NL	def2-TZVP	12.0241	3.0241	-0.906	-0.151	-0.201
2, PBE0+NL	ZORA-def2-TZVP	12.0258	3.0258	-0.892	-0.149	-0.198
2, PBE0+SCNL	ZORA-def2-TZVP	12.0264	3.0264	-0.890	-0.148	-0.198

Table 4.4: Evaluation of the magnetic exchange by the BS-DFT approach for compounds **1** and **2**, using different DFT functionals and basis sets. These calculations were done by Dr. Radovan Herchel, and reported in Ref. [105].

Performing a similar analysis on the deposited samples on graphene was not possible due to their low deposited amount, being below the sensitivity threshold of the setups.

For DC magnetic measurements, the magnetic moment of the samples was measured by magnetometry at a temperature range of 2-300 K, and a magnetic field range of 0-7 T (at 2 K). The results for compounds **1** and **2**, displayed in Fig. 4.13, show an effective magnetic moment μ_{eff}/μ_B of value 4.3 and 4.7 at room temperature for **1** and **2**, respectively, which is consistent with a large contribution of spin-orbit coupling (SOC) and thus the isotropic g-factor ($g_{iso} = 2.20$) is larger than that of the free electron ($g = 2.0023$). The μ_{eff}/μ_B values stayed approximately constant down to 30 K, where a drop of μ_{eff}/μ_B starting from 4.1 to 3.7 at 2 K is observed, suggesting the presence of intermolecular magnetic exchange interaction or zero-field splitting (ZFS). Since we did not observe maxima in the effective magnetization curve, we may conclude that intermolecular magnetic exchange between molecules is small. Nevertheless, we were unable to fit the magnetic data in the absence of exchange coupling, and due to this fact as well as taking into account the results of BS-DFT calculations, we included the exchange coupling for the supramolecular dimer. The measurements are analyzed considering the spin Hamiltonian of Eq. (4.16), as well as the molar magnetization in the direction of the applied

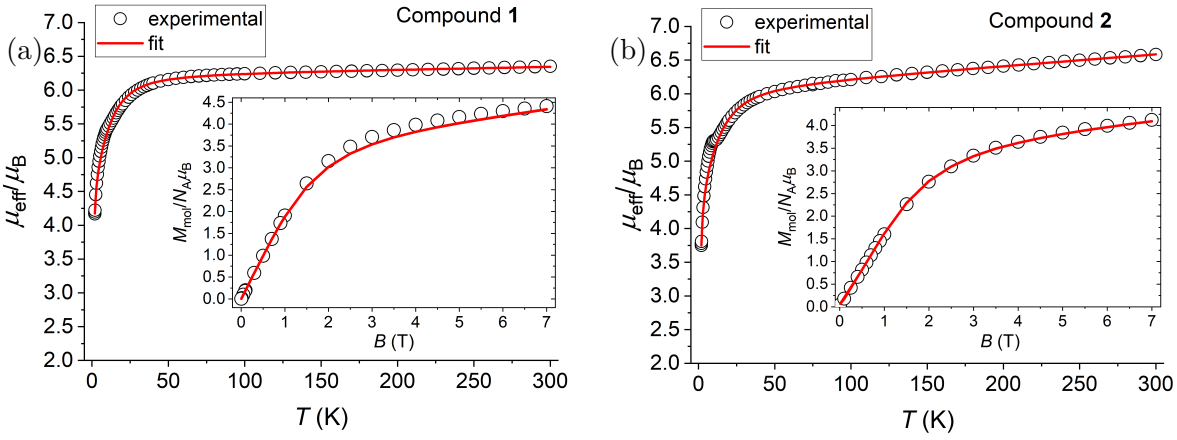

Figure 4.13: (a) Temperature dependence of μ_{eff}/μ_B acquired for **1** in the range from 2 K to 300 K with external magnetic field 0.1 T, and the isothermal magnetization data measured at 2 K shown in the inset. The empty circles represent experimental data, while the red lines represent fittings to Eqs. (4.16-4.19). (b) Similar plots for compound **2**.

magnetic field $\boldsymbol{B}_a$, M_a, that was numerically calculated from the partition function, Z, built from the energy levels of the spin Hamiltonian, as follows

$$M_a = N_A k_{\mathrm{B}} T \frac{d \ln Z}{d \boldsymbol{B}_a}, \tag{4.18}$$

with k_{B} and N_A the Boltzmann and Avogadro constants, respectively. Then, the averaged molar magnetization of the powder sample was calculated as the orientational average

$$M_{\mathrm{mol}} = \frac{1}{4\pi} \int_0^{2\pi} \int_0^{\pi} M_a \sin\vartheta \, d\vartheta d\varphi. \tag{4.19}$$

The experimental magnetic data were fitted using EasySpin [146], analyzing both temperature- and field-dependent measurements simultaneously. The best fit was obtained with the following sets of parameters: for **1**, $J = -0.19$ cm^{-1}, $g_{\mathrm{iso}} = 2.272$, $D = -15.3$ cm^{-1} and $E/D = 0.012$; for **2**, $J = -0.27$ cm^{-1}, $g_{\mathrm{iso}} = 2.213$, $D = -17.5$ cm^{-1} and $E/D = 0.044$. This confirmed the presence of a relatively large and axial magnetic anisotropy. These values are in fair agreement with the ones computed by CASSCF-NEVPT2 for the bulk structure of compounds **1** and **2** (see Table 4.3). Nevertheless, DC magnetization experiments do not give information about the x,y, and z components of the g-factor, and for this reason, it is necessary to perform HFEPR experiments.

Further analysis of the magnetic properties of **1** and **3** was performed by HFEPR. Although measurements were taken on compounds **1**, **2** and **3** both in powder form and deposited on graphene, only the powder spectra of **1** and **3** showed satisfactory results, as the signal-to-noise ratio of the measurements in the remaining samples was too low to be analyzed. Fig. 4.14 (a,b) shows the HFEPR powder spectra of **1** at different frequencies and temperatures, respectively. From the temperature-dependent spectra, we observe strong thermally-activated transitions ascribed to the S=1/2 doublet, indicated by green stars in the spectra, confirming that the ground state has spin 3/2, and thus D is negative. Nevertheless, transitions between the ground-state S=3/2 and the excited state S=1/2 were not observed in the energy range accessible in our experiments, therefore, we can only set a bound for the ZFS term equal to the maximum accessible frequency, $|D| > 600$ GHz=20 cm^{-1}. Simulations with the parameters $g_x = 2.2$, $g_y = 2.15$, $g_z = 2.40$, $D = -20$ cm^{-1}, $E/D = 0.122$, and an exchange coupling term $J = -0.3$ cm^{-1} reproduce most of the spectral features successfully and allow us to infer the existence of an antiferromagnetic coupling between neighboring molecules. Such parameters are in agreement with the ones calculated for **1** in bulk configuration by CASSCF-NEVPT2 (see Table 4.3). Although small, the exchange energy has a noticeable effect on the HFEPR spectra, since it is responsible for the emergence of a second peak in the low magnetic field region (the first two peaks in the simulated spectra of Fig. 4.14 (a)). The separation between those peaks indicates the strength of the exchange coupling, such that at $J = 0$ there is only one peak in the low magnetic field region. Of the spectral features not captured in the simulation, the ones indicated by black crosses correspond to a signal coming from the mirror in the sample holder, while for the ones indicated by red dots, we do not have a conclusive explanation. From the simulations, we can infer that they do not come from plausible values of the spin Hamiltonian parameters for compound **1**.

The frequency- and temperature-dependent HFEPR spectra of compound **3** are shown in Fig. 4.14 (c,d). From the temperature-dependent spectra, we do not observe strong thermally activated transitions in the probed temperature range, allowing us to conclude that the ground state of the system has $S = 1/2$, implying a positive D. In contrast to compound **1**, we do not observe transitions that could be related to a weak exchange coupling, implying that intermolecular interaction can be negligible. The simulated spectra that best represent the

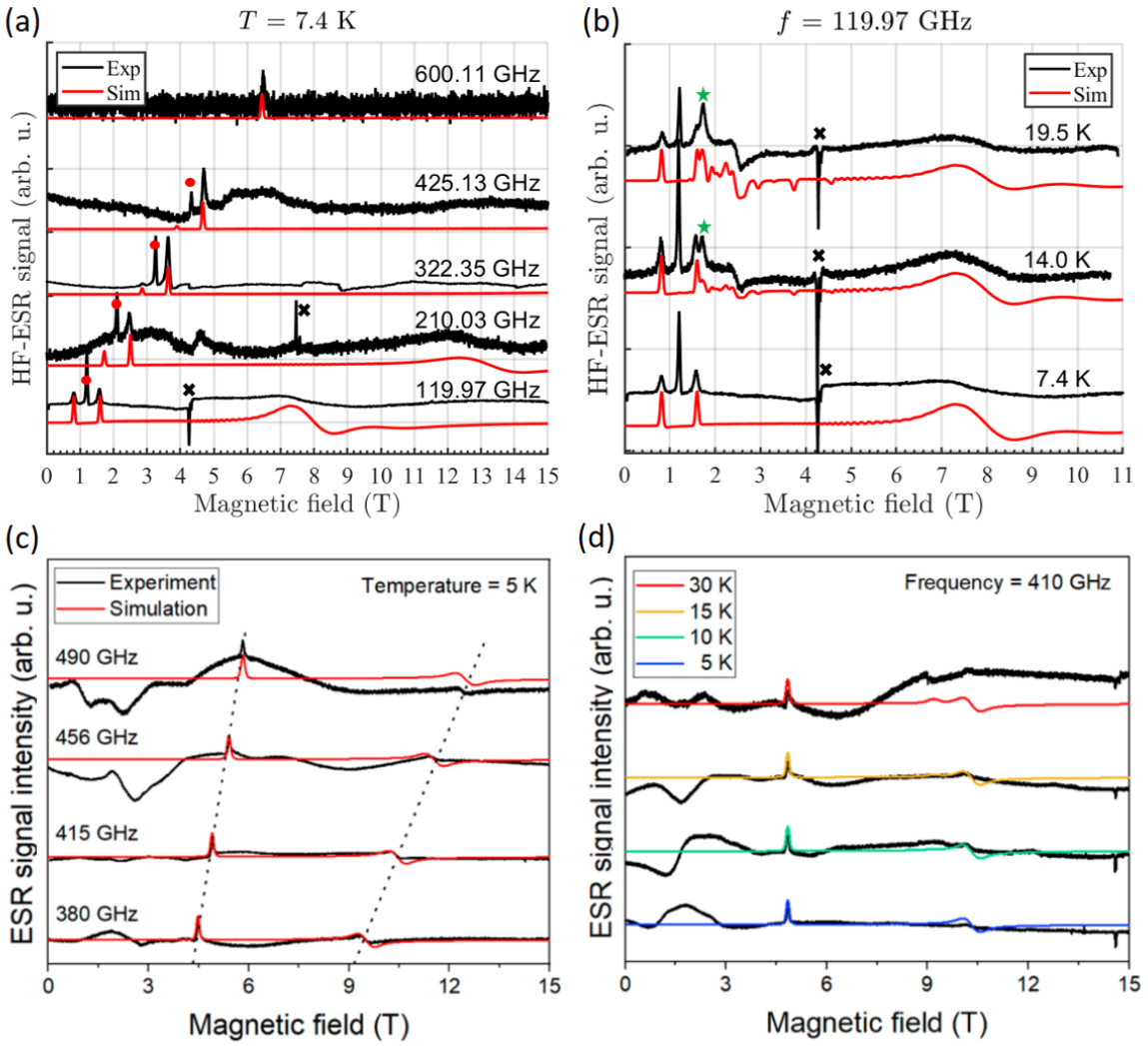

Figure 4.14: (a) Frequency dependence of the HFEPR spectra of compound **1** at 7.3 K. (b) Temperature dependence of the HFEPR spectra of compound **1** at 119.97 GHz. The parameters in the simulated spectra (with offset for more clarity) were $D = -20$ cm^{-1}, $E/D = 0.122$, $g_x = = 2.2$, $g_y = 2.15$, $g_z = 2.40$, and $J' = 0.3$ cm^{-1}. (c) Frequency dependence of the HFEPR spectra of compound **3** at 5 K. (d) Temperature dependence of the HFEPR spectra of compound **3** at 410 GHz (in black) and simulated spectra (in color). The parameters in the simulated spectra were $D = 14.6$ cm^1 with $E/D = 0.235$, and $g_x = 2.32$, $g_y = 2.38$, and $g_z = 2.16$. (a,b) were taken from Ref. [105], (c,d) were taken from Ref. [104].

measurements were found with the following values of the spin Hamiltonian parameters: $D = = 14.6$ cm^1 with $E/D = 0.235$, and $g_x = 2.32$, $g_y = 2.38$, and $g_z = 2.16$.

4.7. Summary and Outlook

We presented a theoretical study of the deposition of three tetracoordinated Co(II) SMMs on graphene, using plane-wave DFT at the PBE level of theory to analyze the optimized molecular structure in the gas phase, and adsorption properties such as the equilibrium distances, binding energies, charge transfer, and changes in the HOMO-LUMO gap. We studied how different DFT procedures affect the computed properties, which allows us to draw the following conclusions: first, van der Waals corrections are essential in these types of systems where the

binding mechanism is governed by physical adsorption (the interaction is through permanent or induced electrical dipoles of the substrate and adsorbent), in contrast with systems governed by chemical adsorption, where a covalent or ionic bond is formed between the constituents. Van der Waals corrections increase the binding energy and decrease the relative distance between molecule and substrate by a considerable amount, as seen in Fig. 4.7 and Table 4.1. Second, we found that although electric dipole corrections do not play a considerable role in the computed equilibrium distances and binding energies, they are important when studying charge transfer dynamics. Charge transfer between molecule and substrate induces an electric dipole, generating an electric field that decays slowly with the distance and leading to errors due to the periodic boundary conditions of plane-wave DFT procedures. Dipole corrections compensate for these errors, and we found that in some cases, they result in a considerable decrease in the charge transfer, while in others they increase it. We infer that dipole corrections are necessary when analyzing charge transfer dynamics, and their effects must be studied on a case-to-case basis. Predictions on charge transfer were validated experimentally by Raman spectroscopy and electric transport measurements, confirming n-doping of graphene due to electron transfer from the molecular compounds. Nevertheless, estimating the precise value of the electron transfer per molecule experimentally is challenging due to several unknown factors, for instance, the precise coverage of the compounds on graphene, and the number of molecules directly in contact with it.

We studied the magnetic properties of the considered molecules by applying the CASSCF-NEVPT2 and BS-DFT methods, which were corroborated experimentally by DC magnetometry and HFEPR spectroscopy for the compounds in bulk form. CASSCF-NEVPT2 was used to obtain the g-factors, and the axial and rhombic magnetic anisotropy parameters D and E; while BS-DFT was applied to the calculation of the exchange interaction in molecular dimers of compounds **1** and **2**. We found that the g-factors and magnetic anisotropy parameters of the molecules in the gas phase and of molecules adsorbed on graphene were almost the same in value due to the negligible structural changes after adsorption (see Table 4.3). Therefore, we predict that the molecular magnetic properties remain unchanged after their adsorption on graphene, which would constitute a main advantage of using graphene as a substrate for the deposition of these compounds. However, we found changes in the magnetic properties calculated for the molecules in the bulk structure found by XRD experiments and the isolated molecules in the gas phase, as seen in Table 4.3; these changes are nonetheless minor and should not affect the overall magnetic behavior of the molecules after deposition. Additionally, we computed the exchange interaction of molecular dimers by BS-DFT using several functionals and basis sets and found an antiferromagnetic coupling in all cases. The g-factors, magnetic anisotropy parameters, and exchange interaction energies of the compounds in bulk form were obtained experimentally using DC magnetometry and HFEPR spectroscopy, finding good agreement with the numerical predictions. In particular, for compounds **1** and **2** we found that although the antiferromagnetic exchange coupling is relatively small, it is necessary for the appropriate analysis of the experimental results. The antiferromagnetic exchange has a significant effect on the HFEPR spectra of compound **1** since it is responsible for the emergence of a peak in the low magnetic field region (see Fig. 4.14 (a,b)) that does not appear if we consider $J = 0$.

An experimental investigation of the magnetic properties of the deposited molecules was not possible due to the small deposited amounts, ranging in the order of micrograms, being below the sensitivity threshold of the experimental setups. A possible route would be to study the deposited samples with more powerful methods, such as X-ray magnetic circular dichroism (XMCD), in which the X-ray absorption spectra of the sample at the two circular polarizations of light are recorded as a function of an external magnetic field. Since this method is mostly available in synchrotron facilities, it presents the disadvantage of not being scalable for the investigation of a large number of samples. Another option is to deposit the molecules onto graphene quantum dot bolometers. When nanostructured into quantum dots, electron transport

in graphene becomes very sensitive to the intensity of light in the THz and sub-THz regions, constituting the key feature of a bolometer. In this sense, graphene quantum dot bolometers could enable the spectroscopic investigation of thin films of deposited compounds.

5. Conclusions

In the present doctoral thesis, we investigated the electronic properties of graphene and graphite in three different situations that highlight their rich physical phenomena, making an emphasis on the response of their ground-state and low-energy excitations to an external electromagnetic field. Most of the studied phenomena arise due to the low dimensionality of the physical systems, whether by enhancing electron-electron interactions, enhancing coherent transport, or determining the unique characteristics of graphene's band structure.

The first problem was the theoretical study of spin-density waves (SDW) in graphite at very high magnetic fields (~ 75 T), and their detection by magneto-optical spectroscopy. The magnetic field induces Landau quantization of the electronic motion, restricting electrons to move in quantized orbits in the direction perpendicular to the field, but remaining free in the parallel direction. This fact implies that electron dynamics is effectively one-dimensional, even though graphite is a three-dimensional system. In our theoretical study, we used the Hartree-Fock approximation to model the Coulomb interaction between electrons in the two Landau bands that remain occupied at high fields. Such an interaction, as well as the trivial nesting of Fermi points in a 1D system, are responsible for the formation of the SDW phase. We arrived at a set of self-consistent equations for the SDW band gap and the electron self-energy that represent the general analytical solution to the problem, and explored their numerical solution to study the SDW behavior as the magnetic field is changed. We found the conditions of Landau band separation and interaction strength via an effective dielectric constant necessary for SDW formation, finding that typical values of the interaction strength imply a first-order electronic phase transition from the normal to the SDW state. Our numerical solutions capture the main characteristics of a first-order phase transition, such as hysteresis of the SDW band gap, which acts as the order parameter, and its sudden change from a finite value to zero at the transition point. We applied the Kubo formula to compute the optical conductivity and evaluate the spectroscopic signature of the SDW phase. We identified the subtle but distinctive features of the SDW phase in the optical spectra, which would permit their experimental detection. Although the magnetic fields involved are fairly high, fields as high as 100 T can be generated in pulsed magnetic field facilities, opening the possibility for the experimental investigation of this problem.

The second problem focused on the investigation of the weak localization (WL) in graphene, and its detection by magneto-optical spectroscopy in the sub-THz range. WL is related to the coherent electronic transport in graphene, emerging at low temperatures since the frequency of inelastic scattering events that destroy phase coherence, or dephasing rate, is lower than the rates of elastic scattering events, such as electron scattering with impurities. The main idea was to demonstrate that as the frequency of an electromagnetic excitation is comparable to the dephasing rate, it affects the dephasing dynamics of electrons in graphene. We studied three samples of epitaxial graphene grown on SiC, characterizing them by Raman spectroscopy, DC transport measurements, and magneto-optical spectroscopy in the X-band (~ 10 GHz) and sub-THz ($95 - 350$ GHz) frequency ranges. Raman measurements showed the presence of monolayer and bilayer graphene terraces in the samples, as it is typical of epitaxial graphene. By fitting the DC transport measurements to the WL theory of graphene we found the most relevant parameters of coherent transport for each sample, namely, the characteristic lengths and rates of

dephasing, intervalley scattering, and long-range scattering. They confirmed that the dephasing rates are of the order of $100 - 600$ GHz at temperatures $1.9 - 20$ K, which are achievable in our spectroscopic setup. AC conductivity measured by magneto-optical spectroscopy in the X-band range, corresponding to a microwave frequency of 10 GHz, resulted in a WL signal with similar properties with that of DC transport, corroborating that microwaves of frequency much lower than the dephasing rate do not affect the coherence of electronic transport. On the other hand, spectroscopic measurements in the sub-THz range revealed a rich frequency dependence of the spectra in all samples, which cannot be explained by the theory of WL of graphene extended to the AC case. The consistent frequency dependence of the WL peaks in three different samples, which remain at temperatures as high as 50 K, leads us to conclude that the effect arises from the electron coherence properties of graphene, which are affected at frequencies comparable to the dephasing scattering rate. We argue that a simple extension of the WL theory by making the coherent transport parameters dependent on the microwave frequency does not explain the observed behavior, and a possible reason is the lack of uniformity of the graphene samples composed of graphene monolayers and bilayers. Nevertheless, it is important to stress that the complete picture of WL at sub-THz frequencies comparable to the dephasing rate could not be achieved in our study, and further measurements on more uniform samples of either monolayer or bilayer graphene are necessary to arrive at a successful explanation, which might involve extensions to the WL theory not considered so far.

For the third problem, we investigated the adsorption properties of three cobalt-based single-molecule magnets (SMMs) on graphene. Using density functional theory (DFT) and the complete active space self-consistent field (CASSCF) approximation, we calculated the most relevant adsorption properties, such as equilibrium distances of the molecules on graphene, binding energies, charge transfer, and changes in the HOMO-LUMO gap. DFT calculations predicted electron transfer from the molecules to graphene, which transport measurements and Raman spectroscopy confirmed. Charge transfer and density of states analysis suggested that electrons are transferred from the HOMO of the adsorbed molecules, which due to its spin polarization, leads to an increase in molecular magnetization. This observation suggests the control of molecular magnetization by electron transfer between the molecules and graphene via electrostatic gating. Furthermore, we calculated the magnetic properties of the SMMs defined by the axial and rhombic magnetic anisotropy parameters, g-factors, and intermolecular exchange interaction energies. CASSCF-NEVPT2 calculations predicted an axial magnetic anisotropy ($D < 0$) in compounds **1** and **2**, and an easy-plane anisotropy in compound **3**, which were confirmed and with good agreement with DC magnetization and HFEPR spectroscopy measurements. For compounds **1** and **2**, broken-symmetry DFT predicted a relatively small antiferromagnetic coupling of neighboring molecules, in good agreement with results from HFEPR spectroscopy. The described magnetic molecular properties were studied experimentally on the compounds in bulk form because the methods were not sensitive enough for their study when deposited on graphene. As a perspective work, we suggest molecular deposition on graphene quantum dots, which serve as very sensitive bolometric detectors that could enable spectroscopic studies of thin molecular films.

6. References

[1] NOVOSELOV, K. S., A. K. GEIM, S. V. MOROZOV, D. JIANG, Y. ZHANG, S. V. DUBONOS, I. V. GRIGORIEVA and A. A. FIRSOV. Electric field in atomically thin carbon films. *Science*. 2004, vol. 306, no. 5696, pp. 666–669. Available from: doi:10.1126/science.1102896.

[2] NOVOSELOV, K. S., A. K. GEIM, S. V. MOROZOV, D. JIANG, M. I. KATSNELSON, I. V. GRIGORIEVA, S. V. DUBONOS and A. A. FIRSOV. Two-dimensional gas of massless Dirac fermions in graphene. *Nature*. 2005, vol. 438, no. 7065, pp. 197–200. Available from: doi:10.1038/nature04233.

[3] YOUNG, A. F. and P. KIM. Quantum interference and Klein tunnelling in graphene heterojunctions. *Nature Physics*. 2009, vol. 5, no. 3, pp. 222–226. Available from: doi:10.1038/nphys1198.

[4] KATSNELSON, M. I., K. S. NOVOSELOV and A. K. GEIM. Chiral tunnelling and the Klein paradox in graphene. *Nature Physics*. 2006, vol. 2, no. 9, pp. 620–625. Available from: doi:10.1038/nphys384.

[5] CHEN, Y., W. RUAN, M. WU, S. TANG, H. RYU, H. Z. TSAI, R. LEE, S. KAHN, F. LIOU, C. JIA, O. R. ALBERTINI, H. XIONG, T. JIA, Z. LIU, J. A. SOBOTA, A. Y. LIU, J. E. MOORE, Z. X. SHEN, S. G. LOUIE, S. K. MO and M. F. CROMMIE. Strong correlations and orbital texture in single-layer 1T-TaSe2. *Nature Physics*. 2020, vol. 16, no. 2, pp. 218–224. Available from: doi:10.1038/s41567-019-0744-9.

[6] TIKHONENKO, F. V., D. W. HORSELL, R. V. GORBACHEV and A. K. SAVCHENKO. Weak localization in graphene flakes. *Physical Review Letters*. 2008, vol. 100, no. 5, pp. 056802. Available from: doi:10.1103/PhysRevLett.100.056802.

[7] FAL'KO, V. I., K. KECHEDZHI, E. MCCANN, B. L. ALTSHULER, H. SUZUURA and T. ANDO. Weak localization in graphene. *Solid State Communications*. 2007, vol. 143, no. 1-2, pp. 33–38. Available from: doi:10.1016/j.ssc.2007.03.049.

[8] ZHANG, H. B., H. L. YU, D. H. BAO, S. W. LI, C. X. WANG and G. W. YANG. Magnetoresistance Switch Effect of a Sn-Doped Bi ₂ Te ₃ Topological Insulator. *Advanced Materials*. 2012, vol. 24, no. 1, pp. 132–136. Available from: doi:10.1002/adma.201103530.

[9] LANG, M., L. HE, F. XIU, X. YU, J. TANG, Y. WANG, X. KOU, W. JIANG, A. V. FEDOROV and K. L. WANG. Revelation of topological surface states in Bi2Se3 thin films by in situ Al passivation. *ACS Nano*. 2012, vol. 6, no. 1, pp. 295–302. Available from: doi:10.1021/nn204239d.

[10] GAMBLE, F. R. and B. G. SILBERNAGEL. Anisotropy of the proton spin-lattice relaxation time in the superconducting intercalation complex TaS2(NH3): Structural and bonding implications. *The Journal of Chemical Physics*. 1975, vol. 63, no. 6, pp. 2544–2552. Available from: doi:10.1063/1.431645.

[11] TAKADA, K., H. SAKURAI, E. TAKAYAMA-MUROMACHI, F. IZUMI, R. A. DILANIAN and T. SASAKI. Superconductivity in two-dimensional CoO2 layers. *Nature*. 2003, vol. 422, no. 6927, pp. 53–55. Available from: doi:10.1038/nature01450.

[12] XIA, F., H. WANG and Y. JIA. Rediscovering black phosphorus as an anisotropic layered material for optoelectronics and electronics. *Nature Communications*. 2014, vol. 5, no. 1, pp. 1–6. Available from: doi:10.1038/ncomms5458.

[13] FLEURENCE, A., R. FRIEDLEIN, T. OZAKI, H. KAWAI, Y. WANG and Y. YAMADA-TAKAMURA. Experimental evidence for epitaxial silicene on diboride thin films. *Physical Review Letters*. 2012, vol. 108, no. 24, pp. 245501. Available from: doi:10.1103/PhysRevLett.108.245501.

[14] WATANABE, K., T. TANIGUCHI and H. KANDA. Direct-bandgap properties and evidence for ultraviolet lasing of hexagonal boron nitride single crystal. *Nature Materials*. 2004, vol. 3, no. 6, pp. 404–409. Available from: doi:10.1038/nmat1134.

[15] WANG, Q. H., K. KALANTAR-ZADEH, A. KIS, J. N. COLEMAN and M. S. STRANO. *Electronics and optoelectronics of two-dimensional transition metal dichalcogenides*. Nature Publishing Group, 2012. Available from: doi:10.1038/nnano.2012.193. URL: www.nature.com/naturenanotechnology.

[16] GEIM, A. K. and I. V. GRIGORIEVA. Van der Waals heterostructures. *Nature*. 2013, vol. 499, no. 7459, pp. 419–425. Available from: doi:10.1038/nature12385.

[17] CAO, Y., V. FATEMI, S. FANG, K. WATANABE, T. TANIGUCHI, E. KAXIRAS and P. JARILLO-HERRERO. Unconventional superconductivity in magic-angle graphene superlattices. *Nature*. 2018, vol. 556, no. 7699, pp. 43–50. Available from: doi:10.1038/nature26160.

[18] SLIZOVSKIY, S., E. MCCANN, M. KOSHINO and V. I. FAL'KO. Films of rhombohedral graphite as two-dimensional topological semimetals. *Communications Physics*. 2019, vol. 2, no. 1, pp. 1–10. Available from: doi:10.1038/s42005-019-0268-8.

[19] MAHAN, G. D. *Many-Particle Physics*. Third Edit. Boston, MA: Springer US, 2000. ISBN 978-1-4419-3339-3. Available from: doi:10.1007/978-1-4757-5714-9. URL: http://link.springer.com/10.1007/978-1-4757-5714-9.

[20] GIULIANI, G. and G. VIGNALE. *Quantum Theory of the Electron Liquid*. Cambridge, 2008. ISBN 9780521527965. URL: https://www.cambridge.org/cz/academic/subjects/physics/condensed-matter-physics-nanoscience-and-mesoscopic-physics/quantum-theory-electron-liquid?format=PB.

[21] YOSHIOKA, D. and H. FUKUYAMA. Electronic phase transition of graphite in a strong magnetic field. *Journal of the Physical Society of Japan*. 1981, vol. 50, no. 3, pp. 725–726. Available from: doi:10.1143/JPSJ.50.725.

[22] YAGUCHI, H., Y. IYE, T. TAKAMASU and N. MIURA. Magnetic-field-induced electronic phase transition in graphite. Pulse field experiment at 3He temperatures. *Physica B*. 1993, vol. 184, no. 1-4, pp. 332–336. Available from: doi:10.1016/0921-4526(93)90376-H.

[23] LINKE, H., P. OMLING, P. RAMVALL, B. K. MEYER, M. DRECHSLER, C. WETZEL, R. RUDELOFF and F. SCHOLZ. Application of microwave detection of the Shubnikov-de Haas effect in two-dimensional systems. *Journal of Applied Physics*. 1993, vol. 73, no. 11, pp. 7533–7542. Available from: doi:10.1063/1.354001.

[24] SOJKA, A., M. ŠEDIVÝ, O. LAGUTA, A. MARKO, V. T. SANTANA and P. NEUGEBAUER. High-frequency EPR: Current state and perspectives. In: *Electron Paramagnetic Resonance, Vol. 27*: [online]. Royal Society of Chemistry, 2021pp. 214–252. ISBN 9781839161711. Available from: doi:10.1039/9781839162534-00214. URL: https://pubs.rsc.org/en/content/chapter/bk9781839161711-00214/978-1-83916-171-1.

[25] SESSOLI, R., D. GATTESCHI, A. CANESCHI and M. A. NOVAK. Magnetic bistability in a metal-ion cluster. *Nature*. 1993, vol. 365, no. 6442, pp. 141–143. Available from: doi:10.1038/365141a0.

[26] WALLACE, P. R. The Band Theory of Graphite. *Physical Review*. 1947, vol. 71, no. 9, pp. 622–634. Available from: doi:10.1103/PhysRev.71.622.

[27] GOERBIG, M. O. Electronic properties of graphene in a strong magnetic field. *Reviews of Modern Physics*. 2011, vol. 83, no. 4, pp. 1193. Available from: doi:10.1103/RevModPhys.83.1193.

[28] ZHOU, S. Y., G. H. GWEON, A. V. FEDOROV, P. N. FIRST, W. A. DE HEER, D. H. LEE, F. GUINEA, A. H. CASTRO NETO and A. LANZARA. Substrate-induced bandgap opening in epitaxial graphene. *Nature Materials*. 2007, vol. 6, no. 10, pp. 770–775. Available from: doi:10.1038/nmat2003.

[29] HAN, M. Y., B. ÖZYILMAZ, Y. ZHANG and P. KIM. Energy band-gap engineering of graphene nanoribbons. *Physical Review Letters*. 2007, vol. 98, no. 20, pp. 206805. Available from: doi:10.1103/PhysRevLett.98.206805.

[30] MCCANN, E. and M. KOSHINO. The electronic properties of bilayer graphene. *Reports on Progress in Physics*. 2013, vol. 76, no. 5, pp. 056503. Available from: doi:10.1088/0034-4885/76/5/056503.

[31] NOVOSELOV, K. S., E. MCCANN, S. V. MOROZOV, V. I. FAL'KO, M. I. KATSNELSON, U. ZEITLER, D. JIANG, F. SCHEDIN and A. K. GEIM. Unconventional quantum Hall effect and Berry's phase of 2π in bilayer graphene. *Nature Physics*. 2006, vol. 2, no. 3, pp. 177–180. Available from: doi:10.1038/nphys245.

[32] SLONCZEWSKI, J. C. and P. R. WEISS. Band structure of graphite. *Physical Review*. 1958, vol. 109, no. 2, pp. 272–279. Available from: doi:10.1103/PhysRev.109.272.

[33] MCCLURE, J. W. Band Structure of Graphite and de Haas-van Alphen Effect. *Physical Review*. 1957, vol. 108, no. 3, pp. 612–618. Available from: doi:10.1103/PhysRev.108.612.

[34] SCHNEIDER, J. M., N. A. GONCHARUK, P. VAŠEK, P. SVOBODA, Z. VÝBORNÝ, L. SMRČKA, M. ORLITA, M. POTEMSKI and D. K. MAUDE. Using magnetotransport to determine the spin splitting in graphite. *Physical Review B*. 2010, vol. 81, no. 19, pp. 195204. Available from: doi:10.1103/PhysRevB.81.195204.

[35] SCHNEIDER, J. M., B. A. PIOT, I. SHEIKIN and D. K. MAUDE. Using the de Haas–van Alphen Effect to Map Out the Closed Three-Dimensional Fermi Surface of Natural Graphite. *Physical Review Letters*. 2012, vol. 108, no. 11, pp. 117401. Available from: doi:10.1103/PhysRevLett.108.117401.

[36] SCHNEIDER, J. M., M. ORLITA, M. POTEMSKI and D. K. MAUDE. Consistent Interpretation of the Low-Temperature Magnetotransport in Graphite Using the Slonczewski-Weiss-McClure 3D Band-Structure Calculations. *Physical Review Letters*. 2009, vol. 102, no. 16, pp. 166403. Available from: doi:10.1103/PhysRevLett.102.166403.

[37] LIFSHITZ, I. M. Anomalies of Electron Characteristics of a Metal in the High Pressure Region. *Zh. Eksp. Teor. Fiz.* 1960, vol. 38, no. 5, pp. 1569.

[38] SCHNEIDER, J. M. *Electronic Properties of Graphite* [online]. 2010. PhD thesis. Université Joseph-Fourier - Grenoble I. URL: https://tel.archives-ouvertes.fr/tel-00547304.

[39] LIFSHITZ, E. M. and L. P. PITAEVSKII. *Statistical Physics, Part 2*. Butterworth-Heinemann Ltd, 1980. ISBN 978-0750626361.

[40] LANDAU, L. and E. LIFSHITZ. *Quantum Mechanics, Non-Relativistic Theory*. Third Edit. Elsevier, 1977. ISBN 9780080209401. Available from: doi:10.1016/C2013-0-02793-4. URL: https://linkinghub.elsevier.com/retrieve/pii/C20130027934.

[41] NEUGEBAUER, P. *Development of Heterodyne High Field / High Frequency Electron Paramagnetic Resonance Spectrometer at 285 GHz* [online]. 2010. Theses. Université Joseph-Fourier - Grenoble I. URL: https://tel.archives-ouvertes.fr/tel-00454862.

[42] NAKAO, K. Landau Level Structure and Magnetic Breakthrough in Graphite. *Journal of the Physical Society of Japan*. 1976, vol. 40, no. 3, pp. 761–768. Available from: doi:10.1143/JPSJ.40.761.

[43] ASHCROFT, N. and N. D. MERMIN. *Solid State Physics*. Saunders College Publishing, 1976. ISBN 0-03-083993-9.

[44] MITTLEMAN, D. M., J. CUNNINGHAM, M. C. NUSS and M. GEVA. Noncontact semiconductor wafer characterization with the terahertz Hall effect. *Applied Physics Letters*. 1997, vol. 71, no. 1, pp. 16–18. Available from: doi:10.1063/1.119456.

[45] LLOYD-HUGHES, J. Terahertz spectroscopy of quantum 2D electron systems. *Journal of Physics D*. 2014, vol. 47, no. 37, pp. 374006. Available from: doi:10.1088/0022-3727/47/37/374006.

[46] SADOWSKI, M. L., G. MARTINEZ, M. POTEMSKI, C. BERGER and W. A. DE HEER. Magneto-spectroscopy of epitaxial graphene. In: *International Journal of Modern Physics B*. World Scientific Publishing Co. Pte Ltd, 2007pp. 1145–1154. Available from: doi:10.1142/s0217979207042586.

[47] SHUBNIKOV, L. W. and W. J. de HAAS. Neue Erscheinungen bei der Widerstandsänderung von Wismuthkristallen im Magnetfeld bei der Temperatur von flüssigem Wasserstoff (I). *Proceedings of the Royal Netherlands Academy of Arts and Science*. 1930, vol. 33, pp. 363–368.

[48] SHUBNIKOV, L. and W. J. de HAAS. Magnetische Widerstandsvergrösserung in Einkristallen von Wismut bei tiefen Temperaturen. *Proceedings of the Royal Netherlands Academy of Arts and Science*. 1930, vol. 33, pp. 130–133.

[49] ADAMS, E. N. and T. D. HOLSTEIN. Quantum theory of transverse galvano-magnetic phenomena. *Journal of Physics and Chemistry of Solids*. 1959, vol. 10, no. 4, pp. 254–276. Available from: doi:10.1016/0022-3697(59)90002-2.

[50] LIFSHITZ, I. M. and A. M. KOSEVICH. On the theory of magnetic susceptibility of metals at low temperatures. *Zh. Eksp. Teor. Fiz.* 1955, vol. 29, no. 6, pp. 730–742.

[51] ARNOLD, F., A. ISIDORI, E. KAMPERT, B. YAGER, M. ESCHRIG and J. SAUNDERS. Charge Density Waves in Graphite: Towards the Magnetic Ultraquantum Limit. *Physical Review Letters*. 2017, vol. 119, no. 13, pp. 136601. Available from: doi:10.1103/PhysRevLett.119.136601.

[52] TAKADA, Y. and H. GOTO. Exchange and correlation effects in the three-dimensional electron gas in strong magnetic fields and application to graphite. *Journal of Physics: Condensed Matter*. 1998, vol. 10, no. 49, pp. 11315–11325. Available from: doi:10.1088/0953-8984/10/49/020.

[53] JIANG, Z., E. A. HENRIKSEN, L. C. TUNG, Y. J. WANG, M. E. SCHWARTZ, M. Y. HAN, P. KIM and H. L. STORMER. Infrared spectroscopy of landau levels of graphene. *Physical Review Letters*. 2007, vol. 98, no. 19, pp. 197403. Available from: doi:10.1103/PhysRevLett.98.197403.

[54] IYE, Y., P. M. TEDROW, G. TIMP, M. SHAYEGAN, M. S. DRESSELHAUS, G. DRESSELHAUS, A. FURUKAWA and S. TANUMA. High-magnetic-field electronic phase transition in graphite observed by magnetoresistance anomaly. *Physical Review B*. 1982, vol. 25, pp. 5478–5485. Available from: doi:10.1103/PhysRevB.25.5478.

[55] UJI, S., J. S. BROOKS and Y. IYE. Field-induced phase transition in Kish graphite. *Physica B*. 1998, vol. 246-247, pp. 299–302. Available from: doi:10.1016/S0921-4526(97)00920-4.

[56] YAGUCHI, H. and J. SINGLETON. A high-magnetic-field-induced density-wave state in graphite. *Journal of Physics: Condensed Matter*. 2009, vol. 21, no. 34, pp. 344207. Available from: doi:10.1088/0953-8984/21/34/344207.

[57] FAUQUÉ, B., D. LEBOEUF, B. VIGNOLLE, M. NARDONE, C. PROUST and K. BEHNIA. Two phase transitions induced by a magnetic field in graphite. *Physical Review Letters*. 2013, vol. 110, no. 26, pp. 266601. Available from: doi:10.1103/PhysRevLett.110.266601.

[58] LATYSHEV, Y. I., A. P. ORLOV, D. VIGNOLLES, W. ESCOFFIER and P. MONCEAU. Interlayer tunneling spectroscopy of the field induced CDW state in graphite. In: *Physica B*. North-Holland, 2012pp. 1885–1888. Available from: doi:10.1016/j.physb.2012.01.055.

[59] ARNOLD, F., B. YAGER, E. KAMPERT, C. PUTZKE, J. NYÉKI and J. SAUNDERS. Spear-anvil point-contact spectroscopy in pulsed magnetic fields. *Review of Scientific Instruments*. 2013, vol. 84, no. 11, pp. 113901. Available from: doi:10.1063/1.4828657.

[60] OVERHAUSER, A. W. Spin Density Waves in an Electron Gas. *Physical Review*. 1962, vol. 128, no. 3, pp. 1437. Available from: doi:10.1103/PhysRev.128.1437.

[61] OVERHAUSER, A. W. Giant spin density waves. *Physical Review Letters*. 1960, vol. 4, no. 9, pp. 462–465. Available from: doi:10.1103/PhysRevLett.4.462.

[62] ZHU, X., J. GUO, J. ZHANG and E. W. PLUMMER. Misconceptions associated with the origin of charge density waves. *Advances in Physics: X*. 2017, vol. 2, no. 3, pp. 622–640. Available from: doi:10.1080/23746149.2017.1343098.

[63] LOMER, W. M. Electronic Structure of Chromium Group Metals. *Proceedings of the Physical Society*. 1962, vol. 80, no. 2, pp. 489. Available from: doi:10.1088/0370-1328/80/2/316.

[64] KOSSACKI, P., C. FAUGERAS, M. KÜHNE, M. ORLITA, A. A. NICOLET, J. M. SCHNEIDER, D. M. BASKO, Y. I. LATYSHEV and M. POTEMSKI. Electronic excitations and electron-phonon coupling in bulk graphite through Raman scattering in high magnetic fields. *Physical Review B*. 2011, vol. 84, no. 23, pp. 235138. Available from: doi:10.1103/PhysRevB.84.235138.

[65] ABRIKOSOV, A. *Fundamentals of the Theory of Metals*. Dover Publications, 2017. ISBN 9780486819013. URL: https://books.google.cz/books?id=tTo2DwAAQBAJ.

[66] DITTRICH, T., P. HÄNGGI, B. KRAMER, G. SCHÖN, G. L. INGOLD and W. ZWERGER. *Quantum Transport and Dissipation*. Wiley, 1998. ISBN 9783527292615. URL: https://books.google.de/books?id=N6jvAAAAMAAJ.

[67] ALTSHULER, B. L., D. KHMEL'NITZKII, A. I. LARKIN and P. A. LEE. Magnetoresistance and Hall effect in a disordered two-dimensional electron gas. *Physical Review B*. 1980, vol. 22, no. 11, pp. 5142–5153. Available from: doi:10.1103/PhysRevB.22.5142.

[68] MCCANN, E., K. KECHEDZHI, V. I. FAL'KO, H. SUZUURA, T. ANDO and B. L. ALTSHULER. Weak-localization magnetoresistance and valley symmetry in graphene. *Physical Review Letters*. 2006, vol. 97, no. 14, pp. 146805. Available from: doi:10.1103/PhysRevLett.97.146805.

[69] SUZUURA, H. and T. ANDO. Crossover from Symplectic to Orthogonal Class in a Two-Dimensional Honeycomb Lattice. *Physical Review Letters*. 2002, vol. 89, no. 26, pp. 266603. Available from: doi:10.1103/PhysRevLett.89.266603.

[70] DRABIŃSKA, A., A. WOŁOŚ, M. KAMIŃSKA, W. STRUPINSKI and J. M. BARANOWSKI. Contactless microwave studies of weak localization in epitaxial graphene. *Physical Review B*. 2012, vol. 86, no. 4, pp. 045421. Available from: doi:10.1103/PhysRevB.86.045421.

[71] LARA-AVILA, S., A. TZALENCHUK, S. KUBATKIN, R. YAKIMOVA, T. J. B. M. JANSSEN, K. CEDERGREN, T. BERGSTEN and V. FAL'KO. Disordered Fermi liquid in epitaxial graphene from quantum transport measurements. *Physical Review Letters*. 2011, vol. 107, no. 16, pp. 166602. Available from: doi:10.1103/PhysRevLett.107.166602.

[72] SUMANASEKERA, G. U., B. D. WILLIAMS, D. V. BAXTER and J. P. CARINI. Effects of weak localization and superconducting fluctuations on the frequency dependence of the conductivity in copper-semiconductor sandwiches. *Physical Review B*. 1994, vol. 50, pp. 2606–2621. Available from: doi:10.1103/PhysRevB.50.2606.

[73] FERRARI, A. C., J. C. MEYER, V. SCARDACI, C. CASIRAGHI, M. LAZZERI, F. MAURI, S. PISCANEC, D. JIANG, K. S. NOVOSELOV, S. ROTH and A. K. GEIM. Raman spectrum of graphene and graphene layers. *Physical Review Letters*. 2006, vol. 97, no. 18, pp. 187401. Available from: doi:10.1103/PhysRevLett.97.187401.

[74] DANIELS, K. M., M. M. JADIDI, A. B. SUSHKOV, A. NATH, A. K. BOYD, K. SRIDHARA, H. D. DREW, T. E. MURPHY, R. L. MYERS-WARD and D. K. GASKILL. Narrow plasmon resonances enabled by quasi-freestanding bilayer epitaxial graphene. *2D Materials*. 2017, vol. 4, no. 2, pp. 025034. Available from: doi:10.1088/2053-1583/aa5c75.

[75] Van der PAUW, L. A Method of Measuring Specific Resistivity and Hall Effect of Discs of Arbitrary Shape. *Philips Research Reports*. 1958, vol. 13, pp. 1–9.

[76] HALL, E. H. On a New Action of the Magnet on Electric Currents. *American Journal of Mathematics*. 1879, vol. 2, no. 3, pp. 287–292.

[77] LINDEMUTH, J. *Hall Effect Measurement Handbook: A Fundamental Tool for Semiconductor Material Characterization*. Lake Shore Cryotronics, Inc. ISBN 978-1-7347078-0-9.

[78] SOJKA, A., M. ŠEDIVÝ, A. LAGIŇ, A. GABRIŠ, T. LÁZNIČKA, V. T. SANTANA, O. LAGUTA and P. NEUGEBAUER. Sample Holders for Sub-THz Electron Spin Resonance Spectroscopy. *IEEE Transactions on Instrumentation and Measurement*. 2022, vol. 71, pp. 1–12. Available from: doi:10.1109/TIM.2022.3164135.

[79] SOJKA, A., M. ŠEDIVÝ, O. LAGUTA, A. MARKO, V. T. SANTANA and P. NEUGEBAUER. High-frequency EPR: current state and perspectives. In: *Electron Paramagnetic Resonance: Volume 27*: [online]. The Royal Society of Chemistry, 2020. ISBN 978-1-83916-171-1. Available from: doi:10.1039/9781839162534-00214. URL: https://doi.org/10.1039/9781839162534-00214.

[80] SOJKA, A. *Development of a Novel Terahertz Magnetic Resonance Spectrometer for Spin Dynamics Investigations* [online]. 2022. PhD thesis. Central European Institute of Technology, Brno University of Technology - CEITEC BUT. URL: http://hdl.handle.net/11012/204114.

[81] ŠEDIVÝ, M., V. SANTANA, A. SOJKA, O. LAGUTA and P. NEUGEBAUER. MEPROS – Modular electron paramagnetic resonance operating software for multifunctional high-frequency EPR spectrometer. *Journal of Magnetic Resonance*. 2023, vol. 355, pp. 107556. Available from: doi:10.1016/j.jmr.2023.107556.

[82] FERRARI, A. C. and D. M. BASKO. Raman spectroscopy as a versatile tool for studying the properties of graphene. *Nature Nanotechnology*. 2013, vol. 8, no. 4, pp. 235–246. Available from: doi:10.1038/nnano.2013.46.

[83] BURTON, J. C., L. SUN, F. H. LONG, Z. C. FENG and I. T. FERGUSON. First- and second-order Raman scattering from semi-insulating 4H-SiC. *Physical Review B*. 1999, vol. 59, no. 11, pp. 7282–7284. Available from: doi:10.1103/PhysRevB.59.7282.

[84] FAUGERAS, C., A. NERRÌRE, M. POTEMSKI, A. MAHMOOD, E. DUJARDIN, C. BERGER and W. A. DE HEER. Few-layer graphene on SiC, pyrolitic graphite, and graphene: A Raman scattering study. *Applied Physics Letters*. 2008, vol. 92, no. 1. Available from: doi:10.1063/1.2828975.

[85] LEE, D. S., C. RIEDL, B. KRAUSS, K. V. KLITZING, U. STARKE and J. H. SMET. Raman spectra of epitaxial graphene on SiC and of epitaxial graphene transferred to SiO2. *Nano Letters*. 2008, vol. 8, no. 12, pp. 4320–4325. Available from: doi:10.1021/nl802156w.

[86] JOUAULT, B., B. JABAKHANJI, N. CAMARA, W. DESRAT, A. TIBERJ, J. R. HUNTZINGER, C. CONSEJO, A. CABONI, P. GODIGNON, Y. KOPELEVICH and J. CAMASSEL. Probing the electrical anisotropy of multilayer graphene on the Si face of 6H-SiC. *Physical Review B*. 2010, vol. 82, no. 8, pp. 085438. Available from: doi:10.1103/PhysRevB.82.085438.

[87] BAKER, A. M. R., J. A. ALEXANDER-WEBBER, T. ALTEBAEUMER, T. J. JANSSEN, A. TZALENCHUK, S. LARA-AVILA, S. KUBATKIN, R. YAKIMOVA, C. T. LIN, L. J. LI and R. J. NICHOLAS. Weak localization scattering lengths in epitaxial, and CVD graphene. *Physical Review B*. 2012, vol. 86, no. 23, pp. 235441. Available from: doi:10.1103/PhysRevB.86.235441.

[88] LIU, C. I., P. WANG, J. MI, H. Y. LEE, Y. T. WANG, I. F. HO, C. ZHANG, X. LIN, R. E. ELMQUIST and C. T. LIANG. Weak localization and microwave-irradiated transport in multilayer epitaxial graphene grown on SiC. *Materials Research Express*. 2015, vol. 2, no. 11, pp. 115002. Available from: doi:10.1088/2053-1591/2/11/115002.

[89] TIKHONENKO, F. V., A. A. KOZIKOV, A. K. SAVCHENKO and R. V. GORBACHEV. Transition between electron localization and antilocalization in graphene. *Physical Review Letters*. 2009, vol. 103, no. 22, pp. 226801. Available from: doi:10.1103/PhysRevLett.103.226801.

[90] WESER, M., Y. REHDER, K. HORN, M. SICOT, M. FONIN, A. B. PREOBRAJENSKI, E. N. VOLOSHINA, E. GOERING and Y. S. DEDKOV. Induced magnetism of carbon atoms at the graphene/Ni(111) interface. *Applied Physics Letters*. 2010, vol. 96, no. 1, pp. 12504. Available from: doi:10.1063/1.3280047.

[91] AVERYANOV, D. V., I. S. SOKOLOV, A. M. TOKMACHEV, O. E. PARFENOV, I. A. KARATEEV, A. N. TALDENKOV and V. G. STORCHAK. High-Temperature Magnetism in Graphene Induced by Proximity to EuO. *ACS Applied Materials and Interfaces*. 2018, vol. 10, no. 24, pp. 20767–20774. Available from: doi:10.1021/acsami.8b04289.

[92] HEERSCHE, H. B., P. JARILLO-HERRERO, J. B. OOSTINGA, L. M. VANDERSYPEN and A. F. MORPURGO. Bipolar supercurrent in graphene. *Nature*. 2007, vol. 446, no. 7131, pp. 56–59. Available from: doi:10.1038/nature05555.

[93] HU, M., Z. YAO and X. WANG. Graphene-Based Nanomaterials for Catalysis. *Industrial & Engineering Chemistry Research*. 2017, vol. 56, no. 13, pp. 3477–3502. Available from: doi:10.1021/acs.iecr.6b05048.

[94] DUNLOP, D. and Ö. ÖZDEMIR. *Rock Magnetism: Fundamentals and Frontiers*. Cambridge University Press, 1997. Cambridge Studies in Magnetism. ISBN 9780521000987. URL: https://books.google.cz/books?id=59apHD8OyhwC.

[95] ARDAVAN, A., O. RIVAL, J. J. MORTON, S. J. BLUNDELL, A. M. TYRYSHKIN, G. A. TIMCO and R. E. WINPENNY. Will spin-relaxation times in molecular magnets permit quantum information processing? *Physical Review Letters*. 2007, vol. 98, no. 5, pp. 057201. Available from: doi:10.1103/PhysRevLett.98.057201.

[96] TANAKA, D., N. AKETA, H. TANAKA, S. HORIKE, M. FUKUMORI, T. TAMAKI, T. INOSE, T. AKAI, H. TOYAMA, O. SAKATA, H. TAJIRI and T. OGAWA. Facile preparation of hybrid thin films composed of spin-crossover nanoparticles and carbon nanotubes for electrical memory devices. *Dalton Transactions*. 2019, vol. 48, no. 21, pp. 7074–7079. Available from: doi:10.1039/c8dt02923g.

[97] URDAMPILLETA, M., S. KLYATSKAYA, J. P. CLEUZIOU, M. RUBEN and W. WERNSDORFER. Supramolecular spin valves. *Nature Materials*. 2011, vol. 10, no. 7, pp. 502–506. Available from: doi:10.1038/nmat3050.

[98] CORONADO, E. Molecular magnetism: from chemical design to spin control in molecules, materials and devices. *Nature Reviews Materials*. 2020, vol. 5, no. 2, pp. 87–104. Available from: doi:10.1038/s41578-019-0146-8.

[99] DUGAY, J., M. AARTS, M. GIMENEZ-MARQUÉS, T. KOZLOVA, H. W. ZANDBERGEN, E. CORONADO and H. S. VAN DER ZANT. Phase transitions in spin-crossover thin films probed by graphene transport measurements. *Nano Letters*. 2017, vol. 17, no. 1, pp. 186–193. Available from: doi:10.1021/acs.nanolett.6b03780.

[100] GOBBI, M., E. ORGIU and P. SAMORÌ. When 2D Materials Meet Molecules: Opportunities and Challenges of Hybrid Organic/Inorganic van der Waals Heterostructures. *Advanced Materials*. 2018, vol. 30, no. 18, pp. 1706103. Available from: doi:10.1002/adma.201706103.

[101] BADER, R. F. W. *Atoms in Molecules: A Quantum Theory*. Oxford University Press, 1994. ISBN 9780198558651. URL: https://global.oup.com/academic/product/atoms-in-molecules-9780198558651?cc=cz&lang=en&.

[102] TANG, W., E. SANVILLE and G. HENKELMAN. A grid-based Bader analysis algorithm without lattice bias. *Journal of Physics: Condensed Matter*. 2009, vol. 21, no. 8, pp. 084204. Available from: doi:10.1088/0953-8984/21/8/084204.

[103] HENKELMAN, G., A. ARNALDSSON and H. JÓNSSON. A fast and robust algorithm for Bader decomposition of charge density. *Computational Materials Science*. 2006, vol. 36, no. 3, pp. 354–360. Available from: doi:10.1016/j.commatsci.2005.04.010.

[104] HRUBÝ, J., Š. VAVREČKOVÁ, L. MASARYK, A. SOJKA, J. NAVARRO-GIRALDO, M. BARTOŠ, R. HERCHEL, J. MONCOL, I. NEMEC and P. NEUGEBAUER. Deposition of Tetracoordinate Co(II) Complex with Chalcone Ligands on Graphene. *Molecules*. 2020, vol. 25, no. 21, pp. 5021. Available from: doi:10.3390/molecules25215021.

[105] NAVARRO GIRALDO, J. A., J. HRUBÝ, Š. VAVREČKOVÁ, O. F. FELLNER, L. HAVLÍČEK, D. HENRY, S. de SILVA, R. HERCHEL, M. BARTOŠ, I. ŠALITROŠ, V. T. SANTANA, P. BARBARA, I. NEMEC and P. NEUGEBAUER. Tetracoordinate Co(II) complexes with semi-coordination as stable single-ion magnets for deposition on graphene. *Physical Chemistry Chemical Physics*. 2023, vol. 25, no. 43, pp. 29516–29530. Available from: doi:10.1039/D3CP01426F.

[106] BOGANI, L. and W. WERNSDORFER. Molecular spintronics using single-molecule magnets. *Nature Materials*. 2008, vol. 7, no. 3, pp. 179–186. Available from: doi:10.1038/nmat2133.

[107] JURÁKOVÁ, J. and I. ŠALITROŠ. Co(II) single-ion magnets: synthesis, structure, and magnetic properties. *Monatshefte für Chemie*. 2022, vol. 153, no. 11, pp. 1001–1036. Available from: doi:10.1007/s00706-022-02920-0.

[108] CAPELLE, K. *A bird's-eye view of density-functional theory*. 2006. URL: https://doi.org/10.48550/arXiv.cond-mat/0211443.

[109] FIOLHAIS, C., F. NOGUEIRA and M. A. L. MARQUES. *A Primer in Density Functional Theory*. Berlin, Heidelberg: Springer Berlin Heidelberg, 2003. Lecture Notes in Physics. ISBN 978-3-540-03083-6. Available from: doi:10.1007/3-540-37072-2. URL: http://link.springer.com/10.1007/3-540-37072-2.

[110] DOBSON, J. F., G. VIGNALE and M. P. DAS. *Electronic Density Functional Theory: Recent Progress and New Directions*. Boston, MA: Springer US, 1998. ISBN 978-1-4899-0318-1. Available from: doi:10.1007/978-1-4899-0316-7. URL: https://link.springer.com/10.1007/978-1-4899-0316-7.

[111] JENSEN, F. *Introduction to Computational Chemistry*. Second Edition. John Wiley & Sons Ltd, 2007.

[112] BARBARA, B., W. WERNSDORFER, L. C. SAMPAIO, J. G. PARK, C. PAULSEN, M. A. NOVAK, R. FERRÉ, D. MAILLY, R. SESSOLI, A. CANESCHI, K. HASSELBACH, A. BENOIT and L. THOMAS. Mesoscopic quantum tunneling of the magnetization. *Journal of Magnetism and Magnetic Materials*. 1995, vol. 140-144, no. PART 3, pp. 1825–1828. Available from: doi:10.1016/0304-8853(94)00585-0.

[113] GUO, F.-S., B. M. DAY, Y.-C. CHEN, M.-L. TONG, A. MANSIKKAMÄKI and R. A. LAYFIELD. Magnetic hysteresis up to 80 kelvin in a dysprosium metallocene single-molecule magnet. *Science*. 2018, vol. 362, no. 6421, pp. 1400–1403. Available from: doi:10.1126/science.aav0652.

[114] WERNSDORFER, W., M. MURUGESU and G. CHRISTOU. Resonant Tunneling in Truly Axial Symmetry Mn_{12} Single-Molecule Magnets: Sharp Crossover between Thermally Assisted and Pure Quantum Tunneling. *Physical Review Letters*. 2006, vol. 96, pp. 057208. Available from: doi:10.1103/PhysRevLett.96.057208.

[115] SCHALLER, C. *Tetrahedral Complexes (Web Page)*. URL: https://chem.libretexts.org/Bookshelves/Inorganic_Chemistry/Inorganic_Chemistry_%28LibreTexts%29/10%3A_Coordination_Chemistry_II_-_Bonding/10.03%3A_Ligand_Field_Theory/10.3.04%3A_Tetrahedral_Complexes.

[116] FROST, J. M., K. L. M. HARRIMAN and M. MURUGESU. The rise of 3-d single-ion magnets in molecular magnetism: towards materials from molecules? *Chemical Science*. 2016, vol. 7, pp. 2470–2491. Available from: doi:10.1039/C5SC03224E.

[117] FIGGIS, B. N. and M. A. HITCHMAN. *Ligand Field Theory and Its Applications*. 1st edition. Wiley VCH, 1999. ISBN 978-0-471-31776-0. URL: https://www.wiley.com/en-us/Ligand+Field+Theory+and+Its+Applications-p-9780471317760.

[118] HOHENBERG, P. and W. KOHN. Inhomogeneous electron gas. *Physical Review*. 1964, vol. 136, no. 3B, pp. B864. Available from: doi:10.1103/PhysRev.136.B864.

[119] KOHN, W. and L. J. SHAM. Self-consistent equations including exchange and correlation effects. *Physical Review*. 1965, vol. 140, no. 4A, pp. A1133. Available from: doi:10.1103/PhysRev.140.A1133.

[120] PERDEW, J. P., K. BURKE and M. ERNZERHOF. Generalized Gradient Approximation Made Simple. *Physical Review Letters*. 1996, vol. 77, no. 18, pp. 3865–3868. Available from: doi:10.1103/PhysRevLett.77.3865.

[121] PERDEW, J. P., K. BURKE and M. ERNZERHOF. Generalized Gradient Approximation Made Simple [Errata Phys. Rev. Lett. 77, 3865 (1996)]. *Physical Review Letters*. 1997, vol. 78, no. 7, pp. 1396–1396. Available from: doi:10.1103/PhysRevLett.78.1396.

[122] GRIMME, S. Semiempirical GGA-type density functional constructed with a long-range dispersion correction. *Journal of Computational Chemistry*. 2006, vol. 27, no. 15, pp. 1787–1799. Available from: doi:https://doi.org/10.1002/jcc.20495.

[123] GRIMME, S., J. ANTONY, S. EHRLICH and H. KRIEG. A consistent and accurate ab initio parametrization of density functional dispersion correction (DFT-D) for the 94 elements H-Pu. *Journal of Chemical Physics*. 2010, vol. 132, no. 15, pp. 154709. Available from: doi:10.1063/1.3382344.

[124] GRIMME, S., S. EHRLICH and L. GOERIGK. Effect of the damping function in dispersion corrected density functional theory. *Journal of Computational Chemistry*. 2011, vol. 32, no. 7, pp. 1456–1465. Available from: doi:10.1002/jcc.21759.

[125] BECKE, A. D. Density-functional exchange-energy approximation with correct asymptotic behavior. *Physical Review A*. 1988, vol. 38, no. 6, pp. 3098–3100. Available from: doi:10.1103/PhysRevA.38.3098.

[126] LEE, C., W. YANG and R. G. PARR. Development of the Colle-Salvetti correlation-energy formula into a functional of the electron density. *Physical Review B*. 1988, vol. 37, no. 2, pp. 785–789. Available from: doi:10.1103/PhysRevB.37.785.

[127] STEPHENS, P. J., F. J. DEVLIN, C. F. CHABALOWSKI and M. J. FRISCH. Ab Initio calculation of vibrational absorption and circular dichroism spectra using density functional force fields. *The Journal of Physical Chemistry*. 1994, vol. 98, no. 45, pp. 11623–11627. Available from: doi:10.1021/j100096a001.

[128] GOERIGK, L. and S. GRIMME. A thorough benchmark of density functional methods for general main group thermochemistry, kinetics, and noncovalent interactions. *Physical Chemistry Chemical Physics*. 2011, vol. 13, no. 14, pp. 6670–6688. Available from: doi:10.1039/c0cp02984j.

[129] KRESSE, G. and J. HAFNER. Ab initio molecular dynamics for liquid metals. *Physical Review B*. 1993, vol. 47, no. 1, pp. 558–561. Available from: doi:10.1103/PhysRevB.47.558.

[130] KRESSE, G. and J. FURTHMÜLLER. Efficiency of ab-initio total energy calculations for metals and semiconductors using a plane-wave basis set. *Computational Materials Science*. 1996, vol. 6, no. 1, pp. 15–50. Available from: doi:10.1016/0927-0256(96)00008-0.

[131] KRESSE, G. and J. FURTHMÜLLER. Efficient iterative schemes for ab initio total-energy calculations using a plane-wave basis set. *Physical Review B*. 1996, vol. 54, no. 16, pp. 11169–11186. Available from: doi:10.1103/PhysRevB.54.11169.

[132] KRESSE, G. and D. JOUBERT. From ultrasoft pseudopotentials to the projector augmented-wave method. *Physical Review B*. 1999, vol. 59, no. 3, pp. 1758–1775. Available from: doi:10.1103/PhysRevB.59.1758.

[133] BLÖCHL, P. E. Projector augmented-wave method. *Physical Review B*. 1994, vol. 50, no. 24, pp. 17953–17979. Available from: doi:10.1103/PhysRevB.50.17953.

[134] NEESE, F. Software update: the ORCA program system, version 4.0. *WIREs Computational Molecular Science*. 2018, vol. 8, no. 1, pp. e1327. Available from: doi:10.1002/wcms.1327.

[135] WEIGEND, F. and R. AHLRICHS. Balanced basis sets of split valence, triple zeta valence and quadruple zeta valence quality for H to Rn: Design and assessment of accuracy. *Physical Chemistry Chemical Physics*. 2005, vol. 7, no. 18, pp. 3297–3305. Available from: doi:10.1039/b508541a.

[136] WEIGEND, F. Accurate Coulomb-fitting basis sets for H to Rn. *Physical Chemistry Chemical Physics*. 2006, vol. 8, no. 9, pp. 1057–1065. Available from: doi:10.1039/b515623h.

[137] XU, L., Y. V. MIRONOV, X. QI and S. J. KIM. A new Co(II) complex with N,O-donor Schiff base: Synthesis, structure and characterization. *Journal of Structural Chemistry*. 2006, vol. 47, no. 5, pp. 998–1001. Available from: doi:10.1007/s10947-006-0418-1.

[138] MONKHORST, H. J. and J. D. PACK. Special points for Brillouin-zone integrations. *Physical Review B*. 1976, vol. 13, no. 12, pp. 5188–5192. Available from: doi:10.1103/PhysRevB.13.5188.

[139] HELLWEG, A., C. HÄTTIG, S. HÖFENER and W. KLOPPER. Optimized accurate auxiliary basis sets for RI-MP2 and RI-CC2 calculations for the atoms Rb to Rn. *Theoretical Chemistry Accounts*. 2007, vol. 117, no. 4, pp. 587–597. Available from: doi:10.1007/s00214-007-0250-5.

[140] BECKE, A. D. Density-functional thermochemistry. III. The role of exact exchange. *The Journal of Chemical Physics*. 1993, vol. 98, no. 7, pp. 5648–5652. Available from: doi:10.1063/1.464913.

[141] MALMQVIST, P. Å. and B. O. ROOS. The CASSCF state interaction method. *Chemical Physics Letters*. 1989, vol. 155, no. 2, pp. 189–194. Available from: doi:10.1016/0009-2614(89)85347-3.

[142] ANGELI, C., R. CIMIRAGLIA, S. EVANGELISTI, T. LEININGER and J. P. MALRIEU. Introduction of n-electron valence states for multireference perturbation theory. *Journal of Chemical Physics*. 2001, vol. 114, no. 23, pp. 10252. Available from: doi:10.1063/1.1361246.

[143] GANYUSHIN, D. and F. NEESE. First-principles calculations of zero-field splitting parameters. *Journal of Chemical Physics*. 2006, vol. 125, no. 2, pp. 024103. Available from: doi:10.1063/1.2213976.

[144] NEESE, F. Efficient and accurate approximations to the molecular spin-orbit coupling operator and their use in molecular g-tensor calculations. *Journal of Chemical Physics*. 2005, vol. 122, no. 3, pp. 034107. Available from: doi:10.1063/1.1829047.

[145] MAURICE, R., R. BASTARDIS, C. de GRAAF, N. SUAUD, T. MALLAH and N. GUIHÉRY. Universal theoretical approach to extract anisotropic spin hamiltonians. *Journal of Chemical Theory and Computation*. 2009, vol. 5, no. 11, pp. 2977–2984. Available from: doi:10.1021/ct900326e.

[146] STOLL, S. and A. SCHWEIGER. EasySpin, a comprehensive software package for spectral simulation and analysis in EPR. *Journal of Magnetic Resonance*. 2006, vol. 178, no. 1, pp. 42–55. Available from: doi:10.1016/j.jmr.2005.08.013.

[147] ADAMO, C. and V. BARONE. Toward reliable density functional methods without adjustable parameters: The PBE0 model. *Journal of Chemical Physics*. 1999, vol. 110, no. 13, pp. 6158–6170. Available from: doi:10.1063/1.478522.

[148] HOSSAIN, S. M., S. KAMILYA, S. GHOSH, R. HERCHEL, M. A. KISKIN, S. MEHTA and A. MONDAL. Tuning of Dimensionality and Nuclearity as a Function of Ligand Field Modulation Resulting in Field-Induced Cobalt(II) Single-Ion Magnet. *Crystal Growth & Design*. 2023, vol. 11, pp. 42. Available from: doi:10.1021/acs.cgd.2c01255.

[149] HAVLÍČEK, L., R. HERCHEL, I. NEMEC and P. NEUGEBAUER. Weak antiferromagnetic interaction in Cu(II) complex with semi-coordination exchange pathway. *Polyhedron*. 2022, vol. 223, pp. 115962. Available from: doi:10.1016/j.poly.2022.115962.

[150] GUSEV, A. N., I. NEMEC, R. HERCHEL, Y. I. BALUDA, M. A. KRYUKOVA, N. N. EFIMOV, M. A. KISKIN and W. LINERT. A new series of Schiff base Ni(II)4 cubanes: Evaluation of magnetic coupling via carboxylate bridges. *Polyhedron*. 2021, vol. 196, pp. 115017. Available from: doi:10.1016/j.poly.2020.115017.

[151] BHANJA, A., L. SMYTHE, R. HERCHEL, I. NEMEC, M. MURRIE and D. RAY. Hydroxido supported and differently networked octanuclear Ni6Ln2[Ln = GdIIIand DyIII] complexes: structural variation, magnetic properties and theoretical insights. *Dalton Transactions*. 2021, vol. 50, no. 14, pp. 5023–5035. Available from: doi:10.1039/d0dt04168h.

[152] RYBNÍČKOVÁ, B., J. KUCHÁR, P. ANTAL and R. HERCHEL. Synthesis, crystal structure and magnetic properties of tetranuclear copper complex based on [(4-bromophenyl)(hydroxy)methylene]bis(phosphonic acid). *Inorg. Chim. Acta*. 2020, vol. 509, pp. 119689. Available from: doi:10.1016/j.ica.2020.119689.

[153] ŠALITROŠ, I., R. HERCHEL, O. FUHR, R. GONZÁLEZ-PRIETO and M. RUBEN. Polynuclear Iron(II) Complexes with 2,6-Bis(pyrazol-1-yl)pyridine-anthracene Ligands Exhibiting Highly Distorted High-Spin Centers. *Inorg. Chem.* 2019, vol. 58, no. 7, pp. 4310–4319. Available from: doi:10.1021/acs.inorgchem.8b03432.

[154] VYDROV, O. A. and T. VAN VOORHIS. Nonlocal van der Waals density functional: The simpler the better. *Journal of Chemical Physics*. 2010, vol. 133, no. 24, pp. 244103. Available from: doi:10.1063/1.3521275.

[155] HUJO, W. and S. GRIMME. Performance of the van der waals density functional VV10 and (hybrid)GGA variants for thermochemistry and noncovalent interactions. *Journal of Chemical Theory and Computation*. 2011, vol. 7, no. 12, pp. 3866–3871. Available from: doi:10.1021/ct200644w.

[156] PRESS, W. H., B. P. FLANNERY, S. A. TEUKOLSKY and W. T. VETTERLING. *Numerical recipes : the art of scientific computing*. New York: Cambridge University Press, 1986. URL: https://archive.org/details/numericalrecipes00pres/page/n9/mode/2up.

[157] PULAY, P. Convergence acceleration of iterative sequences. the case of scf iteration. *Chemical Physics Letters*. 1980, vol. 73, no. 2, pp. 393–398. Available from: doi:10.1016/0009-2614(80)80396-4.

[158] WANG, V., N. XU, J.-C. LIU, G. TANG and W.-T. GENG. VASPKIT: A user-friendly interface facilitating high-throughput computing and analysis using VASP code. *Computer Physics Communications*. 2021, vol. 267, pp. 108033. Available from: doi:https://doi.org/10.1016/j.cpc.2021.108033.

[159] NEUGEBAUER, J. and M. SCHEFFLER. Adsorbate-substrate and adsorbate-adsorbate interactions of Na and K adlayers on Al(111). *Physical Review B*. 1992, vol. 46, no. 24, pp. 16067–16080. Available from: doi:10.1103/PhysRevB.46.16067.

[160] YAN, J., Y. ZHANG, P. KIM and A. PINCZUK. Electric field effect tuning of electron-phonon coupling in graphene. *Physical Review Letters*. 2007, vol. 98, no. 16, pp. 166802. Available from: doi:10.1103/PhysRevLett.98.166802.

[161] FRIEDMAN, J. R., M. P. SARACHIK, J. TEJADA and R. ZIOLO. Macroscopic measurement of resonant magnetization tunneling in high-spin molecules. *Physical Review Letters*. 1996, vol. 76, no. 20, pp. 3830–3833. Available from: doi:10.1103/PhysRevLett.76.3830.

[162] RUIZ, E., J. CANO, S. ALVAREZ and P. ALEMANY. Broken symmetry approach to calculation of exchange coupling constants for homobinuclear and heterobinuclear transition metal complexes. *Journal of Computational Chemistry*. 1999, vol. 20, no. 13, pp. 1391–1400. Available from: doi:10.1002/(SICI)1096-987X(199910)20:13<1391::AID-JCC6>3.0.CO;2-J.

[163] SODA, T., Y. KITAGAWA, T. ONISHI, Y. TAKANO, Y. SHIGETA, H. NAGAO, Y. YOSHIOKA and K. YAMAGUCHI. Ab initio computations of effective exchange integrals for H-H, H-He-H and Mn 2 O 2 complex: Comparison of broken-symmetry approaches. *Chemical Physics Letters*. 2000, vol. 319, no. 3-4, pp. 223–230. Available from: doi:10.1016/S0009-2614(00)00166-4.

[164] ORLITA, M., P. NEUGEBAUER, C. FAUGERAS, A.-L. BARRA, M. POTEMSKI, F. M. D. PELLEGRINO and D. M. BASKO. Cyclotron Motion in the Vicinity of a Lifshitz Transition in Graphite. *Physical Review Letters*. 2012, vol. 108, no. 1, pp. 017602. Available from: doi:10.1103/PhysRevLett.108.017602.

[165] MOMMA, K. and F. IZUMI. VESTA: A three-dimensional visualization system for electronic and structural analysis. *Journal of Applied Crystallography*. 2008, vol. 41, no. 3, pp. 653–658. Available from: doi:10.1107/S0021889808012016.

7. Author Publications and Outputs

Articles

- **Navarro Giraldo J. A.**, Hrubý J., Vavrečková Š., Fellner O. F., Havlíček L., Henry D., de Silva S., Herchel R., Bartoš M., Šalitroš I., Santana V. T., Barbara P., Nemec I., and Neugebauer P. Tetracoordinate Co(II) Complexes with Semi-Coordination as Stable Single-Ion Magnets for Deposition on Graphene, *Phys. Chem. Chem. Phys.* **25**, 29516 (2023).
- Hrubý J., Vavrečková Š., Masaryk L., Sojka A., **Navarro-Giraldo J.**, Bartoš M., Herchel R., Moncol J., Nemec I. and Neugebauer P. Deposition of Tetracoordinate Co(II) Complex with Chalcone Ligands on Graphene. *Molecules* **25** 5021 (2020).
- **Navarro-Giraldo J.** and Quimbay C. Two-dimensional Klein tunneling for massive Dirac fermions with a defined helicity. *Ann. Phys. (N. Y).* **412** 168022 (2020)

Previous Articles

- **Navarro-Giraldo, J. A.** and Quimbay, C. J., Bandgap and pseudohelicity effects over conductance in gapped graphene junctures. *J. Phys. Condens. Matter* **30**, 265304 (2018).

Conferences and Posters

- October 2023 - CEITEC Postdoc and PhD Retreat, Milovy, Czech Republic. Organizer.
- September 2022 - CEITEC PhD Retreat, Telč, Czech Republic. Poster title: Deposition of a Co(II) paramagnetic molecular compound on graphene: theory and experiment. Organizer.
- July 2022 - 8th European Conference on Molecular Magnetism (ECMM), Rennes, France. Poster title: Deposition of a Co(II) paramagnetic molecular compound on graphene: theory and experiment.
- September 2021 - CEITEC PhD Retreat 2021 (Online). Organizer.
- June 2021 - 17th International Conference on Molecule Based Magnets (ICMM), online, Manchester, UK. ePoster title: DFT study of Cobalt-based single-molecule magnet deposition on graphene.
- October 2020 - Graphene online 2020, Grenoble, France. ePoster title: Two-dimensional Klein tunneling for massive Dirac fermions with a defined helicity.
- September 2019 - Hands-On DFT and Beyond: High-throughput screening and big-data analytics, towards exascale computational materials science, Barcelona, Spain. Poster title: Bandgap and pseudohelicity effects over conductance in gapped graphene junctures.
- June 2019 - 1st International workshop on plasmon-enhanced electron paramagnetic resonance, Hirschegg, Austria.

Internships

- November 2019 - National Graphene Institute, Manchester, United Kingdom. Supervisor: Dr. Sergey Slizhovsky.
- May, June 2022 - Laboratoire de Physique et Modélisation des Milieux Condensés (LPMMC), Grenoble, France. Supervisor: Dr. Denis Basko.

Collaborations

- Collaboration with Dr. Denis Basko from Laboratoire de Physique et Modélisation des Milieux Condensés (LPMMC) in Grenoble, France. We study the emergence of charge-density waves in graphite at high magnetic fields and their possible signatures on the magneto-optical response from a theoretical perspective.
- Collaboration with the group of Prof. Paola Barbara at Georgetown University in Washington D.C., U.S.A., on the deposition and transport properties of single-molecule magnets deposited on graphene and graphene quantum dots.

Mentoring of Master's Thesis

- 2021 - Mentorship of the master's thesis entitled "Nízkoenergetická Excitace v Orientovaném Graphitu Pomocí THz Magnetooptické Spektroskopie" by Jan Dubský, Mgr. I oriented Mr. Dubský with the theoretical analysis of the experimental measurements (HFEPR) he performed on graphite. The analysis used numerical computations on Python that I implemented based on existing theory [164].

Other Activities

- Chair of the CEITEC Student Committee. We organize various activities with the aim of bringing cohesion and the dissemination of scientific endeavours between all CEITEC institutes.

A. Spin-Density Waves of Graphite: Intermediate Calculations

In this appendix, we show in more detail the calculations employed to obtain the main results of the SDW of graphite. We start by computing the form factors Eq. (2.25), then we use them to find an approximation to the Coulomb interaction, which is necessary to obtain the Hamiltonian in the Hartree-Fock (HF) approximation. We conclude by showing some numerical results for the SDW gap, self-energy, and total energy per particle for different values of the dielectric constant $\tilde{\varepsilon}$, and the interaction parameters Ξ_0, Ξ_1

A.1. Calculation of the Form Factors

We start by considering the full expression of the Coulomb interaction of electrons in the lowest-lying Landau bands of graphite in second quantization, displayed in Eq. (2.24)

$$\begin{aligned}\hat{\mathcal{H}}_{\text{Coulomb}} = \frac{1}{2}\frac{1}{V}\sum_{\boldsymbol{q}}\sum_{\text{all ind.}} v(\boldsymbol{q})\Big[&\mathcal{F}_{(0\downarrow,p_1,k_1);\,(0\downarrow,p_4,k_4)}(\boldsymbol{q})\,\mathcal{F}_{(0\downarrow,p_2,k_2);\,(0\downarrow,p_3,k_3)}(-\boldsymbol{q})\hat{a}^\dagger_{p_1k_1}\hat{a}^\dagger_{p_2k_2}\hat{a}_{p_3k_3}\hat{a}_{p_4k_4}\\ &+\mathcal{F}_{(-1\uparrow,p_1,k_1);\,(-1\uparrow,p_4,k_4)}(\boldsymbol{q})\,\mathcal{F}_{(-1\uparrow,p_2,k_2);\,(-1\uparrow,p_3,k_3)}(-\boldsymbol{q})\hat{b}^\dagger_{p_1k_1}\hat{b}^\dagger_{p_2k_2}\hat{b}_{p_3k_3}\hat{b}_{p_4k_4}\\ &+2\,\mathcal{F}_{(0\downarrow,p_1,k_1);\,(0\downarrow,p_4,k_4)}(\boldsymbol{q})\,\mathcal{F}_{(-1\uparrow,p_2,k_2);(-1\uparrow,p_3,k_3)}(-\boldsymbol{q})\hat{a}^\dagger_{p_1k_1}\hat{b}^\dagger_{p_2k_2}\hat{b}_{p_3k_3}\hat{a}_{p_4k_4}\Big].\end{aligned} \tag{A.1}$$

with $V = L_xL_yL_z$ the sample volume, $v(\boldsymbol{q}) = e^2/(4\pi\varepsilon_0\tilde{\varepsilon}\,|\boldsymbol{q}|^2)$ the Fourier transform of the Coulomb interaction in S.I units, ε_0 the vacuum permittivity, and $\tilde{\varepsilon}$ a dimensionless effective dielectric constant.

The form factors are defined as

$$\mathcal{F}_{(N\sigma,p,k);\,(N'\sigma',p',k')}(\boldsymbol{q}) = \delta_{\sigma\sigma'}\int d\boldsymbol{r}\, e^{-i\boldsymbol{q}\cdot\boldsymbol{r}}\Psi^{(N\sigma)\dagger}_{pk}(\boldsymbol{r})\Psi^{(N'\sigma')}_{p'k'}(\boldsymbol{r}). \tag{A.2}$$

In this definition, the full wave function in three dimensions of Eq. (2.2) is required:

$$\Psi^{(N\sigma)}_{pk}(\boldsymbol{r}_\parallel,z) = \frac{e^{i\boldsymbol{K}\cdot\boldsymbol{r}_\parallel}}{\sqrt{L_z}}\eta_\sigma\sum_n e^{ikn}\begin{pmatrix} e^{ik/2}\,\psi_{1A}(\boldsymbol{r}_\parallel)\,u_{1A}(\boldsymbol{r}_\parallel,z-c_0n-c_0/2)\\ e^{ik/2}\,\psi_{1B}(\boldsymbol{r}_\parallel)\,u_{1B}(\boldsymbol{r}_\parallel,z-c_0n-c_0/2)\\ \psi_{2A}(\boldsymbol{r}_\parallel)\,u_{2A}(\boldsymbol{r}_\parallel,z-c_0n)\\ \psi_{2B}(\boldsymbol{r}_\parallel)\,u_{2B}(\boldsymbol{r}_\parallel,z-c_0n)\end{pmatrix}, \tag{A.3}$$

with $u_{j\alpha}$ the Bloch-Wannier functions, and the envelope functions

$$\psi^{(N)}_{pk}(\boldsymbol{r}_\parallel) = \begin{pmatrix}\psi_{1A}(\boldsymbol{r}_\parallel)\\ \psi_{1B}(\boldsymbol{r}_\parallel)\\ \psi_{2A}(\boldsymbol{r}_\parallel)\\ \psi_{2B}(\boldsymbol{r}_\parallel)\end{pmatrix} = \frac{e^{ipx}}{\sqrt{L_x}}\begin{pmatrix}\chi^{(N)}_{1A,k}(\xi)\\ \chi^{(N)}_{1B,k}(\xi)\\ \chi^{(N)}_{2A,k}(\xi)\\ \chi^{(N)}_{2B,k}(\xi)\end{pmatrix}, \tag{A.4}$$

with $\xi = y/l_B + pl_B$, and $\chi_k^{(N)}$ proportional to the harmonic oscillator wave functions φ_N. For the lowest-lying Landau bands, the envelope functions take the form

$$\psi_{pk}^{(-1)}(x,y) = \frac{e^{ipx}}{\sqrt{L_x}} \begin{pmatrix} 0 \\ 0 \\ 0 \\ \varphi_0(\xi) \end{pmatrix} = \frac{e^{ipx}}{\sqrt{L_x}} \begin{pmatrix} 0 \\ 0 \\ 0 \\ 1 \end{pmatrix} \frac{e^{-\xi^2/2}}{(\pi l_B^2)^{1/4}}, \tag{A.5}$$

$$\psi_{pk}^{(0)}(x,y) = \frac{e^{ipx}}{\sqrt{L_x}} \frac{1}{\sqrt{\varepsilon_B^2 + \Gamma_1^2}} \begin{pmatrix} 0 \\ \varepsilon_B\ \varphi_0(\xi) \\ 0 \\ -\Gamma_1\ \varphi_1(\xi) \end{pmatrix} = \frac{e^{ipx}}{\sqrt{L_x}} \frac{1}{\sqrt{\varepsilon_B^2 + \Gamma_1^2}} \begin{pmatrix} 0 \\ \varepsilon_B \\ 0 \\ -\Gamma_1\sqrt{2}\xi \end{pmatrix} \frac{e^{-\xi^2/2}}{(\pi l_B^2)^{1/4}}. \tag{A.6}$$

Computing the form factors directly, we have

$$\begin{aligned} \mathcal{F}_{(N\sigma,p,k);(N'\sigma',p',k')}(\boldsymbol{q}) = \delta_{\sigma\sigma'} \frac{1}{L_z} \sum_{n,n'} \int d\boldsymbol{r}\, e^{-i\boldsymbol{q}\cdot\boldsymbol{r}}\, e^{-ikn+ik'n'} \\ \sum_{\alpha=A,B} \Big(e^{-i(k-k')/2} [\psi_{1\alpha,pk}^{(N)}(\boldsymbol{r}_\parallel)]^*\, \psi_{1\alpha,p'k'}^{(N')}(\boldsymbol{r}_\parallel)\, u_{1\alpha}^*(\boldsymbol{r}_\parallel, z - c_0 n - c_0/2)\, u_{1\alpha}(\boldsymbol{r}_\parallel, z - c_0 n' - c_0/2) \\ + [\psi_{2\alpha,pk}^{(N)}(\boldsymbol{r}_\parallel)]^*\, \psi_{2\alpha,p'k'}^{(N')}(\boldsymbol{r}_\parallel)\, u_{2\alpha}^*(\boldsymbol{r}_\parallel, z - c_0 n)\, u_{2\alpha}(\boldsymbol{r}_\parallel, z - c_0 n') \Big) \end{aligned} \tag{A.7}$$

The z dependence of the wave function is contained only in the Bloch-Wannier functions $u_{j\alpha}$. Therefore, we start by integrating with respect to this variable. As an example, taking the first term in the sum of the last equation and considering the orthogonality of the Bloch-Wannier functions, we have

$$\begin{aligned} &\frac{1}{L_z} \int dz\, e^{-iq_z z} \sum_{n,n'} e^{-ikn+ik'n'} e^{-i(k-k')/2} u_{1\alpha}^*(\boldsymbol{r}_\parallel, z - c_0 n - c_0/2)\, u_{1\alpha}(\boldsymbol{r}_\parallel, z - c_0 n' - c_0/2), \\ &= \frac{1}{L_z} \sum_{n=0}^{L_z/c_0} e^{-i(k-k')(n+1/2)} \int dz\, e^{-iq_z z} |u_{1\alpha}(\boldsymbol{r}_\parallel, z - c_0 n - c_0/2)|^2, \\ &= \frac{1}{L_z} \sum_{n=0}^{L_z/c_0} e^{-i(k-k'+q_z c_0)(n+1/2)} \int dz\, e^{-iq_z z} |u_{1\alpha}(\boldsymbol{r}_\parallel, z)|^2, \\ &= \frac{2\pi}{L_z} \sum_{s=-\infty}^{\infty} (-1)^s \delta(k - k' + q_z c_0 - 2\pi s) \int dz\, e^{-iq_z z} |u_{1\alpha}(\boldsymbol{r}_\parallel, z)|^2, \end{aligned} \tag{A.8}$$

where in the last line, we used the representation of the delta function as a sum of plane waves, and we considered the periodicity of the unit cell in the reciprocal space illustrated by the term $2\pi s$, with s integer.

Proceeding with the integrals on x and y, it is noticed that the Bloch-Wannier functions also depend on them; however, such dependence is weak compared to the envelope functions, allowing us to work with the average of $u_{j\alpha}$ over the unit cell instead. Additionally, the wave function dependence on x is through the plane-wave term e^{ipx}, as in Eq. (A.4), allowing us to write

$$\begin{aligned}
&\sum_{j=1,2}\sum_{\alpha=A,B}\int d\boldsymbol{r}_\parallel\, e^{-iq_x x-iq_y y}[\psi^{(N)}_{j\alpha,pk}(\boldsymbol{r}_\parallel)]^*\,\psi^{(N')}_{j\alpha,p'k'}(\boldsymbol{r}_\parallel)\int dz\, e^{-iq_z z}|u_{j\alpha}(\boldsymbol{r}_\parallel,z)|^2\\
&\quad=\sum_{j=1,2}\sum_{\alpha=A,B}\int dx\,\frac{e^{-ix(p-p'+q_x)}}{L_x}\int dy\, e^{-iyq_y}\chi^{(N)}_{j\alpha,k}(\xi)\,\chi^{(N')}_{j\alpha,k'}(\xi')\left[\int_{\text{u.c.}} d\boldsymbol{r}_\parallel dz\,\frac{e^{-iq_z z}}{A_{\text{u.c}}}|u_{j\alpha}(\boldsymbol{r}_\parallel,z)|^2\right]\\
&\quad=\sum_{j=1,2}\sum_{\alpha=A,B}\frac{2\pi}{L_x}\delta(p-p'+q_x)\int dy\, e^{-iyq_y}\chi^{(N)}_{j\alpha,k}(\xi)\,\chi^{(N')}_{j\alpha,k'}(\xi')\left[\int_{\text{u.c.}} d\boldsymbol{r}_\parallel dz\,\frac{e^{-iq_z z}}{A_{\text{u.c}}}|u_{j\alpha}(\boldsymbol{r}_\parallel,z)|^2\right]
\end{aligned}\tag{A.9}$$

with $\xi'=y/l_B+p'l_B$.

Taking into account that $q_x=p'-p$, we arrive at the following result for the form factors

$$\begin{aligned}
\mathcal{F}_{(N\sigma,p,k);(N'\sigma',p',k')}(\boldsymbol{q})=&\frac{4\pi^2}{L_xL_z}\delta_{\sigma\sigma'}\delta(p-p'+q_x)e^{iq_y l_B^2(p+p')/2}\\
&\sum_{j=1,2}\sum_{\alpha=A,B}\varrho_{Nk,N'k',j\alpha}(\boldsymbol{q})\sum_{s=-\infty}^{\infty}(-1)^{js}\delta(k-k'+q_zc_0-2\pi s),
\end{aligned}\tag{A.10}$$

where it was defined

$$\begin{aligned}
\varrho_{Nk,N'k',j\alpha}(\boldsymbol{q})=&\int dy\, e^{-iyq_y}\chi^{(N)}_{j\alpha,k}(y/l_B-q_xl_B/2)\,\chi^{(N')}_{j\alpha,k'}(y/l_B+q_xl_B/2)\\
&\times\left[\int_{\text{u.c.}} d\boldsymbol{r}_\parallel dz\,\frac{e^{-iq_z z}}{A_{\text{u.c}}}|u_{j\alpha}(\boldsymbol{r}_\parallel,z)|^2\right].
\end{aligned}\tag{A.11}$$

Therefore, the specific value for the form factors depends on the term in the last equation. Computing for the first form factor,

$$\begin{aligned}
&\sum_{j=1,2}\sum_{\alpha=A,B}\int dy\, e^{-iyq_y}\chi^{(-1)}_{j\alpha,k}(y/l_B-q_xl_B/2)\,\chi^{(-1)}_{j\alpha,k'}(y/l_B+q_xl_B/2)\\
&\quad=\frac{1}{\sqrt{\pi l_B^2}}\int dy\, e^{-iyq_y}e^{-(y/l_B-q_xl_B/2)^2/2-(y/l_B+q_xl_B/2)^2/2}\\
&\quad=\frac{1}{\sqrt{\pi l_B^2}}\,e^{-q_x^2l_B^2/4}\int dy\, e^{-iyq_y}e^{-y^2/l_B^2}\\
&\quad=e^{-q_\parallel^2l_B^2/4},
\end{aligned}\tag{A.12}$$

with $q_\parallel^2=q_x^2+q_y^2$. For the second form factor,

$$\begin{aligned}
&\sum_{j=1,2}\sum_{\alpha=A,B}\int dy\, e^{-iyq_y}\chi^{(0)}_{j\alpha,k}(y/l_B-q_xl_B/2)\,\chi^{(0)}_{j\alpha,k'}(y/l_B+q_xl_B/2)\\
&\quad=\frac{1}{\sqrt{\pi l_B^2}}\frac{1}{\sqrt{\varepsilon_B^2+\Gamma_{1,k}^2}\sqrt{\varepsilon_B^2+\Gamma_{1,k'}^2}}\int dy\, e^{-iyq_y}e^{-(y/l_B-q_xl_B/2)^2/2-(y/l_B+q_xl_B/2)^2/2}\\
&\quad\times\left[\varepsilon_B^2+2\Gamma_{1,k}\Gamma_{1,k'}(y/l_B-q_xl_B/2)(y/l_B+q_xl_B/2)\right]\\
&\quad=\frac{1}{\sqrt{\pi l_B^2}}\frac{e^{-q_x^2l_B^2/4}}{\sqrt{\varepsilon_B^2+\Gamma_{1,k}^2}\sqrt{\varepsilon_B^2+\Gamma_{1,k'}^2}}\int dy\, e^{-iyq_y}e^{-y^2/l_B^2}\left(\varepsilon_B^2+2\Gamma_{1,k}\Gamma_{1,k'}\left[\frac{y^2}{l_B^2}-\frac{q_x^2l_B^2}{4}\right]\right)\\
&\quad=\frac{e^{-q_\parallel^2l_B^2/4}}{\sqrt{\varepsilon_B^2+\Gamma_{1,k}^2}\sqrt{\varepsilon_B^2+\Gamma_{1,k'}^2}}\left(\varepsilon_B^2+\Gamma_{1,k}\Gamma_{1,k'}\left[1-\frac{q_\parallel^2l_B^2}{2}\right]\right)\\
&\quad\approx e^{-q_\parallel^2l_B^2/4}\left(1-\frac{2\gamma_1^2}{\varepsilon_B^2+4\gamma_1^2}q_\parallel^2l_B^2\right).
\end{aligned}\tag{A.13}$$

In the last line, we approximated $\Gamma_1=2\gamma_1\cos(k/2)$ to its value at $k=k'=0$, justified by the fact that the greatest contribution of the band $\varepsilon_{0\downarrow}$ to the SDW phase is in the vicinity of $k=0$.

The rather complicated expressions of the form factors can be simplified if one considers only the long-range part of the Coulomb interaction, which implies taking only the term with $s=0$ in Eq. (A.10). This way, we arrive at the following results for the form factors of interest:

$$\begin{aligned}
\mathcal{F}_{(-1\uparrow,p,k);(-1\uparrow,p',k')}(\boldsymbol{q})=&\frac{4\pi^2}{L_xL_z}\delta(p-p'+q_x)\delta(k-k'+q_zc_0)e^{iq_yl_B^2(p+p')/2}e^{-q_\parallel^2l_B^2/4}\\
&\times\sum_{j=1,2}\sum_{\alpha=A,B}\left[\int_{\text{u.c.}}d\boldsymbol{r}_\parallel dz\,\frac{e^{-iq_zz}}{A_{\text{u.c}}}|u_{j\alpha}(\boldsymbol{r}_\parallel,z)|^2\right],
\end{aligned}\tag{A.14}$$

$$\begin{aligned}
\mathcal{F}_{(0\downarrow,p,k);(0\downarrow,p',k')}(\boldsymbol{q})=&\frac{4\pi^2}{L_xL_z}\delta(p-p'+q_x)\delta(k-k'+q_zc_0)e^{iq_yl_B^2(p+p')/2}e^{-q_\parallel^2l_B^2/4}\\
&\times\left(1-\frac{2\gamma_1^2}{\varepsilon_B^2+4\gamma_1^2}q_\parallel^2l_B^2\right)\sum_{j=1,2}\sum_{\alpha=A,B}\left[\int_{\text{u.c.}}d\boldsymbol{r}_\parallel dz\,\frac{e^{-iq_zz}}{A_{\text{u.c}}}|u_{j\alpha}(\boldsymbol{r}_\parallel,z)|^2\right].
\end{aligned}\tag{A.15}$$

A.2. Approximated Coulomb Interaction

The form factors allow us to find the Coulomb interaction between electrons in the lowest-lying Landau bands, shown in Eq. (A.1). Performing the sums with respect to q_y, p_1, p_2, k_1, and k_2, using the summation rules $\sum_p\to(L_x/2\pi)\int dp$, $\sum_{q_y}\to(L_y/2\pi)\int dq_y$, and $\sum_k\to(L_z/2\pi c_0)\int dk$[1], and defining $p_3=p'$, $p_4=p$, $\boldsymbol{q}=(q_x,q_y,q_z)=(q,q_y,\kappa/c_0)$, it is straightforward to find

$$\begin{aligned}
\hat{\mathcal{H}}_{\text{Coulomb}}=&\frac{1}{2}\frac{1}{L_xL_z}\sum_{p,p',q}\sum_{k,k',\kappa}e^{iq_yl_B^2(p-p'-q)}\Big[V_{aa}(q,\kappa)\,\hat{a}^\dagger_{p-q,k-\kappa}\hat{a}^\dagger_{p'+q,k'+\kappa}\hat{a}_{p',k'}\hat{a}_{p,k}\\
&+V_{bb}(q,\kappa)\,\hat{b}^\dagger_{p-q,k-\kappa}\hat{b}^\dagger_{p'+q,k'+\kappa}\hat{b}_{p',k'}\hat{b}_{p,k}+2V_{ab}(q,\kappa)\,\hat{a}^\dagger_{p-q,k-\kappa}\hat{b}^\dagger_{p'+q,k'+\kappa}\hat{b}_{p',k'}\hat{a}_{p,k}\Big],
\end{aligned}\tag{A.16}$$

[1]The factor $1/c_0$ comes from the normalization of k with respect to the unit cell length in the z direction.

where it was defined

$$\begin{aligned} V_{aa}(q,\kappa) &= \int \frac{dq_y}{2\pi}\, v\left(q,q_y,\frac{\kappa}{c_0}\right) e^{-q_\parallel^2 l_B^2/2}\left(1-\frac{2\gamma_1^2}{\varepsilon_B^2+4\gamma_1^2}q_\parallel^2 l_B^2\right)^2, \\ V_{bb}(q,\kappa) &= \int \frac{dq_y}{2\pi}\, v\left(q,q_y,\frac{\kappa}{c_0}\right) e^{-q_\parallel^2 l_B^2/2}, \\ V_{ab}(q,\kappa) &= \int \frac{dq_y}{2\pi}\, v\left(q,q_y,\frac{\kappa}{c_0}\right) e^{-q_\parallel^2 l_B^2/2}\left(1-\frac{2\gamma_1^2}{\varepsilon_B^2+4\gamma_1^2}q_\parallel^2 l_B^2\right), \end{aligned} \tag{A.17}$$

in agreement with Eq. (2.26).

A.3. Hamiltonian in the Hartree-Fock Approximation

The Coulomb interaction is of fourth order in the fermionic creation and annihilation operators. The Hartree-Fock (HF) approximation aims to approximate it to a second-order interaction by taking a pair-wise average of the operators with respect to the Hartree-Fock ground state, as follows

$$\begin{aligned} \hat{a}^\dagger_{p-q,k-\kappa}\hat{a}^\dagger_{p'+q,k'+\kappa}\hat{a}_{p',k'}\hat{a}_{p,k} &\approx 2\hat{a}^\dagger_{p-q,k-\kappa}\hat{a}_{p,k}\left\langle \hat{a}^\dagger_{p'+q,k'+\kappa}\hat{a}_{p',k'}\right\rangle - 2\hat{a}^\dagger_{p-q,k-\kappa}\hat{a}_{p',k'}\left\langle \hat{a}^\dagger_{p'+q,k'+\kappa}\hat{a}_{p,k}\right\rangle \\ &= 2\hat{a}^\dagger_{pk}\hat{a}_{pk}\left\langle \hat{a}^\dagger_{p'k'}\hat{a}_{p'k'}\right\rangle \delta_{q,0}\delta_{\kappa,0} - 2\hat{a}^\dagger_{pk}\hat{a}_{pk}\left\langle \hat{a}^\dagger_{p'k'}\hat{a}_{p'k'}\right\rangle \delta_{q,p-p'}\delta_{\kappa,k-k'}. \end{aligned} \tag{A.18}$$

Although the HF ground state, $|\Psi_{\mathrm{HF}}\rangle$, is still undetermined at this point, we made the reasonable assumption that it does not mix electron states with different momentum components, allowing us to write $\langle \hat{a}^\dagger_{pk}\hat{a}_{p'k'}\rangle = \langle \hat{a}^\dagger_{pk}\hat{a}_{pk}\rangle \delta_{pp'}\delta_{kk'}$. The first term of the right-hand side of the equation, proportional to $\delta_{q,0}\delta_{\kappa,0}$, is called the Hartree term, and it is canceled out with the energy contribution of the ions in the graphite lattice. Therefore, the only contribution to the interaction Hamiltonian in the Hartree-Fock approximation is through the second term, called the Fock term.

It is worth taking a look at the interband interaction term:

$$\hat{a}^\dagger_{p-q,k-\kappa}\hat{b}^\dagger_{p'+q,k'+\kappa}\hat{b}_{p',k'}\hat{a}_{p,k} \approx -\left(\hat{a}^\dagger_{pk}\hat{b}_{pk}\left\langle \hat{b}^\dagger_{p'k'}\hat{a}_{p'k'}\right\rangle + \hat{b}^\dagger_{pk}\hat{a}_{pk}\left\langle \hat{b}^\dagger_{p'k'}\hat{a}_{p'k'}\right\rangle\right)\delta_{q,p-p'}\delta_{\kappa,k-k'}. \tag{A.19}$$

In the normal phase, the ground state consists of the filling of the Landau bands up to the Fermi level; therefore, we have the trivial result $\langle \hat{b}^\dagger_{p'k'}\hat{a}_{p'k'}\rangle = 0$. In the SDW phase, the ground state consists of a mix of electronic states in both bands, yielding a non-zero value for the correlator.

Inserting these approximations in the Coulomb interaction of Eq. (A.16), and adding over p', k', q and κ, we find

$$\begin{aligned} \hat{\mathcal{H}}_{\mathrm{Coulomb}} \approx -\sum_{pk}\Bigg[&\hat{a}^\dagger_{pk}\hat{a}_{pk}\int \frac{dk'}{2\pi c_0}\frac{dq}{2\pi}V_{aa}(q,k-k')\left\langle \hat{a}^\dagger_{p'k'}\hat{a}_{p'k'}\right\rangle \\ &+ \hat{b}^\dagger_{pk}\hat{b}_{pk}\int \frac{dk'}{2\pi c_0}\frac{dq}{2\pi}V_{bb}(q,k-k')\left\langle \hat{b}^\dagger_{p'k'}\hat{b}_{p'k'}\right\rangle \\ &+ \left(\hat{b}^\dagger_{pk}\hat{a}_{pk}+\hat{a}^\dagger_{pk}\hat{b}_{pk}\right)\int \frac{dk'}{2\pi c_0}\frac{dq}{2\pi}V_{ab}(q,k-k')\left\langle \hat{b}^\dagger_{p'k'}\hat{a}_{p'k'}\right\rangle\Bigg]. \end{aligned} \tag{A.20}$$

Defining

$$\begin{aligned}\Sigma_k^a &= -\int \frac{dk'}{2\pi c_0}\frac{dq}{2\pi} V_{aa}(q,k-k')\left\langle \hat{a}^\dagger_{p'k'}\hat{a}_{p'k'}\right\rangle,\\ \Sigma_{k+Q}^b &= -\int \frac{dk'}{2\pi c_0}\frac{dq}{2\pi} V_{bb}(q,k-k')\left\langle \hat{b}^\dagger_{p'k'}\hat{b}_{p'k'}\right\rangle,\\ \Delta_k &= \int \frac{dk'}{2\pi c_0}\frac{dq}{2\pi} V_{ab}(q,k-k')\left\langle \hat{b}^\dagger_{p'k'}\hat{a}_{p'k'}\right\rangle,\end{aligned} \tag{A.21}$$

and adding the Coulomb interaction in the Hartree-Fock approximation with the kinetic energy term, we arrive at the effective Hamiltonian of Eq. (2.28):

$$\begin{aligned}\hat{\mathcal{H}}_{\text{HF}} = \sum_{pk}\Big[&(\varepsilon_{0\downarrow}(k)+\Sigma_k^a)\,\hat{a}^\dagger_{pk}\hat{a}_{pk} + \left(\varepsilon_{-1\uparrow}(k+Q)+\Sigma_{k+Q}^b\right)\hat{b}^\dagger_{pk}\hat{b}_{pk}\\ &-\Delta_k\,\hat{a}^\dagger_{pk}\hat{b}_{pk} - \Delta_k^*\,\hat{b}^\dagger_{pk}\hat{a}_{pk}\Big].\end{aligned} \tag{A.22}$$

A.4. Total Energy and SDW Gap for Different Values of Ξ_0/Ξ_1, $\tilde{\varepsilon}$

We now study the dependence of the total energy as a function of Ξ_0/Ξ_1. In Fig. A.1, we plot the total energy computed from the energy functional $\mathcal{E}[\vartheta_k]$ (Eq. 2.50) as a function of the band separation δ for different values of Ξ_0/Ξ_1. For $\Xi_0/\Xi_1 \geq 1$, the total energy continuously and smoothly turns into the energy in the normal phase, $\mathcal{E}[\vartheta_k = 0] = 0$, as δ is increased. This smooth change of the energy of the collective phase to the energy of the normal phase is characteristic of second-order phase transitions. On the contrary, we see that $\Xi_0/\Xi_1 < 1$ does not result in such a smooth change, and therefore, this situation corresponds to a first-order phase transition.

Another way of verifying the order of the phase transition is by studying the behavior of the SDW gap at different values of δ and under different initial conditions of the self-consistent calculation. Fig. A.2 (a) shows the maximum value of Δ_k as a function of δ for different values

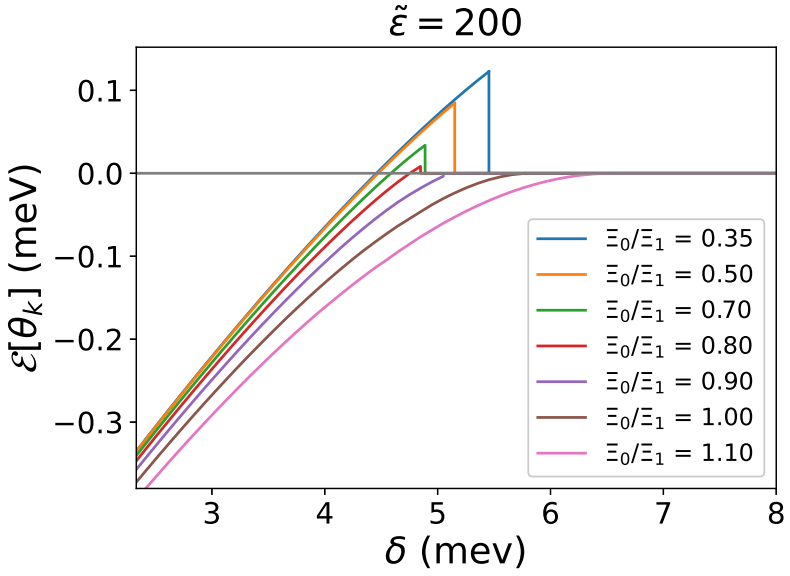

Figure A.1: Total energy as a function of the band separation δ for different values of Ξ_0/Ξ_1. The terms ϑ_k were computed taking as initial condition the values of Σ_k and Δ_k obtained from the calculation with a previous δ.

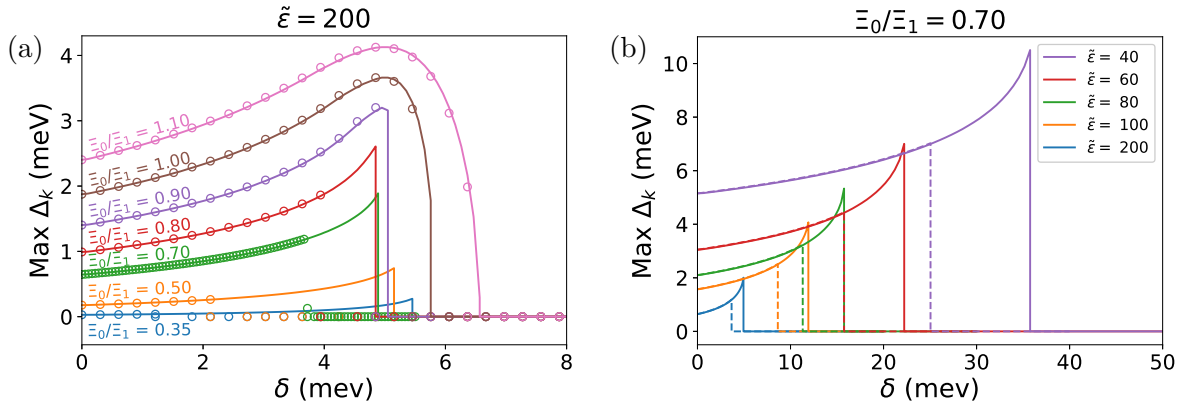

Figure A.2: Maximum value of Δ_k as a function of δ for different values of Ξ_0/Ξ_1 (a) and $\tilde{\varepsilon}$ (b). Circles and dashed lines indicate calculations with $\Sigma_k = -0.1$ meV and $\Delta_k = 0.1$ meV as constant initial conditions, while lines represent the initial conditions taken from the results of previous calculations. In both cases, $\Xi_1 = 70$ meV.

of Ξ_0/Ξ_1, and two different initial conditions: small and constant $\Delta_k = 0.1$ meV and $\Sigma_k = = -0.1$ meV, and taking as the initial condition the computed values of the previous δ. The results show that for small ratios Ξ_0/Ξ_1, the gap goes to zero abruptly at different values of δ for the two different initial conditions. This is typical of first-order phase transitions: it manifests as the hysteresis of physical quantities depending on the increase or decrease of external stimuli, as discussed in the main text. For $\Xi_0/\Xi_1 = 0.9$, the maximum gap also goes to zero abruptly, and thus, it can be classified as a phase transition of the first order. On the other hand, the gap goes to zero continuously for $\Xi_0/\Xi_1 = 1$ and 1.1, so we can infer that they correspond to a second-order phase transition. The value of δ at which they go to zero differs slightly in the two initial conditions, but this could be ascribed to numerical errors. In Fig. A.2 (b), we display the maximum Δ_k for different values of the effective dielectric constant $\tilde{\varepsilon}$, at a fixed ratio $\Xi_0/\Xi_1 = 0.7$. A lower $\tilde{\varepsilon}$ implies a higher value of Δ_k and a higher band gap δ at which the SDW phase can appear. Thus, we infer that a stronger Coulomb interaction conduces to higher values of the SDW gap.

B. Weak Localization in Graphene: Supplementary Information

In this Appendix, we present supplementary results of sample characterization by Raman spectroscopy, and the weak localization measurements by transport and high-frequency electron paramagnetic resonance (HFEPR) spectroscopy.

B.1. Raman Spectroscopy

In Chapter 3, Section 3.3, we displayed the results of Raman spectra and Raman maps on the three samples under study. In this section, we expand the analysis by showing the Raman maps of the 2D peak width, intensity, and its integration in different locations of each sample. In the aforementioned Section, it was pointed out that the presence of impurities in the sample manifests in the appearance of Raman peaks in the region 2800−3000 cm^{-1}; therefore, we studied the width of these peaks in the maps as well. The Raman maps and optical images of the scanned region are found in Figs. B.1, B.2 for sample 1; Figs. B.3, B.4, B.5 for sample 2; and Figs. B.6, B.7, B.8 for sample 3. Sample 1 is characterized by a high amount of impurities, as evidenced in the optical microscopy images of Fig. 3.4 (a) in the main text, and Figs. B.1 (a), B.2 (a). Nevertheless, the 2D peak is still present in the Raman maps, allowing us to conclude that graphene is still present below the residues of an unidentified substance. From the two scanned regions, the 2D peak width presents values from 20 to 70 cm^{-1}, typical of monolayer and bilayer graphene. This feature is also observed in the other two samples and is consistent with the fabrication process of epitaxial graphene on SiC [74, 85, 86]. In samples 2 and 3, linear regions of constant width are seen, indicating that bilayer graphene grows along those lines, as observed in the literature [74, 85, 86]. A careful inspection of the optical microscopy images of samples 2 and 3 also reveals the presence of these linear regions. The width of the peaks in the region 2800−3000 cm^{-1} is also illustrated in the subfigures (e) of the maps for samples 1 and 3. Comparing them with the corresponding optical microscope images, we conclude that they correlate with the impurities in the samples. Sample 2, on the other hand, has a very low amount of these impurities, and the corresponding impurity maps were omitted.

From the analysis of the Raman spectra and maps, we derive the following conclusions. First, all samples are composed of monolayer and bilayer graphene, as is expected of epitaxial graphene on SiC. In samples 1 and 3, impurities or residues manifest as peaks in the region 2800−3000 cm^{-1}, with the concentration of defects being higher in sample 1. Nevertheless, the characteristic graphene peaks were also observed, allowing us to infer that the sample is undamaged by these residues. Sample 2, on the other hand, presented a very low concentration of defects. we conclude that the non-uniformity and high concentration of impurities in sample 1 make it not optimal for the analysis of weak localization at high frequencies since this method probes a large sample area. In contrast, as evidenced in the main text, weak localization in transport measurements follows the expected behavior. This could be explained by the preference for high-conductance channels in the sample, which might ignore the lower-conductivity places induced by the impurities.

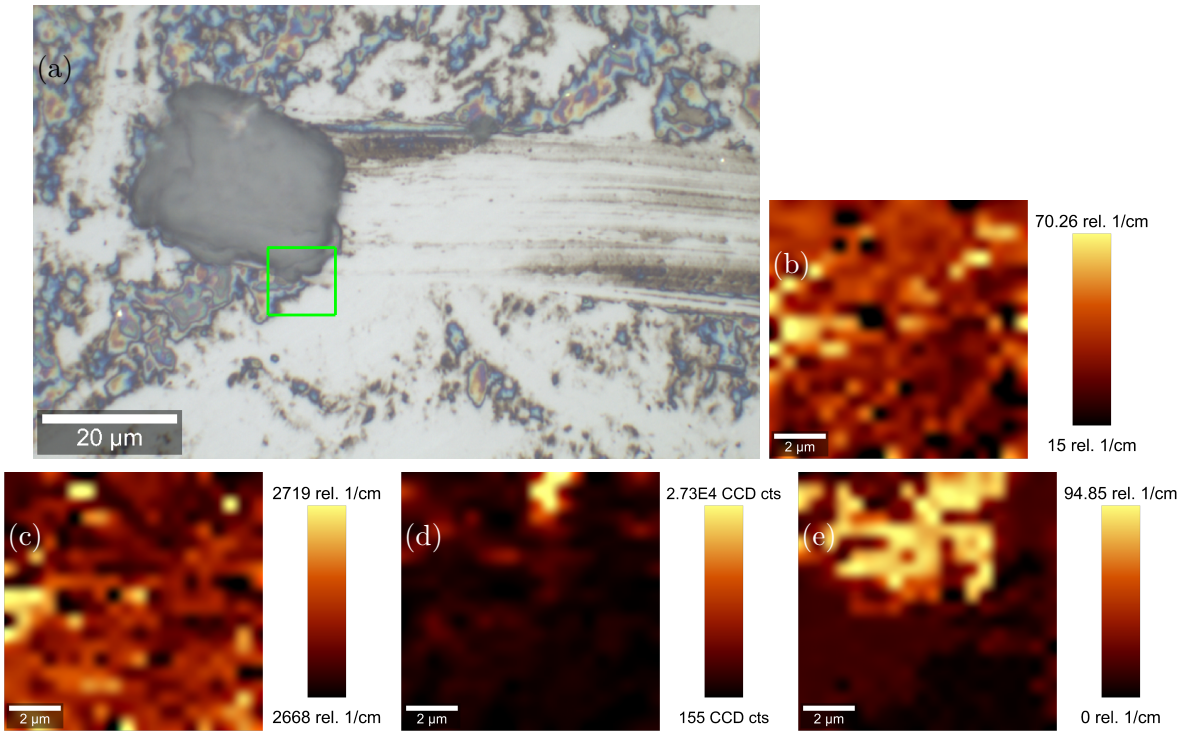

Figure B.1: Raman map #1 of sample 1. (a) Optical microscopy image, the green square is the area scanned in the Raman map. (b) 2D peak width. (c) 2D peak maximum. (d) Integration of the 2D peak. (e) Width of the peaks in the region $2800 - 3000$ cm^{-1}, indicating the presence of impurities.

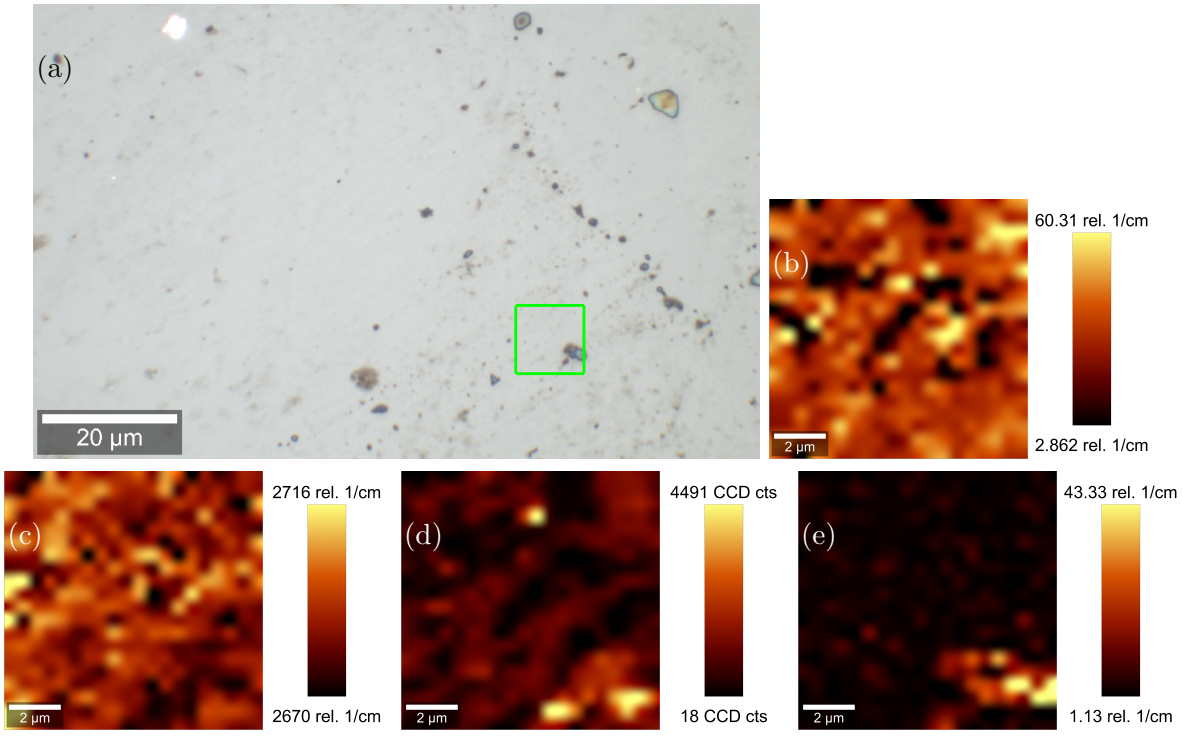

Figure B.2: Raman map #2 of sample 1. (a) Optical microscopy image, the green square is the area scanned in the Raman map. (b) 2D peak width. (c) 2D peak maximum. (d) Integration of the 2D peak. (e) Width of the peaks in the region $2800 - 3000$ cm^{-1}, indicating the presence of impurities.

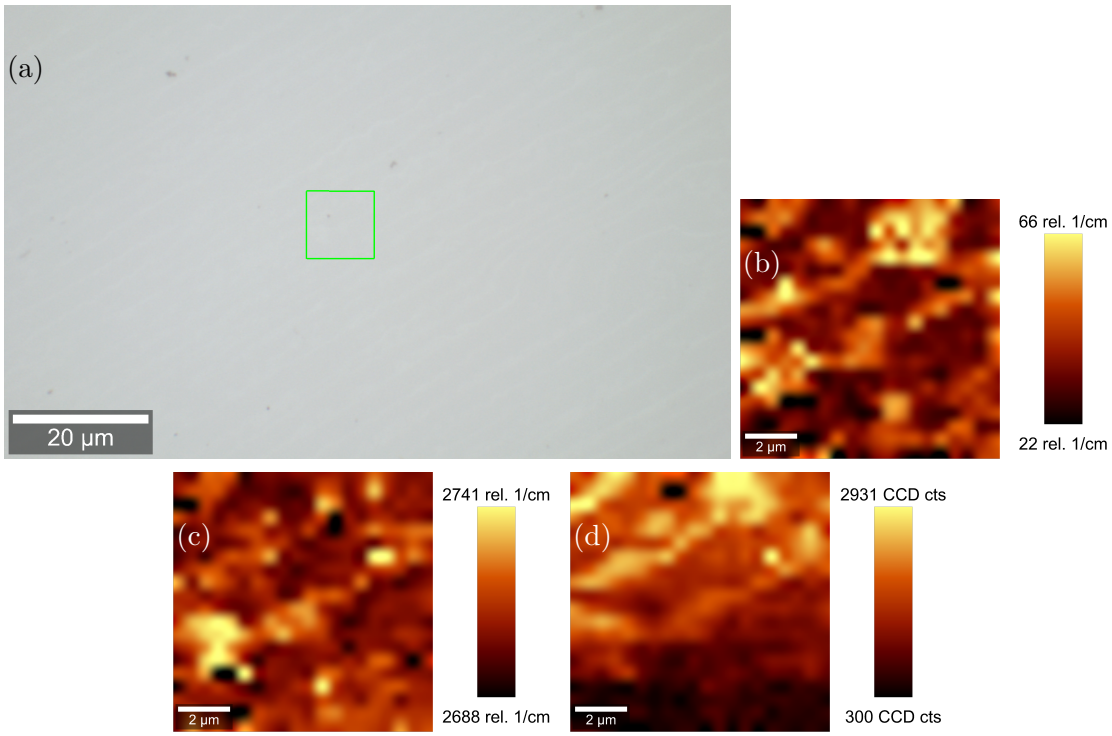

Figure B.3: Raman map #1 of sample 2. (a) Optical microscopy image, the green square is the area scanned in the Raman map. (b) 2D peak width. (c) 2D peak maximum. (d) Integrated 2D peak.

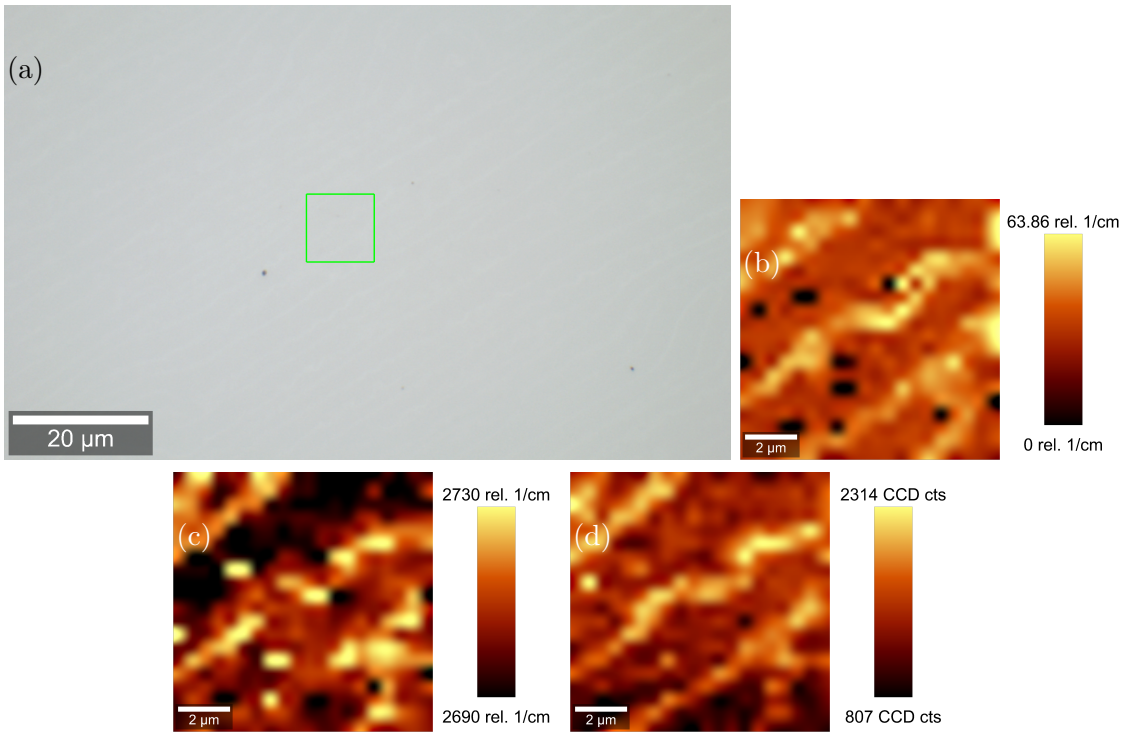

Figure B.4: Raman map #2 of sample 2. (a) Optical microscopy image, the green square is the area scanned in the Raman map. (b) 2D peak width. (c) 2D peak maximum. (d) Integrated 2D peak.

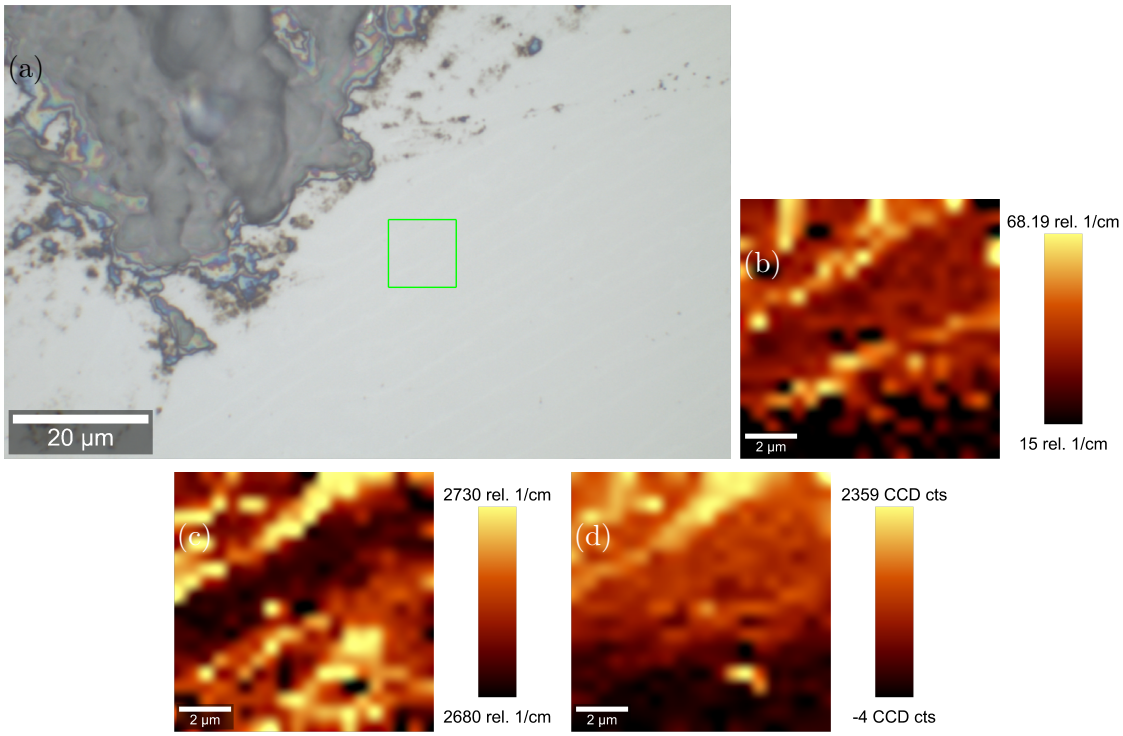

Figure B.5: Raman map #3 of sample 2. (a) Optical microscopy image, the green square is the area scanned in the Raman map. (b) 2D peak width. (c) 2D peak maximum. (d) Integrated 2D peak.

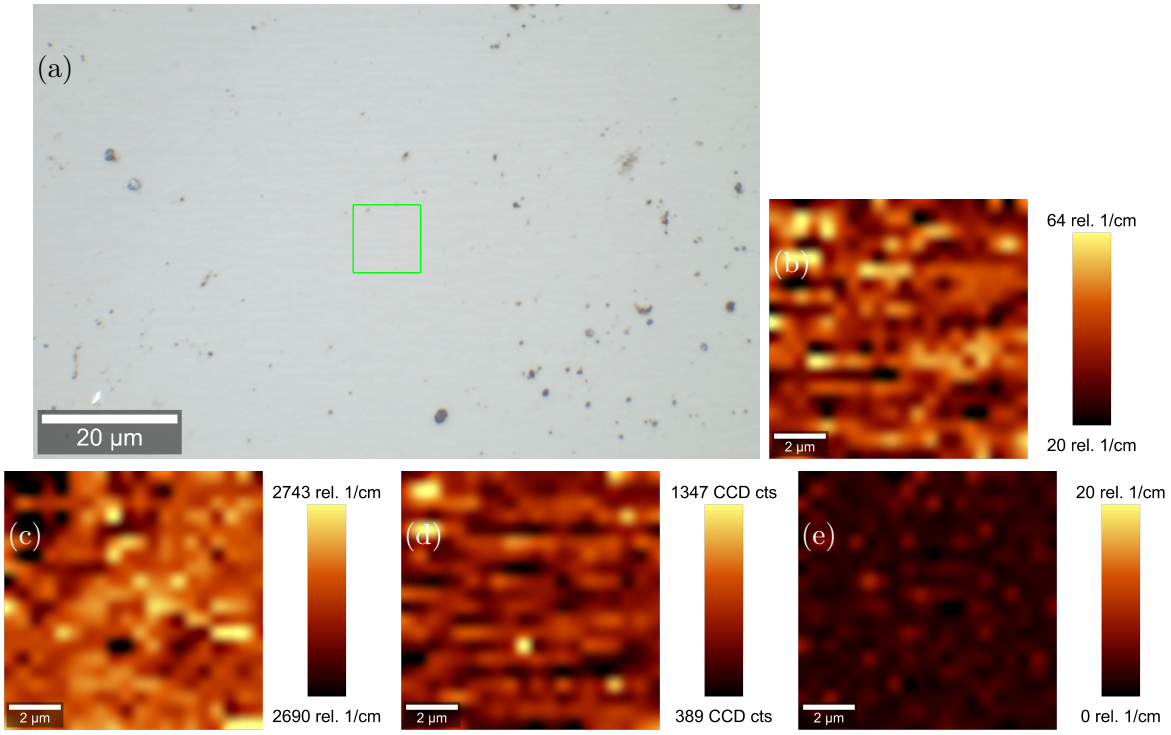

Figure B.6: Raman map #1 of sample 3. (a) Optical microscopy image, the green square is the area scanned in the Raman map. (b) 2D peak width. (c) 2D peak maximum. (d) Integration of the 2D peak. (e) Width of the peaks in the region $2800 - 3000$ cm^{-1}, indicating the presence of impurities.

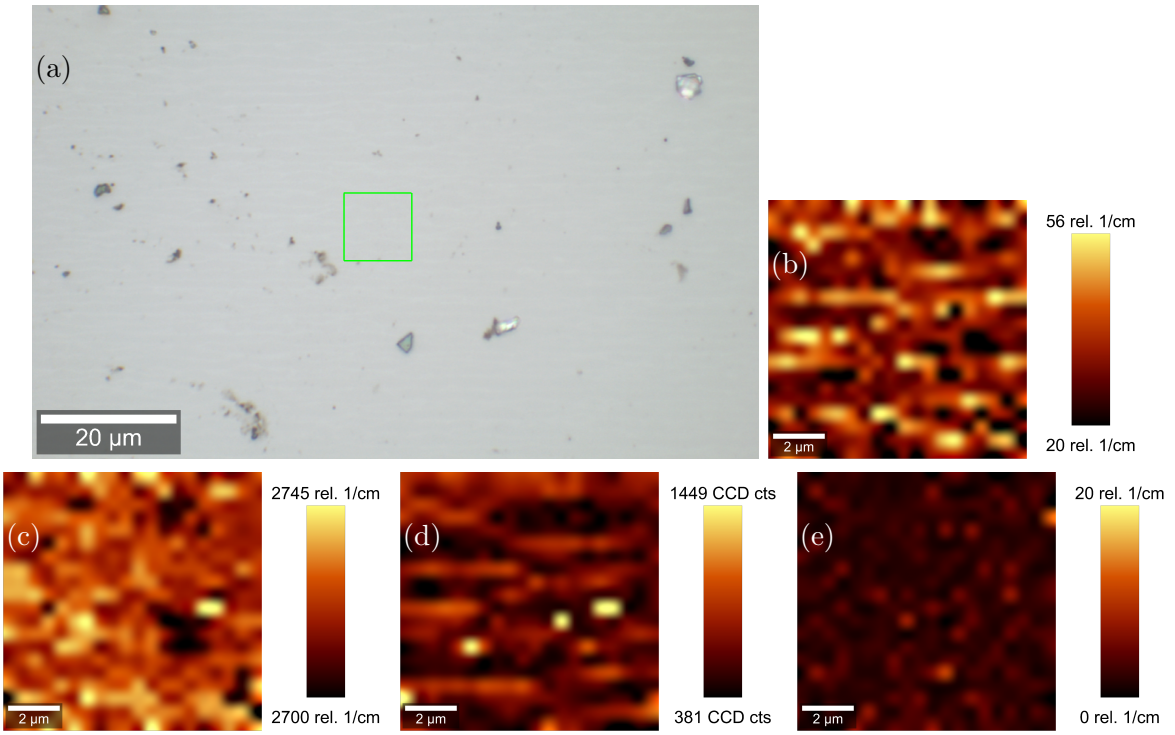

Figure B.7: Raman map #2 of sample 3. (a) Optical microscopy image, the green square is the area scanned in the Raman map. (b) 2D peak width. (c) 2D peak maximum. (d) Integration of the 2D peak. (e) Width of the peaks in the region $2800 - 3000$ cm^{-1}, indicating the presence of impurities.

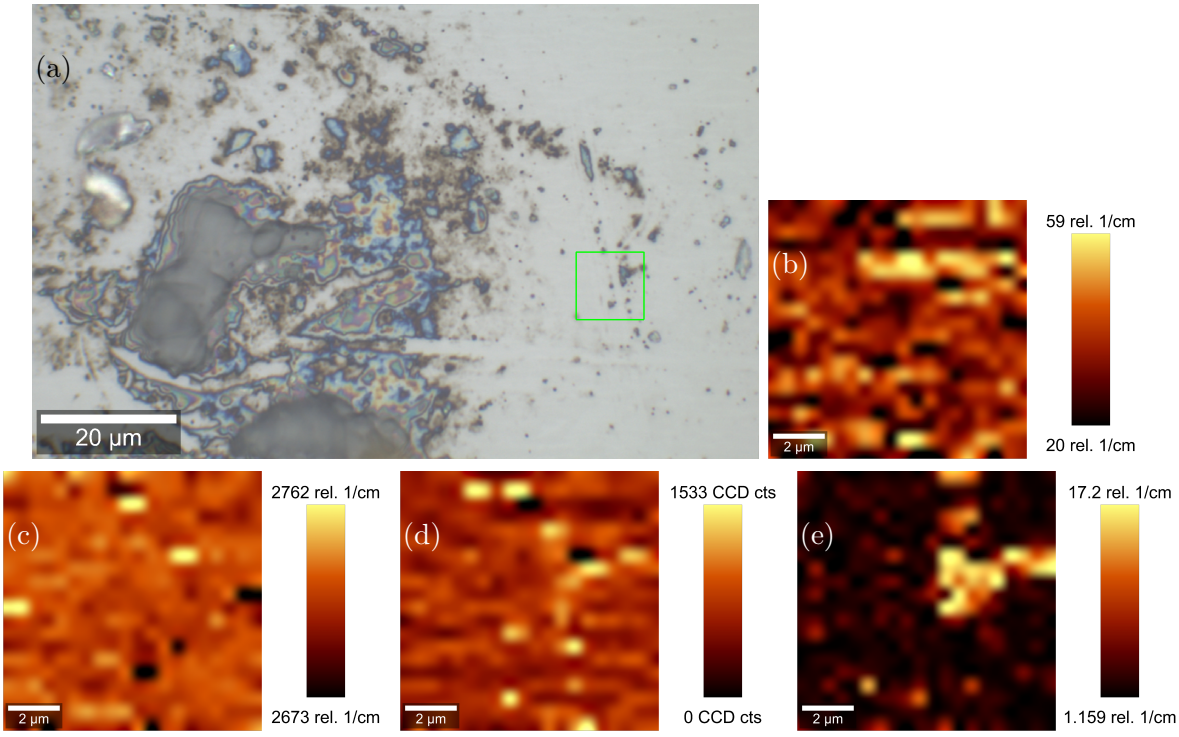

Figure B.8: Raman map #3 of sample 3. (a) Optical microscopy image, the green square is the area scanned in the Raman map. (b) 2D peak width. (c) 2D peak maximum. (d) Integration of the 2D peak. (e) Width of the peaks in the region $2800 - 3000$ cm^{-1}, indicating the presence of impurities.

B.2. Transport Measurements

This section shows supplementary results on the transport measurements on samples 2 and 3. The measurements were done in the 2-point configuration at a fixed bias current of 5 μA. Fig. B.9 (a) shows the measured resistance as a function of the magnetic field at low temperatures, evidencing the lack of SdHO in both samples. The WL signal of sample 3 is visible due to the scale change in the plot and to the small increase of the magnetoresistance of just 0.15 kΩ in the field range $0-9$ T. In sample 2, the WL signal is also present, but it is much weaker than the overall increase in magnetoresistance of 1.2 kΩ in the field range $0-15$ T. In Fig. B.9 (b), the WL of sample 3 and fittings to the WL theory of Eq. (3.10) are displayed, with the obtained characteristic scattering lengths and rates shown in Fig. B.9 (c,d). Due to the high correlation of the parameters B_i and B_*, the resulting uncertainties were very high. Therefore, we followed a different approach to determine the error than the one exposed in the main text. To determine the uncertainty of B_i, we performed a new fitting keeping the obtained B_* constant and B_φ, B_i as free parameters, with the uncertainty corresponding to two standard deviations as obtained from the fittings. A similar procedure was done for B_*. This resulted in low uncertainties in the parameters, but they are likely underestimated as the procedure omits the mentioned correlation. Compared to samples 1 and 2, where the characteristic lengths of intervalley and long-range scattering follow $L_* \ll L_i$, these parameters are closer in value in sample 3, but the inequality $L_* < L_i$ still holds. The dephasing scattering rate τ_φ^{-1} is in the range $200-600$ GHz for temperatures $5-20$ K, in a similar way as samples 1 and 2 shown in the main text.

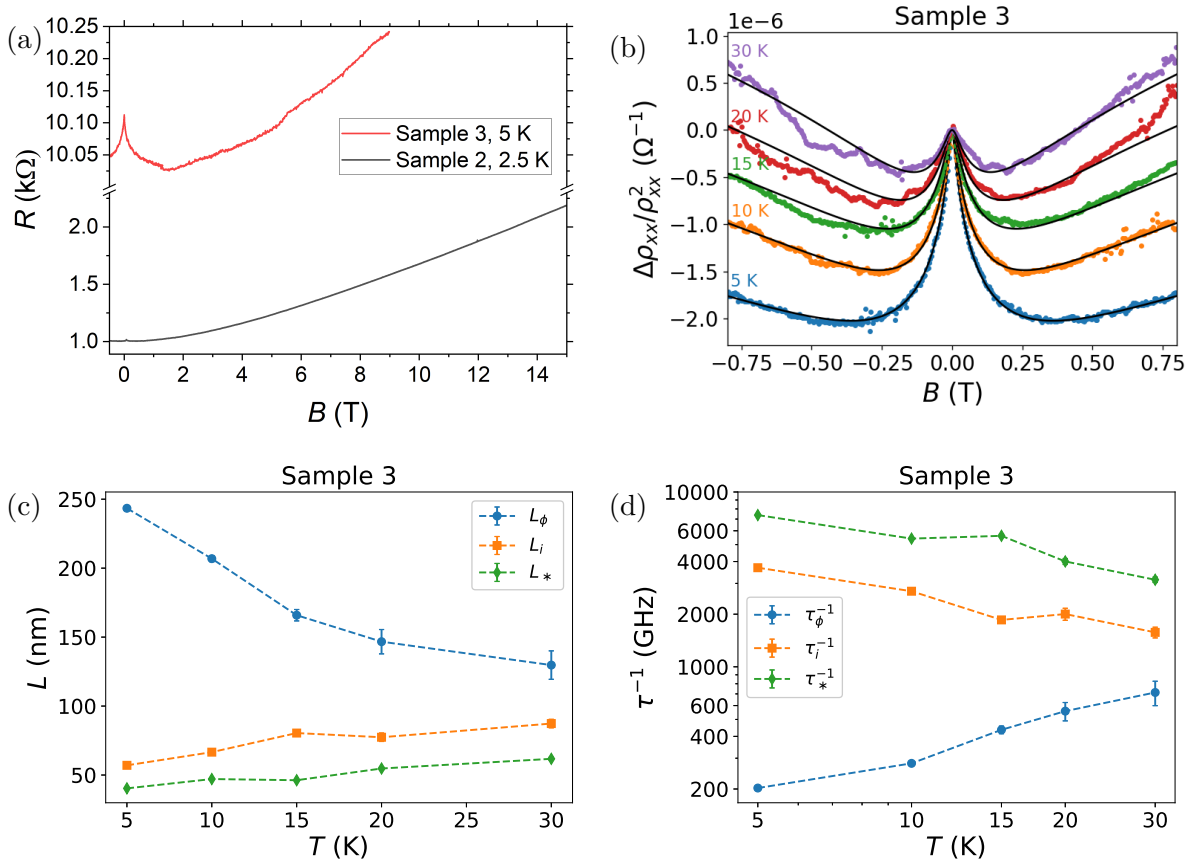

Figure B.9: (a) Resistance as a function of the magnetic field of samples 2 and 3. (b) Resistivity of sample 3 and fittings to the WL theory. Continuous black lines indicate the fittings. (c) Characteristic scattering lengths. (d) Characteristic scattering rates.

B.3. HFEPR Spectroscopy

HFEPR spectroscopy on the graphene samples revealed a rich spectrum with multiple signals originating from different sources. Fig. B.10 (a,b) displays the low-temperature spectra of sample 2 in the full magnetic field accessible of $-15-15$ T, at different frequencies. We observe that the signal background depends strongly on the frequency, having a parabolic shape around $B = 0$ at $f = 319.9$ GHz, but flat at 298.09 GHz. Such change is induced by the detection scheme of the spectrometer, corresponding to the phase-sensitive heterodyne detection [24, 80]. The weak localization peak is observed at $B = 0$, with a much lower intensity than the background. We verified that the change in the signal background does not correlate with the changes in the weak localization signal exhibited in Fig. 3.8 (c,d) of the main text. Fig. B.10 (b) displays a closer view of the spectra at 319.9 GHz. We observe weak Shubnikov-de Haas oscillations, the electron paramagnetic resonance (EPR) signal from vanadium impurities at $g = 2$, typically present in SiC, and an EPR signal that could originate from molecular oxygen impurities, which has a total spin $S = 1$.

The frequency dependence of the weak localization was observed in all samples, in both continuous wave and spectral maps of sub-THz magneto-optical spectroscopy. Fig. B.10 displays continuous wave measurements on samples 1 and 3 at different frequency ranges. For sample 1, represented in Fig. B.10 (c,d), it is observed that although the signal shape remains fairly similar along the studied range, an overall broadening and peak shift towards higher values of $|B|$ can be noticed. The behavior of the peaks is complex and is better understood by looking at the corresponding spectral maps in Fig. B.11 (b,c). For sample 3, the continuous wave spectra of Fig. B.10 (e) demonstrate a rapid change in the peak shape, occurring in a frequency range of less than 1 GHz. Fig. B.10 (f) shows clearly how the peak changes its shape, broadens, and shifts in the frequency range $323-343$ GHz.

The spectral maps of sample 1 at different frequency ranges and a temperature of 5 K are displayed in Fig. B.11. We observe that in the range $120-170$ GHz, the signal experiences a series of rapid changes in the shape. Such behavior is observed in the spectral map of sample 3, Fig. 3.9 (b), although with a lower signal-to-noise ratio. At higher ranges, we observe a beating behaviour of the signal, with the beating frequency being higher at a higher frequency. Nevertheless, as observed by optical microscopy and Raman spectroscopy, the high amount of residues and impurities in the sample make it difficult to conclude if the effect originates from graphene or is induced by impurities. It is worth mentioning that such beating behavior was not observed in sample 3 with the highest uniformity, as discussed in Section 3.7, Fig. 3.9 of the main text.

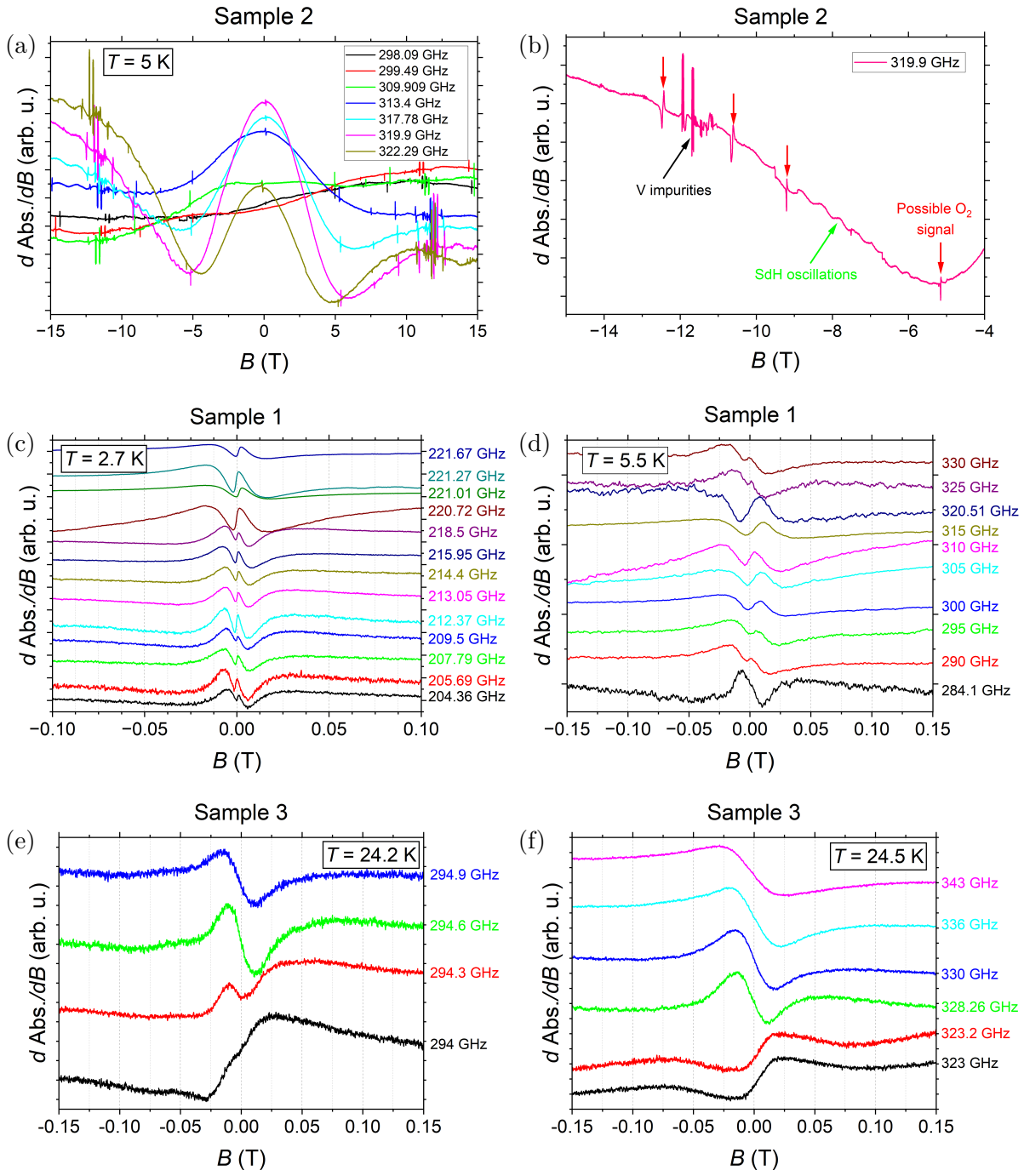

Figure B.10: (a) Continuous wave HFEPR spectra of sample 2 in the magnetic field range $-15-15$ T, at $T = 5$ K. (b) Closer view of the spectrum of sample 2 at $f = 319.9$ GHz. (c) HFEPR spectra of sample 1 in the range $204.34-221.67$ GHz at $T = 2.7$ K, exhibiting WL behaviour. (d) Spectra of sample 1 in the range $284.1-330$ GHz at $T = 5.5$ K. (e) Spectra of sample 3 in the range $294-294.9$ GHz. (f) Spectra of sample 3 in the range $323-343$ GHz.

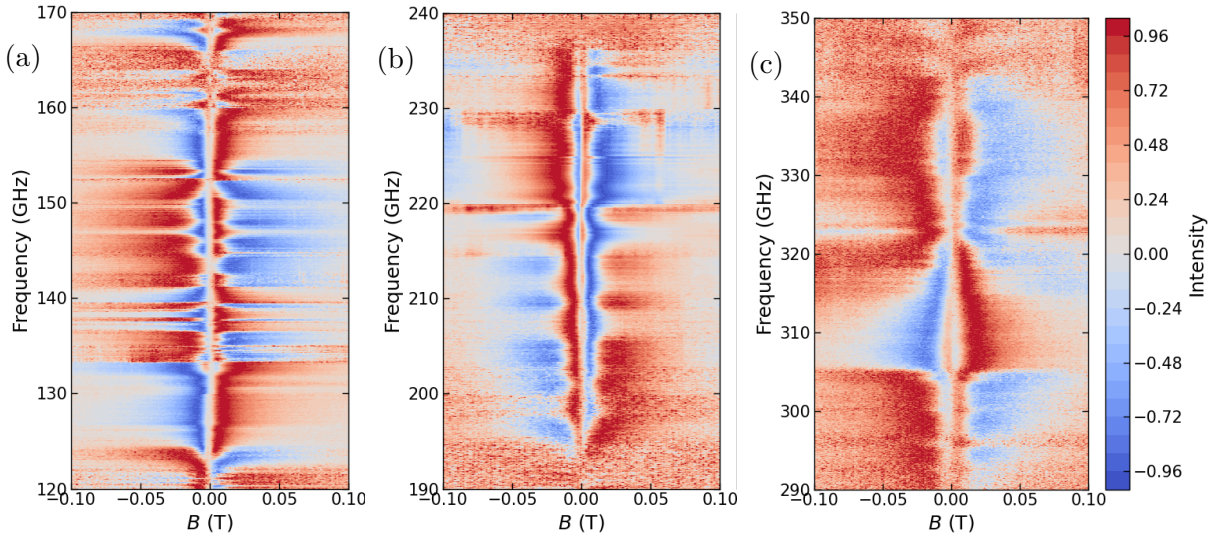

Figure B.11: Spectral maps of weak localization in sample 1 at $T = 5$ K.

B.3.1. Simulated Spectra

In the main text, we presented the results of the simulated spectra according to the theory of frequency-dependent WL of Eqs. (3.15, 3.38), which we reproduce below,

$$\frac{d\Delta\sigma_{xx}^{(\mathrm{ML})}(\omega)}{dB} = \frac{4De}{\hbar} N \,\mathrm{Re}\left[\frac{1}{\tau_\varphi^{-1}+i\omega}F'\left(\frac{\tau_B^{-1}}{\tau_\varphi^{-1}+i\omega}\right) - \frac{1}{\tau_\varphi^{-1}+2\tau_i^{-1}+i\omega}F'\left(\frac{\tau_B^{-1}}{\tau_\varphi^{-1}+2\tau_i^{-1}+i\omega}\right) - \frac{2}{\tau_\varphi^{-1}+\tau_*^{-1}+i\omega}F'\left(\frac{\tau_B^{-1}}{\tau_\varphi^{-1}+\tau_*^{-1}+i\omega}\right)\right], \tag{B.1}$$

$$\frac{d\Delta\sigma_{xx}^{(\mathrm{BL})}(\omega)}{dB} = \frac{4De}{\hbar} N \,\mathrm{Re}\left[\frac{1}{\tau_\varphi^{-1}+i\omega}F'\left(\frac{\tau_B^{-1}}{\tau_\varphi^{-1}+i\omega}\right) - \frac{1}{\tau_\varphi^{-1}+2\tau_i^{-1}+i\omega}F'\left(\frac{\tau_B^{-1}}{\tau_\varphi^{-1}+2\tau_i^{-1}+i\omega}\right) + \frac{2}{\tau_\varphi^{-1}+\tau_*^{-1}+i\omega}F'\left(\frac{\tau_B^{-1}}{\tau_\varphi^{-1}+\tau_*^{-1}+i\omega}\right)\right], \tag{B.2}$$

for monolayer and bilayer graphene, respectively, with $\tau_B^{-1} = 4eDB/\hbar$.

We computed the spectra considering that the scattering rates and the diffusion constant do not depend on the frequency, and acquire values similar to those found in transport experiments, that is, $D = 0.024$ m^2/s, $\tau_\varphi^{-1} = 250$ GHz, $\tau_i^{-1} = 1500$ GHz, and $\tau_*^{-1} = 10$ THz. Due to the high value of τ_*^{-1}, it plays a minor role in the dynamic conductivity, resulting in similar spectra for monolayer and bilayer graphene. This section explores the simulated spectra with a lower value for long-range scattering rate of $\tau_*^{-1} = 1000$ GHz, which can be present in graphene samples not tightly attached to the substrate [7]. The results, depicted in Fig. B.12, evidence a difference in the spectra of monolayer and bilayer graphene, especially at higher frequencies. In the spectra of monolayer graphene, we identify the emergence of two peaks, around 30 GHz and 250 GHz, compared to only one peak appearing in bilayer graphene at 50 GHz. This feature is a consequence of the contribution of τ_i^{-1} and τ_*^{-1} in the dynamic conductivity of Eq. (B.1), both of which have a negative sign in the prefactor accompanying $F'(z)$. In bilayer graphene, Eq. (B.2) shows that only the contribution of τ_i^{-1} has a negative sign, explaining the appearance of only one peak across the frequency range. Nevertheless, as was pointed out in the main text, the dynamic conductivity in Eqs. (B.1, B.2) with frequency-independent parameters

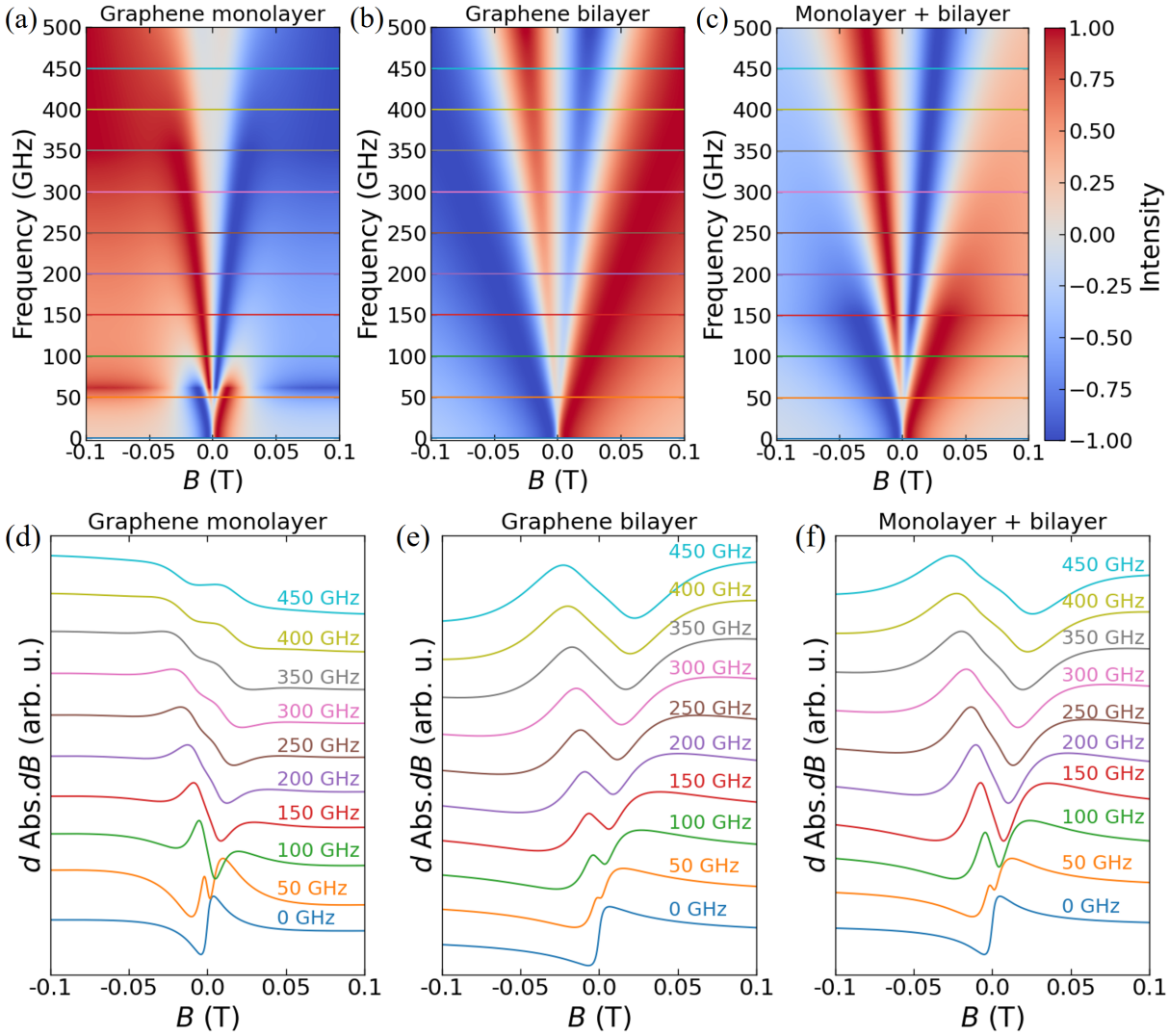

Figure B.12: Simulated frequency maps of the frequency dependence of the WL in (a) monolayer graphene, (b) bilayer graphene, and (c) considering the signal coming from both monolayer and bilayer graphene in equal proportion. The horizontal lines correspond to the selected frequencies for the CW spectra in (d-f). Simulated CW spectra at selected frequencies, as extracted from the frequency maps, for (d) monolayer graphene, (e) bilayer graphene, and (f) the sum of monolayer and bilayer graphene contributions. In all cases, the parameters used in the simulation are $D = = 0.024$ m^2/s, $\tau_\varphi^{-1} = 250$ GHz, $\tau_i^{-1} = 1500$ GHz, and $\tau_*^{-1} = 1000$ GHz.

do not explain the emergence of several spectral peaks in a relatively short frequency range, as observed experimentally.

B.3.2. Temperature Dependence

We investigated the temperature dependence of the WL signal in the spectral maps. In the main text and for sample 3, we identified that as the temperature is increased, the peaks broaden and decrease in intensity, but the transition points of the signal, i.e., the frequencies at which the sharp features appear and expand, are unaffected by the temperature (see Fig. 3.12). We studied the temperature dependence in sample 1, analyzing the spectral maps in the frequency range 290−350 GHz as displayed in Fig. B.13. The main conclusions remain: as the temperature increases, the peaks broaden and decrease in intensity. At approximately 322 GHz, a transition in the beating is observed, which remains unchanged as the temperature increases. The sharper peaks observed at low temperatures, indicated by the green arrows in the figure, experience a considerable decrease as the temperature increases until being barely visible at $T = 50$ K. The broader peaks, on the other hand, are still visible at the highest temperature.

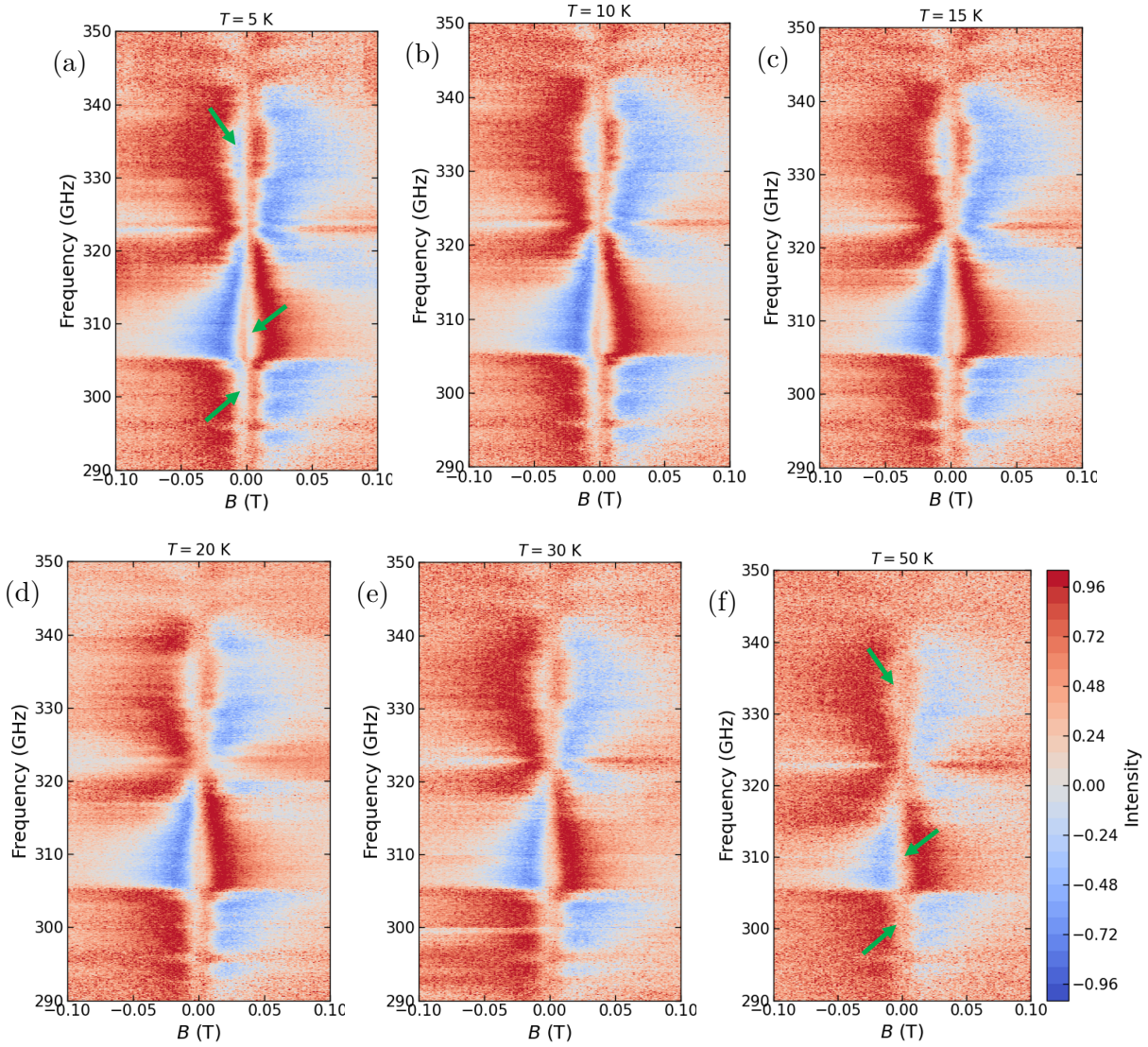

Figure B.13: Spectral maps of the temperature dependence of weak localization in sample 1, the temperature is indicated at the top of each figure. The frequency range is 290 − 350 GHz.

C. Files and Scripts for DFT and CASSCF-NEVPT2 Calculations

We present the source files we employed for plane-wave DFT calculations on VASP 5.4.4, and CASSCF-NEVPT2 calculations on ORCA 4.2.2. All the relevant files necessary for the calculations exposed in this Appendix are in the GitHub repository https://github.com/Jorge-NavarroG/Molecular-deposition-on-graphene.

C.1. Plane-Wave DFT Files

C.1.1. Isolated Molecules

All calculations used the PBE functional with projector-augmented wave (PAW) pseudopotentials of VASP 5.4.4. The files below correspond to the isolated molecules in the bulk configuration. The POSCAR file for compound **1** in a unit cell of the same size as a 10×10 graphene supercell is:

```
Compound 1
1.0
       24.6729106903          0.0000000000          0.0000000000
      -12.3364553452         21.3673674431          0.0000000000
        0.0000000000          0.0000000000         30.0000000000
    C     H     N     O    Co
   26    22     4     2     1
Cartesian
 9.164888     8.026765    12.181348
 8.728077     7.260759    13.261932
 7.512239     6.559945    13.234917
 6.739390     6.691144    12.156584
 7.148247     7.464484    11.019717
 4.769112     8.107440     5.589777
 4.081934     7.912679     4.378621
 4.487484     7.187418     3.365573
 5.747301     6.568094     3.529912
 6.467897     6.698478     4.698295
 6.098507     7.448186     5.783382
 8.315931     8.197894    11.062491
 4.281506     9.012794     6.641096
 8.931437     8.988347    10.089964
 4.229168    10.186251     8.712218
 8.934816    10.121058     8.000833
 2.996938    10.715935     8.637928
10.242410    10.658892     8.018843
 2.615678    11.465643     9.684745
 4.651374    11.089974    10.742818
 8.474424    11.058193     5.911702
```

```
10.626373   11.481941    6.954016
 3.506979   11.628623   10.724808
 5.663792   11.237472   11.938216
 7.560377   11.123385    4.804102
 9.815117   11.710114    5.873431
 9.258193    7.209421   14.025096
 7.254082    6.020481   13.946302
 5.912003    6.268211   12.138574
 3.979851    7.079851    2.593405
 6.100045    6.066116    2.829782
 7.270421    6.229096    4.756826
10.004018    8.430956   12.199356
 3.262167    8.344576    4.286322
 3.447374    9.390093    6.488013
 9.787540    9.319197   10.245298
 2.440961   10.568439    7.906282
10.828109   10.470651    8.716721
 1.774830   11.861685    9.709509
11.461802   11.884502    6.981030
 3.254516   12.156679   11.445199
 5.182272   11.229322   12.768915
 6.141566   12.065410   11.852669
 6.286080   10.505692   11.922458
 6.719768   11.477052    5.101263
 7.425870   10.240034    4.448409
 7.924510   11.689741    4.121982
10.085690   12.235723    5.157543
 4.850368    9.346903    7.748696
 8.327866    9.282526    8.971108
 5.146331   10.308485    9.720764
 8.125847   10.362268    6.983282
 6.415333    7.435963    9.925625
 6.867879    7.481597    6.814441
 6.593821    8.598662    8.352023
```

Listing C.1: POSCAR for the isolated compound **1** in bulk structure.

The POSCAR of compound **2** in the same unit cell is

```
Compound 2
1.0
       24.6729106903          0.0000000000          0.0000000000
      -12.3364553452         21.3673674431          0.0000000000
        0.0000000000          0.0000000000         30.0000000000
    C    H    N    O   Co
   28   26    4    2    1
Cartesian
    12.675147057          9.197207451          8.270439148
    12.812131882          8.445707321          7.058019161
    11.802335739          7.597989082          6.503769875
     9.693418503          6.484011173          6.489257813
     9.745568275          5.898405552          5.235877037
    14.024785995          8.542755127          6.339460850
     8.678133965          5.086354256          4.875428200
    13.794729233          9.957830429          8.670679092
     7.643137455          5.555004597          6.978438854
     7.631159782          4.908847332          5.746123791
    15.097956657          9.288449287          6.751402855
    14.952489853          9.991009712          7.952121258
```

```
     6.504342079          5.477034569          7.959142208
    16.375734329          9.344853401          5.950924873
     7.341971397          9.197207451          9.283910751
     7.204987049          8.445707321         10.496331215
     8.214780807          7.597989082         11.050580025
    10.323698997          6.484011173         11.065092087
    10.271550179          5.898405552         12.318472862
     5.992333889          8.542755127         11.214888573
    11.338984489          5.086354256         12.678921700
     6.222387791          9.957830429          8.883670807
    12.373979568          5.555004597         10.575910568
    12.385956764          4.908847332         11.808225632
     4.919160843          9.288449287         10.802947044
     5.064628601          9.991009712          9.602229118
    13.512776375          5.477034569          9.595208168
     3.641383648          9.344853401         11.603425026
    12.010130882          7.130676746          5.542332172
    10.585107803          6.067373276          4.563165188
    14.110788345          7.992346287          5.403739929
     8.672870636          4.590614319          3.905822039
    13.732219696         10.540452003          9.588592529
     6.795085907          4.265962601          5.474833012
    15.789184570         10.581068039          8.323188782
     6.842587471          4.986392498          8.870614052
     5.687664986          4.905084133          7.521155357
     6.159811020          6.482963085          8.194355965
    17.154617310          8.790685654          6.472612858
    16.684982300         10.382306099          5.832709789
    16.209224701          8.900526047          4.970736980
     8.006988525          7.130676746         12.012018204
     9.432008743          6.067373276         12.991185188
     5.906329632          7.992346287         12.150609970
    11.344246864          4.590614319         13.648528099
     6.284897804         10.540452003          7.965756416
    13.222032547          4.265962601         12.079517365
     4.227932453         10.581068039          9.231161118
    13.174530029          4.986392498          8.683735847
    14.329451561          4.905084133         10.033193588
    13.857307434          6.482963085          9.359993935
     2.862499237          8.790685654         11.081736565
     3.332135201         10.382306099         11.721639633
     3.807893276          8.900526047         12.583613396
    10.659297943          7.343340874          7.056147099
     8.673143387          6.318946362          7.342399120
     9.357820511          7.343340874         10.498203278
    11.343973160          6.318946362         10.211951256
    11.593741417          9.248634338          8.985136032
     8.423377037          9.248634338          8.569213867
    10.008559227          8.115661621          8.777174950
```

Listing C.2: POSCAR for the isolated compound **2** in bulk structure.

The POSCAR of compound **3** in the same unit cell of a 17×8 graphene supercell is

```
Compound 3
1.0
       41.9439468384          0.0000000000          0.0000000000
       -9.8691667430         17.0938929707          0.0000000000
        0.0000000000          0.0000000000         30.0000000000
```

```
    C   Cl   Co    H    N    O
   38    2    1   32    4    4
Cartesian
    11.023197174         7.987173557         3.993885040
    12.748552322         9.281407356         4.001142025
    13.789656639         3.633691788         4.209249973
    15.379472733         4.939015865         4.870560169
    11.685165405        10.066811562         4.248421669
    14.668560028         2.853210211         4.849530697
     9.213452339         9.628032684         4.479743481
    16.858304977         3.298155546         6.017689705
     8.242378235         8.653335571         4.697253704
     8.875249863        10.970203400         4.490589619
    17.156415939         1.949819326         6.159120560
    17.670370102         4.267930508         6.589108467
     6.916395187         9.031908989         4.869116306
     7.552684784        11.334020615         4.692182064
    18.305801392         1.593398809         6.854491234
    18.826759338         3.895497561         7.268522263
     6.553540230        10.390052795         4.862601280
    19.168914795         2.543481588         7.396141052
     5.165884972        10.837448120         5.042423248
    20.372014999         2.076421022         8.095179558
     4.104593277        10.098786354         5.316505909
    21.245845795         2.821274519         8.760820389
     2.768994808        10.730512619         5.461525917
    22.423231125         2.191971302         9.410543442
     1.568161488         9.844326019         5.617431164
    23.465526581         3.076926470        10.013095856
     1.637307167         8.456682205         5.768264771
     0.316950321        10.449052811         5.623244286
    23.341674805         4.468262672        10.134200096
    24.625640869         2.472200155        10.506172180
     0.478268147         7.714328766         5.958971500
    -0.839344501         9.723891258         5.819023609
    24.332866669         5.204501152        10.748379707
    25.608226776         3.194900036        11.144268990
    -0.755843639         8.353439331         5.991588593
    25.463722229         4.581351280        11.265372276
    -3.120700359         8.156800270         6.298326969
    27.526876450         4.771837234        12.465446472
    12.052666664         5.455089092         1.682810426
    15.324093819         7.467753887         2.341350555
    13.462594986         6.461607456         3.127080917
    10.479142189         7.234960556         3.936610699
    13.628276825         9.573944092         3.948236942
    12.999953270         3.338732481         3.815506935
    15.905379295         5.689997673         5.027206898
    11.695803642        10.984933853         4.391256809
    14.604877472         1.933857799         4.979335308
     8.480390549         7.754867554         4.726983547
     9.525892258        11.620403290         4.363711834
    16.598617554         1.299631715         5.797253132
    17.442562103         5.167616844         6.518022537
     6.263468266         8.380491257         4.988776684
     7.328647137        12.236167908         4.713952541
    18.507650375         0.691238582         6.961081028
    19.375112534         4.548159599         7.639791965
```

```
64      5.016819000        11.750684738         4.953233719
65     20.540565491         1.161991596         8.069078445
66      4.194569111         9.179394722         5.419467449
67     21.119230270         3.740626812         8.821021080
68      2.463068008         8.027750015         5.740719795
69      0.257323265        11.367214203         5.490553379
70     22.588916779         4.897195339         9.799175262
71     24.737224579         1.555270791        10.399581909
72      0.528159618         6.792476177         6.065561771
73     -1.664801598        10.151631355         5.835682869
74     24.243768692         6.127545357        10.817983627
75     26.358995438         2.767198086        11.489438057
76     -3.781002045         7.506599903         6.547752380
77     -3.102180481         8.861051559         6.951639175
78     -3.341745377         8.524271965         5.439053535
79     27.254753113         4.068790913        13.061484337
80     28.031368256         5.426960468        12.952006340
81     28.069717407         4.404327393        11.764964104
82     12.333246231         7.971198559         3.835833788
83     14.232128143         4.952515602         4.220876694
84     10.571798325         9.238408089         4.249865055
85     15.694572449         3.684088707         5.281703949
86      2.645372391        11.942400932         5.460082054
87     22.536588669         0.980082691         9.462745667
88     -1.831382751         7.529958725         6.233795643
89     26.368675232         5.386409760        11.897693634
```

Listing C.3: POSCAR for the isolated compound **3** in bulk structure.

To arrive at the correct ground state of the molecules with a total spin of 3/2 from DFT, it is necessary to perform a spin-polarized calculation. The correct procedure is to start from a pre-converged solution using a spin-unpolarized calculation with a non-strict energy convergence criterion, using the following INCAR

```
1  Startparameters
2  SYSTEM = spin-unpolarized
3  PREC = Accurate
4  ALGO = Fast
5  ENCUT = 520
6  EDIFF = 1E-1      ! energy convergence criterion
7  LREAL = Auto      ! Auto: Useful for large unit cells
8
9  Paralelization
10 NCORE = 8
11 NSIM = 1
12 LPLANE = TRUE
13 KPAR = 1
```

Listing C.4: INCAR for spin-unpolarized calculations.

The output files of this calculation (CHGCAR, WAVECAR) will be the starting point for (collinear) spin-polarized calculations.

The molecules were relaxed to obtain their structure in the gas phase. The relaxation was done in two stages, first, using the conjugate-gradient algorithm until residual forces were below 0.1 eV/Å, and then applying the RMM-DIIS algorithm until residual forces were below 0.02 eV/Å. The INCAR for ionic relaxation is (make sure to start from a pre-converged calculation described in the previous paragraph)

```
Startparameters
SYSTEM = spin-polarized and relaxation
ISTART = 1       ! 0: begin from scratch. 1: Continuation
ICHARG = 1       ! 1: Reads the charge density from CHGCAR file
PREC = Accurate
ALGO = Fast
ENCUT = 520
EDIFF = 1E-6     ! energy convergence criterion
LREAL = Auto     ! Auto: Useful for large unit cells

Paralelization
NCORE = 8
NSIM = 1
LPLANE = TRUE
KPAR = 1

Magnetism
ISPIN = 2        ! spin polarized calculation
MAGMOM = 26*0.001 22*0.001  4*0.01  2*0.01 3.2   ! 26*C 22*H 4*N 2*O Co
                 ! For compound 1. Change accordingly for the others
LORBIT= 11       ! write atomic moments of all atoms to OUTCAR

DOS related values
ISMEAR = 0       ! 0: Gaussian smearing
SIGMA = 0.1      ! broadening in eV

Ionic relaxation, delete or comment each block as needed
# Conjugate gradient algorithm:
IBRION = 2       ! 1: RMM-DIIS, 2:conjugate gradient algorithm
ISIF = 2         ! relaxation of atomic positions
NSW = 30         ! max number of ionic steps
EDIFFG = -0.1    ! max residual forces

# RMM-DIIS method:
IBRION = 1       ! 1: RMM-DIIS, 2:conjugate gradient algorithm
ISIF = 2         ! relaxation of atomic positions
NSW = 30         ! max number of ionic steps
EDIFFG = -0.02   ! max residual forces
NFREE = 10       ! number of remembered steps in the history of
                 ! ionic convergence runs
NELMIN = 6       ! minimum number of electronic SCF steps.
POTIM = 0.5      ! scaling constant for the step widths
```

Listing C.5: INCAR for spin-polarized calculation and ionic relaxation of the isolated molecules.

In the calculations described above, the sampling of the reciprocal space was done with only one k-point at the Brillouin zone center (Γ-point). The KPOINTS file is

```
Gamma point
0
Gamma
1 1 1
0 0 0
```

Listing C.6: KPOINTS file for Γ-point calcuations.

Van der Waals and electric dipole corrections were not considered at this point.

C.1.2. Molecules on Graphene

The relaxed molecules were placed on the graphene substrate, changing their orientation relative to it. To generate the energy profiles of Fig. 4.7, we performed a Γ-point calculation varying the distance of the molecule to the substrate without employing ionic relaxation. To get the ground-state energy, we first employed a non-spin-polarized calculation as described in the previous section and then performed a spin-polarized calculation using the following INCAR:

```
Startparameters
SYSTEM = spin-polarized calculation
ISTART = 1       ! 0: Begin from scratch. 1: Continuation
ICHARG = 1       ! 1: Reads the charge density from CHGCAR file
PREC = Accurate
ALGO = Fast
ENCUT = 520
EDIFF = 1E-6     ! Energy convergence criterion
LREAL = Auto     ! Auto: Useful for large unit cells
LWAVE = FALSE    ! Do not write the WAVECAR

Paralelization
NCORE = 8
NSIM = 1
LPLANE = TRUE
KPAR = 1

Magnetism
ISPIN = 2        ! Spin polarized calculation
MAGMOM = 200*0 26*0.001 22*0.001  4*0.01  2*0.01 3.2
                 ! 200*substrate 26*C 22*H 4*N 2*O Co
                 ! For compound 1. Change accordingly for the others
LORBIT = 11      ! Write atomic moments of all atoms to OUTCAR

DOS related values
ISMEAR = 0       ! 0: Gaussian smearing
SIGMA = 0.1      ! Broadening in eV

Van der Waals forces
IVDW = 12   !10: D2 method, 12: DFT-D3 method with Becke-Jonson damping
LVDW_EWALD = TRUE

workfunction:
IDIPOL = 3  ! Dipole corrections
LDIPOL = TRUE
LVHAR = TRUE
```

Listing C.7: INCAR for spin-polarized calculation of the molecule on graphene.

When the equilibrium distance of the molecule on graphene was found, ionic relaxation of the whole system with the RMM-DIIS method was performed by adding the following lines to the previous INCAR:

```
# RMM-DIIS method:
IBRION = 1       ! 1: RMM-DIIS, 2:conjugate gradient algorithm
ISIF = 2         ! relaxation of atomic positions
NSW = 30         ! max number of ionic steps
EDIFFG = -0.02   ! max residual forces
NFREE = 10       ! number of remembered steps in the history of
                 ! ionic convergence runs
```

```
8 NELMIN = 6        ! minimum number of electronic SCF steps.
9 POTIM = 0.5       ! scaling constant for the step widths
```

Listing C.8: Relaxation tags for the RMM-DIIS method.

If the residual forces after ionic relaxation cannot get below 0.02 eV/Å, a lower value for the `POTIM` tag might be useful, for instance, 0.3 or 0.2.

Calculation of the charge density of the system was performed after ionic relaxation. A self-consistent energy calculation of the relaxed system with a k-point sampling of $2 \times 2 \times 1$ centered at the Γ-point is performed using the KPOINTS file:

```
1 2x2x1 Gamma centered
2 0
3 Gamma
4 2 2 1
5 0 0 0
```

Listing C.9: KPOINTS file for a Γ-centered $2 \times 2 \times 1$ k-point sampling.

To speed up the calculations, the CHGCAR from the relaxation calculation can be used as starting point. Calculations of the charge density were performed by adding the following lines to the INCAR of Listing C.7, which are necessary for the Bader charge analysis:

```
1 Bader chg analysis
2 LAECHG = TRUE
3 NSW = 0
```

Listing C.10: INCAR tags for the Bader charge analysis.

To obtain the charge density difference, the final positions of the molecule and graphene were extracted from the relaxed structure, and a self-consistent calculation was performed on them individually, using the Γ-centered $2 \times 2 \times 1$ sampling of the reciprocal space. The INCAR file for the isolated molecule was similar to the one in Listing C.7, but deleting the substrate contribution of the `MAGMOM` tag. For the graphene substrate, the calculation did not consider spin polarization (lines 18 to 23 of Listing C.7) and dipole corrections (lines 33 to 36 of Listing C.7).

The total charge density of the system was used as the starting point of DOS calculations of the molecule on graphene, and was kept constant during the self-consistent cycles. The INCAR file of Listing C.7 was used, but replacing the `ICHARG` tag of line 4 to `ICHARG = 11`, and adding the following lines

```
1 NEDOS = 2000    ! Number of points for DOS calculation
2 EMAX = 10       ! Limits for DOS calculation
3 EMIN = -10
4 NSW=0
```

C.2. Files for CASSCF-NEVTP2 Calculations

For CASSCF-NEVPT2 calculations in ORCA 4.2.2 and 5.0, we used the structural parameters of the molecules shown in Listings C.1-C.3 in XYZ format. The structures resulting from plane-wave relaxation processes of the molecules on graphene were also considered. To apply the CASSCF-NEVPT2 method, it is necessary to select the orbitals of the complete-active space manually; for this reason, we did preliminary Gaussian-basis DFT calculations to identify the molecular orbitals (MOs) with the highest 3d character of the Co atom's orbital angular

momentum. We used the B3LYP functional with def2-TVZP basis for all atoms, except for carbon and hydrogen which used the def2-SVP basis. We also used the def2/J auxiliary basis set and the RIJCOSX approximation. Since we deal with open-shell systems, we work with an unrestricted Kohn-Sham calculation (`UKS` tag). The input file is as follows

```
! UKS B3LYP RI RIJCOSX def2-TZVP def2/J grid6 gridx6 nofinalgrid UNO UCO

%basis
newgto C "def2-SVP" end
newgto H "def2-SVP" end
end
%pal nprocs 4 end

!Printbasis
%scf print[p_mos] 1 end

* xyzfile 0 4 Compound1.xyz #TotalCharge SpinMultiplicity StructureFile.xyz

%output
 Print [P_Loewdin ] 1
 Print [P_BondOrder_L ] 1
 Print [P_ReducedOrbPop_L] 1
 Print [P_FragPopMO_L] 1
 Print [P_ReducedOrbPopMO_L] 1
end
```

Listing C.11: Input file for preliminary DFT calculations in ORCA.

The tag `UNO` prints the unrestricted natural orbitals and quasi-restricted orbitals, necessary for the Loewdin population analysis, and the tag `UCO` prints the corresponding orbitals. For a CASSCF calculation, we require the active space, corresponding to the highest occupied MOs, to be comprised of the five 3d orbitals of cobalt. The objective is to identify which MOs have the highest contribution from cobalt's d orbitals. However, the orbitals printed from the DFT calculation, so-called canonical orbitals, are often difficult to interpret since they are rather delocalized. It is more convenient to look at the quasi-restricted orbitals, since they are easier to interpret and are as valid as the canonical ones. To analyze their occupations, we perform a non-self-consistent calculation using the tag `!NOITER` and reading the computed quasi-restricted orbitals (output "jobname.qro"), using the following input file:

```
! UKS B3LYP RI RIJCOSX def2-TZVP def2/J grid6 gridx6 nofinalgrid

%basis
newgto C "def2-SVP" end
newgto H "def2-SVP" end
end
%pal nprocs 4 end


! MOread
%moinp "jobname.qro" #Reading the quasi-restricted orbitals
!NOITER
!Printbasis
%scf print[p_mos] 1 end

* xyzfile 0 4 Compound1.xyz #TotalCharge SpinMultiplicity StructureFile.xyz

```

```
%output
 Print [P_Loewdin ] 1
 Print [P_BondOrder_L ] 1
 Print [P_ReducedOrbPop_L] 1
 Print [P_FragPopMO_L] 1
 Print [P_ReducedOrbPopMO_L] 1
end
```

Listing C.12: Input file for a non-self-consistent calculation used to read the occupations of the quasi-restricted orbitals.

The MOs with the highest d character are found from the Loewdin population analysis in the main output file. As an example, below we display the results of the Loewdin population analysis for compound **1** in bulk structure.

```
----------------------------------------
LOEWDIN REDUCED ORBITAL POPULATIONS PER MO
----------------------------------------
THRESHOLD FOR PRINTING IS 0.1%
SPIN UP
....
                120        121        122        123        124        125
              -0.20382   -0.19220   -0.18862   -0.15726   -0.12688   -0.11815
               1.00000    1.00000    1.00000    1.00000    1.00000    1.00000
              --------   --------   --------   --------   --------   --------
 0 Co s          0.6        0.0        0.1        0.0        0.0        0.2
 0 Co pz         0.0        0.3        0.0        0.5        0.8        0.0
 0 Co px         0.0        0.4        0.0        0.7        0.5        0.0
 0 Co py         0.2        0.0        0.7        0.0        0.0        1.5
 0 Co dz2       17.4        0.0        2.8        0.0        0.0       43.7
 0 Co dxz       53.7        0.0        0.3        0.0        0.0       20.4
 0 Co dyz        0.0        0.3        0.0        7.8       79.4        0.0
 0 Co dx2y2      0.2        0.0       13.5        0.0        0.0       19.0
 0 Co dxy        0.0        1.3        0.0       84.2        6.3        0.0
....
```

Listing C.13: Loewdin population analysis from a DFT calculation of compound **1** in ORCA.

Line 7 is the assigned number of the MO, line 8 is its energy in Hartree units, and line 9 is its occupation in number of electrons. The next lines give information about the contribution of each atomic orbital to the MO. For example, line 17 tells us that the $3d_{yz}$ orbital of cobalt contributes 79.4% to the MO 124. In the calculation, orbital 125 is the HOMO, and it can be seen that the MOs 121 and 122 do not have significant contributions from cobalt's d orbitals. Instead, orbitals 119 and 120 have high cobalt d orbital contributions and must be part of the complete-active space.

Now, we perform the CASSCF-NEVPT2 calculation. We use the same basis set and auxiliary basis, and request to perform second-order perturbation theory through the NEVPT2 method using the tag `RI-NEVPT2` (strongly-contracted NEVPT2 with the resolution of identity approximation). The complete active space is set to cobalt's five 3d orbitals, with seven electrons corresponding to the valence of Co(II). The canonical orbitals from the last DFT calculation are also read, and a rotation of the MOs 119 and 120 into 121 and 122 is done to account for the correct active space. We used the following input file for CASSCF-NEVPT2 calculations:

```
! def2-TZVP def2/J def2-TZVP/C RIJCOSX tightscf grid6 gridx6 SOMF(1X) RI-
   NEVPT2 nofrozencore
%basis
newgto C "def2-SVP" end
```

```
newgto H "def2-SVP" end
end

%pal nproc 50 end  # Number of processing cores
%maxcore 4000      # Memory per core

%scf
rotate {119,121,90} {120,122,90} end #Rotating MOs 119 and 120 into the CAS
end

! MOread
%moinp "jobname2.gbw"  # Canonical orbitals from the second calc.

!Printbasis
%output
    print[p_mos] 1
end

%casscf
    nel 7          # Number of active electrons
    norb 5         # Number of active orbitals
    MaxIter 400    # Max number of casscf iterations
    trafostep RIMO # speed up the integral trafo
    actorbs dorbs  # perform ligand field theory analysis
                   # the active space must be the 3d orbitals
    mult 4,2       # Multiplicity blocks
    nroots 10,40   # Roots per multiplicity block

    rel
        dosoc true    # Compute spin-orbit coupling
        dossc true    # Compute spin-spin coupling
        gtensor true  # Compute the g-tensor
    end
end

* xyzfile 0 4 compound1.xyz
```

Listing C.14: Input file for CASSCF-NEVPT2 calculations for compound **1**.

D. Plane-wave DFT calculations: Supercell Size, Charge Density Difference, and Density of States

We present the supercells used in plane-wave DFT calculations for the molecular compounds on graphene, as well as the charge density difference and density of states plots of the configurations not shown in chapter 4.

D.1. Supercell Shape and Size

For compounds **1** and **2**, we used a unit cell that can accommodate a 10×10 graphene supercell, while for compound **3** two different sizes of unit cells were for each configuration. Fig. D.1 shows the supercells.

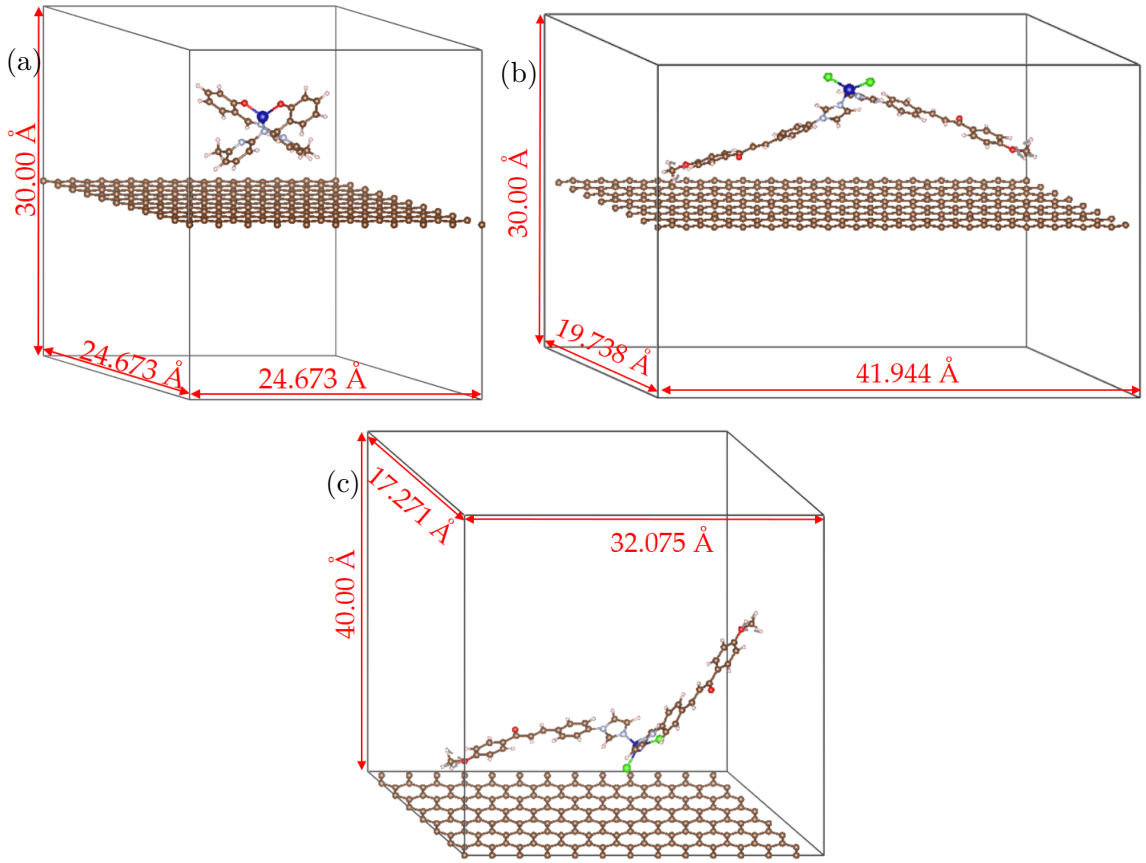

Figure D.1: Supercells used in plane-wave DFT calculations. (a) Supercell for compounds **1** and **2**. As an example, conf. 1 of compound **1** is shown. (b) Supercell for compound **3** in conf 1. (c) Supercell for compound **3** in conf 2. The figures were generated on VESTA [165].

D.2. Charge Density Difference

Fig. D.2 shows the charge density difference plots for compounds **1** and **2** in Confs. 3 and 4, calculated with electric dipole corrections. Comparing with Fig. 4.8, we observe that Confs. 1 and 3 of both compounds have a similar behavior of charge accumulation near the graphene substrate, while Confs. 2 and 4 the behavior is more complex due to the emergence of regions of charge accumulation in the molecule close to the hydrogen, nitrogen, and oxygen atoms, as discussed in chapter 4.

Figs. D.3 and D.4 plot the comparison of the planar average of the charge density difference computed with and without electric dipole corrections. As explained in the main text, dipole corrections change considerably the charge transfer behavior and the regions of charge accumulations in each molecule, in some cases reducing and in others increasing the charge transfer.

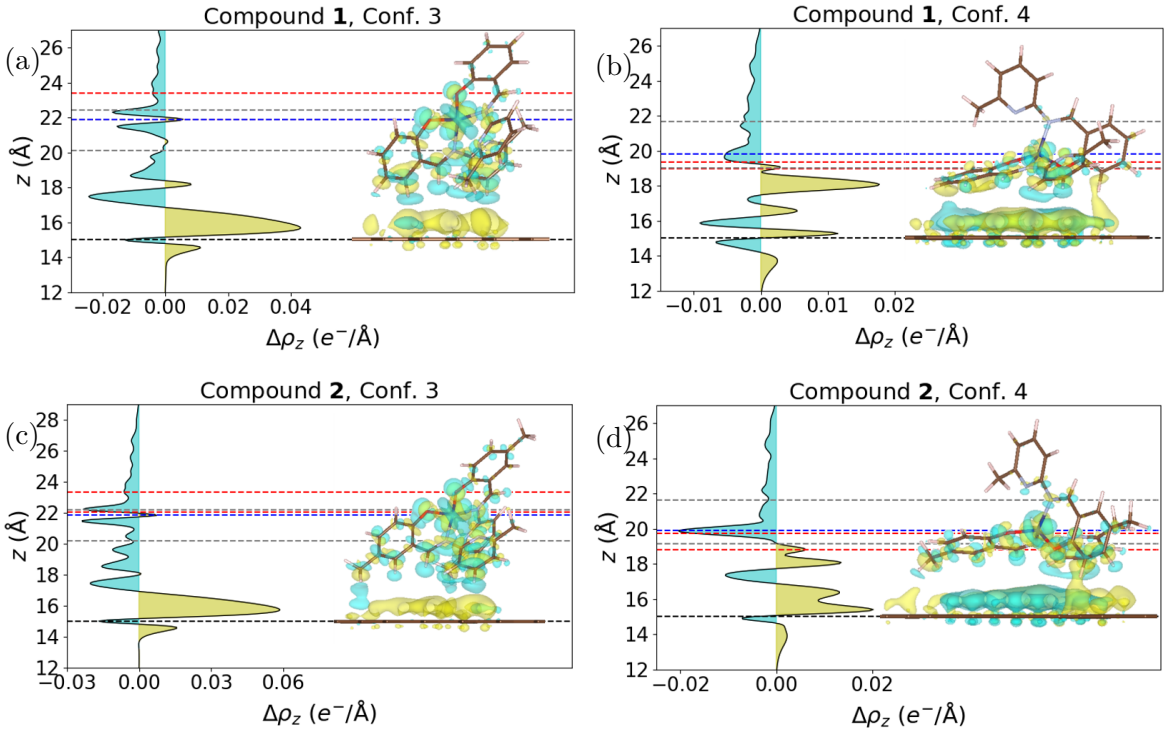

Figure D.2: Planar average of the charge-density difference of compound **1** in Confs. 3 and 4 (a,b), and **2** in Confs. Confs. 3 and 4 (c,d). Superimposed on each figure are isosurface plots of the charge density difference, with isosurface level 10^{-3} e/Å^3. Yellow and cyan colors represent charge accumulation and depletion, respectively. The dashed lines correspond to the vertical locations of graphene (in black), the Co center (blue), the coordinating oxygens (red), and coordinating nitrogens (grey).

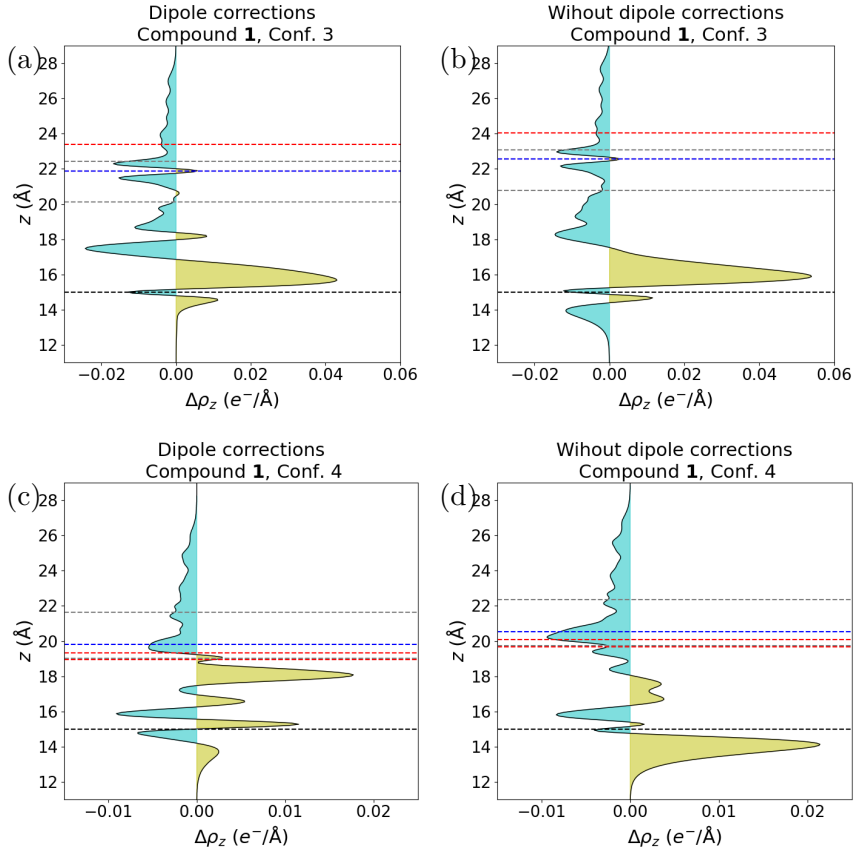

Figure D.3: Comparison of the planar average of the charge-density difference computed with (a,c) and without (b,d) electric dipole corrections, for molecule **1** in Confs. 3 and 4. Dashed lines indicate the locations of the graphene substrate (black), the cobalt center (blue), coordinating oxygens (red), and coordinating nitrogens (grey).

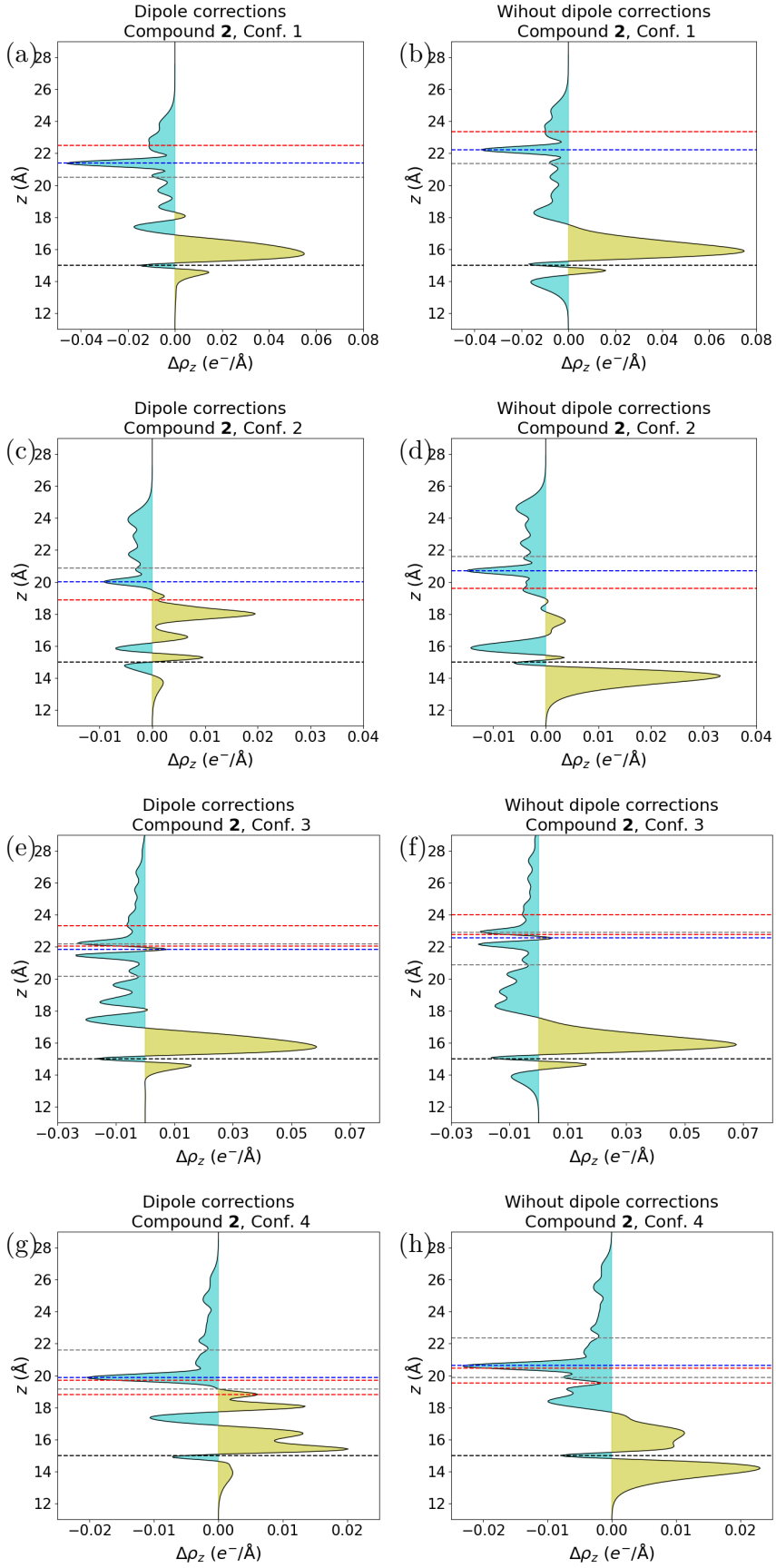

Figure D.4: Comparison of the planar average of the charge-density difference computed with (a,c,e,g) and without (b,d,f,h) electric dipole corrections, for molecule **2** in Confs. 1-4. Dashed lines indicate the locations of the graphene substrate (black), the cobalt center (blue), coordinating oxygens (red), and coordinating nitrogens (grey) atoms.

D.3. Density of States

Fig. D.5 shows the partial density of states (PDOS) of the studied compounds on graphene and the PDOS of the graphene substrate in each configuration. In all cases, except Conf. 3 of compound **3**, there is charge transfer from the HOMO of the molecule to graphene, leading to n-doping. The PDOS was obtained by calculating the DOS of each molecule + substrate system and then selecting the atoms of molecule and substrate separately, considering the contribution from all atomic orbitals (s, p, and in Co case, d orbitals).

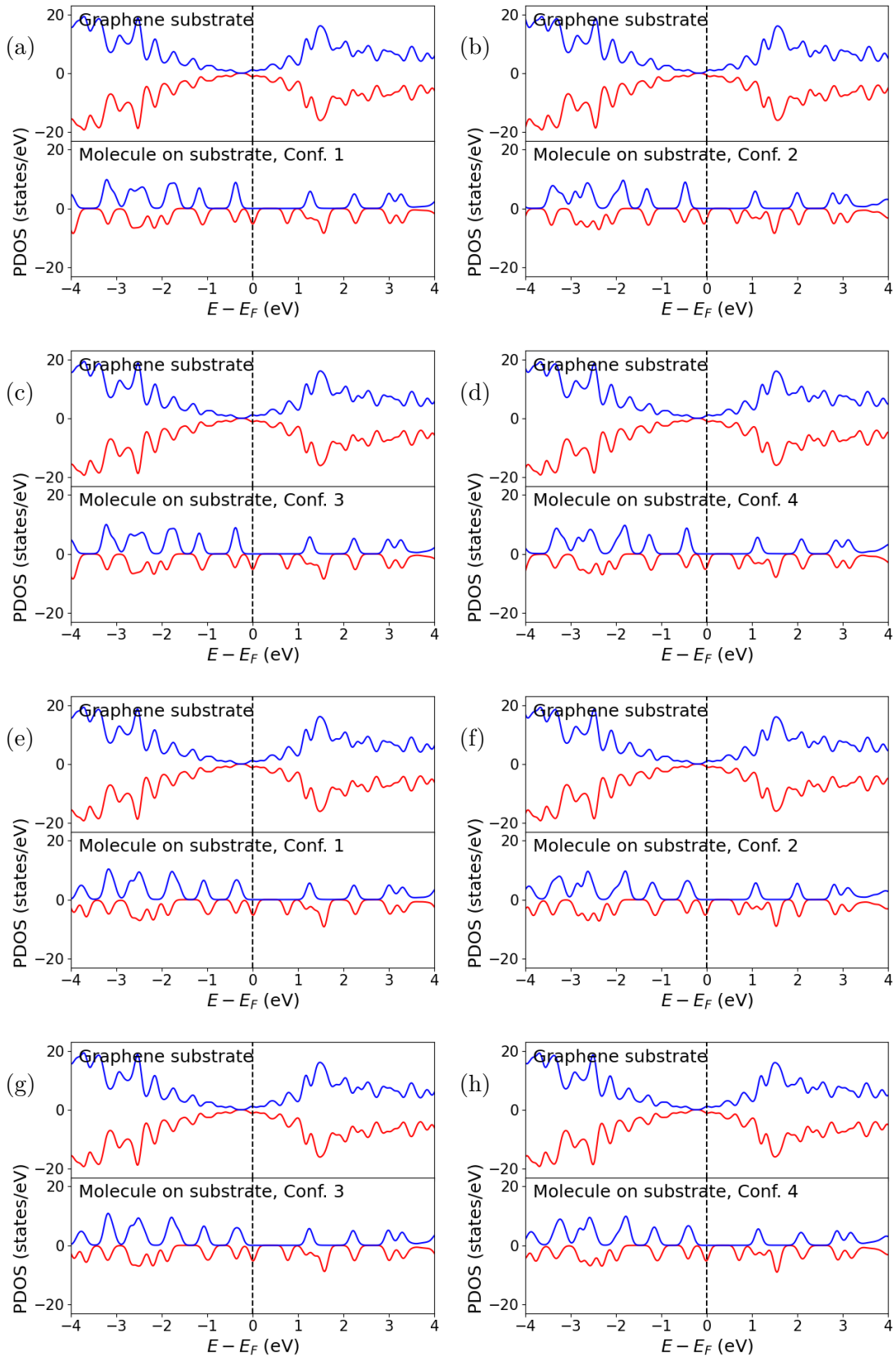

Figure D.5: (a-d) Partial density of states (PDOS) for all Configs. of compound **1** on graphene. (e-h) Partial density of states (PDOS) for all Configs. of compound **2**.

List of Abbreviations

AC	Alternating Current
AFM	Atomic Force Microscopy
B3LYP	Becke, 3-parameter, Lee–Yang–Parr
BS-DFT	Broken Symmetry Density Functional Theory
BUT	Brno University of Technology
BZ	Brillouin Zone
CAS	Complete Active Space
CASSCF	Complete Active Space Self-Consistent Field
CDW	Charge-Density Wave
CEITEC	Central European Institute of Technology
CVD	Chemical Vapor Deposition
CW	Continuous Wave
DC	Direct Current
DFT	Density Functional Theory
DOS	Density of States
EPR	Electron Paramagnetic Resonance
GFET	Graphene Field-Effect Transistor
HF	Hartree-Fock
HFEPR	High-Frequency Electron Paramagnetic Resonance
HOMO	Highest-Occupied Molecular Orbital
LLs	Landau Levels
LUMO	Lowest-Unoccupied Molecular Orbital
MEYS CR	Ministry of Education, Youth, and Sports of the Czech Republic
MOTES	Magneto-Optical and THz Spectroscopy
NEVPT2	N-Electron Valence State Second-Order Perturbation Theory
PBE	Perdew-Burke-Ernzerhof
PDOS	Partial Density of States
RMM-DIIS	Residual Minimization Scheme, Direct Inversion in the Iterative Subspace
SdHO	Shubnikov-de Haas Oscillations
SDW	Spin-Density Wave
SMMs	Single-Molecule Magnets
SOC	Spin-Orbit Coupling
SWM	Slonczewski-Weiss-McClure
VASP	Vienna Ab-Initio Simulation Package
vdW	van der Waals
WAL	Weak Antilocalization
WL	Weak Localization
XPS	X-ray Photoelectron Spectroscopy
XRD	X-Ray Diffraction
ZFS	Zero-Field Splitting